Université du Québec
Institut National de la Recherche Scientifique (INRS)
Centre Armand-Frappier Santé Biotechnologie

Le rôle des adhésines bactériennes dans la motilité de type « *gliding* » chez la bactérie *Myxococcus xanthus*

Par

Nicolas Yann JOLIVET

Thèse présentée pour l'obtention du grade de
Philosophiae Doctor (Ph.D.)
en Biologie

Jury d'évaluation

Président du jury et examinateur interne	Pr. Charles Dozois Institut National de la Recherche Scientifique Centre Armand-Frappier Santé Biotechnologie
Examinateur externe	Pr. Sven van Teeffelen Université de Montréal Dépt. de Microbiologie, Infectiologie et Immunologie
Examinateur externe	Pre. Stephanie C. Weber McGill University Dept. of Biology
Directeur de recherche	Pr. Salim Timo Islam Institut National de la Recherche Scientifique Centre Armand-Frappier Santé Biotechnologie

REMERCIEMENTS

En commençant mon doctorat, on m'avait expliqué que la recherche était une activité qui nécessitait de travailler à plusieurs et de partager les expertises pour avancer. Je n'ai compris qu'après que cela n'impliquait pas que les groupes de recherches, mais l'ensemble des personnes qui gravitent autour du domaine et que le partage était primordial.

Les remerciements ne sont jamais vraiment lus par qui que ce soit. Néanmoins, je me dois de remercier mon père pour ses nombreux conseils et encouragements ; lui qui a cru en moi et qui m'a soutenu dans toute l'épreuve qu'a été mon doctorat. Je remercie également les frères, Thomas, et Baptiste pour leur soutien et les distractions bienvenues au long de mon doctorat.

Je me dois de remercier ma conjointe, Gladys, qui m'a encouragé à me lancer dans cette aventure. Je remercie mes collègues, avec qui nous nous sommes soutenus : Aurélie, Émilie, Martin, Eve, Farès, Rose, Clément, Antoine, et bien d'autres que je ne citerais pas, par manque de place. Je remercie également mon directeur, Pr. Salim Islam qui m'a fait confiance et ma guidée dans les méandres de la vie en recherche. Je remercie les membres de mon jury de thèse, qui ont la responsabilité de corriger et évaluer ma thèse. Je remercie l'ensemble de l'INRS—Centre Armand-Frappier Santé Biotechnologie pour l'opportunité qu'il donne à de jeunes étudiants et étudiantes de participer à l'aventure qu'est la Recherche.

Petite pensée également pour nos collaborateurs et collègues du Laboratoire d'Adhésion et Inflammation de Marseille qui m'ont accueilli et guidé dans ma découverte de la microfluidique.

Enfin, un remerciement spécial à ma mère qui, je l'espère, est fière de moi.

RESUME

La motilité est une caractéristique essentielle au développement du vivant. Chez les procaryotes, les systèmes permettant à une cellule ou à un groupe de cellules de coloniser l'environnement sont nombreux. Certains de ces systèmes, regroupés en catégorie selon leurs mécanismes, ont été l'objet d'études depuis plusieurs décennies. C'est le cas de la motilité de type « *gliding* », et notamment de celui du modèle d'étude : *Myxococcus xanthus*. Cette bactérie Gram négative est un sujet d'étude en raison de son cycle de vie dit « social » de par sa capacité à mettre en avant des caractéristiques typiques d'une coordination des cellules telle que la prédation, la motilité dépendante des *pili* de type IV, ou encore la différenciation cellulaire en spores. D'autre part, la bactérie présente un mécanisme de *gliding* qui est proposé pour participer à la coordination des phénotypes « sociaux ». Ce *gliding*, réalisé par des cellules individuelles sur surface solide n'utilise pas d'organelle, mais la machinerie protéique transmembranaire Agl–Glt. Cette motilité implique le transport dirigé du complexe *gliding transducer* (Glt) du pôle avant vers le pôle arrière de la cellule. Ces complexes de motilité liés au substrat apparaissent fixés dans l'espace par rapport à la surface, formant un complexe d'adhésion focale bactérienne (bFA). L'ancrage du complexe au substrat implique une adhésine qui fixe la surface et relie la surface au reste de la machinerie. Les travaux présentés ici portent sur les protéines CglB et CglD, identifiées depuis 1977 comme nécessaires au *gliding*, mais non caractérisées. Le suivi des comportements de *gliding* des mutants, ainsi que l'étude de la formation des bFAs par plusieurs techniques de microscopie, m'a permis de mettre en évidence les fonctions de ces deux protéines et le lien que peuvent avoir ces dernières avec le reste de la machinerie Agl–Glt, notamment au niveau de la membrane externe. Les travaux de biochimies et de microscopie ont pu mettre en avant la relation entre les protéines et la machinerie Agl-Glt permettant l'identification d'un complexe protéique CglB–GltKBAH. De plus, la bio-informatique a permis de mettre en avant plusieurs domaines typiques des intégrines. Enfin l'étude de CglD a mis en évidence un caractère mécanosenseur de la protéine, caractéristique des intégrines eucaryotes. Cette thèse met en avant les points communs entre les intégrines eucaryotes et les protéines CglB et CglD dans la mise en place d'une adhésion focale et une motilité cellulaire efficace.

Mots-clés : *Myxococcus xanthus*, *gliding*, adhésion focale bactérienne, intégrines, motilité, adhésines.

ABSTRACT

Motility is an essential characteristic for the development of living organisms. In prokaryotes, numerous systems allow a single cell or group of cells to colonize the environment. Some of these systems have been grouped into categories and their mechanisms have been studied for several decades. This is the case for “gliding”, and in particular gliding in the model organism *Myxococcus xanthus*. This Gram-negative bacterium is a subject of study because of its so-called "social" life cycle due to its ability to display characteristics typical of a significant degree of cell coordination such as predation, cell-dependent motility, type IV pili, or cell differentiation into spores. On the other hand, the bacterium exhibits a gliding mechanism which is proposed to participate in the coordination of “social” phenotypes. This gliding, carried out by individual cells on a solid surface, does not use an external appendage, but rather an Agl–Glt transmembrane protein machinery. This form of motility involves the directed transport of the gliding transducer complex (Glt) from the front pole to the rear pole of the cell. These substrate-bound motility complexes appear spatially fixed relative to the substratum, forming a focal adhesion (FA) complex. Prior to my work, the mechanism of Agl–Glt substratum-anchoring was unknown. The work presented here focuses on the proteins CglB and CglD, which have been identified as essential for gliding since 1977 but have not been characterized until now. The tracking of gliding behavior in mutants, along with the study of bFA formation using various microscopy techniques, allowed me to highlight the functions of these two proteins and the link they may have with the rest of the Agl–Glt machinery, particularly at the outer membrane level. Biochemical and microscopy work helped reveal the relationship between the proteins and the Agl-Glt machinery, leading to the identification of a protein complex called CglB–GltKBAH. Additionally, bioinformatics highlighted several typical integrin domains. Furthermore, the study of CglD revealed a mechanosensory characteristic of the protein, similar to eukaryotic integrins. This thesis emphasizes the commonalities between eukaryotic integrins and the proteins CglB and CglD in establishing focal adhesion and efficient cell motility.

Keywords: *Myxococcus xanthus*, gliding, bacterial focal adhesion, integrins, motility, adhesins.

TABLE DES MATIÈRES

LISTE DES FIGURES & TABLEAUX

LISTE DES ABRÉVIATIONS

BPS : biosurfactant polysaccharide

bFA : bacterial focal adhesion

COMP : cartillage oligomeric matrix protein

Cgl : conditional gliding

Cys : cystéine

DTT : dithiothreitol

ECM : extracellular matrix

EDTA : ethylene diaminetetraacetic acid

EPS : exopolysaccharide

eFA : eukaryotic focal adhesion

FA: focal adhesion

Glt : gliding transducer

GFP : green-fluorescent protein

IM : inner membrane

MASC : major spore coat

MIDAS : metal ion-dependent adhesion site

MSD : mean squared displacement

OM : outer membrane

T2SS : système de sécrétion de type II/*type II secretion system*

T4P : type IV pilus

TCA : trichloroacetic acid

TFM : traction force microscopy

TIRFM : total internal reflection fluorescence microscopy

VWA : von Willebrand A

YFP : yellow-fluorescent protein

WT : wild type

Ω*gène* : Mutation par insertion d'une cassette de résistance à un antibiotique de le gène

Δ*gène* : Délétion propre du gène

Chapitre 1 : REVUE DE LITTÉRATURE

1.1 LES MOUVEMENTS DES BACTÉRIES

1.1.1 Introduction

L'étude du mouvement chez les organismes unicellulaires et multicellulaires apporte de nouvelles informations bénéficiant aux domaines de recherches de la médecine à l'agriculture ; en passant par l'agroalimentaire, écologie et même à l'industrie du transport (Arora *et al.*, 2007; Babalola, 2010; Grossart *et al.*, 2001; Josenhans & Suerbaum, 2002).

L'étude du mouvement du vivant s'est développée au cours du temps, et les outils pour sa compréhension ont évolué : des microscopes plus performants, des outils génétiques permettant l'amplification (ou la délétion) des gènes impliqués, les analyses des structures des protéines, l'imagerie de pointe, jusqu'à la mesure d'une simple molécule. Toutes ces avancées dans les domaines de la recherche ont permis d'identifier les mécanismes de déplacements, leurs spécificités et leurs différences (Miyata *et al.*, 2020).

Le mouvement du vivant est, depuis l'invention du premier microscope, une thématique de recherche très étudiée. Déjà Leeuwenhoek lors de l'utilisation de son microscope observait de « petits animaux » mouvant dans de l'eau de pluie (Leeuwenhoek, 1677). Le déplacement d'un organisme peut être une caractéristique déterminante pour l'évolution et la survie de ce dernier. Le mouvement permet aux organismes (i) de coloniser de nouveaux milieux pour obtenir des nutriments (ii) d'éviter la présence de toxines/prédateurs/stresses environnementaux, ou (iii) de partager d'informations génétiques avec d'autres organismes. Chez les Eucaryotes plus spécifiquement, le déplacement permet le développement d'activités telles que la réponse immunitaire et la cicatrisation (Miyata *et al.*, 2020). Dans toutes ces situations, la capacité d'un organisme à se déplacer dans son environnement est un facteur important à la survie et à l'adaptation de l'espèce à son milieu de vie.

La définition du mouvement, ou de la motilité, peut être sujet à interprétations : selon Makoto Hiyata *et al.* ou Robert Day Allen : *« La motilité est la capacité de déplacement d'un organisme ou d'une cellule à convertir de l'énergie chimique en un déplacement de l'ensemble de l'organisme ou d'une cellule en utilisant une machinerie motrice dédiée »* (Allen, 1981). Selon les dictionnaires Larousse, la motilité est une « *Aptitude à effectuer des*

mouvements spontanés ou réactionnels, constituant l'un des caractères du vivant à toutes les échelles d'observation. »

Une définition intermédiaire sera utilisée : la motilité étant la capacité de déplacement d'une cellule à se déplacer dans son environnement avec ou sans organelles.
Cette définition simplifiée permet de regrouper un large éventail de déplacements dans le Vivant (**Figure 1.1**). Je ne détaillerai pas l'ensemble de ces derniers, et je m'attarderai sur les stratégies évolutives mises en place par les bactéries et certains organismes eucaryotes présentant des parallèles pertinents avec mes études.

La classification des mouvements des organismes vivants dépend des paramètres que l'on étudie : selon l'ordre du vivant (Procaryote/Eucaryote), selon l'ordre de vitesse, selon les sources d'énergie utilisées ou même selon l'environnement dans lequel l'organisme se déplace (air/liquide/surface). Je choisirai pour cet exposé de classer les mouvements, selon l'utilisation d'appendices.

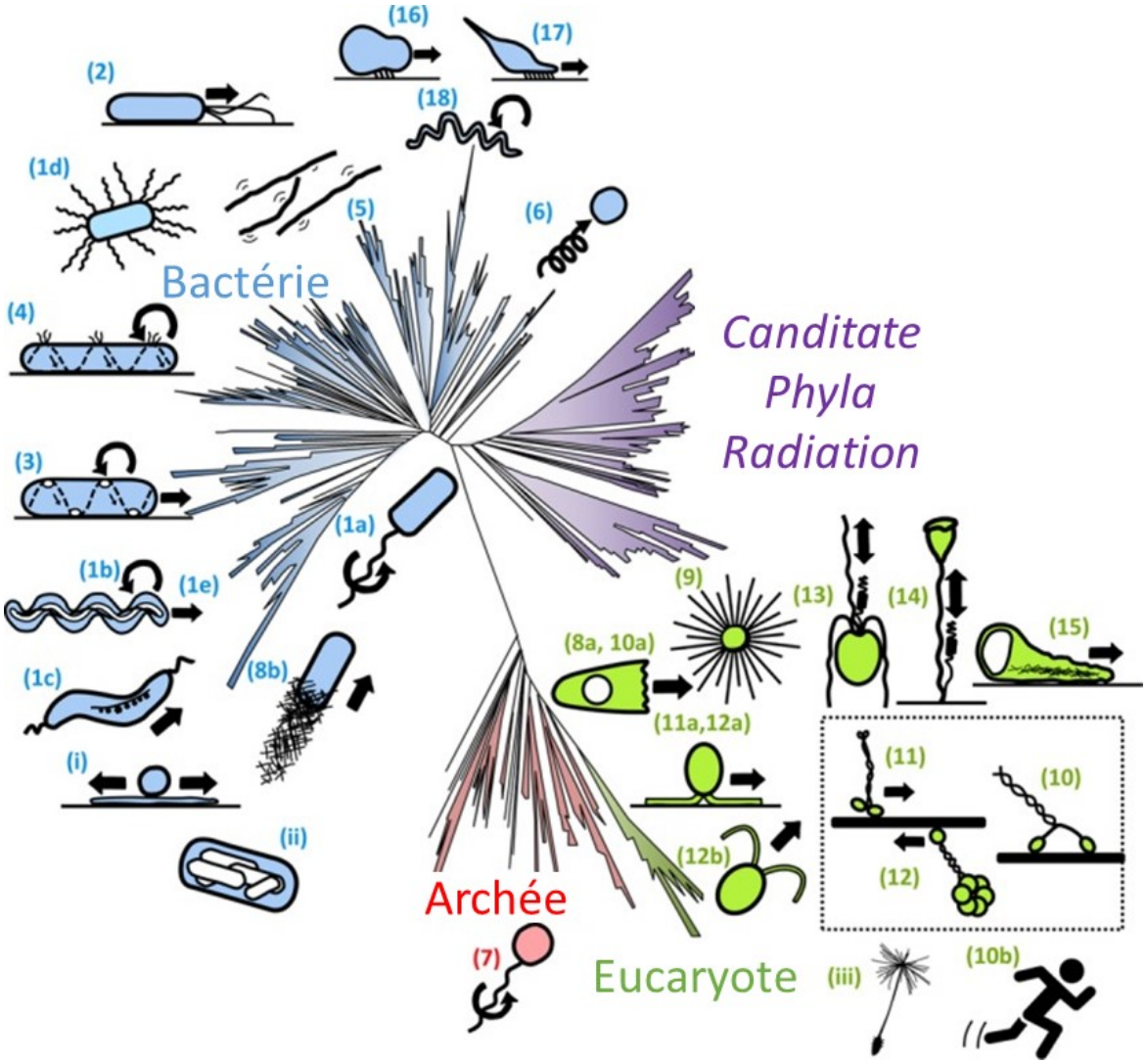

Figure 1.1. Représentation des différents types de motilité du Vivant.

1a : Motilité bactérienne flagellaire. 1b : Motilité flagellaire des spirochètes. 1c : Motilité bactérienne flagellaire magnétotactique. 1d : *Swarming* bacterien. 1e : Crawling de *leptospira spp.* 2 : Motilité avec *pili.* 3 : Gliding de *M. xanthus*. 4 : Gliding des *Bacteriodetes.* 5 : Motilité de surfaces de *Chloroflexus aggregans*. 6 : *Swimming* non flagellaire de *Synechococcus spp*. 7 : *Swimming* de *archaella spp*. 8a : Motilité basée sur la polymérisation d'actine de *amoeba.* 9 : Motilité basée sur la dépolymérisation de microtubules de *heliozoa.* 10 : *Sliding* de myosine. 11 : *Sliding* de kynésine. 12: Sliding de dynéine. 10a : Contraction actin–myosin. 10b : Contraction musculaire animale. 11a et 12a : Motilité de surface flagellaire. 12b : Swimming flagellaire. 13 : Contraction haptonémique. 14 : Contractions de spasmonème. 15 : Motilité amiboïde du sperme de nématode. 8b : Motilité en queue de comète basée sur l'actine. 16 : Gliding de *Mycoplasma mobile* 17 : Gliding de *Mycoplasma pneumoniae.* 18 : *Swimming* de *Spiroplasma.* (i) : *Sliding* bactérien. (ii) : vésicule gazeuse. (iii) : Graine de pissenlit. Adaptée de **(Miyata *et al.*, 2020)**.

1.1.2 Physiologie bactérienne

Afin de mieux comprendre les spécificités de mouvement des bactéries, une présentation de la physiologie et de l'architecture des bactéries est nécessaire. Ce groupe du vivant a été identifié pour la première fois grâce à l'invention du microscope en 1676 (van Leeuwenhoek, 1677). Depuis plusieurs travaux ont permis de catégoriser et de classer les organismes, mais c'est en 1938 que les bactéries ont été classées comme un règne. Les bactéries se distinguent des autres embranchements du vivant par l'absence d'organelles membranés (tel que le noyau, le chloroplaste et la mitochondrie) (Stanier & Van Niel, 1962).

La caractérisation d'une bactérie à se faire selon plusieurs critères : la possibilité de respirer (anaérobie/aérobie strict, ou non), la possibilité de fermentation, ou encore la morphologie. Si la plupart des bactéries sont en forme sphérique (coque) ou en bâton (bacille), certaines comme les Spirochètes sont en forme de bacille hélicoïdal.

Une autre façon de regrouper les bactéries, basée elle aussi sur la morphologie, est le test de Gram, développé par le chercheur du même nom en 1884 (Gram, 1884). Ce test utilise les propriétés de coloration de la paroi bactérienne pour déterminer si la bactérie possède une fine couche de peptidoglycane et deux membranes lipidiques (Gram négatif), ou bien une grande quantité de peptidoglycane, mais une seule membrane (Gram positif) (**Figure 1.2**). Cette différence entre les deux groupes de bactéries est importante dans cette thèse en raison de la localisation des protéines que nous étudierons et qui sont associées à la membrane externe de la bactérie Gram négative *Myxococcus xanthus*.

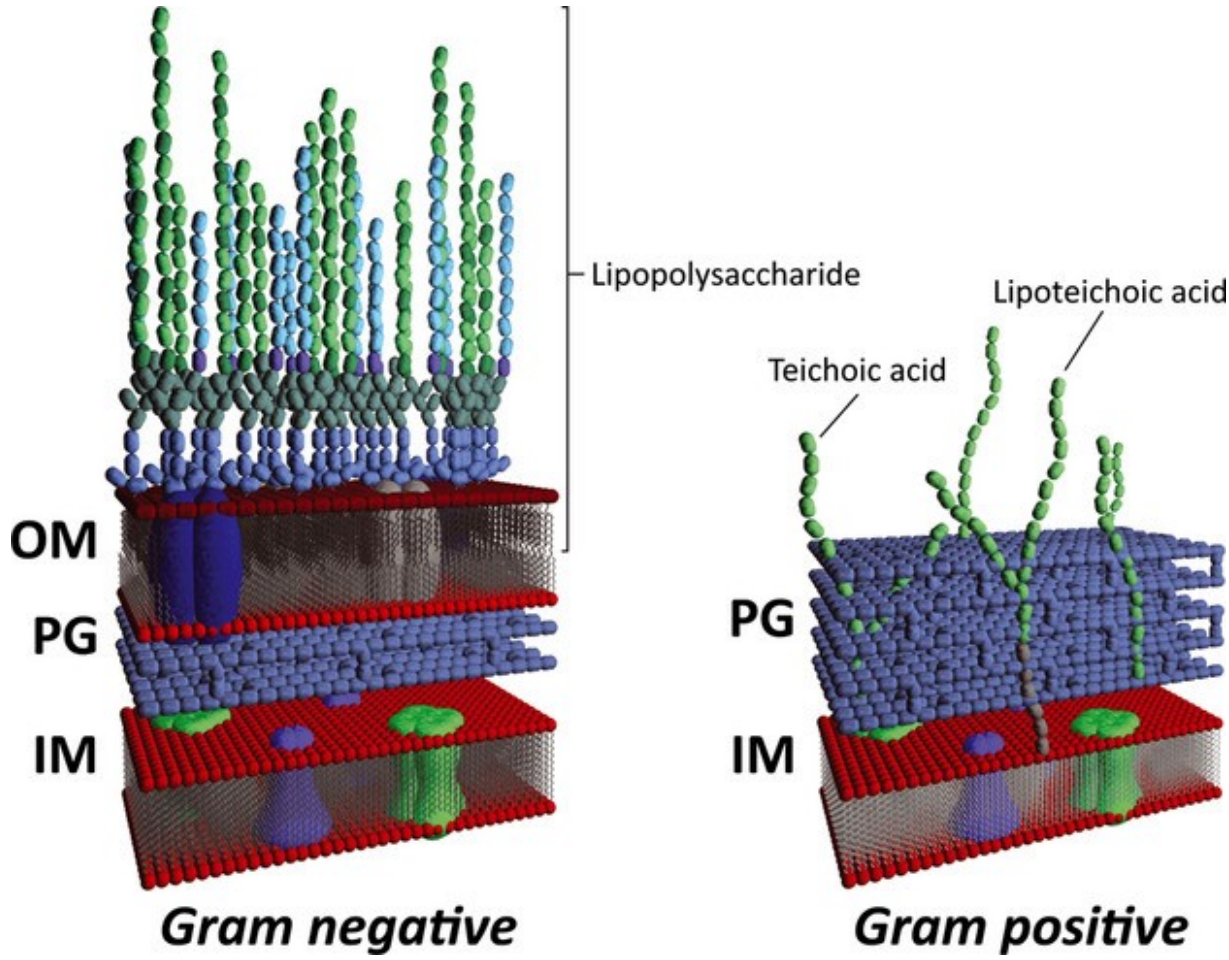

Figure 1.2. Architecture des bactéries Gram négatives et Gram positifs.

Architecture de l'enveloppe cellulaire chez les bactéries Gram négatifs et Gram positifs. Les protéines transmembranaires sont présentes dans la membrane interne des deux types de bactéries et sont également présentes dans la membrane externe de ces dernières. IM, membrane interne ; PG, peptidoglycane ; OM, Membrane externe. Adapté de (Islam & Lam, 2013)

1.1.3 Mouvements utilisant des appendices de motilité

1.1.3.1 Motilité flagellaire

Le mouvement des bactéries est souvent représenté par la motilité de type flagellaire, notamment avec une bactérie en forme de bacille. Les flagelles permettent aux bactéries de « nager » (*swim*) dans un milieu liquide par rotation de l'appendice (Nakamura & Minamino, 2019; Silverman & Simon, 1974). Ce type d'appendice, biens que retrouver chez plusieurs espèces est particulièrement étudié chez la bactérie modèle *Escherichia coli* (Berg, 2003; Berg, 2004). Cet appendice est composé du filament (externe ou interne, détaillé plus loin), du moteur et du crochet. On peut retrouver des flagelles à différentes positions sur les cellules : sur les pôles (on parle de position polaire pour lorsqu'il y a un flagelle, et de *lophotrichious* lorsqu'il y a plusieurs flagelles), le long de la cellule (on parle de position médiale lorsqu'il y a un seul flagelle et de petrichious lorsqu'il y en a plusieurs) (Guttenplan *et al.*, 2013; Schuhmacher *et al.*, 2015).

Le mouvement circulaire est énergisé par un moteur à protons composé de plus de 20 protéines différentes assemblées au travers des membranes (uniquement la membrane interne chez les Gram-positives) et du peptidoglycane (Cheng *et al.*, 2018; Minamino *et al.*, 2008) (**Figure 1.2**). Je ne détaillerai pas ici les composants, mais je noterai que la machinerie protéique transmembranaire peut être divisée en 3 parties : (i) le corps basal, comprenant le *C-ring* cytoplasmique, le *MS-ring* dans la membrane interne, le moteur (MotA/MotB) dans le périplasme et la membrane interne, le *P-ring* dans le périplasme, et le *L-ring* dans la membrane externe ; (ii) le crochet (*Hook)* et (iii) le filament avec son extrémité, ces derniers dans le milieu extracellulaire (**Figure 1.3**) (Berg, 2003; Minamino *et al.*, 2008). (Je note que les Gram positifs ne possèdent pas les parties *P-ring* et *L*-ring (Cheng *et al.*, 2018).

Le mécanisme de *swimming* d'*E. coli* représente la forme la plus « classique », mais il existe du *swimming* chez d'autres espèces bactériennes divergeant notamment en raison de la forme des bactéries qui l'utilisent (Wadhwa & Berg, 2022). En effet, si le filament dans le mouvement précédent était en forme d'hélice, dans ces autres mécanismes c'est la bactérie elle-même qui à cette forme. Le genre *Spirilla* ou l'espèce *Campylobacter jejuni* sont des exemples de modèle où la bactérie possède 2 pôles où ces deux pôles ont une implémentation de flagelles (Cohen *et al.*, 2020; Krieg, 1976). La différence avec les bacilles classiques vus

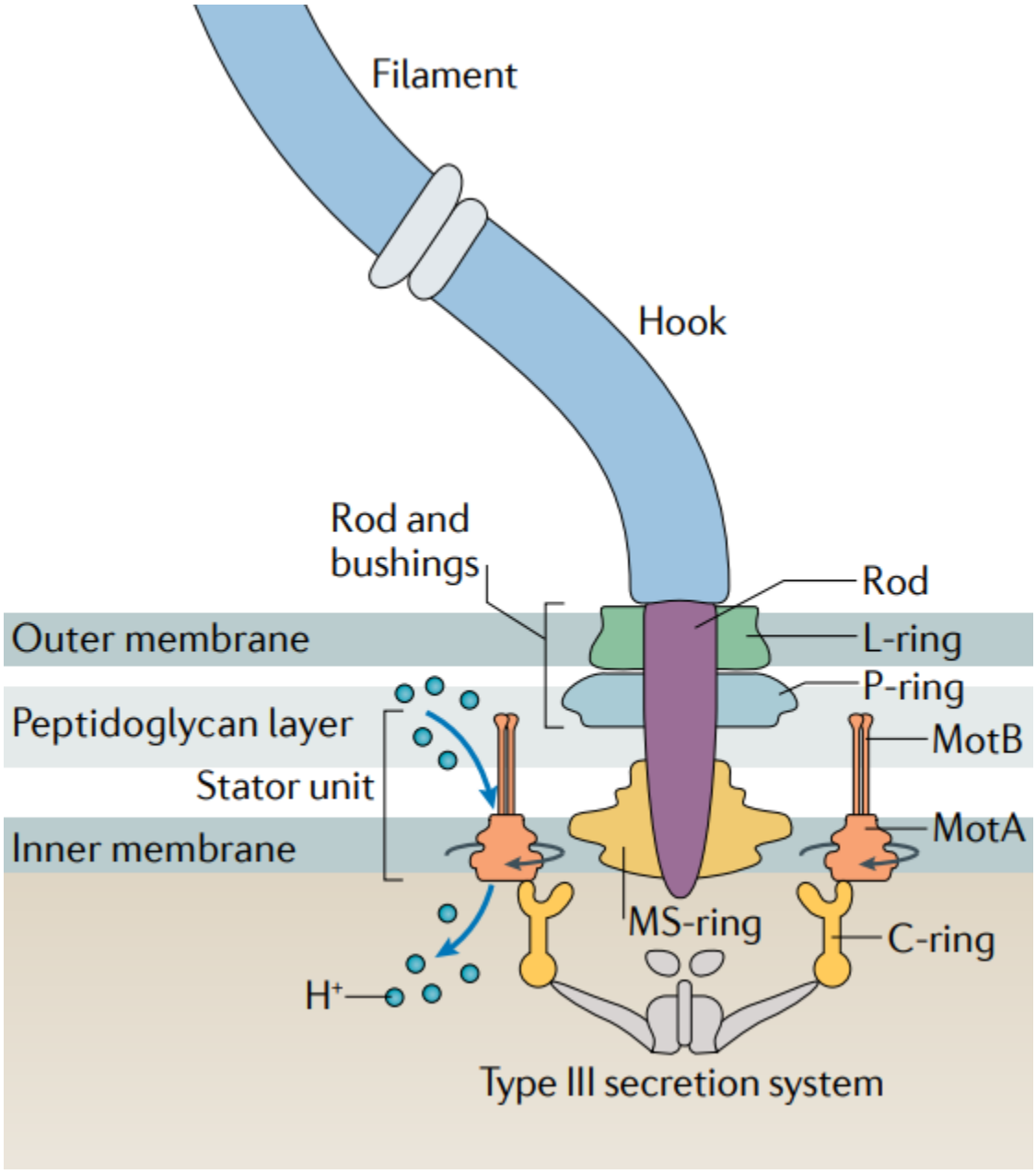

Figure 1.3. Schéma d'architecture de la machinerie de flagelle de *E. coli*.

Le rotor est constitué de l'anneau MS (MS-ring (FliF) qui s'emboite dans la membrane interne. L'anneau C (C-ring) (FliGMN) se situe dans le cytoplasme. Le moteur à proton (MotAB) traverse la membrane interne et fixe le peptidoglycane et l'anneau C. La force de mouvement est transmise par la tige (Rod) au crochet (Hook) et vers le filament. Adaptée de (Wadhwa & Berg, 2022).

classiques vues plus haut est que les deux pôles de flagelles : le faisceau de flagelles (*bundle*) à l'arrière de la cellule pousse cette dernière, alors que celui à l'avant tourne autour de la cellule (Krieg *et al.*, 1967).

D'autres espèces utilisent un système flagellaire interne. C'est le cas de l'embranchement Spirochaetes : un groupe de bactérie à Gram négatif qui, comme pour le genre *Spirilla,* a une forme en hélice avec l'implémentation des flagelles aux pôles. La différence avec les autres types de *swimming* vues plus tôt est que les filaments sont localisés entre le peptidoglycane et la membrane externe (Berg, 1976; Wolgemuth *et al.*, 2006). Cette localisation permet aux cellules de se déplacer en se « vissant » au travers du milieu dans lequel elles évoluent. Ce système permet aux bactéries l'utilisant d'évoluer dans des milieux plus denses (Berg & Turner, 1979).

La dernière catégorie de déplacement utilisant les flagelles est le « *swarming* » ou le fourmillement. Le *swarming* est un type de déplacement qui implique des groupes de cellules possédant des flagelles (en grand nombre) qui permettent le déplacement dans le cadre d'un laboratoire sur des surfaces molles (0.3 – 1 % Agar) (Kearns, 2010). L'activation ou la différenciation des cellules d'un état végétatif à un état de *swarming* est à la fois dû à des signaux chimiques (*quorum sensing*) et à des signaux physiques (contact avec une surface/mécano-senseur) (Belas, 2014). Le mouvement des cellules alignées, associé à une production de biosurfactants et à une hyperflagellation, permet aux groupes de cellules différenciés de se déplacer et donc de coloniser rapidement une surface (Darnton *et al.*, 2010; Harshey & Matsuyama, 1994; Partridge & Harshey, 2013). Ce type de déplacements implique donc un certain degré de coordination et de communication entre les cellules, notamment via le *quorum sensing* (Daniels *et al.*, 2004).

1.1.3.2 La motilité par pili

La motilité par *pili*, ou communément appelée « *twitching* » chez certaines espèces, est un système de motilité très rependue chez les bactéries. Il permet, tout comme le *swarming*, aux bactéries de se déplacer sur des surfaces solides (Burrows, 2012; Maier & Wong, 2015). Ce système utilise le *pilus* comme appendice, plus précisément le *pilus* de type IV (T4P). Ce *pilus* est impliqué dans beaucoup de processus du vivant : la récupération d'ADN, la prédation, le chimiotactisme, la virulence, et comme senseur de surface (Ellison *et al.*, 2017; Evans *et al.*, 2007; Oliveira *et al.*, 2016; Persat *et al.*, 2015; Piepenbrink, 2019). Le

système du T4P partage beaucoup de points communs avec le système de sécrétion de type II des Gram-négatives ou du système des flagelles des Archaea (Jarrell & Albers, 2012; Korotkov *et al.*, 2012). Son fonctionnement revient à un cycle d'extension-fixation-rétractation permettant de tracter les cellules vers la direction de l'extension (Skerker & Berg, 2001). La majorité des bactéries utilise plusieurs *pili* en même temps pour évoluer sur une surface (Saïdi *et al.*, 2021; Talà *et al.*, 2019).

On y retrouve des points communs avec les systèmes transmembranaires évoqués plus haut : des protéines formant des anneaux à différents niveaux des membranes, un pore pour la sécrétion du *pilus*. L'extension du *pilus* étant énergisée par de l'ATP permettant la polymérisation de monomère de la protéine (PilA). Les mécanismes et les protéines impliquées dans cette motilité seront détaillés avec le modèle de *Myxococcus xanthus* dans la section 1.2.

Bien que cette motilité soit possible pour des cellules isolées, on la retrouve généralement utilisée par des groupes de cellules, ce qui explique que cette motilité soit désignée par le terme « social » dans les études portant sur *Myxococcus xanthus* (Spormann, 1999; Wu & Kaiser, 1995). D'autre part, il existe des liens importants entre la production de polysaccarides et l'utilisation de cette motilité par les bactéries : certaines études récentes ont montré que l'absence de certains polysaccarides secrétés impactait la motilité utilisant les T4Ps, notamment chez *M. xanthus* (Islam *et al.*, 2020; Li *et al.*, 2003; Saïdi *et al.*, 2021).

1.1.4 Mouvement sans appendice

1.1.4.1 Généralité

Il existe également la possibilité pour les bactéries de coloniser une surface ou un milieu sans utiliser des appendices. Une façon basique pour cela est d'utiliser l'environnement à sa disposition. La présence d'un courant si la bactérie est dans un liquide lui permet de suivre ce dernier, bien que le contrôle soit limité pour cette dernière. Un autre mécanisme serait la simple division de la cellule sur une surface qui permettrait aux cellules-filles d'occuper de plus en plus de terrain et donc de coloniser l'environnement. Ces mécanismes ne seront pas détaillés ici, car ils impliquent des paramètres en majorité extérieurs aux bactéries directement étudier tels que le milieu et les conditions

environnementales (bien que le temps de génération et une coordination pourraient être impliqués). De plus ces systèmes n'engageraient pas de mécanismes dédiés au mouvement.

Il existe dans la littérature, une catégorie de mouvement qui n'implique pas des appendices, mais d'autres mécanismes permettant aux bactéries de se déplacer. Ces mécanismes ont longtemps été regroupés sous le terme général de « *gliding* ». Ce terme était utilisé pour désigner la motilité sur une surface utilisant une propulsion inconnue et n'utilisant ni *pilus*, ni flagelles. Cette définition large regroupait donc la motilité aventurière de *Myxococcus xanthus*, le *darting* (mouvement de propulsion observé chez *Staphylococcus epidermidis* mais trop peut étudier), et le *sliding*. On retrouve certains articles qui utilisent le terme de *gliding* pour parler des motilités impliquant des cellules seules sur une surface. On pouvait alors lire « le *gliding* utilisant le T4P » dans certaines vieilles revues et études. Par la suite, ce terme a été associé aux mouvements hélicoïdaux des cellules isolées en bacille n'utilisant pas d'organelles visibles (cette redéfinition est notamment due aux travaux sur le *gliding* de *Myxococcus xanthus*).

Les types de motilités dites « *gliding* » de la littérature ont été redéfinis et regroupés dans plusieurs catégories (**Tableau 1.1**). Pour simplifier et être claire dans mes études, j'utiliserai le terme « *gliding* » pour parler d'une motilité impliquant des cellules isolées se déplaçant sur une surface, n'utilisant pas des appendices, mais utilisant une machinerie transmembranaire et des adhésines localisées aux membranes externes. Par ailleurs je ne détaillerai que certaines motilités de type *gliding* qui servent de modèles d'études : les modèles de *Mycoplasma mobile*, *Mycoplasma pneumoniae*, *Flavobacterium johnsoniae* et le modèle de mes études : *Myxococcus xanthus*.

Tableau 1.1. Redéfinition des motilités de type « *gliding* »

Catégorie de motilité	Appendices	Différenciation cellulaire	Vitesse moyenne (µm/s)	Fonction	Bactéries utilisant ce système (non exhaustif)
Sliding	Non	Non	0,03 à 6	Colonisation de surface	*Acinetobacter, Alcaligenes, Bacillus, Escherichia, Flavobacterium, Mycobacterium, Serratia, Streptococcus, Vibrio*
Darting	Non	Non	Trop peu étudié à ce jour	Trop peu étudié à ce jour	*Staphylococcus epidermidis*
Gliding	Mécanismes variables	Non	0,025 à 0,2 variable selon les mécanismes	Colonisation de surface	*Anabaena, Cytophaga, Flavobacterium, Flexibacter, Mycoplasma, Myxococcus, Phormidium, Saprospira, Stigmatella*

1.1.4.2 Modèle Mycoplasma mobile

Le premier modèle de *gliding* que je détaillerai est le modèle de *Mycoplasma mobile*. Cette bactérie Gram positive est un modèle d'étude notamment en raison de cette motilité atypique (Miyata, 2010). Parmi les espèces de *Mycoplasma* capable de *gliding*, *Mycoplasma mobile* est la plus rapide (2–4.5 µm/s) (Miyata & Uenoyama, 2002). Le *gliding* est le seul système actif de déplacement connu chez cette bactérie (Miyata, 2010). La bactérie possède une déformation au pôle avant de la cellule, donnant à la bactérie une forme de poire (Miyata, 2010; Miyata & Uenoyama, 2002). La machinerie de *gliding* est localisée à la base de cette protrusion (Miyata, 2010). Plusieurs protéines ont été identifiées comme étant impliquées dans ce mécanisme de *gliding* : Gli123 (Uenoyama & Miyata, 2005), Gli349 (Adan-Kubo *et al.*, 2006), Gli521 (Nonaka *et al.*, 2010) and P42 (Ohtani & Miyata, 2007). Ces quatre protéines ont été identifiées comme nécessaires au *gliding*, mais pas au maintien de la structure *jellyfish* (ou méduse) qui donne la forme de poire à la cellule (Nakane & Miyata, 2007). Le rôle identifié de la protéine Gli123 est de localiser les autres protéines à des sites précis (Uenoyama & Miyata, 2005). La fonction de la protéine Gli349 est celle de « jambe » et celle de la protéine Gli521 est de la « rotule » ou de l'engrenage de la machinerie (Adan-Kubo *et al.*, 2006; Nonaka *et al.*, 2010). La dernière protéine P42 possède une activité ATPase ce qui indique une fonction dans la motorisation de la machinerie (Ohtani & Miyata, 2007). Plus en détail, Gli349 pourrait être divisé avec un segment transmembranaire, un bras court, un coude, un second bras court, un filament flexible et un pied qui permet la fixation aux surfaces. La protéine Gli521 se divisant en 3 parties : un crochet, un bras, et un ovale en N-terminal liant Gli349 (Adan-Kubo *et al.*, 2006; Uenoyama *et al.*, 2004; Uenoyama *et al.*, 2009) (**Figure 1.4**).

Le mouvement prend origine avec l'hydrolyse de l'ATP dans le cytoplasme par P42, puis l'énergie du moteur est transmise à travers Gli521 à Gli349 permettant la propulsion de la bactérie vers l'avant. L'ensemble de cette machinerie est rattachée aux tentacules de la structure en méduse à la base de la protrusion (Miyata, 2010).

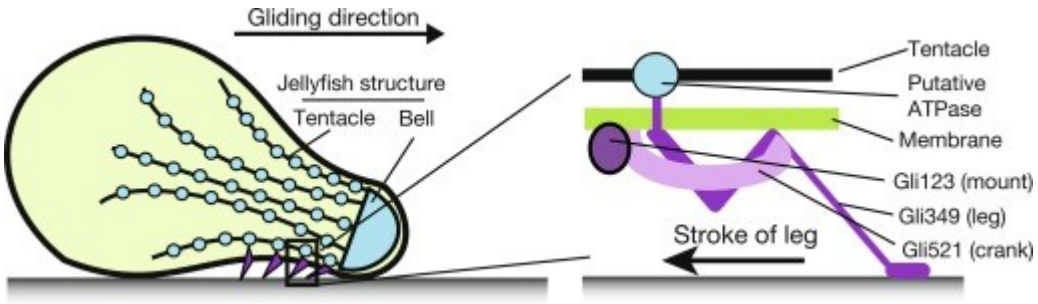

Figure 1.4. Schéma représentatif du gliding de *Mycoplasma mobile.*
À gauche : le schéma de *Myc. mobile* avec la structure de méduse (*jellyfish*). À droite : une représentation détaillée de la région en contact avec la surface. Adaptée de (Nan & Zusman, 2016).

1.1.4.3 Modèle Mycoplasma pneumoniae

Le second type de *gliding* que je résumerai ici est le *gliding* présent chez une autre espèce du genre *Mycoplasma* : *Mycoplasma pneumoniae*. Cette bactérie bien que du genre *Mycoplasma*, le modèle de *gliding* est très différent de celui présenté plus haut. Là où le modèle de *Myc. mobile* était décrit comme celui d'un millepatte, celui de *Myc. pneumoniae* est décrit comme celui d'une chenille. Ce système est généralement moins étudié et montre par ailleurs une vitesse de déplacement moindre (1 µm/s). La partie de la bactérie associée au déplacement se situe à l'avant de la cellule, qui à l'instar de *Myc. mobile* possède elle aussi une forme atypique. Les protéines impliquées dans le *gliding* n'ont pas d'homologue connue chez *Myc. mobile*. La machinerie est divisée en deux parties : interne et exposée à la surface, elle-même divisée en plusieurs parties. La structure interne comprend : le *Bowl* ; les *Paired Plates*, et le *Terminal button*, alors que la structure principale de la partie externe est le domaine d'adhésion GPCA (Miyata, 2008) (**Figure 1.5**).

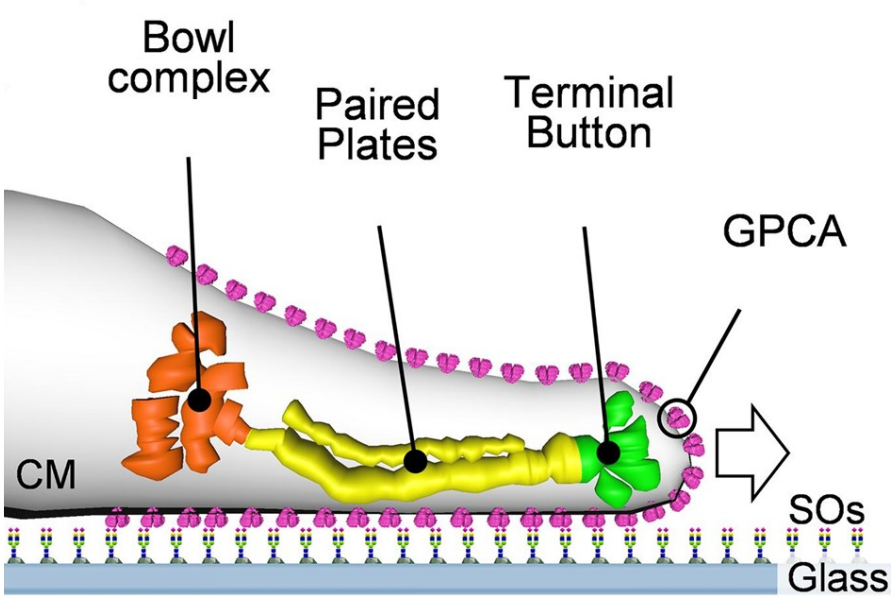

Figure 1.5 : Représentation schématique de la machinerie de gliding chez *Myc. pneumoniae.*

L'illustration montre le gliding sur une lamelle de verre (Glass) recouverte d'oligosaccharides sialylés (SOs). Adaptée de (Mizutani *et al.*, 2021).

1.1.4.4 Modèle Flavobacterium johnsoniae

Le troisième modèle est le genre Bacteriodetes et notamment la bactérie *Flavobacterium johnsoniae*. La vitesse de *gliding* de cette bactérie est de 2 µm/s, énergisés par un moteur à protons (Nakane *et al.*, 2013). Son fonctionnement est très différent des deux modèles précédents : chez *F. Johnsoniae*, le mouvement sur les surfaces est dû à des adhésines disposées à la surface des cellules selon un tracé hélicoïdal, permettant aux cellules de tourner sur leur axe. Les adhésines se détachent de la surface lorsqu'elles atteignent le pôle arrière des cellules et sont recyclées vers le pôle avant (Nakane *et al.*, 2013). La protéine adhésine associée au *gliding* SprB a été identifiée et localisée à la membrane externe où elle forme des filaments (Nakane *et al.*, 2013). Elle bouge rapidement le long de la surface et son mouvement a été identifié comme étant dépendant d'un moteur à protons (Vincent *et al.*, 2022). Par ailleurs, d'autres protéines ont été identifiées comme essentielles au gliding (GldJ/K/L/M/N et SprA/E), mais également dans la formation du système de sécrétion de type 9 (T9SS) (Braun *et al.*, 2005; Braun & McBride, 2005; Lauber *et al.*, 2018). Une autre

protéine SprB-*like* a été identifiée comme impliquée dans la motilité : RemA. Cette protéine se déplace également le long des cellules et se présente comme étant une lectine capable de fixer le galactose et le rhamnose (Shrivastava *et al.*, 2012). La présence de cette protéine, couplée au fait que la bactérie produise des traces de polysaccarides a permis l'hypothèse que la bactérie puisse utiliser ces derniers pour renforcer la possibilité de déplacement sur des surfaces moins compatibles (Shrivastava *et al.*, 2013; Shrivastava *et al.*, 2012).

Le modèle de structure proposé dans la littérature est le suivant : le moteur (GldLM) est énergisé par un gradient de protons, permettant une modification de conformation de GldM dans le périplasme, qui génère un couplage avec les protéines GldKNO qui permettent la sécrétion de SprB à travers SprA. GldLM est également associé via un complexe inconnu à ce jour à la protéine SprB et permettrait le déplacement de cette dernière le long d'une « plaque » (**Figure 1.6**) (Vincent *et al.*, 2022). Ce modèle reste à compléter, notamment sur le lien entre le moteur et le mouvement des adhésines.

Le dernier modèle de *gliding* et celui que nous présenterons ici est celui de *Myxococcus xanthus*. Ce modèle de *gliding* sera détaillé dans la section 1.3.

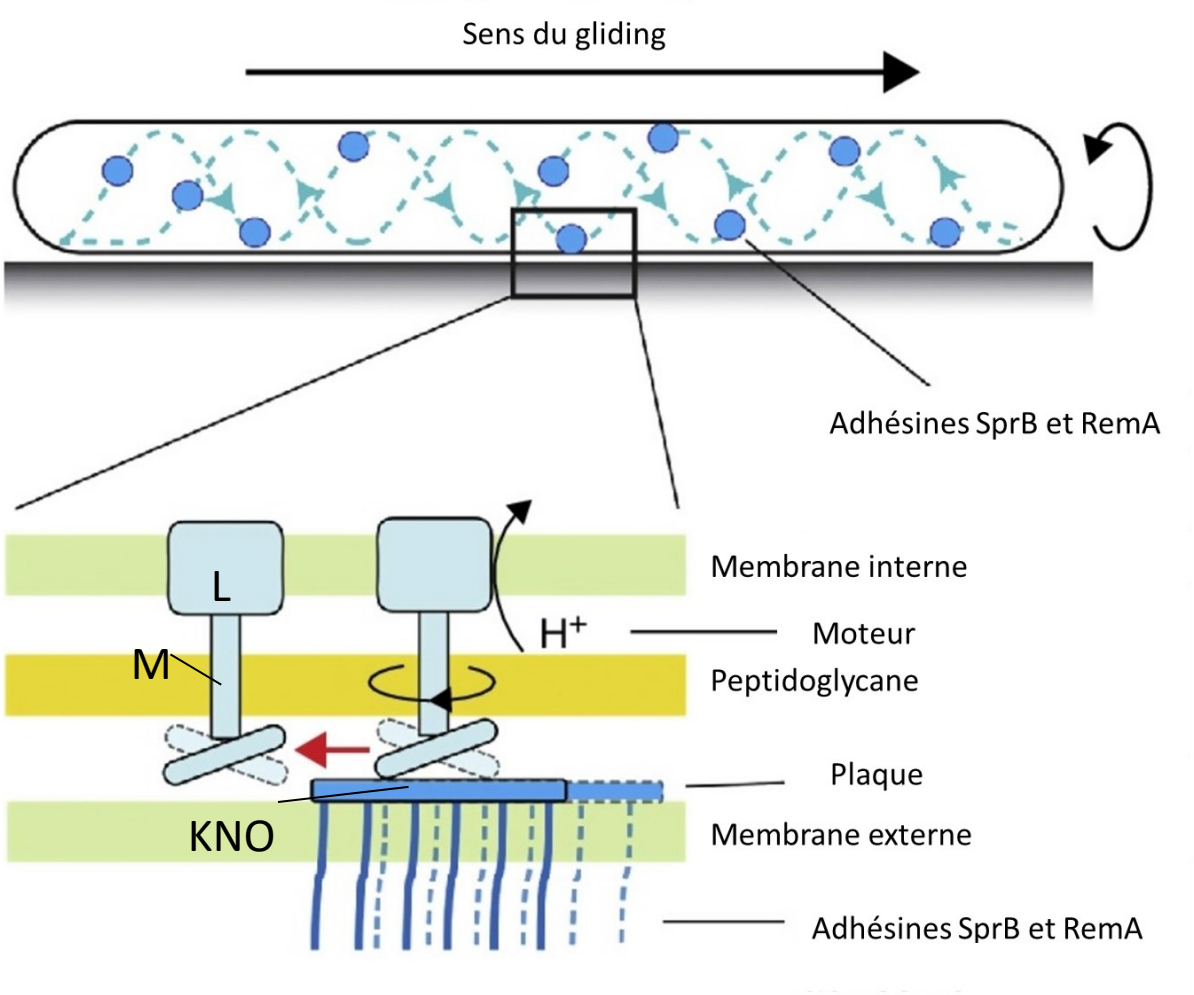

Figure 1.6. Schéma de la machinerie de gliding de *F. johnsoniae*.

En haut : mouvement des adhésine SprB et RemA sur un axe hélical. En bas : section agrandie du point de contact entre la machinerie transmembranaire de gliding et la surface. Les protéines Gld sont annotées avec la lettre correspondante. Adaptée de (Nan *et al.*, 2014).

1.2 LA BACTÉRIE *MYXOCOCCUS XANTHUS*

1.2.1 Définition et historique

Le nom de *Myxococcus xanthus* est défini selon le genre *Myxococcus* du grec *Muxa* (pour mucus) et du latin *coccus* (dérivé du grec *Kokkos* pour graine) et le nom de l'espèce *xanthus* est dérivé du grec *xanthos* qui signifie jaune et qui fait référence à la couleur jaune orangé de la bactérie.

La classification complète de la bactérie est la suivante : Embranchement : Proteobacteria, Classe : Deltaproteobacteria, Ordre : Myxococcales, Famille : Myxococcaceae, Genre : *Myxococccus*, Espèce : *Myxococcus xanthus*. En 1941, JM Beebe a décrit pour la première fois la bactérie *Myxococcus xanthus* (Beebe, 1941). Les cellules sont décrites comme larges, flexibles, en forme de bâtons avec les extrémités arrondies. La taille de ces cellules oscille entre 0,5 et 1 µm de largeur, pour 4 à 10 µm de longueur, la moyenne étant de 0,75 par 6 µm. Elle a été trouvée se développant sur du fumier de vaches dans un pâturage en Iowa. Cette bactérie est impressionnante par rapport aux autres bactéries à Gram négatif tel qu'*E. coli* dont la longueur moyenne varie de 0,5 à 3 µm.

Cette bactérie a été étudiée au cours des années pour plusieurs raisons : son caractère sociable et multicellulaire, son cycle de vie atypique, sa capacité de prédation, sa production de métabolites secondaires et ses systèmes de déplacements (Konovalova *et al.*, 2010; Zhang *et al.*, 2012).

1.2.2 La multicellularité de *M. xanthus*

Avant de détailler l'aspect social et multicellulaire de *M. xanthus*, il faut définir le concept de la multicellularité :

La multicellularité est définie par la présence de plusieurs cellules proches dans un organisme. Pour qualifier un organisme de multicellulaire, il faut qu'il y ait la présence d'un ou plusieurs systèmes de coordination. En général, il n'est pas suffisant que des cellules soient regroupées pour parler de multicellularité, car il n'y a pas de coordination entre cellules malgré une démonstration occasionnelle de croissance organisée. Un dernier critère pour qualifier un organisme de multicellulaire est la différenciation qui permet aux cellules d'assurer des tâches différentes au sein des tissus.

Cette définition peut être raccourcie en une liste de prérequis : la multicellularité requière de l'adhésion cellule à cellule (proximité), une coordination de ces dernières et une coopération des cellules individuelles pour un processus physiologique (différentiation et coordination) (Bretl & Kirby, 2016; Claessen *et al.*, 2014; Grosberg & Strathmann, 2007). Dans l'étude de la multicellularité, *M. xanthus* est un modèle en raison de nombreux phénotypes que cette bactérie présente : la formation de corps fructifères et de spores, la formation de biofilm, la capacité à prédater d'autres bactéries, sa capacité d'échange de membrane externe et sa capacité à se déplacer avec les T4Ps. Or, l'ensemble de ces phénotypes mettent en évidence une coordination, une proximité des cellules et une coordination, répondant au critère de la multicellularité, même si cette dernière est généralement réservée aux organismes eucaryotes.

1.2.2.1 Cycle de vie

Les bactéries Myxococcales comme *M. xanthus* présentent un remarquable cycle de vie dit « multicellulaire » (**Figure 1.7**). En effet, en cas de carence en nutriments, les cellules peuvent entrer dans un programme de développement, commençant avec l'agrégation pour former des amas de cellules contenant 10^5 à 10^6 cellules (O'Connor & Zusman, 1991). Cette étape est suivie par la formation des corps fructifères de taille macroscopique pouvant atteindre plusieurs millimètres (Dworkin, 1963). Ces corps fructifères contiennent alors des spores qui peuvent survivre à la carence pour germer lorsque les conditions de croissances redeviennent compatibles avec la croissance de la bactérie (**Figure 1.7**) (Dworkin & Voelz, 1962).

La capacité à former des spores (myxospores) diffère des autres bactéries capables de sporulation comme les espèces *Bacillus* ou *Clostridium* car la cellule entière chez les myxobactéries est convertie en spore qui est alors capable de résister aux stress (Shimkets & Seale, 1975).

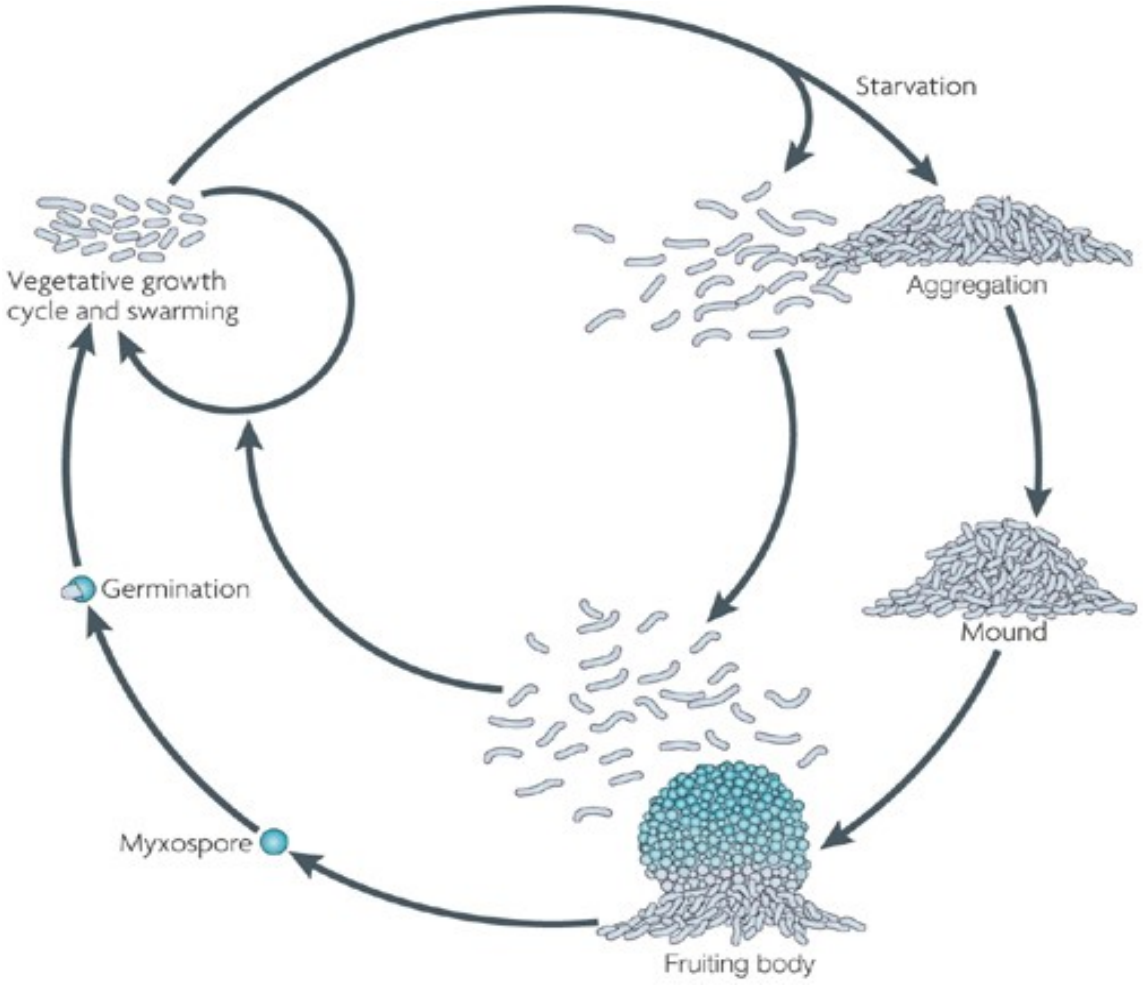

Figure 1.7. Schéma du cycle de vie de *Myxococcus xanthus*.
Cercle interne représente le cycle de vie végétatif, et le cercle extérieur représente le cycle de développement avec formation des corps fructifères contenant des spores. Adaptée de (Zusman *et al.*, 2007).

La synthèse de (p)ppGpp est nécessaire pour l'induction de la formation des corps fructifère lors de la réponse stringente (Harris *et al.*, 1998). Les premières étapes de la formation des corps fructifère étant activées par la détection de carence en nutriments et une densité cellulaire élevée (Kaiser, 2004). Je ne détaillerai pas ici les mécanismes de formation des corps fructifères, bien que l'observation de ce phénotype soit utilisée dans cette thèse afin de mesurer l'impact de mutations sur le comportement général des cellules. Il a été noté que la formation des corps fructifère est impactée par la T4P (Hodgkin & Kaiser, 1979). Il est donc important de noter que la formation des corps fructifère est un phénotype qui nécessite la

coordination et le déplacement des cellules afin de regrouper les cellules. En conséquence, l'observation des corps fructifères peut être utilisée comme témoins de l'efficacité de la coordination et de la capacité de mouvement des bactéries lors de l'étude de ces derniers.

En cas d'absence de stress ou lors d'une culture pure en condition favorable, la bactérie suit un rythme de croissance végétatif (**Figure 1.7**) (croissance/division/mort) que l'on retrouve classiquement chez l'ensemble des bactéries.

1.2.2.2 Prédation

La capacité de *M. xanthus* à prédater d'autres espèces bactériennes est décrite comme étant reliée au cycle de vie décrit précédemment : La prédation est décrite comme étant « l'opposé » de la formation des corps fructifères notamment en raison du fait que la formation des corps fructifères est une réponse à l'absence de nutriment, là où la prédation est une réponse à la présence de nutriments potentiels (Berleman *et al.*, 2006). Cette caractéristique de *M. xanthus* nécessite un haut degré de coordination entre les cellules et la production d'enzymes pour relâcher les acides aminés N-acétyles (Hart & Zahler, 1966). La coordination entre les cellules est observable via l'observation de *rippling* (ondulation). Ces ondulations sont formées par le mouvement des cellules et contrôlées par une coordination cellules à cellules contacte-dépendent (Anderson & Vasiev, 2005). Ces ondulations ont été observées également lors du développement des corps fructifères, ce qui accentue le lien entre ces deux phénotypes (Reichenbach, 1966). Je ne détaillerai pas dans ce mémoire les mécanismes de *rippling* ou de prédations, mais je noterai que ces phénotypes utilisent tous deux des mécanismes de coordination contact-dépendent et illustrent la notion de multicellularité bactérienne de *M. xanthus*.

1.2.2.3 Le pilus de type IV chez M. xanthus

La motilité dite « sociale » de *M. xanthus* est la motilité utilisant le T4P décrite précédemment. Dans cette section je m'attarderai sur le caractère multicellulaire et la dépendance qu'ont les phénotypes sociaux envers cette motilité.

Comme mentionné plus haut, la prédation et le développement des corps fructifères impliquent que les cellules se déplacent et se coordonnent. Le déplacement en *swarm* (essaim) se fait avec la motilité utilisant les T4Ps. Cette motilité, représentée largement chez

les bactéries évoluant sur les surfaces, est essentielle à la mise en place des phénotypes sociaux chez *M. xanthus* (Kaiser, 1979; Zusman *et al.*, 2007). Historiquement, la motilité utilisant les T4Ps a été décrite chez *M. xanthus* comme « le *gliding* social » ou la « *S motility* » (« S » pour « social »), en raison de l'observation du mouvement sur des surfaces de large groupe de cellule (Wall & Kaiser, 1999).

Chez *M. xanthus*, cette motilité a fait l'objet de nombreuses études afin de mieux comprendre les mécanismes et les systèmes impliqués. Il est à noter que le mécanisme général de T4P reste commun entre les espèces bactériennes, même si les fonctions de cette motilité peuvent différer (Berry & Pelicic, 2015; Li *et al.*, 2003; Skerker & Berg, 2001). Le *pilus* est sécrété, fixe le substrat ce qui induit la rétractation du *pilus* et le déplacement de la cellule (ou l'apport d'ADN dans le cas de compétence (Ellison *et al.*, 2018), ou encore le rapprochement avec une cellule hôte dans le cas de la pathogénicité (Imhaus & Duménil, 2014))

La machinerie du T4P (**Figure 1.8**) est composée d'un module transmembranaire et de la fibre de quelques microns qui est sécrétée hors de la cellule. Cette dernière est composée majoritairement de PilA. Le module transmembranaire, quant à lui, peut être divisé en plusieurs complexes selon leur localisation dans les compartiments de la cellule. Le complexe localisé à la membrane externe est composé de PilQ qui forme un pore autour duquel on retrouve TsaP qui forme un anneau autour de PilQ dans le domaine périplasmique. La protéine PilP constitue un anneau périplasmique également tout comme PilO et PilN. La protéine PilC forme un dôme dans l'axe des anneaux dans le cytoplasme dans l'anneau PilM. Les protéines PilB et PilT, les ATPases retrouvées dans le cytoplasme, fixent de façon mutuellement exclusive la base du complexe transmembranaire lors de l'extension (PilB) ou de la rétractation (PilT) de la fibre. Plus en détail, la fixation de PilB permettrait la rotation de PilC permettant l'incorporation de sous unité de PilA depuis la membrane externe à la base du *pilus*, là où la fixation de PilT aurait l'effet opposé. Ces deux actions étant liées à des ATPases, cela confirme que cette motilité est énergisée par de l'ATP, à l'opposition des moteurs à gradient de protons comme certains exemples mentionnés plus haut (Chang *et al.*, 2016; Jakovljevic *et al.*, 2008).

La fibre est composée majoritairement de PilY1, FimU, PilW PilX et PilV (Treuner-Lange *et al.*, 2020). Ces protéines sont retrouvées dans le périplasme, mais également à l'extrémité du *pilus*. Les protéines PilY1.1 et PilY1.3 ont été identifiées comme impliquées dans la fixation du *pilus* aux substrats. La protéine PilY1.1 a notamment été proposée comme impliquée dans la fixation de l'exopolysaccharide (EPS) sur la surface des cellules. La protéine

PilY1.3 contient un domaine von WiIllebrand A (VWA) en N terminal indiquant la possibilité que cette protéine soit responsable de la fixation d'autres protéines (Xue *et al.*, 2022). Par ailleurs, il a été montré chez *P. aeruginosa* que la protéine PilY1 (homologue des protéines PilY1.1 et PilY1.3) contient un domaine fixant les intégrines (motif RGD) de façon calcium dépendante.

Le lien entre l'efficacité de la motilité T4P-dépendente et les polysaccarides a, par ailleurs, été démontré par l'étude des machineries de production des polysaccarides de *M. xanthus*. Plusieurs recherches sur les systèmes de production ont mis en avant la présence de polysaccarides jusqu'ici inconnue qui joue un rôle sur la motilité T4P-dépendente. Ce nouveau polysaccaride, baptisé BPS (*biosurfactant polysaccaride*), a montré avoir un rôle dans l'efficacité de la motilité T4P-dépendente au même titre que l'EPS (**Figure 1.9**), déjà identifié comme cible de la protéine PilY1.1 (Islam *et al.*, 2020; Pérez-Burgos & Søgaard-Andersen, 2020; Saïdi *et al.*, 2022b).

En laboratoire, la motilité T4P-dépendente est étudiée sur un Agar « mou » (0,5% agar). Dans ces conditions, les cellules forment des agrégats qui utilisent les T4Ps pour se déplacer en larges essaims. L'efficacité de ce type de déplacement est alors déterminée par la mesure de l'expansion de l'essaim par rapport à des souches de références en mesurant le diamètre et/ou l'aire de la colonie. La motilité T4P est alors utilisée comme un indicateur de l'efficacité de la coordination des cellules.

1.2.2.4 Échange de membrane externe et « stimulation »

Une autre caractéristique atypique de *M. xanthus* est sa capacité à échanger par contact des morceaux de sa membrane externe avec d'autres cellules de *M. xanthus* compatibles. Ce processus a été historiquement appelé « stimulation » en raison de son identification. En 1977, une équipe de chercheurs ont créé une banque de mutants aléatoires avec du méthanosulfate d'éthyle. Ils ont identifié 6 classes de mutants chez lesquels l'observation des « *flares* » (cellules sortant au bord des colonies) était absent. Ce phénotype étant utilisé comme indicateur de *gliding*, ils ont conclu que ces 6 classes de mutants étaient incapables de réaliser le *gliding* (classe A-F).

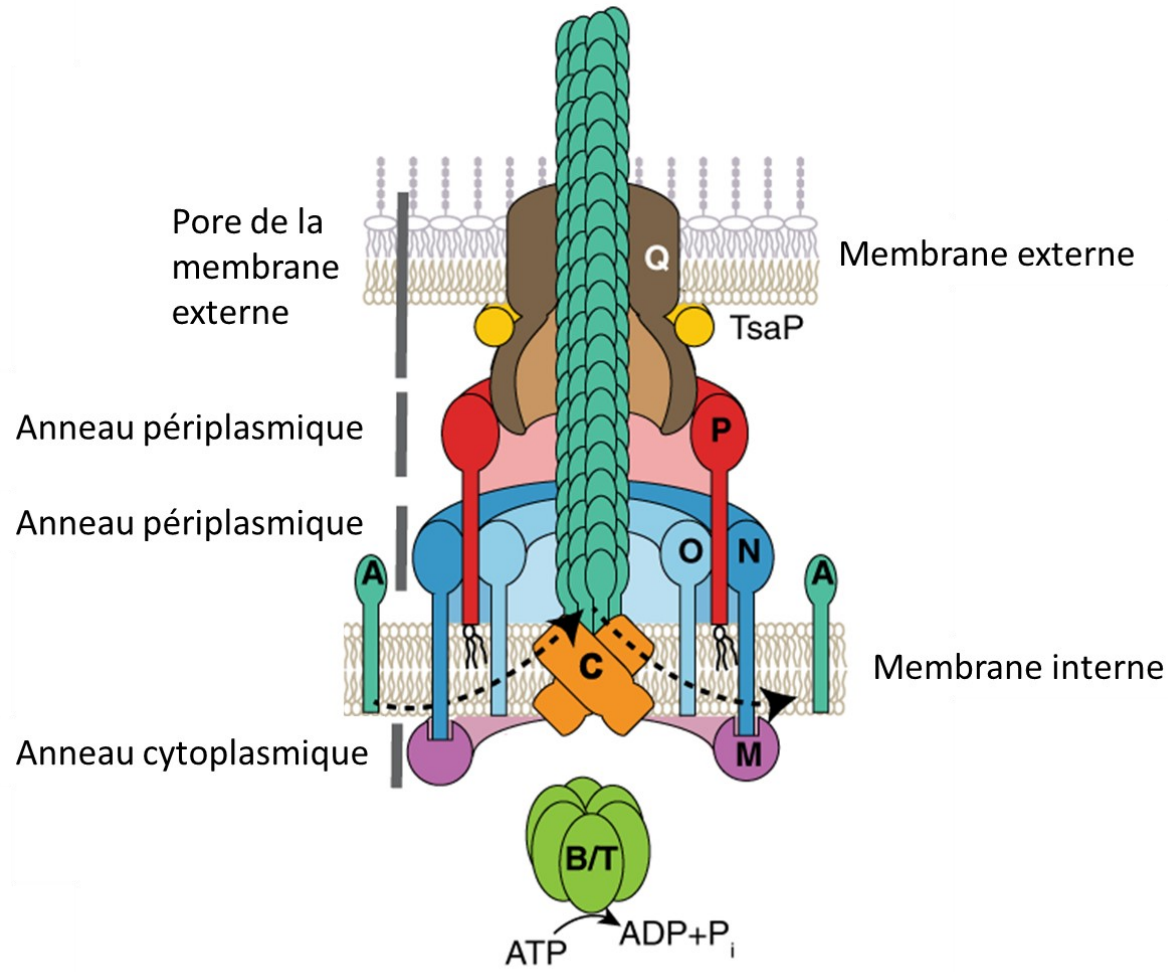

Figure 1.8. Schéma de la machinerie de pilus de type IV.
Les protéines Pil sont annotées avec la lettre qui correspond. Adaptée de (Treuner-Lange *et al.*, 2020).

Une analyse de liaison à l'aide d'un phage de transduction généralisé a montré que chacun des types B, C, D, E et F correspond à un seul locus génétique distinct. Les mutants de type A, en revanche, appartiennent à au moins 17 *loci* génétiques différents.

Par ailleurs, en mélangeant deux de ces classes de mutants incapables de *gliding*, l'observation de flares pouvait être restaurée temporairement (**Figure 1.9**) (Hodgkin & Kaiser, 1977). Donc, ces classes de mutants ont été nommées « Cgl » (*conditional gliding*). Cette caractéristique implique un changement de phénotype, mais aucun changement génomique :

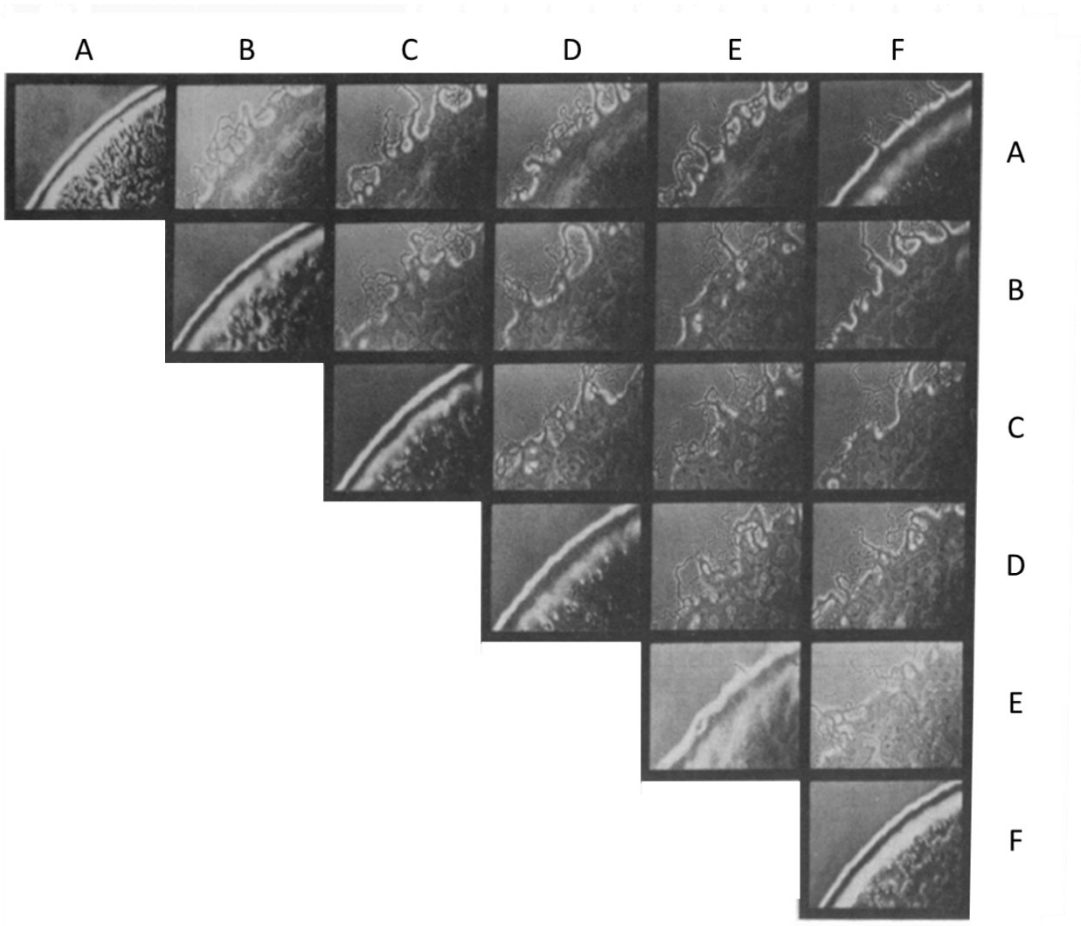

Figure 1.9. Résultat des tests de stimulation de Hodgkin et Kaiser.
Les photographies se présentent en tableau à double entrée. Chaque lettre correspond à une classe de mutant où ils ont noté une absence de « flares » et déduit une impossibilité de gliding. Le mélange des groupes de mutant restaure la présence de « flares ». Adaptée de (Hodgkin & Kaiser, 1977).

il n'y a pas de transfert de gènes. La stimulation consiste donc en un échange des protéines (et lipides) manquantes d'une bactérie donneuse, vers une receveuse. De plus, les protéines pouvant être échangées doivent être des protéines de la membrane externe telles que les protéines Cgl ou Tgl. Deux protéines ont été identifiées comme indispensable à la mise en place de la stimulation : TraA et TraB (Pathak *et al.*, 2012). Je ne détaillerai pas ici le mécanisme de transfert, mais je noterai que la possibilité d'échange et de partage de la membrane externe des cellules de *M. xanthus* est souvent présenté comme un outil pour la communication et la coordination des phénotypes sociaux observés chez la bactérie (Pathak *et al.*, 2012).

1.2.2.5 Polysaccarides

Comme mentionné plus haut, *M. xanthus* sert également de modèle d'étude des polysaccarides et des machineries impliquées. À ce jour, on dénombre plusieurs machineries impliquées dans la production des polysaccarides sécrétés : la machinerie pour la production d'EPS, connue depuis plusieurs années comme importante pour la motilité T4P-dépendante (**Figure 1.10**) et la formation des biofilms. Une seconde machinerie, également identifiée depuis plusieurs années, est impliquée dans la formation du MASC (*major spore coat*) ; ce polysaccaride entoure et protège les myxospores. La dernière machinerie, identifier plus récemment et mentionnée plus haut, est la machinerie de production du BPS (Islam *et al.*, 2020). Ces trois machineries sont des machineries Wzx/Wzy dépendante (**Figure 1.11**). Le fonctionnement de ces machineries ne sera pas développé ici. Je noterai néanmoins que l'étude des machineries de production des polysaccarides chez *M. xanthus* a permis de mettre en évidence un nouveau modèle de sécrétion des polysaccarides par la mise en évidence d'une protéine jouant un rôle de porine dans la membrane externe (**Figure 1.11**), ce qui n'était jusqu'ici qu'associé aux machineries de type « synthase-dépendante » et non Wzx/Wzy dépendante (Saïdi *et al.*, 2022b). Intéressement, l'importance des polysaccarides a également été étudiée au niveau des cellules individuelles et notamment sur des phénotypes tels que le *gliding* (Saïdi *et al.*, 2021). En parallèle de ces 3 machineries de production des polysaccarides et de l'impact que ces derniers ont sur le comportement des cellules isolées, le développement de la technique de microscopie Wet-SEEC (*wet surface-enhanced ellipsometric contrast*) ; permettant de topographier les substrats à une échelle nanoscopique ; a mis en évidence la présence d'un composé sécrété par les cellules en arrière des cellules : le *slime* (Ducret *et al.*, 2013; Ducret *et al.*, 2012; Wolgemuth *et al.*, 2002). Ce composé est constitué de polysaccarides et de vésicules et tubes de la membrane externe. Néanmoins, à ce jour, aucune machinerie de sécrétion de polysaccarides n'a été associée à la production du *slime*. On note que plusieurs études mettent en avant l'importance du mouvement dans les phénotypes sociaux. Le principal mouvement étant la motilité T4P-dépendente, mais on retrouve plusieurs fois la mention que le *gliding* jouerait un rôle important dans l'organisation et la coordination de la multicellularité tel que pour l'alignement des cellules lors de la stimulation, ou dans l'essaim d'une motilité T4P-dépendente. Il est donc nécessaire de s'intéresser à la motilité de type *gliding* et de comprendre son mécanisme pour avoir une meilleure vision sur les mécanismes de coordination de la bactérie.

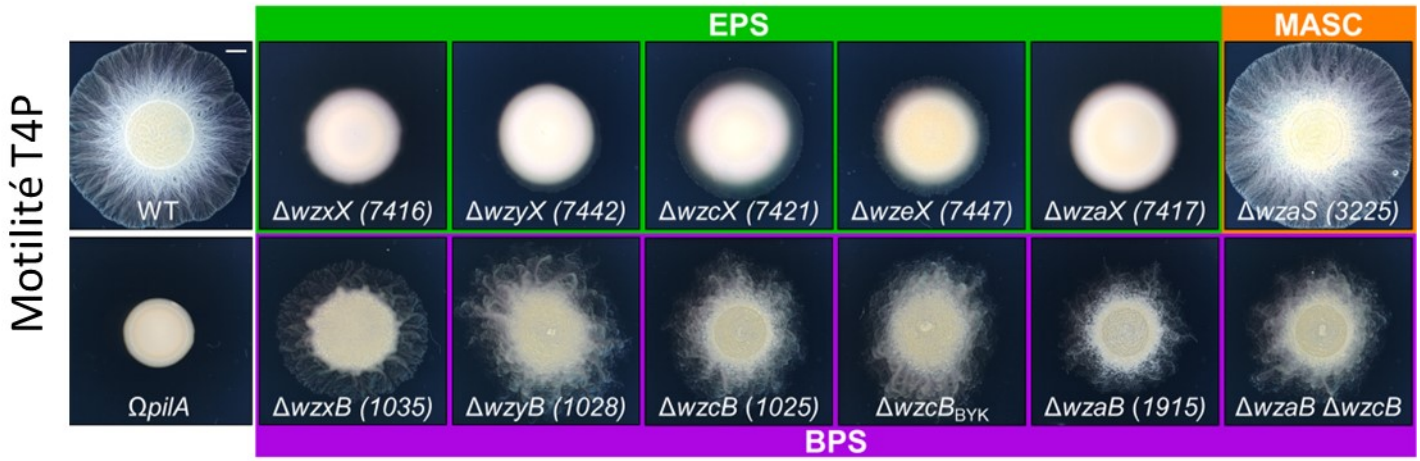

Figure 1.10. Impact de l'absence des polysaccarides sur la motilité T4P.

Les photographies ont été réalisées sur Agar molle après 48 h de croissance. Barre blanche : 400 µm. Les couleurs des encadrés correspondent à la machinerie affectée par la mutation (vert : mutants défectueux pour la machinerie de production d'EPS, violet : mutants défectueux pour la machinerie de production de BPS, orange : mutant défectueux pour la machinerie de production de MASC. Les souches WT et Ω*pilA* sont présentes comme références. Les codes à 4 chiffres suivant chaque nom de gène indiquent l'étiquette de locus MXAN pour chaque gène correspondant. Adaptée de (Islam ***et al.***, 2020).

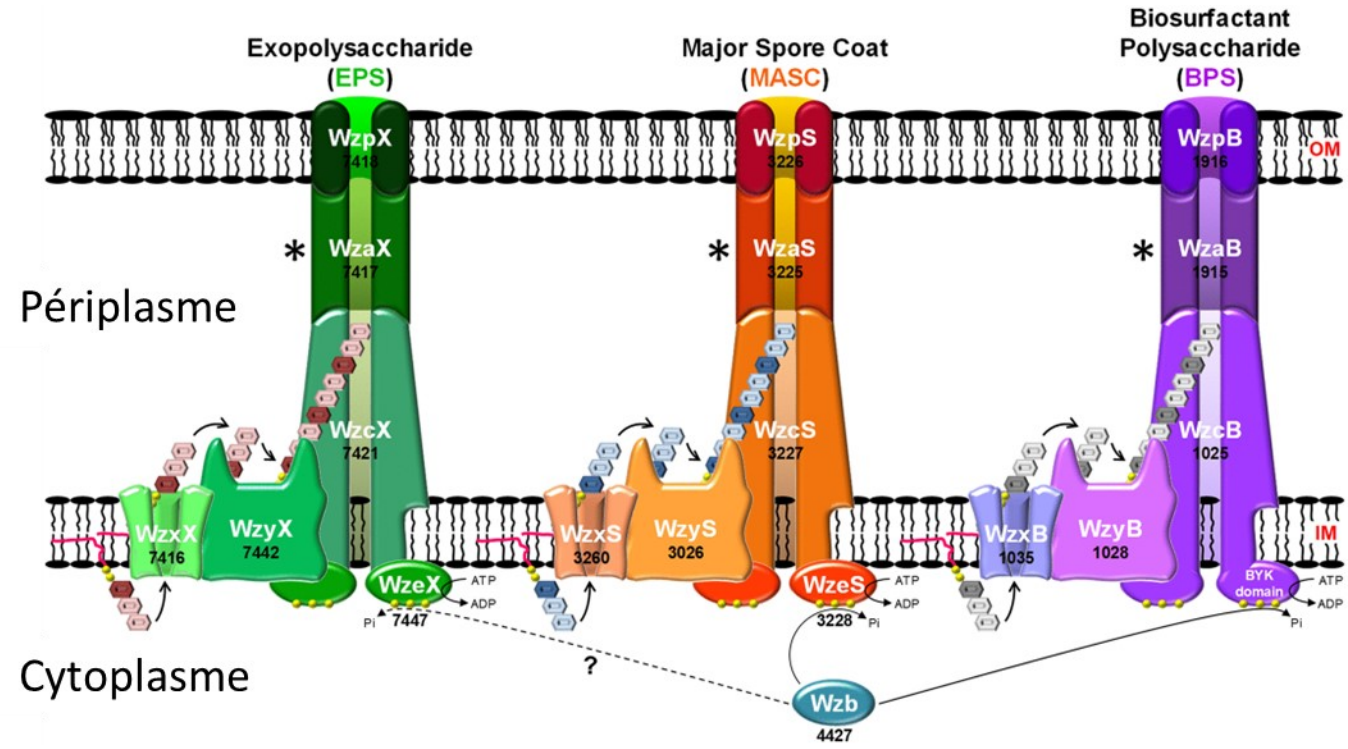

Figure 1.11. Schéma des machineries Wzx/Wzy dépendantes de *M. xanthus*

Les couleurs des protéines correspondent au polysaccaride associé (vert, EPS ; orange, MASC ; violet, BPS). L'astérisque (*) indique un rôle actuellement incertain pour les protéines WzaX/S/B dans ces voies. Les codes à 4 chiffres sous chaque nom de protéine indiquent l'étiquette de locus MXAN pour chaque gène correspondant. Adaptée de (Saïdi *et al.*, 2022b).

1.3 LA MOTILITÉ DE TYPE « GLIDING » CHEZ *M. XANTHUS*

Le *gliding* (ou motilité aventurière ou motilité A) chez *M. xanthus* utilise un mécanisme très différent des mécanismes décrit précédemment. Les premiers travaux mettant en évidence les protéines impliquées dans le *gliding* ont été réalisés par mutagenèse en 1977 et les travaux de 2012 ont permis de mettre en évidence 5 gènes impliqués dans le gliding (Hodgkin & Kaiser, 1977; Pathak & Wall, 2012). Au cours des décennies suivantes, plusieurs autres protéines ont été identifiées comme impliquées dans la motilité aventurière.

Une étude a identifié une protéine comme nécessaire au *gliding* (et pas pour la motilité T4P-dépendente) : la protéine AglZ (Mignot *et al.*, 2007; Yang *et al.*, 2004). Le marquage par un fluorochrome de la protéine AglZ et le suivi du fluorochrome ont mis en évidence l'enrichissement de AglZ dans le pôle avant des cellules, mais également dans des points dans la cellule, immobiles vis-à-vis de la surface sur laquelle se déplace la cellule. Par ailleurs, la présence du *slime,* déposé par les cellules se déplaçant par *gliding*, a ouvert la voie à une hypothèse de *gliding* propulsé par la sécrétion du *slime*. Aussi, plusieurs modèles ont été proposés pour expliquer le mécanisme du *gliding* : un modèle par propulsion de *slime*, un par déformation du peptidoglycane au point d'enrichissement d'AglZ, et un modèle d'adhésion focale. Les deux derniers modèles proposent l'utilisation d'une machinerie appelés la machinerie Agl–Glt, en référence aux noms des protéines la constituant (**Figure 1.12**) (Mignot *et al.*, 2007).

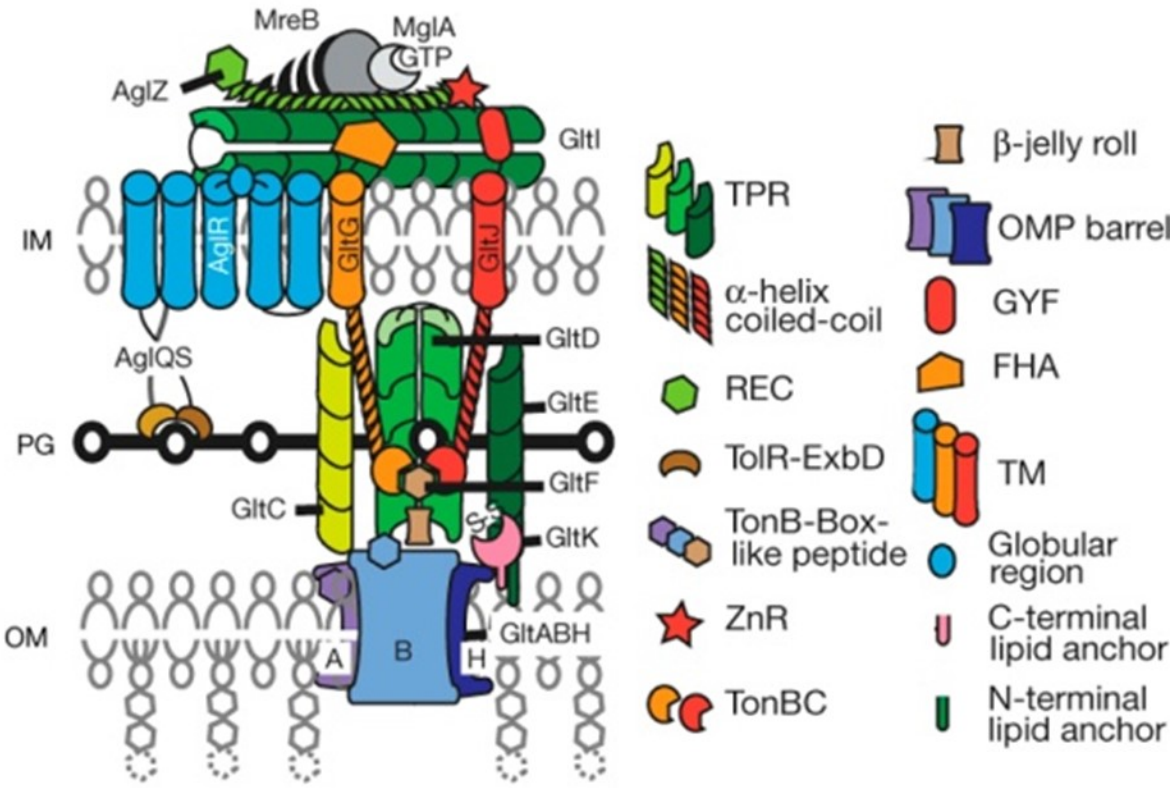

Figure 1.12. Schéma de la machinerie de *gliding* transmembranaire Agl–Glt de *M. xanthus.*

Architecture de domaine prédite de la machinerie Agl-Glt est basée sur des prédictions bio-informatiques, des analyses de séquences et des travaux antérieurs. Les différentes protéines du complexe sont représentées en fonction de leurs structures de domaine issues des prédictions bio-informatiques. On retrouve les protéines en tonneaux β de la membrane externe GltABH, la protéine GltK associée à la membrane externe, mais exposée dans le périplasme, les protéines périplasmique GltC, GltD et GltE et GltF. Les protéines proposées pour transmettre les forces au travers du périplasme : les protéines GltG et GltJ avec des domaines TonB dans le périplasme et les domaines transmembranaires dans la membrane interne. Le moteur AglRQS est représenté avec les domaines TolR-ExbD et transmembranaire. Le schéma représente également les protéines cytoplasmiques associées (AglZ, MglA, GltI et MreB) proposées comme étant à l'initiation de la formation du complexe via leurs interactions avec le domaine ZnR de GltJ. Adaptée de (Faure *et al.*, 2016).

1.3.1 Anciens modèles de *gliding*

1.3.1.1 Propulsion par sécrétion du slime

Plusieurs modèles pour expliquer le *gliding* chez *M. xanthus* ont vu le jour depuis le début des travaux sur ce modèle d'étude. Des travaux ont mis en avant l'importance du *slime* pour le *gliding*, et ont mis en avant qu'un mutant décrit comme sécrétant du *slime* par les deux pôles (et non un seul) simultanément voyait sa capacité de *gliding* fortement réduite. La conclusion de ces travaux était que la sécrétion du *slime* jouait un rôle de « propulsion » permettant le déplacement, et que le mutant ne pouvait se déplacer en raison de la compensation des forces de propulsion en les deux pôles (Wolgemuth *et al.*, 2002; Yu & Kaiser, 2007). De plus l'identification de « buses » aux pôles des cellules, associée à la construction d'un modèle mathématique montrant que l'hydratation pouvait permettre au *slime* de fournir une force suffisante à la propulsion renforçait l'idée d'un modèle de gliding par sécrétion de *slime* (Wolgemuth, 2005; Yu & Kaiser, 2007).

Néanmoins, d'autres travaux, ont montré que l'élongation de la cellule n'altérait pas la vitesse de *gliding*, démontrant que le moteur du *gliding* devait être disposé le long de la cellule et non aux pôles (comme il le serait si la sécrétion de *slime* était responsable du mouvement). Par ailleurs, il a été démontré par inactivation du gradient de protons que la source d'énergie du *gliding* était un moteur à protons (Sun *et al.*, 2011), écartant davantage l'idée d'un système basé sur la sécrétion du *slime* (Sliusarenko *et al.*, 2007). De plus, l'identification des clusters de gènes impliqués dans le gliding codant pour une machinerie Agl-Glt (**Figure 1.12**) a permis de confirmer un système utilisant les points d'enrichissements d'AglZ observés (Mignot *et al.*, 2007).

1.3.1.2 Rotor hélicoïdal et la déformation du peptidoglycane

Un second modèle de mécanisme a vu le jour afin d'expliquer le fonctionnement du *gliding* chez *M. xanthus* : celui de la déformation du peptidoglycane. Ce modèle, basé sur un rapport de distorsion de la paroi cellulaire, propose que le moteur à proton « pince » ou perturbe la paroi par son interaction avec la protéine AglZ (détaillée plus loin) créant une force d'entrainement entre la surface de la cellule et le substrat (Nan *et al.*, 2011). Ce modèle est en accord avec les observations d'enrichissements de la protéine AglZ le long de la cellule, et avec la connaissance qu'était la machinerie Agl-Glt et du moteur à proton. Afin de vérifier

la validité de ce modèle, une équipe de recherche a modélisé le comportement des cellules, notamment vis-à-vis de l'interaction cellules à cellules et entre les cellules et les surfaces. Leur modèle prévoyait que deux cellules entrant en collisions devaient changer de direction de *gliding*. Or, les données expérimentales obtenues dans la même étude démontraient qu'une seule des deux cellules changeait de sens, ce qui indiquait une force de couplage « élastique » et non « visqueuse » comme cela aurait été le cas dans le modèle de *gliding* de « pincement ». De plus les travaux ont cherché à déterminer la force du moteur et à la comparer à leur modèle prévisionnel. Une fois encore, les données expérimentales n'étaient pas en faveur du modèle de pincement, mais en faveur d'un troisième modèle expliquant le gliding : le mécanisme par adhésion focale (Balagam *et al.*, 2014) (**Figure 1.13**).

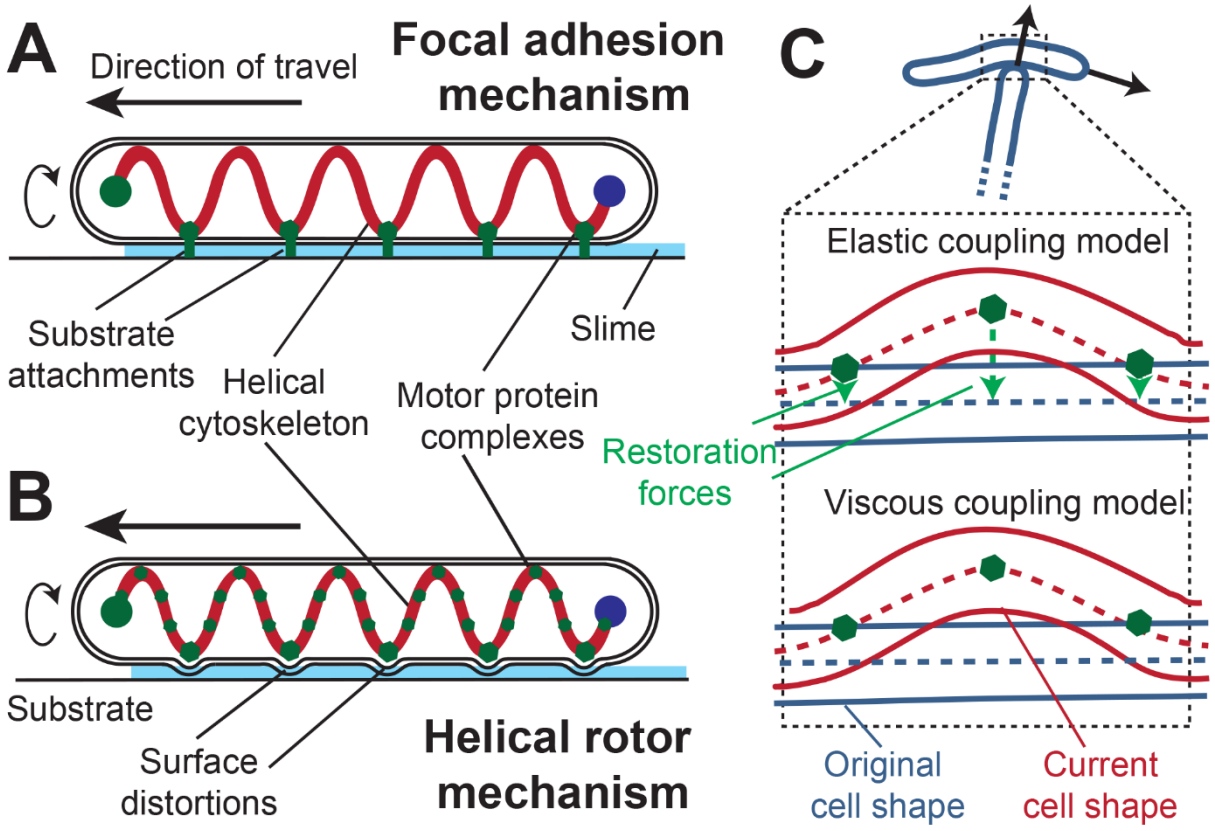

Figure 1.13. Comparaison des modèles de rotor hélicoïdal et de l'adhésion focale.

(A) Mécanisme d'adhésion focale. Les complexes multiprotéiques (barres vertes) s'étendent du cytoplasme vers l'extérieur de la cellule, se fixant au substrat sous-jacent à des points spécifiques. Les cellules avancent en utilisant la force générée par les composants de ces complexes qui agissent contre le cytosquelette (rouge).
(B) Mécanisme du rotor hélicoïdal (HRM). Le suivi des protéines motrices (points verts) le long d'un cytosquelette hélicoïdal entraine des distorsions dans la paroi cellulaire. Ces distorsions génèrent des forces d'entrainement entre le substrat et la surface cellulaire, permettant le mouvement.
(C) Distinctions dans les interactions cellule-substrat pour les deux modèles alternatifs de motilité de gliding. Dans le modèle de couplage élastique, lors d'une collision entre cellules, une force de restauration agit sur la cellule au niveau des points d'interaction cellule-substrat (pointillés verts) dans une direction perpendiculaire à l'axe de la cellule. Une telle force n'existe pas dans le modèle de couplage visqueux (modèle HMR). Adaptée de (Balagam *et al.*, 2014) .

1.3.2 Mise en évidence des adhésions focales bactérienne

La mise en évidence d'un fonctionnement de *gliding* par sites d'adhésion focale bactérienne (bFA) chez *M. xanthus* a été mis en avant par l'identification de la présence de la protéine AglZ en des points fixe vis-à-vis du substrat, de l'identification des clusters de gènes codant pour la machinerie Agl-Glt, et des comparaisons entre les modèles mathématiques et les données expérimentales validant le modèle par adhésion focale et écartant le modèle par « pincement » (Mignot *et al.*, 2007; Yang *et al.*, 2004; Balagam *et al.*, 2014). Ce modèle propose que la machinerie de *gliding* Agl-Glt (**Figure 1.13**) s'assemble en des points d'adhésions, permettant la fixation de la cellule aux surfaces et se désassociant lorsqu'ils atteignent le pôle arrière de la cellule. Ce modèle prévoit la présence de protéines d'adhésions à la surface de la cellule permettant de faire le lien entre la machinerie Agl-Glt et la surface.

1.3.2.1 Protéines du cytoplasme

Dans la partie cytoplasmique de la cellule, on retrouve les protéines MglA, MreB, et AglZ (**Figure 1.12**). Ces trois protéines stimulent l'assemblage du reste de la machinerie. C'est notamment la protéine MglA qui, couplée à une GTP, va se localiser sur le pôle avant de la cellule afin d'activer le *gliding* (Hartzell and Kaiser, 1991). Son antagoniste MglB va, lui, se localiser au pôle arrière de la cellule évitant la présence de la machinerie aux deux pôles en même temps (Treuner-Lange et al., 2015). Le système de régulation du changement de sens de *gliding* (le système Frz) va jouer sur la localisation de MglA et de MglB pour faire changer le sens de *gliding* (Treuner-Lange et al., 2015). De plus, la protéine MglC (localisé elle aussi au pôle arrière) permet un renforcement du signal Frz. La protéine MglA-GTP brise l'interaction entre les protéines MglB et MglC, alors que MglC en interagissant avec MglB stimule la localisation des protéines restante au pôle arrière (Carreira *et al.*, 2023).

MreB a, quant à elle, été identifiée comme homologue à l'actine et semble stimuler l'assemblage du reste de la machinerie lorsqu'elle est associée à MglA. La protéine AglZ est en contact avec la protéine GltI (*gliding transducer I*), également dans le cytoplasme. Des travaux ont montré des interactions entre MglA, AglZ et GltI (Nan et al., 2010, Faure et al., 2016). Par ailleurs, des travaux récents ont montré que les protéines MglA, MglB et AglZ interagissaient avec la protéine de la membrane interne GltJ (via son domaine

cytoplasmique) et dont l'interaction sur les domaines ZnR et GYF de GltJ permettait l'activation et la désactivation de la formation des bFAs (Mignot *et al.*, 2023).

1.3.2.2 Protéines de la membrane interne

Dans la membrane interne, deux protéines, GltJ et GltG, interagissant avec la protéine GltI, possèdent à leurs extrémités N-terminal (dans le périplasme) des domaines TonB_C connus pour interagir avec des domaines Ton-box (**Figure 1.12**) (Islam & Mignot, 2015). Le système TonB, composé des protéines ExbB, ExbD et TonB) est connus pour être utilisés dans le transport des nutriments à travers de la membrane externe chez les bactéries à Gram négatives. Il est classiquement couplé à un moteur à proton dans la membrane interne. La protéine TonB, dans le système du même nom, fixe directement une région conservé Ton-box présente en N-terminal du transporteur protéique localisé dans la membrane externe (Noinaj *et al.*, 2010; Shultis *et al.*, 2006).

Bien que la cible des extrémités N-terminal de GltG et GltJ ne soit à ce jour pas encore déterminée, cette donnée a permis de proposer que les protéines GltJ et GltG soient celles permettant le transfert de la force au travers du périplasme de la même manière que le système TonB interagit avec les transporteurs dans le système TonB (Shultis et al., 2006).

Par ailleurs, pour tout système de déplacement actif, comme le *gliding*, la cellule a besoin d'un moteur pour énergiser la machinerie. Le moteur, dans le cas du *gliding*, se présente sous la forme du complexe protéique AglRQS qui utilise un gradient de protons entre le périplasme et le cytoplasme (**Figure 1.12**). Ce système est similaire au moteur MotAB utilisé pour faire tourner les flagelles chez d'autres espèces bactériennes ou pour des mécanismes de gliding comme ceux mentionnés plus haut (Zhou et al., 1998). L'interaction entre AglR et GltG a été déterminée, justifiant le modèle développé ici (Luciano et al., 2011).

1.3.2.3 Protéines du périplasme

Des protéines nécessaires au *gliding* ont également été retrouvées dans le périplasme. C'est le cas des protéines GltD, GltE, et GltF dont la fonction proposée à ce jour est une fonction de liens entre les autres composants de la machinerie (**Figure 1.12**) (Luciano et al., 2011). La protéine GltC, identifiée comme étant soluble dans le périplasme, et interagissant avec les protéines de la membrane externe GltA et GltB, permettant l'hypothèse que cette

protéine couplerait le domaine de la membrane externe au reste de la machinerie (Jakobczak *et al.*, 2015).

1.3.2.4 Protéines de la membrane externe

Les protéines de *gliding* GltA, GltB, GltH, et GltK localisées dans la membrane externe (**Figure 1.12**) sont encore mal comprises (Kahnt et al., 2010, Luciano et al., 2011). Les travaux de cette dernière décennie ont néanmoins mis en avant des interactions et une stabilisation mutuelle des protéines GltA et GltB (Jakobczak *et al.*, 2015) ; la localisation à la membrane externe dans le périplasme de la protéine GltK ainsi que son rôle dans la stabilisation des protéines GltA et GltB (Jakobczak *et al.*, 2015). Par ailleurs, les protéines GltA, GltB, GltH sont prédites comme contenant une architecture en tonneau β qui traverse la membrane externe (Islam & Mignot, 2015; Jakobczak *et al.*, 2015). Néanmoins, les fonctions détaillées de ces protéines restent encore à être explorées.

Parmi ces 11 protéines Glt, on retrouve 3 protéines qui ont été identifiées dès 1977 comme nécessaires au *gliding* (**Figure 1.9**). Ces recherches ont identifié qu'il s'agissait de protéines pouvant être transférées (donc rattaché à la membrane externe) et ont montré que les protéines Cgl(B-F) étaient impliquées dans le *gliding*. Les travaux qui ont suivi ont permis de rattacher et de renommer les gènes mutés : *cglC* a été renommé en *gltK, cglE* en *gltH*, et *cglF* en *gltF*. Les gènes *cglB* et *cglD* et les protéines associées, quant à eux, ont été l'objet des travaux présentés dans cette thèse, et seront par conséquent détaillées dans les chapitres associés.

1.3.3 Fonctionnement du *gliding* par bFA

Le modèle « récent » du fonctionnement du *gliding* par adhésion focale propose que le complexe MglA–MreB localisé au pôle avant favorise l'assemblage de la machinerie Agl–Glt, notamment via l'interaction entre AglZ, MglA et GltJ (Mignot *et al.*, 2023). Au repos, la protéine GltJ ne fixe aucune des protéines AglZ et MglA. Lorsque le domaine ZnR de GltJ est libéré, les protéines MglA (associé à MreB) et AglZ peuvent se fixer sur la protéine GltJ ; entrainant l'assemblage de la machinerie. Cela permettrait au moteur AglRQS d'énergiser et de changer la conformation des protéines associées de la membrane interne (GltG/GltJ) dont les domaines homologues à TonB flexibles s'étendraient au travers du peptidoglycane pour fixer le module de la membrane externe via les protéines GltA et GltB (stabilisées par GltC et

GltK) (Faure *et al.*, 2016). Ce module aurait pour fonction de fixer la surface via une ou plusieurs protéines d'adhésion. L'ensemble de ce modèle expliquant partiellement comment l'énergie du moteur AglRQS est utilisée et transférée à travers les différents compartiments de la cellule.

Lorsque le complexe transmembranaire atteint le pôle arrière de la cellule, la protéine MglB (renforcé par MglC) se fixe au domaine ZnR de GltJ et hydrolyserait la protéine MglA-GTP en MglA-GDP désactivant l'interaction entre MglA, GltJ et AglZ, désassemblant la machinerie (Carreira *et al.*, 2023; Mignot *et al.*, 2023).

On note que ce modèle de fonctionnement, bien qu'appuyer par les recherches et l'expérimentation est fortement retrouver ailleurs dans le Vivant, et notamment chez les Eucaryotes.

1.4 LES ADHÉSIONS FOCALES ET LES INTÉGRINES

1.4.1 Adhésions focales eucaryotes

Les mécanismes d'adhésion des cellules à la matrice extracellulaire, ont été, et sont encore très étudiés de nos jours, notamment chez les Eucaryotes. L'adhésion des cellules à leur environnement peut varier selon la taille, la forme ou la distribution dans la cellule ; mais certains mécanismes et acteurs de ces adhésions restent communs : l'adhésion est contrôlée par des intégrines, et ces dernières interagissent avec le cytosquelette (Geiger *et al.*, 2001).

Chez les eucaryotes, le mécanisme d'adhésion le mieux caractérisé est l'adhésion focale eucaryote (eFA) ou « contact focal ». Par définition, ce type d'adhésion est formée par les cellules évoluant sur une surface solide (Geiger *et al.*, 2001). La mise en place des eFAs est stimulée par une protéine GTPase (de la famille des protéines Rho) connue notamment pour contrôler l'assemblage du cytosquelette d'actine. Elle est caractérisée par une structure localisée à la périphérie des cellules, permettant une adhésion forte de la cellule à la surface via un ancrage au cytosquelette par un domaine en plaque constitué de plusieurs types de protéines (Izzard & Lochner, 1976; Liu *et al.*, 2000; Zamir & Geiger, 2001).

Les travaux de ces quarante dernières années ont mis en évidence une liste de plus de 50 différentes molécules intervenant dans les eFAs (Zamir & Geiger, 2001). Il ne sera pas détaillé dans cette thèse que les éléments nécessaires à la compréhension des travaux effectués. Le composant essentiel des eFAs et celui que nous détaillerons est l'intégrine et sa fonction dans l'adhésion et la formation des eFAs.

1.4.2 Intégrines

1.4.2.1 Vue d'ensemble

Le nom « intégrine » a été utilisé la première fois en 1986 et décrit comme un complexe intégral impliqué dans l'association de la matrice extracellulaire avec la cellule à travers la membrane (Tamkun *et al.*, 1986). Les travaux de recherche des décennies suivantes ont considérablement augmenté la compréhension de ces protéines. Comme mentionné plus haut, les intégrines sont des protéines d'adhésion. Elles se présentent en hétérodimères (sous-unité α et β) s'assemblant et formant des récepteurs pouvant lier différents ligands (Barczyk *et al.*, 2010; Campbell & Humphries, 2011; Hynes, 2002). Chaque sous-unité est présente à la surface des cellules, traverse la membrane cellulaire, et possède (en général) une partie cytoplasmique non structurée. La taille des sous-unités varie de 750 à 1000 acides aminés, avec la sous unité β étant la plus grande.

Comme mentionné, ces récepteurs varient et leurs ligands également ; par conséquent, je ne détaillerai pas l'ensemble des intégrines identifié à ce jour, mais le mécanisme général et les domaines protéiques impliqués (**Figure 1.14**).

1.4.2.2 Les ectodomaines des sous-unités α et β

Les ectodomaines (ou domaine des protéines présentes à la surface des cellules) varient selon la sous-unité étudiée. Dans la chaine α, on retrouve 4 à 5 domaines : un domaine constitué de β-*propeller* à 7 feuillets ; un domaine *thigh* et deux domaines *calf*. Parmi les 18 intégrines α, 9 possèdent également un domaine α-I inséré entre les feuillets 2 et 3 du β-*propeller* (Xie *et al.*, 2010). Ce dernier est homologue à un domaine de la chaine β et possède 5 feuillets β entourés d'hélices α ; similaire a un domaine von Willebrand A. Les derniers feuillets du β-*propeller* contiennent des sites de fixation du calcium. Les domaines *calf* et *thigh* contiennent des sandwiches β et les modèles présentent ces domaines comme ayant des jonctions flexibles permettant le repliement de la sous-unité (**Figure 1.14**) (Campbell & Humphries, 2011; Dong *et al.*, 2018; Xiong *et al.*, 2001).

La chaine β, de plus grande taille, possède 7 domaines. Le domaine β-I, mentionné plus haut, est inséré dans un domaine hybride, lui-même inséré dans un domaine *plexin-*

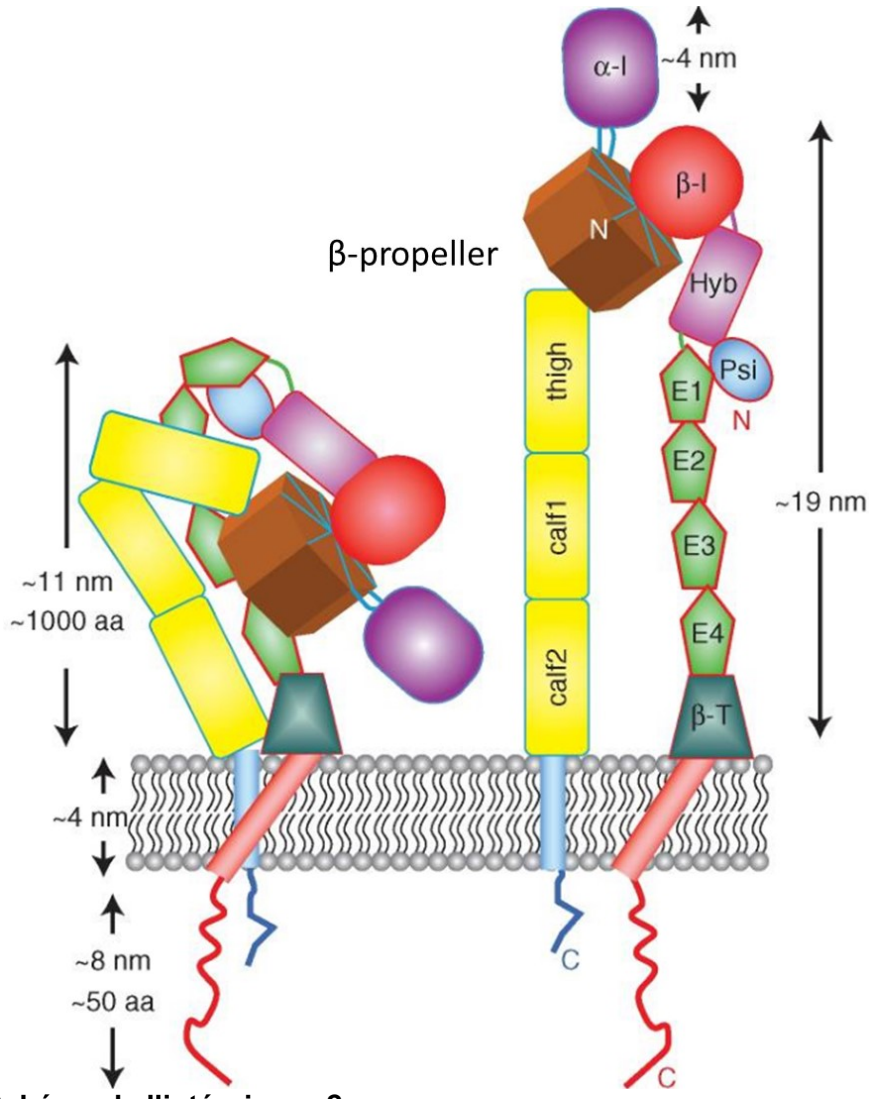

Figure 1.14. Schéma de l'intégrine $\alpha_x\beta_2$.

À gauche, la représentation pliée (*bent)* et à droite une représentation dépliée. Les domaines EGF-like sont annotés par la lettre E. Le domaine Tail est annoté β-T. Le β-*propeller* est en marron. Le domaine hybride est noté Hyb. Adaptée de (Campbell & Humphries, 2011).

semaphorin-integrin (PSI) (Dong *et al.*, 2018). Ces 3 domaines sont suivis par 4 domaines *epidermal growth factor* (EGF) riches en cystéine (pouvant atteindre jusqu'à 56 cystéines) et une queue β. Le domaine EGF montre plusieurs liaisons disulfure entre les cystéines (Campbell & Humphries, 2011; Zhu *et al.*, 2008). La chaine β est plus flexible que la chaine α (Dong *et al.*, 2018; Xie *et al.*, 2010).

La fixation du ligand se situant entre les deux chaines α et β, plus précisément à l'interface du domaine β-*propeller* de la chaine α et le domaine β-I de la chaine β (Dong *et*

al., 2018). Cette fixation est dépendante de la présence de cations divalents (magnésium, manganèse et calcium) sur un domaine « *metal ion-dependent adhesion site* » ou MIDAS. Ce site possède un motif conservé DXSXS indispensable à la fixation du ligand (Lee *et al.*, 1995b; Zhu *et al.*, 2008). Les modèles d'intégrines montrent que la fixation du ligand se fait via l'ion magnésium au site MIDAS. Deux autres sites de fixation d'ions sont adjacents au MIDAS. L'un, nommé ADMIDAS (*ADjacent MIDAS*), fixe le calcium, et la fixation de manganèse sur ce site résulte d'une activation de l'intégrine (Humphries *et al.*, 2003). Le second site fixant le calcium appelé « *Synergistic Metal Ion Binding Site* » (SyMBS) a une action positive sur la fixation du ligand et la synergie au calcium (Zhu *et al.*, 2008).

1.4.2.3 Les fonctions des intégrines dans les eFAs

La formation des eFAs implique une réponse à une force mécanique. Cela implique généralement un contact entre la cellule et une surface solide dans le milieu extracellulaire (ou bien une autre cellule). Ce contact est perçu par la cellule via des intégrines qui jouent le rôle de mécanosenseurs et vont former des clusters d'intégrines ((Geiger *et al.*, 2001)). Le « *clustering* » des intégrines est une étape indispensable à la bonne formation des eFAs. On note par ailleurs que des glycosaminoglycanes peuvent également participer au renforcement de l'adhésion lors de la formation des eFAs. De plus des études ont montré que la rigidité de la surface influait sur la réponse des intégrines et leurs changements de conformation en plus de modifier le « *clustering* » (Qian & Gao, 2010).

Cette première étape de formation d'adhésion focale (complexe focal) peut ne pas aboutir à une eFA. Les forces impliquées dans la stabilisation peuvent provenir de l'intérieur de la cellule par une machinerie contractile, ou bien de l'extérieur (Shattil *et al.*, 2010). Les mécanismes de renforcement ne seront pas détaillés ici, mais il est important de noter que ce renforcement est indispensable à la stabilisation et à la formation de l'eFA. L'effet de « *clustering* », couplé à l'attachement des intégrines au cytosquelette, permet une adhésion forte entre les cellules et la surface, donnant alors un point d'ancrage pour la mise en place d'une motilité.

L'ensemble de ces étapes et mécanismes permettent de présenter les intégrines comme à la fois des « senseurs de surfaces » et des sites de fixation de surfaces (Geiger *et al.*, 2001).

1.5 HYPOTHÈSES ET PROBLÉMATIQUE

L'ensemble des travaux précédents portant sur la machinerie de *gliding* et de bFA chez *M. xanthus* ont laissé plusieurs axes de recherche à approfondir. En effet, le modèle de bFA, comme décrit jusqu'en 2016 (Faure *et al.*, 2016) chez *Myxococcus xanthus* n'expliquait pas quelle(s) protéine(s) étaient impliquées dans la fixation entre la membrane externe de la cellule et la surface. De plus, l'importance du *slime* dans le processus d'adhésion reste à ce jour une hypothèse. Les protéines Agl–Glt, décris jusqu'alors de la membrane externe ont été écartées comme adhésines potentielles. Néanmoins, deux protéines ont été retenues comme candidat pour la fonction d'adhésine : Comme mentionné plus haut, les travaux de stimulation de 1977 (Hodgkin & Kaiser, 1977) ont montré 6 classes de mutants où le *gliding* est impacté, et depuis les groupes de mutants ont été associés à des protéines de la machinerie Agl–Glt . Ce n'est pas le cas de deux groupes de mutant, bien que les protéines associées aux gènes mutés ont été identifiées pour les classes B et D (respectivement CglB et CglD). La fonction de ces deux protéines dans le *gliding* et le lien éventuel que ces protéines pourraient avoir avec la machinerie Agl–Glt est l'axe de recherche qui sera développé dans cette thèse. Par ailleurs, le fonctionnement de *gliding* par adhésion focale rappelant les mécanismes observés chez les eucaryotes, les homologies entre la machinerie Agl–Glt, les protéines CglB et CglD et les protéines impliquées dans l'adhésion chez les Eucaryotes tels que les intégrines seront explorées.

Les chapitres suivants de cette thèse doctorale seront présentés sous la forme d'articles scientifiques, et chaque chapitre présentera les travaux portant sur une des deux protéines mentionnées plus haut. Le premier article (chapitre 2), portant sur la fonction de la protéine CglB, et le deuxième article (chapitre 3) sur la protéine CglD. Ces deux chapitres sont par conséquent rédigés dans la langue de publication (anglais), et présentent une discussion intégrée à l'article. Une discussion générale des travaux est présentée en chapitre 4.

Chapitre 2 : Unmasking of the von Willebrand A-domain surface adhesin CglB at bacterial focal adhesions mediates myxobacterial gliding motility

Titre de l'article :

Unmasking of the von Willebrand A-domain surface adhesin CglB at bacterial focal adhesions mediates myxobacterial gliding motility

Auteurs :

Salim T. Islam[1,2,3†*], **Nicolas Y. Jolivet**[1,2†], Clémence Cuzin[3†], Akeisha M. Belgrave[4,5], Laetitia My[3], Betty Fleuchot[3], Laura M. Faure[3], Utkarsha Mahanta[6,7], Ahmad A. Kezzo[1,2], Fares Saïdi[1,2], Gaurav Sharma[6,7], Jean-Bernard Fiche[8], Benjamin P. Bratton[5], Julien Herrou[3], Marcelo Nollmann[8], Joshua W. Shaevitz[5], Eric Durand[3], Tâm Mignot[3*]

† **These authors contributed equally to this work**

* Corresponding authors

1 Institut National de la Recherche Scientifique (INRS), Centre Armand-Frappier Santé Biotechnologie, Université du Québec, Institut Pasteur International Network, Laval, QC, H7V 1B7, Canada.

2 PROTEO, the Quebec Network for Research on Protein Function, Engineering, and Applications, Université Laval, Quebec, QC, G1V 0A6, Canada.

3 Laboratoire de Chimie Bactérienne, CNRS - Université Aix-Marseille UMR7283, Institut de Microbiologie de la Méditerranée, Marseille, 13009, France.

4 Integrated Sciences Program, Harrisburg University of Science & Technology, Harrisburg, PA, 17101, USA.

5 Lewis-Sigler Institute for Integrative Genomics, Princeton University, Princeton, NJ, 08540, USA.

6 Institute of Bioinformatics and Applied Biotechnology, Electronic City, Bengaluru, Karnataka, 560100, India.

7 Department of Biotechnology, Indian Institute of Technology Hyderabad, Telangana, 5502284, India.

8 Centre de Biochimie Structurale, CNRS UMR5048, INSERM U1054, Montpellier, 34090, France.

Détails bibliographiques :

Revue : *Science Advances*
Volume : 9
Édition : 8
Pages : eabq0619
DOI : 10.1126/sciadv.abq0619
Date de soumission : 29 juin 2022
Date d'acceptation : 24 janvier 2023
Date de publication : 22 février 2023

Contribution des auteurs :

Conceptualisation : **NYJ**, STI, CC, ED, TM

Méthodologie : **NYJ**, STI, CC, AMB, LM, JH, ED, TM

Développement de méthode pour l'immunofluorescence chez *M. xanthus*, et l'analyse associée ; développement de méthode pour le test de perméabilisation des membranes.

Recherche : **NYJ**, STI, CC, ED, AMB, LM, UM, BF, LMF, GS, AAK, FS, J-BF, BPB, JH

J'ai obtenu les données pour les Figures : 2.2A (mesures des vitesses de gliding), 2.4B&E (Westernblot avec l'agent dénaturant DTT et Westernblot de sensibilité à la Protéinase K), 2.6 (immunofluorescence et analyses associées), 2.7A (quantification de la fluorescence in-gel de la protéine AglZ-YFP), 2.9ACDEF (Westernblot du surnageant de culture des différentes combinaisons de mutants, test de perméabilité à la protéinase K des cellules en présence d'EDTA, test de récupération de CglB après traitement à l'EDTA, et test de sensibilité à la vancomycine en présence et absence d'EDTA), 2.10ADE (Westernblot pour CglB des différents mutants, test de sensibilité à la protéinase K et analyses de l'immunofluorescence), 2.11 (Westernblot pour CglB des différentes combinaisons de mutants, test de sensibilité à la protéinase K du triple mutant et analyses de l'immunofluorescence du triple mutant), 2.12 (analyses d'immunofluorescence des doubles mutants), et 2.13A&B (Westernblot ciblant les protéines GltA/B/H/K, et test de sensibilité à la protéinase K ciblant ces même protéines).

Visualisation : **NYJ**, STI, GS, JH, TM

Supervision : STI, TM, JWS, MN, ED, GS

Rédaction-manuscrit initiale : **NYJ**, STI, TM

Rédaction—révision & édition : **NYJ**, STI, TM, JWS, GS, MN

2.1 ABSTRACT

The predatory deltaproteobacterium *Myxococcus xanthus* uses a helically-trafficked motor at bacterial focal-adhesion (bFA) sites to power gliding motility. Using total internal reflection fluorescence and force microscopies, we identify the von Willebrand A domain-containing outer-membrane (OM) lipoprotein CglB as an essential substratum-coupling adhesin of the gliding transducer (Glt) machinery at bFAs. Biochemical and genetic analyses reveal that CglB localizes to the cell surface independently of the Glt apparatus; once there, it is recruited by the OM module of the gliding machinery, a heterooligomeric complex containing the integral OM β barrels GltA, GltB, and GltH, as well as the OM protein GltC and OM lipoprotein GltK. This Glt OM platform mediates the cell-surface accessibility and retention of CglB by the Glt apparatus. Together, these data suggest that the gliding complex promotes regulated surface exposure of CglB at bFAs, thus explaining the manner by which contractile forces exerted by inner-membrane motors are transduced across the cell envelope to the substratum.

2.2 INTRODUCTION

Directed surface motility of cells from all biological kingdoms involves highly-dynamic cell–substratum interactions. In eukaryotic cells, this process involves the engagement and activation of surface-exposed integrin(-like) adhesins, directionally transported by molecular motors (myosin) via integrin coupling to the internal cytoskeleton (actin) (Sun *et al.*, 2016). For metazoan organisms, nascent integrin adhesions to the extracellular matrix (ECM) lead to integrin nucleation and the formation of large eukaryotic focal-adhesion (eFA) sites; these assemblies remain fixed-in-space relative to a translocating cell, promoting local traction, transduction of motor forces, and cell translocation (Kanchanawong *et al.*, 2010). Such surface motility is not however restricted to eukaryotic cells. Though known to move in groups on softer substrata via type IV pilus (T4P) extension/retraction (in concert with exo- and biosurfactant-polysaccharide secretion) (Islam *et al.*, 2020; Saïdi *et al.*, 2021; Saïdi *et al.*, 2022b), individual cells of the Gram-negative predatory deltaproteobacterium *Myxococcus xanthus* utilize gliding motility on harder substrata. Gliding occurs in the absence of outward appendages (e.g. flagella or T4P) (Islam & Mignot, 2015), instead utilizing a trans-envelope multi-protein Agl–Gliding transducer (Glt) complex (**Figure 2.1A**) to power cell locomotion

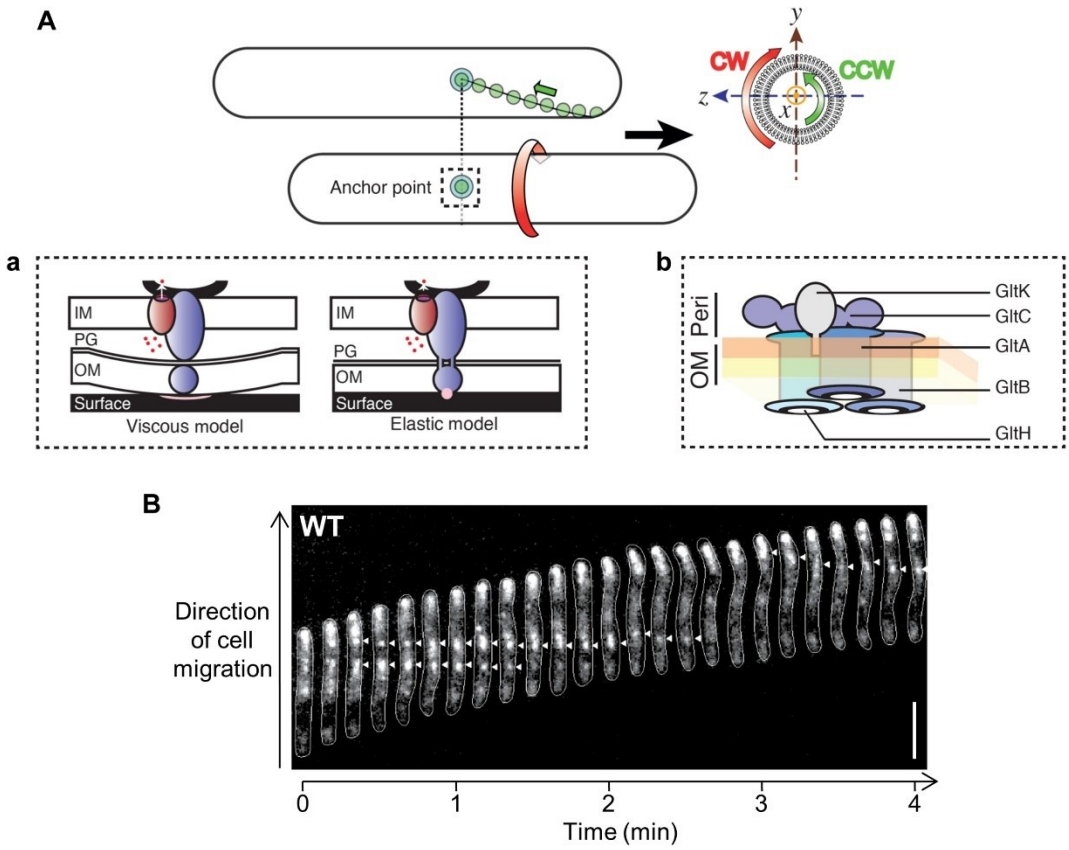

Figure 2.1. Concept of bFA-mediated gliding motility.

(A) Gliding motility mediated by bFAs in *M. xanthus*. Following their assembly at the leading pole, motility complexes move toward the lagging cell pole in a counter clockwise (CCW) rotational trajectory. Clockwise (CW) and CCW directionalities are defined by observing the cell cylinder from the leading pole in the *y,z* plane. When the complexes interact with the substratum, they form bacterial focal adhesion (bFA, concentric circles) sites and propel rotational movements of the cell. *Panel (i)*: bFAs are formed according to two possible mechanisms: In the viscous interaction model, the periplasmic complex accumulates at bFAs and pushes against the elastic peptidoglycan (PG) to create cell envelope deformations at bFAs and thus create viscous interactions with the substratum. The function of the outer-membrane (OM) complex is not accounted for in this model. In the elastic model, the periplasmic complex establishes transient interactions through the PG, contacting the OM complex which itself interacts with the substratum via an unknown adhesive molecule (*pink circle*). Legend: Trans-envelope Glt complex (*blue components*); IM AglRQS H^+-driven motor (*dark red component*); protons (*red dots*); MreB (*black curve*). *Panel (ii):* Proposed Glt OM platform based on previous reports and this study. The OM localization of GltA, GltB, GltH, GltC and GltK is based on structural bioinformatic as well as fractionation analyses presented here and elsewhere (Jakobczak *et al.*, 2015; Kahnt *et al.*, 2010; Luciano *et al.*, 2011). The integral association of GltA, B and H is based on bioinformatic and Proteinase K accessibility assays in this study and another report (Jakobczak *et al.*, 2015). Direct GltA–GltB, GltA–GltC, and GltB–GltC interactions were already biochemically demonstrated by pull-down assays(Jakobczak *et al.*, 2015). The connection with GltH is further indicated from results reported in this study. The periplasmic leaflet (*orange*) and outer leaflet (*yellow*) of the OM are indicated. Legend: Peri, periplasm.

(B) Position of a bFA (*arrowheads*) revealed via fluorescence microscopy of WT *M. xanthus* expressing AglZ-YFP.

(Luciano *et al.*, 2011; Nan *et al.*, 2010). In gliding cells, Agl–Glt complexes associate at the leading pole and move directionally in the bacterial inner membrane (IM) toward the lagging cell pole, following a right-handed helical trajectory (Faure *et al.*, 2016; Fu *et al.*, 2018; Nan *et al.*, 2013) (**Figure 2.1A**). These rotational movements likely probe the substratum beneath gliding cells, leading to immobilization of the Agl–Glt complex at fixed bacterial focal-adhesion (bFA) sites (**Figure 2.1B**) as well as cell translocation via left-handed rotation of the bacterium around its long axis (Faure *et al.*, 2016) (**Figure 2.1A**).

Direct imaging of bFAs is possible via live-cell microscopy (Mignot *et al.*, 2007), where they appear as bright fluorescent clusters that retain fixed positions relative to the substratum in a gliding cell (**Figure 2.1B**). At the molecular level, polar activation of bFAs is driven by a cytoplasmic scaffold formed by bacterial actin MreB, the Ras-like protein MglA and the coiled-coil protein AglZ (Mauriello *et al.*, 2010; Treuner-Lange *et al.*, 2015). This scaffold recruits the IM components of the gliding complex by as-yet-undefined interactions, activating the molecular motor within (Treuner-Lange *et al.*, 2015). The motor itself is constituted by the proteins AglR, Q, and S, which form a TolQR/ExbBD/MotAB-like H^+-gated channel that uses the proton gradient formed across the bacterial IM to energize long-range movements of the IM complex in the bacterial envelope (Sun *et al.*, 2011). However, the manner in which these intracellular motions are coupled to the substratum in order to propel the cell is unknown. One hypothesis states that trafficking motor units deform the peptidoglycan meshwork in the periplasm, propagating surface-wave deformations and viscous interactions between the outer membrane (OM) and the substratum (**Figure 2.1A, panel i**). However, observations and mechanical modelling of cell–cell collision events suggest that interactions between a gliding cell and the substratum are elastic in nature, consistent with localized adhesion points and the existence of an anchored adhesin (Balagam *et al.*, 2014) (**Figure 2.1A, panel i**). Also, when gliding on glass surfaces, cells occasionally abandon patches of OM motility-complex proteins on the substratum at positions formerly occupied by bFA sites (detected with a GltC-mCherry protein) (Faure *et al.*, 2016). In the cell envelope, the IM motor moves by establishing transient contacts with a group of Glt proteins localized in the OM (herein called the OM platform, see below), linked via periplasmic domains of putatively-contractile proteins that traverse the peptidoglycan meshwork (Faure *et al.*, 2016) (**Figure 2.1A**). When in contact with the substratum, these motions tether the OM platform at bFAs (Jakobczak *et al.*, 2015), which is proposed to create local adhesions and movement of the cell (**Figure 2.1A**).

A putative protein platform at the cell surface could be constituted by multiple integral-OM Glt proteins, including predicted β-barrels GltA, GltB, and GltH (formerly CglE/AgmV), as well as the OM-lipoprotein GltK (formerly CglC/AgmO) and OM-associated periplasmic protein GltC (Islam & Mignot, 2015; Jakobczak *et al.*, 2015; Luciano *et al.*, 2011) (**Figure 2.1A**). While little is known about GltH function (except that it is required for gliding motility (Hodgkin & Kaiser, 1977; Luciano *et al.*, 2011)), GltK/B/A/C are all encoded by the same gene cluster (Luciano *et al.*, 2011) and there is evidence they form a functional complex (Jakobczak *et al.*, 2015). Specifically, GltA interacts with GltB and each protein cannot be stably expressed in absence of the other (Jakobczak *et al.*, 2015). The periplasmic protein GltC also interacts with both GltA and GltB and its expression can only be detected if these two proteins are also expressed (Jakobczak *et al.*, 2015). Lastly, GltK appears to be required for the proper insertion of GltA and GltB into the OM (Jakobczak *et al.*, 2015). During gliding, GltA, GltB and GltC are all recruited at bFAs (Jakobczak *et al.*, 2015) suggesting that they are important for contact with the substratum. However, a precise adhesion function could not be established because single deletions of *gltA/B/C* all abolish bFA formation (Faure *et al.*, 2016; Jakobczak *et al.*, 2015), revealing that this OM complex is also essential for the assembled structure at bFAs.

In this study, we identify a hetero-oligomeric OM complex formed by GltABCHK. Furthermore, we demonstrate that the OM platform regulates recruitment, exposure, and retention of the OM lipoprotein CglB at the cell surface. In turn, CglB is shown to function as a principal adhesin essential for coupling the trans-envelope Glt apparatus to the substratum, thus mediating gliding. These results support a gliding model in which a CglB-loaded OM platform selectively unmasks the adhesin upon stimulation by the motorized IM complex, thus coupling the gliding machinery to the substratum and creating a bFA.

2.3 RESULTS

2.3.1 CglB, a predicted VWA domain-containing protein, is a candidate motility adhesin

We first searched for a candidate adhesin that might interact with the OM platform. The CglB protein is an ideal candidate because it is essential for single-cell gliding motility (Hodgkin & Kaiser, 1977; Luciano *et al.*, 2011; Rodriguez & Spormann, 1999; Youderian *et al.*, 2003) (analogous to Glt OM-platform constituents) (**Figure 2.2A**), and it localizes to the *M.*

xanthus OM as a lipoprotein (Bhat *et al.*, 2011; Kahnt *et al.*, 2010). Homology searching across diverse bacterial genomes revealed that *cglB* co-occurs with genes encoding the complete Agl–Glt machinery in bacterial genomes, supporting a functional link (**Figure 2.3**).

CglB has been proposed to contain a von Willebrand A (VWA) domain (Jakobczak *et al.*, 2015; Pathak & Wall, 2012). Indeed, fold-recognition analysis of CglB indicated structural analogies with numerous metazoan α-integrins (**Table 2.1**); of the 18 identified human α-subunit integrin variants, half possess an intervening module (termed αI or αA) containing a VWA domain (Shimaoka & Springer, 2003), characterized by a Rossmann fold with multiple α-helices shielding an interior β-sheet (Whittaker & Hynes, 2002). Structurally-similar Apicomplexan parasite gliding motility adhesins (MIC2 and TRAP from *Toxoplasma* and *Plasmodium*, respectively) (Song *et al.*, 2012; Song & Springer, 2014) containing VWA domains (Pfam: PF00092) typically involved in adhesion (Whittaker & Hynes, 2002) were also matched to CglB (**Table 2.1**). The top bacterial match was the αI/αA domain-like GBS104 adhesive tip pilin (Krishnan *et al.*, 2013) from *Streptococcus agalactiae* (**Table 2.1**). In bacteria, VWA domains have been much less studied but they are also involved in adhesion as it has recently been shown that Type-IV pili in *Streptococcus sanguinis* adhere via the VWA module in two-domain pilins inserted in the pilus fiber (Raynaud *et al.*, 2021).

Generation of a CglB tertiary-structure model using AlphaFold2 (Jumper *et al.*, 2021; Mirdita *et al.*, 2022) confirmed that CglB likely contains a VWA domain (**Figure 2.4A, Figure 2.5**). In turn, the VWA domain contains a predicted MIDAS (metal ion-dependent adhesion site) motif, a discontinuous structural feature (Asp-x-Ser-x-Ser…Thr…Asp). In general, the coordination of a divalent metal ion (e.g. Ca^{2+}/Mg^{2+}/Mn^{2+}) at this site induces structural changes in VWA domains upon ligand binding that stabilize this adhesive domain in a high-affinity state for the ligand (Shimaoka *et al.*, 2002). For CglB, highly-conserved

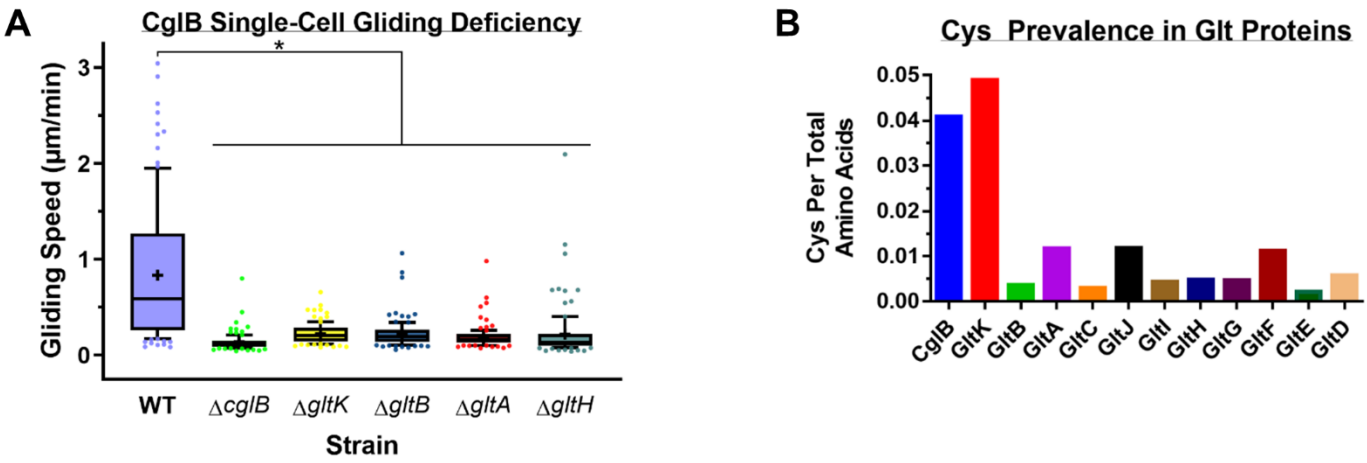

Figure 2.2. CglB gliding motility importance and protein characteristics.

(A) Single-cell gliding speeds for *M. xanthus* OM-module mutant strains (n = 100 cells) on CYE hard (1.5%) agar. The lower and upper boundaries of the boxes correspond to the 25th and 75th percentiles, respectively. The median (line through centre of boxplot) and mean (+) of each dataset are indicated. Lower and upper whiskers represent the 10^{th} and 90^{th} percentiles, respectively; data points above and below the whiskers are drawn as individual points. Asterisks denote datasets displaying statistically significant differences in dataset distributions ($p < 0.0001$) relative to WT, as determined via unpaired two-tailed Mann-Whitney tests.

(B) Ratio of number of Cys residues per gliding motility-complex protein, divided by the total number of amino acids in that protein

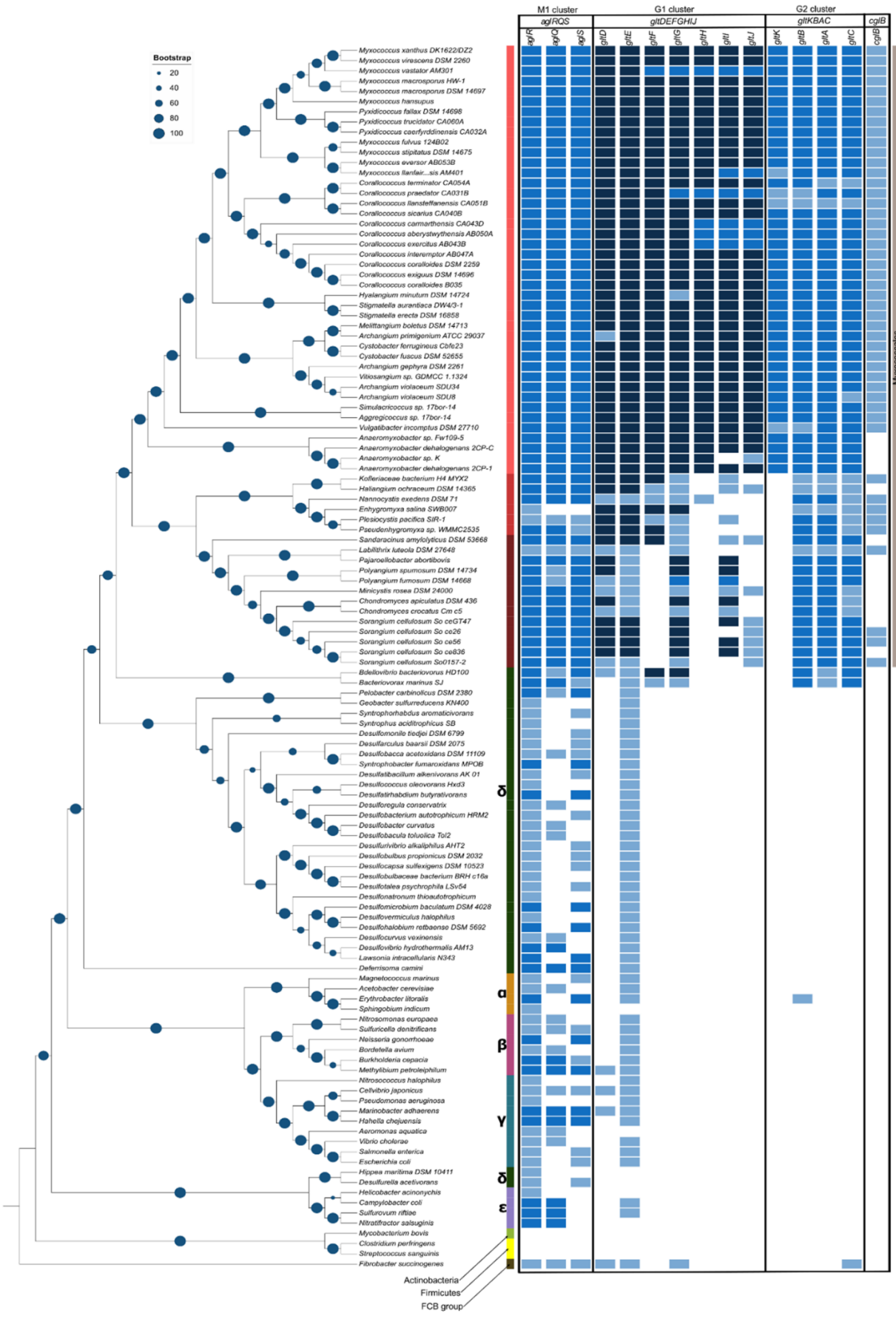
M1 cluster
aglRQS
G1 cluster
gltDEFGHIJ
G2 cluster
gltKBAC
cglB
aglR
aglQ
aglS
gltD
gltE
gltF
gltG
gltH
gltI
gltJ
gltK
gltB
gltA
gltC
cglB
Bootstrap
20
40
60
80
100
Myxococcus xanthus DK1622/DZ2
Myxococcus virescens DSM 2260
Myxococcus vastator AM301
Myxococcus macrosporus HW-1
Myxococcus macrosporus DSM 14697
Myxococcus hansupus
Pyxidicoccus fallax DSM 14698
Pyxidicoccus trucidator CA060A
Pyxidicoccus caerfyrddinensis CA032A
Myxococcus fulvus 124B02
Myxococcus stipitatus DSM 14675
Myxococcus eversor AB053B
Myxococcus llanfair...sis AM401
Corallococcus terminator CA054A
Corallococcus praedator CA031B
Corallococcus llansteffanensis CA051B
Corallococcus sicarius CA040B
Corallococcus carmarthensis CA043D
Corallococcus aberystwythensis AB050A
Corallococcus exercitus AB043B
Corallococcus interemptor AB047A
Corallococcus coralloides DSM 2259
Corallococcus exiguus DSM 14696
Corallococcus coralloides B035
Hyalangium minutum DSM 14724
Stigmatella aurantiaca DW4/3-1
Stigmatella erecta DSM 16858
Melittangium boletus DSM 14713
Archangium primigenium ATCC 29037
Cystobacter ferrugineus Cbfe23
Cystobacter fuscus DSM 52655
Archangium gephyra DSM 2261
Vitiosangium sp. GDMCC 1.1324
Archangium violaceum SDU34
Archangium violaceum SDU8
Simulacricoccus sp. 17bor-14
Aggregicoccus sp. 17bor-14
Vulgatibacter incomptus DSM 27710
Anaeromyxobacter sp. Fw109-5
Anaeromyxobacter dehalogenans 2CP-C
Anaeromyxobacter sp. K
Anaeromyxobacter dehalogenans 2CP-1
Kofleriaceae bacterium H4 MYX2
Haliangium ochraceum DSM 14365
Nannocystis exedens DSM 71
Enhygromyxa salina SWB007
Plesiocystis pacifica SIR-1
Pseudenhygromyxa sp. WMMC2535
Sandaracinus amylolyticus DSM 53668
Labilithrix luteola DSM 27648
Pajaroellobacter abortibovis
Polyangium spumosum DSM 14734
Polyangium fumosum DSM 14668
Minicystis rosea DSM 24000
Chondromyces apiculatus DSM 436
Chondromyces crocatus Cm c5
Sorangium cellulosum So ceGT47
Sorangium cellulosum So ce26
Sorangium cellulosum So ce56
Sorangium cellulosum So ce836
Sorangium cellulosum So0157-2
Bdellovibrio bacteriovorus HD100
Bacteriovorax marinus SJ
Pelobacter carbinolicus DSM 2380
Geobacter sulfurreducens KN400
Syntrophorhabdus aromaticivorans
Syntrophus aciditrophicus SB
Desulfomonile tiedjei DSM 6799
Desulfarculus baarsii DSM 2075
Desulfobacca acetoxidans DSM 11109
Syntrophobacter fumaroxidans MPOB
Desulfatibacillum alkenivorans AK 01
Desulfococcus oleovorans Hxd3
Desulfatirhabdium butyrativorans
Desulforegula conservatrix
Desulfobacterium autotrophicum HRM2
Desulfobacter curvatus
Desulfobacula toluolica Tol2
Desulfurivibrio alkaliphilus AHT2
Desulfobulbus propionicus DSM 2032
Desulfocapsa sulfexigens DSM 10523
Desulfobulbaceae bacterium BRH c16a
Desulfotalea psychrophila LSv54
Desulfonatronum thioautotrophicum
Desulfomicrobium baculatum DSM 4028
Desulfovermiculus halophilus
Desulfohalobium retbaense DSM 5692
Desulfocurvus vexinensis
Desulfovibrio hydrothermalis AM13
Lawsonia intracellularis N343
Deferrisoma camini
Magnetococcus marinus
Acetobacter cerevisiae
Erythrobacter litoralis
Sphingobium indicum
Nitrosomonas europaea
Sulfuricella denitrificans
Neisseria gonorrhoeae
Bordetella avium
Burkholderia cepacia
Methylibium petroleiphilum
Nitrosococcus halophilus
Cellvibrio japonicus
Pseudomonas aeruginosa
Marinobacter adhaerens
Hahella chejuensis
Aeromonas aquatica
Vibrio cholerae
Salmonella enterica
Escherichia coli
Hippea maritima DSM 10411
Desulfurella acetivorans
Helicobacter acinonychis
Campylobacter coli
Sulfurovum riftiae
Nitratifractor salsuginis
Mycobacterium bovis
Clostridium perfringens
Streptococcus sanguinis
Fibrobacter succinogenes
δ
α
β
γ
δ
ε
Actinobacteria
Firmicutes
FCB group
Myxococcales
Cystobacterineae
Nannocystineae
Sorangiineae

Figure 2.3. CglB co-occurrence and gene synteny in bacteria.

Taxonomic distribution and co-occurrence of *agl* and *glt* genes in bacteria. Bootstrap values at each node are indicated as shown in the side legends. Colour of gene hit indicates synteny with the G1 *gltDEFGHIJ* (dark blue) or G2 *gltKBAC* (blue) gene clusters or lack thereof (light blue), respectively. Herein, synteny denotes a minimum of three genes in the vicinity of each other.

Table 2.1. HHpred fold-recognition hits in the PDB to CglB.

PDB Hit	Name *(Species)*	Probability	E-value	Score	Aligned Coils	Identitiy	Similarity
1MF7_A	Integrin αM *(Homo sapiens)*	99.4%	6.4E-14	123.84	187	19%	0.191
4FX5_A	Von Willebrand factor type A *(Catenulispora acidiphila)*	99.36%	3E-13	140.21	199	19%	0.161
4OKR_A	Micronemal protein MIC2 *(Toxoplasma gondii)*	99.34	3.8E-13	127.97	180	20%	0.242
4F1J_B	TRAP *(Plasmodium falciparum)*	99.18	1.1E-11	110.16	178	17%	0.257
3TXA_A	GBS104 tip pilin (*Streptococcus agalactiae* serogroup V*)*	99.13	7.2E-12	136.34	188	17%	0.239

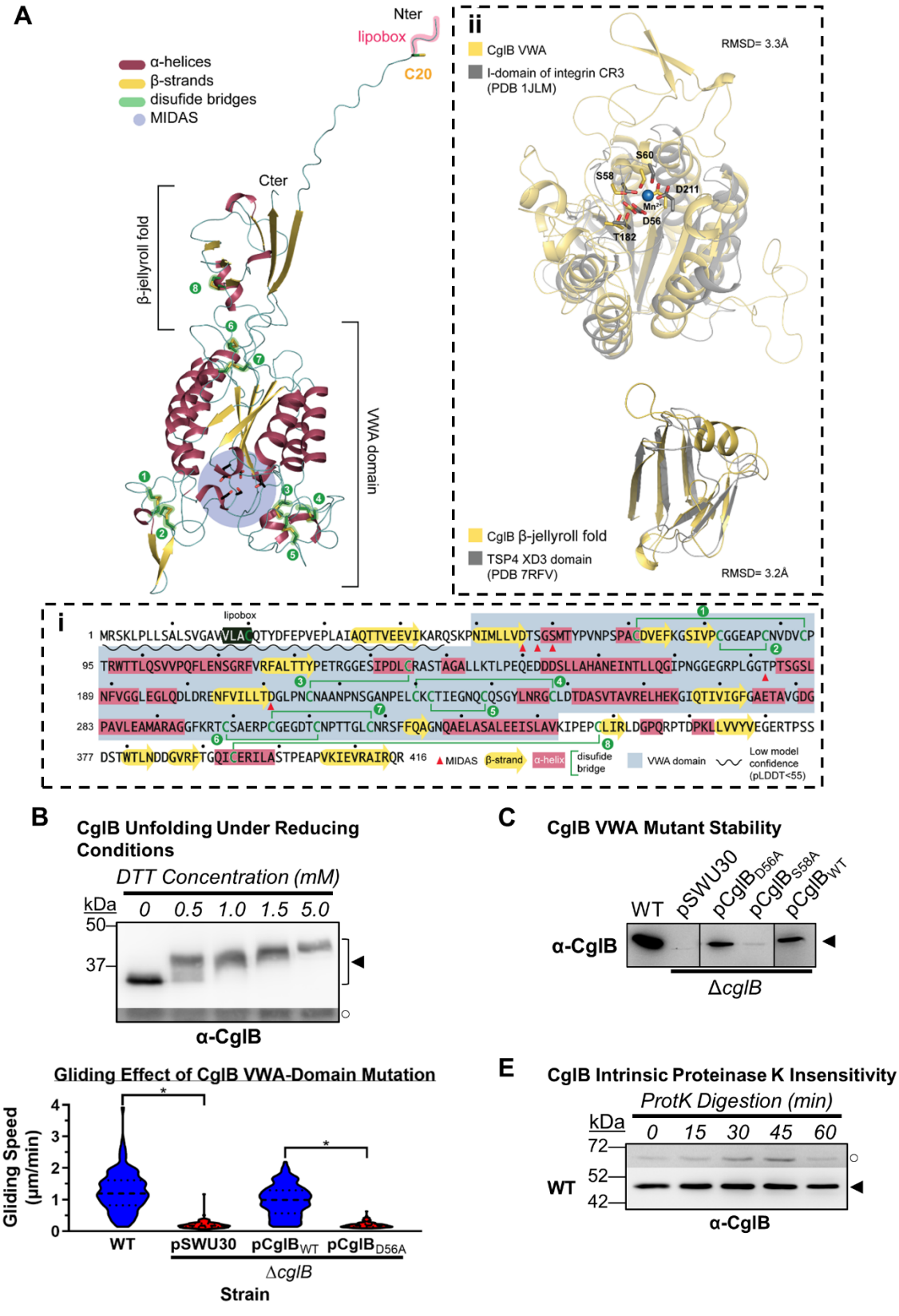
A
Nter
lipobox
C20
α-helices
β-strands
disufide bridges
MIDAS
Cter
β-jellyroll fold
VWA domain
ii
CglB VWA
I-domain of integrin CR3
(PDB 1JLM)
RMSD= 3.3Å
S60
S58
D211
Mn2+
D56
T182
CglB β-jellyroll fold
TSP4 XD3 domain
(PDB 7RFV)
RMSD= 3.2Å
i
lipobox
MIDAS
β-strand
α-helix
disufide bridge
VWA domain
Low model confidence (pLDDT<55)
B
CglB Unfolding Under Reducing Conditions
DTT Concentration (mM)
kDa
0 0.5 1.0 1.5 5.0
50
37
α-CglB
C
CglB VWA Mutant Stability
WT
pSWU30
pCglBD56A
pCglBS58A
pCglBWT
α-CglB
ΔcglB
D
Gliding Effect of CglB VWA-Domain Mutation
Gliding Speed (μm/min)
WT
pSWU30
pCglBWT
pCglBD56A
ΔcglB
Strain
E
CglB Intrinsic Proteinase K Insensitivity
ProtK Digestion (min)
kDa
0 15 30 45 60
72
52
42
WT
α-CglB

Figure 2.4. CglB is a cell-surface protein with a potential integrin αI domain-like VWA fold.
(A) AlphaFold model of CglB. CglB is predicted to contain a VWA domain and a smaller domain adopting a β-jellyroll fold. Within the CglB VWA domain, conserved residues previously described in VWA domains to coordinate divalent cations and constituting the metal ion-dependent adhesion site (MIDAS) are also present (*blue circle*). CglB also contains a lipobox motif with a conserved cysteine (C20). The other 16 cysteines are likely involved in disulfide bridges that stabilize the CglB structure. *Panel i:* Amino acid sequence of CglB. Secondary structures are reported as well as the cysteines potentially forming disulfide bonds (*green lines*). The limits of the VWA domain are also reported in grey and the MIDAS residues are highlighted with red triangles. *Panel ii:* The Dali server was used to scan the CglB structural model against the Protein Data Bank. Top: structural alignment of CglB VWA model (*yellow*) to the αI-domain of integrin CR3 (*grey*, PDB: 1JLM) (Lee *et al.*, 1995a). Predicted CglB MIDAS residues superimpose with the MIDAS residues (coordinating Mn^{2+}) of the integrin CR3. Bottom: structural alignment of CglB smaller domain adopting a β-jellyroll fold (*yellow*) to the XD3 domain of the bacteriophage tailspike protein 4 (TSP4 in *grey*, PDB: 7RFV) (Chao *et al.*, 2022).
(B) α-CglB Western blot of WT whole-cell extracts treated with increasing concentrations of DTT to break disulphide bonds. The lower, darker zone on the blot corresponds to the same section of the same blot image for which the contrast has been increased to highlight lower-intensity protein bands. Legend: ◄, full-length CglB; ○, loading control (non-specific protein band labelled by α-CglB pAb).
(C) α-CglB Western immunoblot of CglB MIDAS-motif amino acid substitution mutants from whole-cell extracts. Non-adjacent lanes on the blot are separated by vertical black lines.
(D) Violin plots of single-cell gliding speeds on hard (1.5%) agar pads for *M. xanthus* DZ2 Δ*cglB* (n = 120 cells) complemented with $CglB_{WT}$ or $CglB_{D56A}$ ectopically expressed from the *attB* phage-attachment site in the chromosome. The median (*dashed line*) as well as lower and upper quartiles (*dotted lines*) are indicated. Asterisks denote datasets displaying statistically significant dataset differences ($p < 0.0001$) compared to strains harbouring either the pSWU30 empty-vector control or the $pCglB_{D56A}$ VWA-domain mutant CglB complementation construct, as determined via two-tailed Mann-Whitney tests.
(E) Protein samples from WT cells resuspended in TPM buffer and digested with exogenous Proteinase K. Aliquots of the digestion mixture were removed at 15-min intervals and TCA-precipitated to stop digestion. The higher, darker zone on the blot corresponds to a section of the same blot image for which the contrast has been increased to highlight lower-intensity protein bands. The lack of CglB degradation was not due to lack of Proteinase K activity (see below). Legend: ◄, full-length CglB; ○, loading control (non-specific protein band labelled by α-CglB antibody).

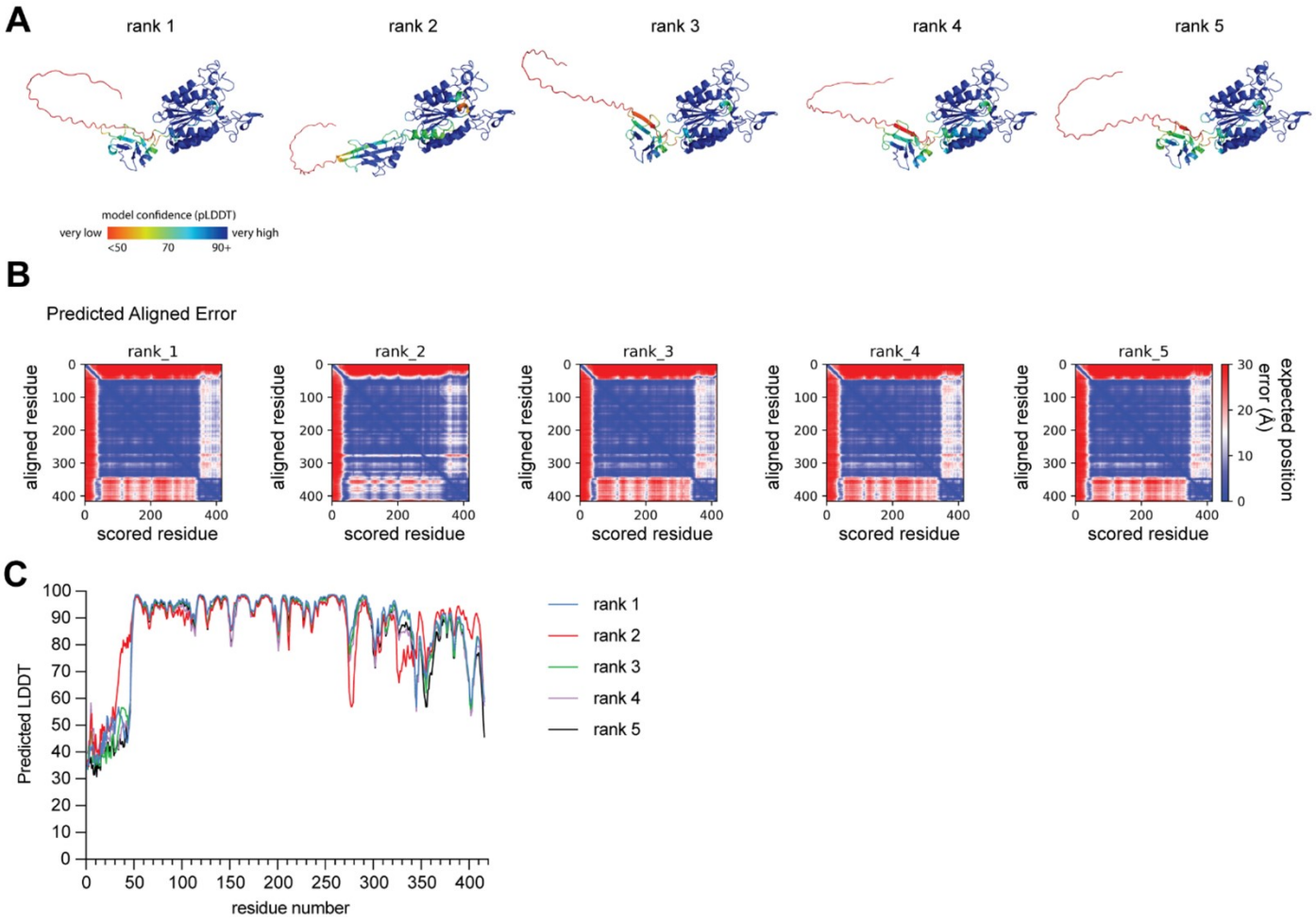

Figure 2.5. AlphaFold prediction quality for the CglB tertiary-structure model.

(A) AlphaFold CglB models ranked from 1 to 5. Per-residue confidence scores (pLDDT: predicted local-distance different test) are directly reported on the 3D structure of CglB (with the range of possible values from 50 [*red*] to 90 [*blue*]).
(B) Corresponding predicted aligned error for each ranked model.
(C) Plot showing the corresponding pLDDT scores per residue for each ranked model

putative MIDAS residues map to D56, S58, S60, T182 and D211 (**Figure 2.4Ai**). An N-terminal β-jelly-roll domain was also predicted for CglB (**Figure 2.4Aii**). While the function of such a domain in CglB is unknown, these domains promote oligomerization in viral capsid proteins (Cheng & Brooks III, 2013). Lastly, CglB contains a high number of Cys residues (17 out of 416 aa = 4.1%) (**Figure 2.2B**) that are predicted to stabilize structural loops of the protein by forming disulphide bonds (**Figure 2.4A, Figure 2.5**) at the necks of these loops; this notion was supported by the observation that titration of reducing agent resulted in a migration shift from faster- to slower-moving CglB-specific bands (via SDS-PAGE and α-CglB Western immunoblot) (**Figure 2.4B**).

We thus tested the potential function of the MIDAS motif *in vivo* by complementing a *cglB* mutant via ectopic expression of a $CglB_{D56A}$ mutant. Contrary to Δ*cglB* cells in which $CglB_{WT}$ expression restored motility, $CglB_{D56A}$ was stably expressed (unlike $CglB_{S58A}$) but failed to complement gliding deficiency (**Figure 2.4C,D**). These data are consistent with the MIDAS motif being functionally significant, suggesting overall that the predicted VWA domain and intra-protein disulphide bonds are important structural determinants of CglB.

2.3.2 CglB is exposed at the cell surface at bFA sites in gliding cells

If CglB functions as an adhesin to anchor the Glt complex to the substratum, it would be expected for CglB to be detectable at the cell surface. This would be an important determination as OM lipoproteins are generally considered to localize to the periplasmic leaflet of the OM. However, this does not preclude surface localization, with a growing list of OM lipoproteins having been shown to be surface-exposed in bacteria (Cole *et al.*, 2021; Wilson & Bernstein, 2016). To probe cell-surface exposure of CglB, its susceptibility to non-specific digestion by Proteinase K was tested on intact liquid-grown cells (Jakobczak *et al.*, 2015). In WT cells, the cellular pool of CglB was not significantly depleted by this treatment (**Figure 2.4E**), suggesting that CglB is either (i) present at the cell surface, but protected from digestion, or (ii) located in the periplasmic leaflet of the OM and is thus protected from extracellular digestion by Proteinase K.

To visualize CglB localization, we first attempted to express the protein with a C-terminal translational fusion to either the fluorescent mNeonGreen reporter, or the self-labelling Halo tag; however, both approaches were unsuccessful due to loss of CglB functionality. To circumvent this problem, we instead used an immunofluorescence approach, treating WT and

Δ*cglB* cells with α-CglB primary antibodies and fluorescently-labelled 2° antibodies, followed by live-cell fluorescence microscopy. As expected, 100% of individual Δ*cglB* cells (361 in total) imaged on agar pads did not exhibit any immunofluorescence (**Figure 2.6A**). Conversely, 53% of single gliding WT cells (i.e. 295/552) across 4 independent experiments displayed a fluorescent signal, manifesting as a single fluorescent cluster in each (**Figure 2.6A**). Consistent with localization at bFAs, α-CglB immunofluorescent clusters detected along the length of the motile cell body (~8% [25/295] of labelled cells) remained stationary relative to the substratum while the cell glided forward relative to the fixed fluorescent signal (**Figure 2.6A**). Once the rear of a gliding cell arrived at the position of the fluorescent cluster, the cell began to drag the cluster behind it at the lagging pole (**Figure 2.6A**), demonstrating that the cluster is attached to the cell (and not transiently associated). Dragged clusters accounted for ~92% (i.e. 270/295) of fluorescent foci in motile cells suggesting that CglB does not adhere to the substratum at the back of the cells. Incidentally, only ~1% of cells (i.e. 3/270) that dragged a cluster later left this cluster behind on the substratum. However, upon reversal of gliding direction, it was possible for a "dragged" fluorescent cluster to become immobilized once again relative to the substratum, while the gliding cell moved relative to the fixed cluster (**Figure 2.6B**). The above-described results are consistent with CglB being associated with bFAs that become active at the leading cell pole and maintain a fixed position relative to the substratum until they are disassembled at the lagging cell pole (**Figure 2.1B**). To probe for signal overlap between CglB and bFA sites, WT cells expressing fluorescently-tagged AglZ were immunolabelled for simultaneous detection of CglB and imaged via live-cell fluorescence microscopy. This analysis revealed that CglB is indeed detected at bFA sites (**Figure 2.6C**). It is intriguing that only single CglB clusters were observed at bFAs, given that multiple bFAs can sometimes be detected in the same cell (**Figure 2.1B**). However, it is unclear how each of these bFAs contribute to locomotion. For example, a specific mutant strain ($MglA_{Q82A/L}$) that only assembles one bFA per cell, moves as fast as cells that assemble several bFAs (Treuner-Lange *et al.*, 2015), so there may be distinct features of these bFAs that need to be clarified. It is also possible that the immunolabelling procedure, which requires pre-labelling of CglB before imaging, is also limiting the detection of additional clusters. Thus, together with the lack of intrinsic Proteinase K susceptibility for CglB in WT cells, these results suggest that CglB is either (i) selectively transported from the periplasmic face of the OM to the cell surface at bFAs or (ii) masked at the cell surface until it is exposed at bFA sites during cell-gliding events.

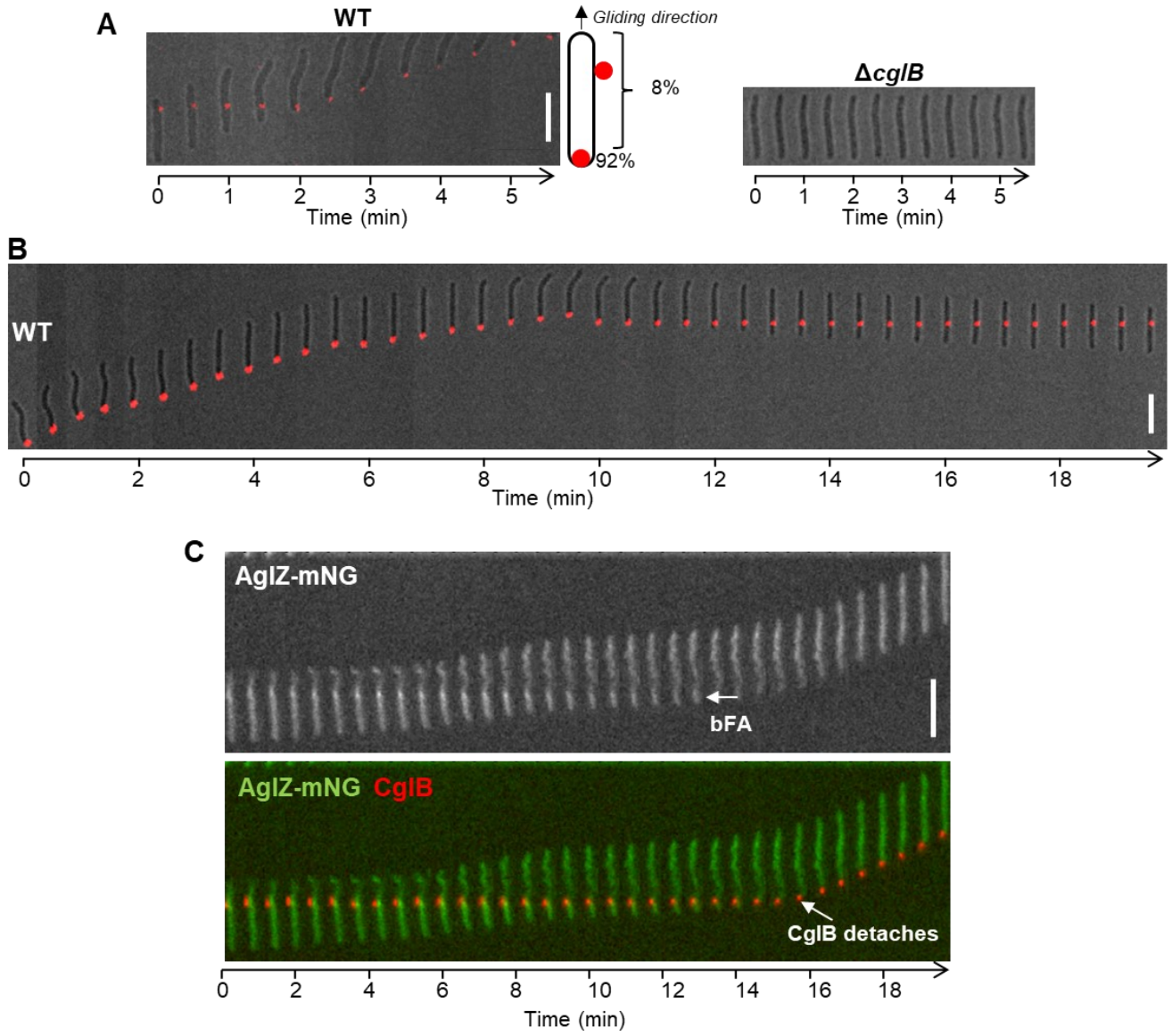

Figure 2.6. CglB is a cell-surface protein that localizes to bFA sites.

(A) Montage of live WT and Δ*cglB* cells immunolabelled with α-CglB 1º antibody, followed by goat α-rabbit 2º antibody conjugated to AlexaFluor647 on agar pads at 32 ºC. Images were acquired at 30 s intervals. Scale bar: 5 μm.

(B) Montage of a live immunolabelled WT cell (labelled as in Panel A) in which a dragged fluorescent cluster becomes immobilized relative to the substratum upon reversal of gliding direction. Scale bar: 5 μm.

(C) Montage of a live immunolabeled cell expressing AglZ-mNeonGreen (Seef *et al.*, 2021) in which an α-CglB antibody co-localizes with a fixed AglZ-mNeonGreen cluster at a bFA site. Note that the CglB cluster detaches from the surface when it reaches the lagging cell pole. Scale bar: 5 μm.

2.3.3 CglB is essential for substratum-coupling of the Agl–Glt machinery

We subsequently investigated the contribution of CglB to surface coupling of the Agl–Glt complex. To probe the role of CglB in bFA formation, we analyzed the dynamics of AglZ-YFP clusters in cells on hard agar for the Δ*cglB* mutant (which stably expresses AglZ-YFP [**Figure 2.7A**]). AglZ-YFP clusters still appeared in Δ*cglB* cells; however, in marked contrast to WT cells (**Figure 2.1B**), AglZ-YFP clusters in Δ*cglB* cells were not stationary relative to the substratum but rather moved directionally from one pole to the other (**Figure 2.8A,B, Figure 2.7B**). This behaviour was consistent with that observed previously in non-adhered motility complexes (Faure *et al.*, 2016). CglB is therefore required to immobilize trafficked AglZ-YFP clusters (relative to the substratum) and assemble bFAs on hard agar surfaces. The function of CglB is clearly distinct from the OM-platform β-barrel proteins because trafficking AglZ-YFP clusters are not formed in any of the Δ*gltA/B/H* mutant backgrounds (Faure *et al.*, 2016). In Δ*cglB* cells, trafficking AglZ-YFP clusters move in-and-out of the epifluorescence focal plane as they rotate counter-clockwise around the cell envelope (**Figure 2.1B, Figure 2.7B**), making it difficult to precisely track the non-adhered foci and thus accurately study their dynamic properties. To resolve these difficulties, we recently developed a TIRFM assay in which *M. xanthus* cells glide in chitosan-coated microfluidic chambers (**Figure 2.7C**); in this system, trafficking AglZ-YFP clusters are also observable in WT cells due to the suboptimal nature of the chitosan surface for *M. xanthus* bFA adhesion (Faure *et al.*, 2016; Tréguier *et al.*, 2019). Since the depth-of-field in TIRFM is restricted to near the cell–substratum interface, photobleaching is reduced and thus tracking of the trafficking AglZ-YFP clusters near the ventral face of the cell can be performed at high spatio-temporal resolution (Faure *et al.*, 2016). On chitosan, Δ*cglB* cells were also non-motile and again, immobilized AglZ-YFP clusters could not be detected (**Figure 2.7C**). Trafficking AglZ-YFP clusters in Δ*cglB* cells behaved similarly to those in WT cells; although slight effects were observed via TIRFM on the trafficking frequency of AglZ-YFP clusters (from the leading to the lagging cell poles), the trafficking speed and lifetime of AglZ-YFP clusters were unchanged in the absence of CglB (**Figure 2.8C-F**). Since AglZ-YFP trafficking reflects the activity of the motility engine (Faure *et al.*, 2016), we conclude that CglB does not affect the activity of the motor, but rather its adhesion to the underlying substratum at bFAs. To test the contribution of adhesive properties by CglB to the tip of the motility complex, we adopted a

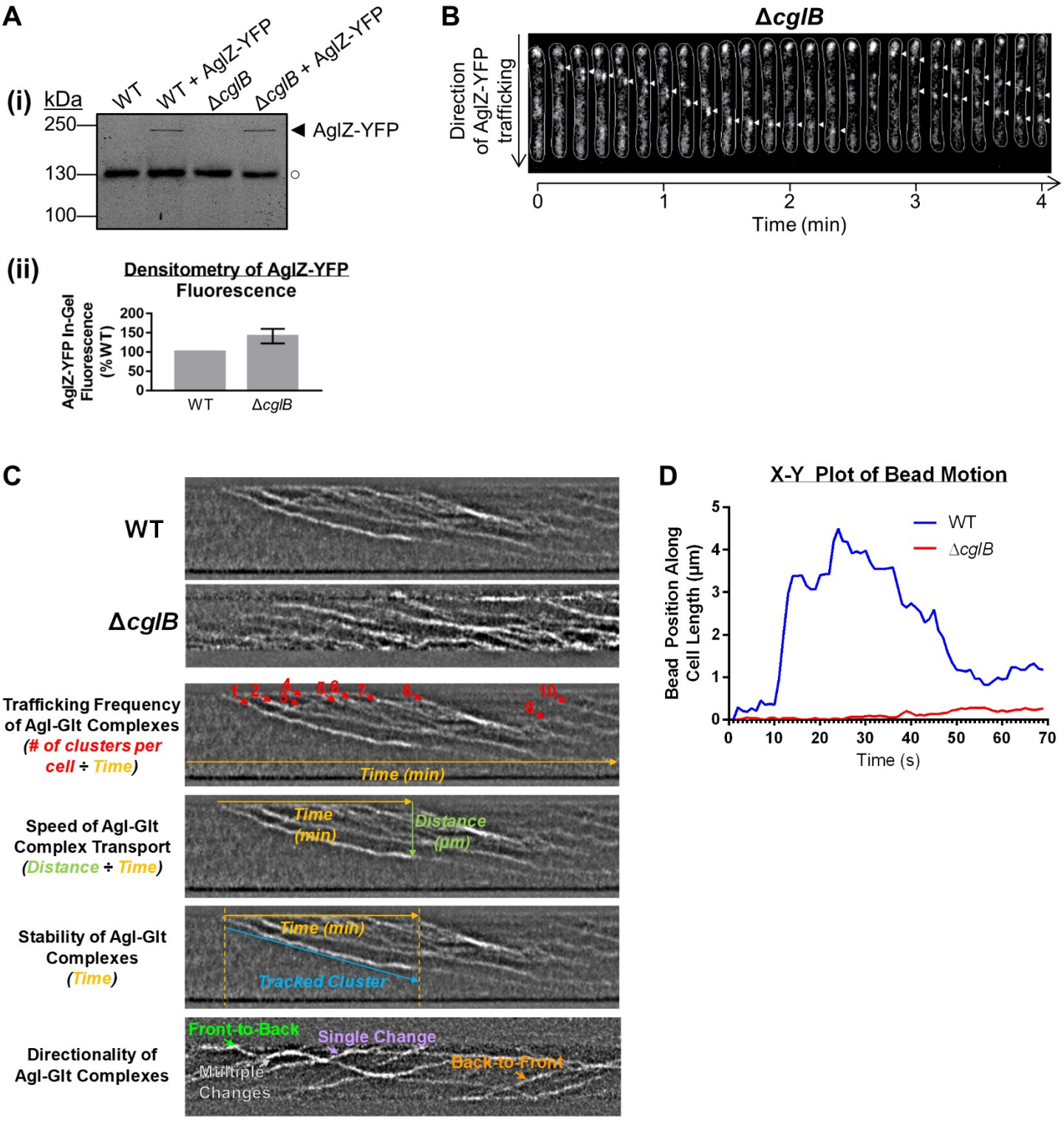
A
(i)
kDa
WT
WT + AglZ-YFP
ΔcglB
ΔcglB + AglZ-YFP
250
130
100
AglZ-YFP
(ii)
Densitometry of AglZ-YFP Fluorescence
AglZ-YFP In-Gel Fluorescence (% WT)
200
150
100
50
0
WT
ΔcglB
B
ΔcglB
Direction of AglZ-YFP trafficking
0
1
2
3
4
Time (min)
C
WT
ΔcglB
Trafficking Frequency of Agl-Glt Complexes
(# of clusters per cell ÷ Time)
1
2
3
4
5
6
7
8
9
10
Time (min)
Speed of Agl-Glt Complex Transport
(Distance ÷ Time)
Time (min)
Distance (μm)
Stability of Agl-Glt Complexes
(Time)
Time (min)
Tracked Cluster
Directionality of Agl-Glt Complexes
Front-to-Back
Single Change
Back-to-Front
Multiple Changes
D
X-Y Plot of Bead Motion
Bead Position Along Cell Length (μm)
5
4
3
2
1
0
WT
ΔcglB
0
10
20
30
40
50
60
70
Time (s)

Figure 2.7. Role of CglB in Agl–Glt complex localization and directed surface transport.

(A) In-gel fluorescence (i) scan and (ii) densitometry analysis of AglZ-YFP levels in WT vs. Δ*cglB* crude-cell lysates resolved via SDS-PAGE. Fluorescence levels were analyzed across six biological replicates and are displayed +/− SEM. Despite a higher mean value for AglZ-YFP levels in Δ*cglB* cells than in WT cells, this difference was not statistically significant, as determined via Wilcoxon signed-rank test performed relative to "100" (p = 0.0938).

(B) Fluorescence microscopy time-course montage of *M. xanthus* Δ*cglB* (on hard agar) expressing AglZ-YFP, clusters of which are indicated (*white arrowheads*). Images were acquired at 10 s intervals.

(C) Kymograph of AglZ-YFP localization in *M. xanthus* cells on chitosan-coated PDMS microfluidic chambers via TIRFM. Arrows in *orange* denote sequential kymograph slices over time. Arrows in *cyan* indicate positions of trafficked Agl–Glt clusters in the cell. The manners in which various fluorescent-cluster tracking data (see **Figure 2.8C-F**) were obtained have been indicated in the example images.

(D) Representative time course of polystyrene bead position tracking along the length of a cell (see **Figure 2.8H**).

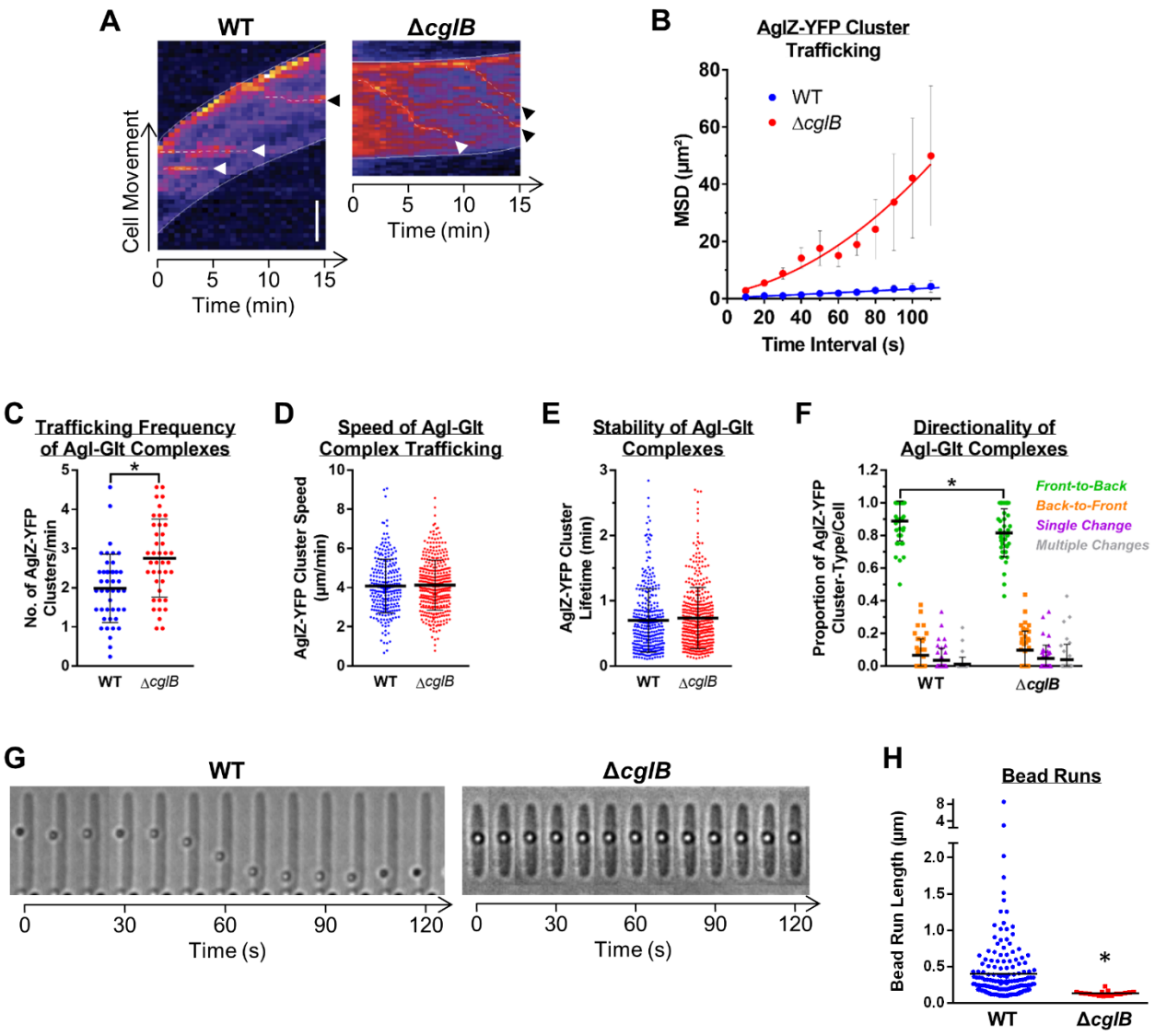

Figure 2.8. CglB is essential for gliding motility-complex adhesion to the substratum.

(A) Kymograph of WT vs. Δ*cglB* cells on agar pads indicating AglZ-YFP cluster position over time (hashed lines). Scale bar: 2 μm. Legend: white arrowheads, AglZ-YFP clusters followed for their entire lifetime; black arrowheads, AglZ-YFP clusters followed for an incomplete lifetime.

(B) Mean-squared displacement (MSD) analysis of AglZ-YFP cluster position tracking in WT (n = 48 clusters) and Δ*cglB* (n = 23 clusters) *M. xanthus* cells. The mean of MSD at each time interval is displayed ± SEM, with a second-order polynomial line fit to each dataset.

(C) Frequency of trafficking AglZ-YFP complexes via TIRFM (of AglZ-YFP) on chitosan-coated glass surfaces in PDMS microfluidic chambers for WT (n = 44 cells) and Δ*cglB* (n = 41 cells) strains. The mean of all values is indicated by a solid black line +/− standard deviation. The distributions of the two datasets are significantly different (*), as calculated via unpaired two-tailed Mann-Whitney U-test ($p < 0.05$).

(D) Speed of Agl–Glt complex trafficking via TIRFM (of AglZ-YFP) on chitosan-coated glass surfaces in PDMS microfluidic chambers for WT (n = 260 clusters) and Δ*cglB* (n = 371 clusters) strains. The mean of all values is indicated by a solid black line +/− standard deviation. The

distributions of the two datasets are not significantly different, as calculated via unpaired two-tailed Mann-Whitney U-test ($p > 0.05$).
(E) Stability of trafficking Agl–Glt complexes via TIRFM (of AglZ-YFP) on chitosan-coated glass surfaces in PDMS microfluidic chambers for WT (n = 333 clusters) and Δ*cglB* (n = 409 clusters) strains. The mean of all values is indicated by a solid black line +/− standard deviation. The distributions of the two datasets are not significantly different, as calculated via unpaired two-tailed Mann-Whitney U-test ($p > 0.05$).
(F) Directionality of trafficked Agl–Glt complexes via TIRFM (of AglZ-YFP) on chitosan-coated glass surfaces for WT (n = 44 cells) and Δ*cglB* (n = 41 cells) strains. "Front" and "back" are defined as cell poles with high and low AglZ-YFP fluorescence intensity, respectively. The mean of all values is indicated by a solid black line +/− standard deviation. Relative to the respective reference WT cluster type, only the distribution of front-to-back clusters were significantly different in the Δ*cglB* cells ($p < 0.05$); all other cluster types did not display distributions different from WT ($p > 0.05$), as calculated via unpaired two-tailed Mann-Whitney U-test.
(G) Trafficking phenotypes of surface-deposited polystyrene beads on *M. xanthus* cells.
(H) Lengths of tracked bead runs > 0.1 μm in *M. xanthus* cells. Images from 10-s intervals were analyzed. The distributions of the two datasets are significantly different (*), as calculated via unpaired two-tailed Mann-Whitney U-test ($p < 0.05$).

force microscopy approach; herein, force generation by the motility complex can be directly monitored in live *M. xanthus* cells immobilized atop a semi-solid agarose matrix deposited on glass slides (Sun *et al.*, 2011). In this environment, the motility complex cannot propel cells (likely because it cannot adhere to the substratum) but its activity can transport polystyrene beads that are non-specifically adsorbed to the cell surface after being deposited using an optical trap (**Figure 2.8G**). Trafficking gliding-machinery units that collide with and recruit such beads move them directionally over long distances (Balagam *et al.*, 2014; Sun *et al.*, 2011) (**Figure 2.7D**). We therefore tested whether bead transport requires the CglB adhesin. While beads were transported multiple times, at lengths up to ~8 μm, along the surface of WT cells, such events were nonexistent in Δ*cglB* cells (**Figure 2.8G,H**). This demonstrates that bead recruitment and trafficking require CglB, consistent with adhesion and force-transduction functions for CglB.

Taken together, we conclude that CglB is required for tethering the gliding motility complex to an engaged extracellular motif, be it a solid surface for cell gliding or cargo for transport in immobilized cells. Contrary to the OM-platform proteins GltA/B/H (Faure *et al.*, 2016) (see below), CglB is not required for Agl–Glt-complex assembly and trafficking. suggesting that it functions to couple trafficking units to the substratum, as would be expected for an adhesin essential for gliding motility.

2.3.4 The Glt OM platform regulates CglB exposure and retention at the cell surface

We next set out to examine the factors that regulate exposure of the CglB adhesin at the cell surface. Since the surface dynamics of CglB suggest a direct connection between CglB and the Agl–Glt complex, we first compared CglB levels in whole-cell samples of each respective *glt* mutant strain. While present at comparable levels in Δ*gltC/D/E/F/G/H/I/J* backgrounds, cell-associated CglB was severely depleted in OM-platform mutants Δ*gltA*, Δ*gltB*, and Δ*gltK* (but not Δ*gltH*) (**Figure 2.10A**). Given that Δ*gltK* cells are deficient in OM-inserted GltA and GltB (Jakobczak *et al.*, 2015), the nature of the CglB deficiency in Δ*gltK* cells may be the same as that in both Δ*gltA* and Δ*gltB* cells, namely an absence of OM-integrated GltA and GltB β-barrels.

Fractionation analysis revealed that CglB was still produced by the Δ*gltA/B/K* mutants (**Figure 2.10B**); however, unlike in WT cells — where CglB was detected in whole-cell and outer-membrane vesicle (OMV) fractions — CglB in these three mutant backgrounds was only recovered in culture supernatants (**Figure 2.10B, Figure 2.9A**). In the Δ*gltA* and Δ*gltB* mutants, such shedding to the supernatant was not observed for (i) GltK (**Figure 2.10B**) which remained OMV-associated, nor for (ii) the cytoplasmic protein MglA, which was detected at levels comparable to the WT strain (**Figure 2.10B**). Therefore, cell-association (and thus OM localization) of CglB depends on GltA, GltB, and GltK.

Supernatant-localized CglB from Δ*gltA/B/K* cultures was found to migrate faster than cell-associated CglB via SDS-PAGE (in both whole-cell and OMV samples) under equivalent denaturing conditions (**Figure 2.10B**), suggesting that supernatant CglB is of reduced molecular weight and may have been proteolytically cleaved. Further support for proteolytic processing of CglB was provided via mass spectrometry analysis of tryptic peptides obtained from CglB immunoprecipitated from supernatant, which revealed that the first 76 N-terminal residues were unaccounted for (**Figure 2.9B**). Our efforts at N-terminal sequencing of supernatant-isolated CglB were inconclusive, and as such we were unable to identify the initial amino acids of the truncated protein. Nonetheless, these data suggest that CglB may be cleaved by a protease in Δ*gltA/B/K* cells prior to its release into the supernatant. To test this hypothesis, we screened the effect of various protease inhibitors for their capacity at restoring CglB localization to the cell envelope in Δ*gltB* cells. Growth in the presence of EDTA restored cell-associated CglB in this background (**Figure 2.10C**). Similarly, EDTA also restored cell-associated CglB in the Δ*gltK* and Δ*gltA* mutants

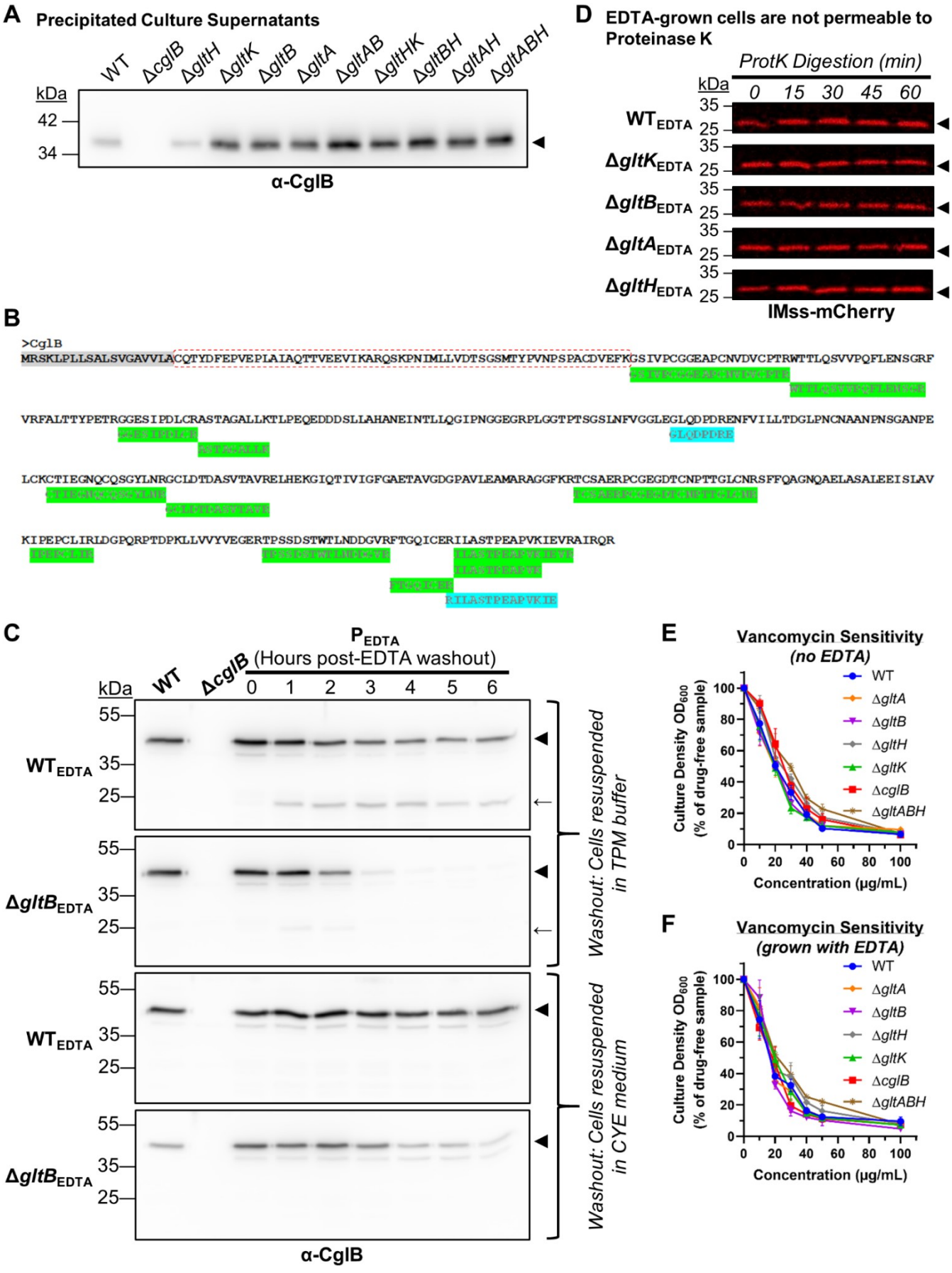
A
Precipitated Culture Supernatants
WT
ΔcglB
ΔgltH
ΔgltK
ΔgltB
ΔgltA
ΔgltAB
ΔgltHK
ΔgltBH
ΔgltAH
ΔgltABH
kDa
42
34
α-CglB
D
EDTA-grown cells are not permeable to Proteinase K
ProtK Digestion (min)
kDa
0
15
30
45
60
WT EDTA
ΔgltK EDTA
ΔgltB EDTA
ΔgltA EDTA
ΔgltH EDTA
35
25
IMss-mCherry
B
>CglB
MRSKLPLLSALSVGAVVLACQTYDFEPVEPLAIAQTTVEEVIKARQSKPNIMLLVDTSGSMTYPVNPSPACDVEFKGSIVPCGGEAPCNVDVCPTRWTTLQSVVPQFLENSGRF
VRFALTTYPETRGGESIPDLCRASTAGALLKTLPEQEDDDSLLAHANEINTLLQGIPNGGEGRPLGGTPTSGSLNFVGGLEGLQDPDRENFVILLTDGLPNCNAANPNSGANPE
LCKCTIEGNQCQSGYLNRGCLDTDASVTAVRELHEKGIQTIVIGFGAETAVGDGPAVLEAMARAGGFKRTCSAERPCGEGDTCNPTTGLCNRSFFQAGNQAELASALEEISLAV
KIPEPCLIRLDGPQRPTDPKLLVVYVEGERTPSSDSTWTLNDDGVRFTGQICERILASTPEAPVKIEVRAIRQR
C
P EDTA
(Hours post-EDTA washout)
kDa
WT
ΔcglB
0
1
2
3
4
5
6
55
35
25
WT EDTA
ΔgltB EDTA
Washout: Cells resuspended in TPM buffer
Washout: Cells resuspended in CYE medium
α-CglB
E
Vancomycin Sensitivity
(no EDTA)
Culture Density OD600
(% of drug-free sample)
100
80
60
40
20
0
0
20
40
60
80
100
Concentration (μg/mL)
WT
ΔgltA
ΔgltB
ΔgltH
ΔgltK
ΔcglB
ΔgltABH
F
Vancomycin Sensitivity
(grown with EDTA)
Culture Density OD600
(% of drug-free sample)
Concentration (μg/mL)
WT
ΔgltA
ΔgltB
ΔgltH
ΔgltK
ΔcglB
ΔgltABH

Figure 2.9. Possibility of post-translational processing of CglB.

(A) Precipitated soluble supernatant samples from Δglt mutants that exhibit depleted levels of cell-associated CglB. Equivalent supernatant volumes from different strains were filtered through a 0.2 µm filter, sedimented in an ultracentrifuge (120 000 × g, 85 min, 4 ºC), then treated with TCA to precipitate all remaining soluble proteins. Legend: ◄, truncated CglB.

(B) Peptides identified via trypsin/V8 digestion and mass spectrometric analysis of immunoprecipitated CglB from ΔgltB culture supernatant. Legend: grey, predicted signal peptide; green, trypsin-derived peptide; cyan, V8- derived peptide; red box, N-terminal tract of CglB unaccounted for by mass spectrometry.

(C) α-CglB Western immunoblot demonstrating the resumption of CglB release from EDTA-grown cells upon transfer to an EDTA-free minimal buffer (TPM) or rich medium (CYE). Legend: ◄, full-length CglB; ←, CglB degradation band; P_{EDTA}, parent strain (WT or *ΔgltB*) grown in the presence of EDTA.

(D) In-gel fluorescence (following SDS-PAGE) of EDTA-grown cells treated with Proteinase K. Each strain (WT, Δ*gltK/B/A/H*) was made to express IMss-mCherry, a modified fluorescent mCherry that is expressed in the periplasm but remains tethered to the IM. Digestion aliquots were removed at 15-min intervals and heat-inactivated to stop digestion.

(E) Vancomycin sensitivity curves for mutant strains defective for various constituents of the Glt OM platform. Strains (n = 3) were grown in CYE liquid broth with increasing concentrations of the antibiotic.

(F) Vancomycin sensitivity curves for mutant strains defective for various constituents of the Glt OM platform. Strains (n = 3) were grown in CYE liquid broth in the presence of EDTA (1 mM) with increasing concentrations of the antibiotic. For Panels E and F, mean values for each mutant strain were compared to that of WT at each concentration using two-way ANOVA and Dunnett's multiple comparisons test, with a single pooled variance. No statistically significant differences were detected ($p < 0.05$) at any vancomycin concentration.

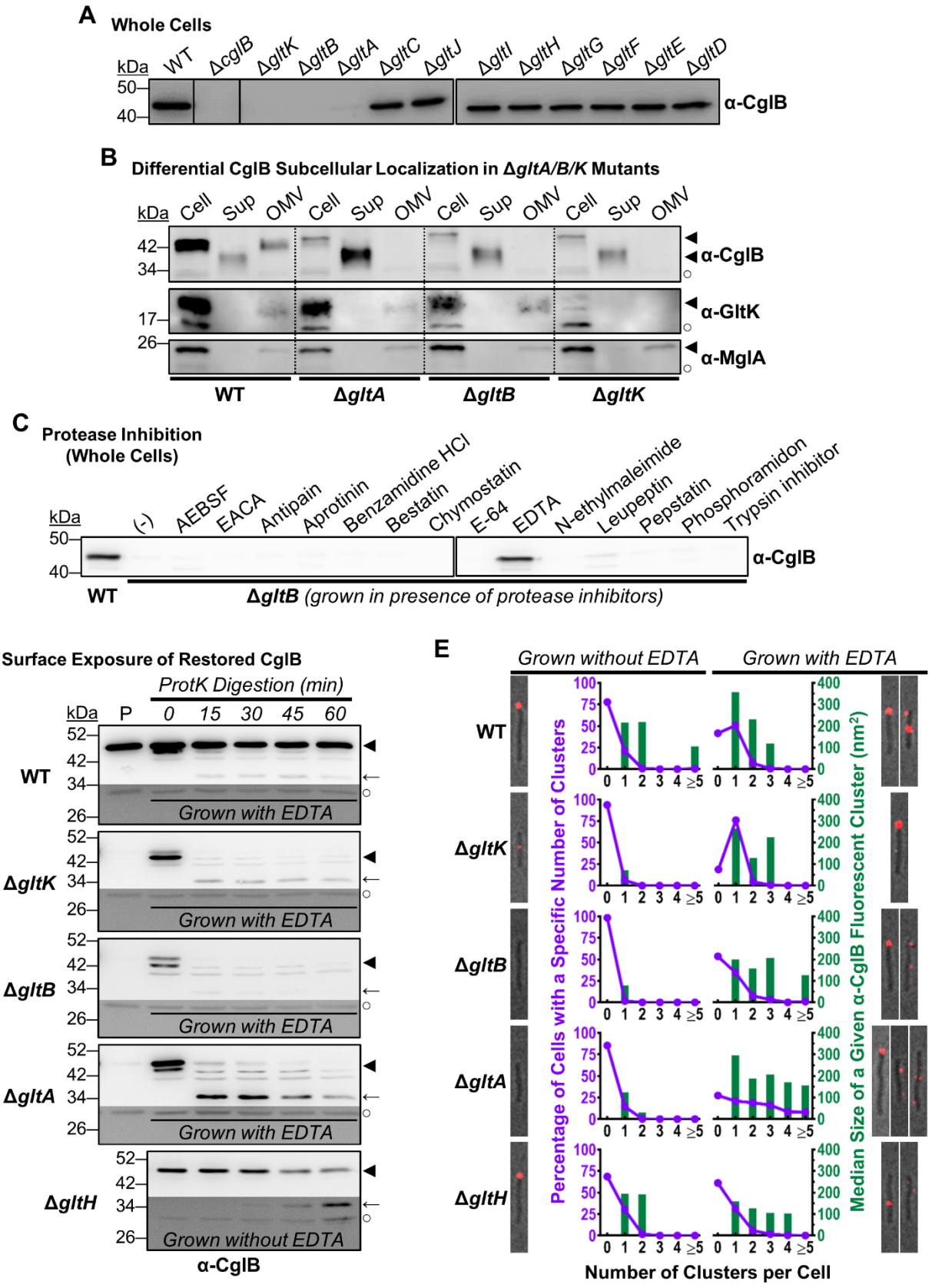
A
Whole Cells
kDa
WT
ΔcglB
ΔgltK
ΔgltB
ΔgltA
ΔgltC
ΔgltJ
ΔgltI
ΔgltH
ΔgltG
ΔgltF
ΔgltE
ΔgltD
50
40
α-CglB
B
Differential CglB Subcellular Localization in ΔgltA/B/K Mutants
kDa
Cell
Sup
OMV
42
34
17
26
α-CglB
α-GltK
α-MglA
WT
ΔgltA
ΔgltB
ΔgltK
C
Protease Inhibition
(Whole Cells)
kDa
(-)
AEBSF
EACA
Antipain
Aprotinin
Benzamidine HCl
Bestatin
Chymostatin
E-64
EDTA
N-ethylmaleimide
Leupeptin
Pepstatin
Phosphoramidon
Trypsin inhibitor
50
40
α-CglB
WT
ΔgltB (grown in presence of protease inhibitors)
D
Surface Exposure of Restored CglB
ProtK Digestion (min)
kDa
P
0
15
30
45
60
52
42
34
26
WT
ΔgltK
ΔgltB
ΔgltA
ΔgltH
Grown with EDTA
Grown without EDTA
α-CglB
E
Grown without EDTA
Grown with EDTA
WT
ΔgltK
ΔgltB
ΔgltA
ΔgltH
100
75
50
25
0
400
300
200
100
0 1 2 3 4 ≥5
Percentage of Cells with a Specific Number of Clusters
Median Size of a Given α-CglB Fluorescent Cluster (nm²)
Number of Clusters per Cell

Figure 2.10. CglB surface exposure is mediated by the Glt OM platform.
(A) Whole-cell extracts from different Δ*glt* mutants. Non-adjacent lanes on the blot are separated by vertical black lines. White space separates two distinct blots processed at the same time.
(B) Fractionated samples containing whole cells (WC), supernatants (Sup), and outer-membrane vesicles (OMV) from various genetic backgrounds. Detection of the gliding motility OM lipoprotein GltK was added as a control, with the protein only detected in WC and OMV samples, showing that the various mutations do not affect OM integrity, with the supernatant localization in this instance being specific to CglB. MglA is a cytoplasmic protein added as a control to show that cell lysis is negligible and does not account for the presence of CglB in supernatants. Legend: ◄, full-length protein; ○, loading control (non-specific protein band labelled by the respective pAb).
(C) Whole-cell extracts from Δ*gltB* cells grown in the presence of different protease inhibitors. White space separates two distinct blots from the same experiment.
(D) Protein samples from cells resuspended in TPM buffer and digested with exogenous Proteinase K. Aliquots of the digestion mixture were removed at 15-min intervals and TCA-precipitated to stop digestion. "P" denotes lanes containing the untreated parent strain grown in the absence of EDTA. Lower, darker zones on each blot correspond to sections of the same blot image for which the contrast has been increased to highlight lower-intensity protein bands. The samples and blot for Δ*gltH* was obtained at the same time as that for WT (Figure 2.4E) indicating that the Proteinase K was indeed active during treatment of the latter. Legend: ◄, full-length CglB; ←, CglB degradation band; ○, loading control (non-specific protein band labelled by α-CglB antibody).
(E) Fluorescence micrographs of live immunolabelled WT, Δ*gltK*, Δ*gltB*, Δ*gltA* and Δ*gltH* cells grown with(out) EDTA (labelled with α-CglB 1º antibody, followed by goat α-rabbit 2º antibody conjugated to AlexaFluor647) on agar pads at 32 ºC. Representative images are provided for cluster labelling patterns observed on ~20% or more of analyzed cells for a given strain and treatment. For each strain grown with(out) EDTA, the number of fluorescent clusters detected per cell was counted (*X-axis*) and compared against the proportion of cells with such a labelling phenotype (*purple left-side Y-axis*). The size of each cluster was also measured, with the median area (*dark green right-side Y-axis*) given for each labelling phenotype. The number of cells analyzed for each treatment is as follows (−/+ EDTA): WT 304/347, Δ*gltK* 306/306, Δ*gltB* 437/199, Δ*gltA* 424/251, Δ*gltH* 505/471.

(**Figure 2.10D**). Interestingly, under these conditions CglB was detected as a doublet band, the relative ratio of which varied depending on the mutant background (**Figure 2.10D**) (discussed below). Nevertheless, resuspension of EDTA-grown Δ*gltB* cells in EDTA-free buffer resulted in the resumption of CglB release from the cells, indicating that CglB restoration is not permanent, consistent with a protease-inhibition effect rather than a non-specific effect of EDTA on the cell envelope (**Figure 2.9C**). Since EDTA chelates divalent cations, CglB release from Δ*gltA*/*B*/*K* cells would be consistent with the activity of a metalloprotease, the identification of which was not within the scope of this paper and which will require downstream experimentation.

The CglB doublet band described above was only detected in all EDTA-grown WT and Δ*gltA*/*B*/*K* samples that were subjected to protein denaturation-and-precipitation via

treatment with TCA and acetone (**Figures. 2.5D, 2.6B**). As such, the doublet is very likely an artefact of altered refolding (following TCA precipitation) in samples initially depleted of divalent cations by the effect of EDTA. These data are consistent with the proposed coordination of a divalent cation by CglB (**Figure 2.2Aii**). Altered CglB refolding is further supported by the observation that no doublet band was detected in EDTA-grown samples that were not subjected to TCA precipitation prior to sample resolution via SDS-PAGE (**Figure 2.10C, Figure 2.9C**).

To determine the subcellular localization of restored CglB in EDTA-grown Δ*gltA*, *B* and *K* mutants, we probed CglB sensitivity to exogenous Proteinase K. In WT cells grown with EDTA, CglB was again protected from Proteinase K attack (**Figure 2.10D**), analogous to results in the absence of the chelator (**Figure 2.4E**). In stark contrast, cell-associated restored CglB was immediately digested by Proteinase K in the EDTA-grown Δ*gltK*, Δ*gltB*, and Δ*gltA* backgrounds (**Figure 2.10D**). Interestingly, upon digestion of full-length CglB in Δ*gltA* cells, there was an immediate appearance of a ~34 kDa CglB degradation product that was detected throughout the time course, suggesting that it was partially protected from further digestion. This protection required GltK and GltB as the ~34 kDa product was almost undetectable in the respective mutant backgrounds (**Figure 2.10D**). As a predicted β-barrel gliding-motility protein, GltH could also be a component of the OM platform. If so, its connection to CglB may not be as central as GltA and GltB given that CglB remained cell-associated in the Δ*gltH* mutant (**Figure 2.10A**). Nevertheless, the cellular pool of full-length CglB decreased steadily throughout the Proteinase-K digestion time course in the absence of GltH, with a concurrent appearance and steady accumulation of an ~34 kDa Proteinase K-resistant band (**Figure 2.10D**).

In these putative OM-platform mutants, to assure that differences in Proteinase-K (a 28 900 Da protein) susceptibility of CglB were not somehow due to increased OM permeability in the various EDTA-grown mutant strains, we first tested the Proteinase K susceptibility of an IMss-mCherry construct expressed in these backgrounds; this is a modified fluorescent mCherry reporter that localizes to the periplasmic space, but which remains tethered to the IM (Ducret *et al.*, 2013). No degradation of the mCherry signal was detected in this experiment (**Figure 2.9D**). Next, we probed the sensitivity of these mutants to killing with vancomycin (a 1449 Da molecule), an antibiotic that disrupts periplasmic peptidoglycan biosynthesis and more effectively so if the OM is permeable (Ruiz *et al.*, 2005). This analysis revealed no increased drug susceptibility of the various mutants relative to WT

(irrespective of growth in the absence/presence of EDTA) (**Figure 2.9E,F**). Thus, EDTA treatment and mutations in the OM platform do not make cells more permeable than WT cells for entry of bulky molecules such as Proteinase K (or antibodies, see below).

To directly demonstrate that the Proteinase K-sensitivity of CglB in Δ*gltA*, Δ*gltB*, Δ*gltK* cells (with EDTA) and Δ*gltH* cells (without EDTA) reflects exposure of CglB at the cell surface, we probed these cells with α-CglB antibodies for immunolabelling as described above. In each of Δ*gltA*/*B*/K_{EDTA}, CglB was detected in typically 1-3 clusters (**Figure 2.10E**, *see purple lines*) spread around the cell periphery, confirming cell-surface localization of CglB in these cells. Scattered foci were also 26-65% smaller in median size than those in WT_{EDTA} cells (**Figure 2.10E**, *see green bars*); these data are consistent with compromised gliding motor-mediated CglB transport-and-clustering, which in WT cells would typically result in bFA formation (Faure *et al.*, 2016). Similar data were obtained for Δ*gltH* cells, in which α-CglB signal was detected around the periphery in dispersed foci (**Figure 2.10E**, *see purple lines*) of smaller median size (**Figure 2.10E**, *see green bars*) than those in WT cells.

Together, the abovementioned results further support the notion that interactions between GltA, B, H, and K regulate CglB exposure at the cell surface. Specifically, these results indicate that CglB becomes surface-exposed in the absence of individual OM-platform components GltA, B, K, and to a lesser extent GltH. The differential effects observed in the various OM-platform mutant strains for both Proteinase K-susceptibility and immunofluorescence point to complex interaction schemes between these proteins that will need to be further explored (see Discussion).

2.3.5 The Glt OM β-barrel proteins are not required for CglB secretion to the cell surface

Two hypotheses could explain the cell-surface protease sensitivity of CglB in Δ*gltA*/*B*/*K*/*H* cells: (i) CglB accesses the cell surface via an as-yet unknown system and subsequently interacts with the Glt OM platform proteins, which shield the adhesin from the action of the putative surface metalloprotease. Alternatively, (ii) the Glt OM platform proteins are directly responsible for CglB cell-surface exposure through a regulated pore-like function that becomes constitutive as soon as one of its components (i.e. GltA, B, K, and to a lesser extent H) is removed.

To examine whether the OM-platform β-barrel proteins form a pore through which CglB is exported across the OM and reaches the cell surface, we first probed cell-association

of CglB in double- and triple-mutant cells lacking various combinations of the OM-platform β-barrel proteins. The rationale herein was that by removing all potential β-barrel pore components, this would prevent secretion of CglB to the cell surface (and its downstream release from the cell). However, in all tested β-barrel mutant combinations, the level of cell-associated CglB remained depleted relative to WT cells, even in Δ*gltABH* triple-mutant cells lacking any of the β-barrel components of the OM platform (**Figure 2.11A**). Expectedly, CglB was instead found to be enriched in the supernatants of the various β-barrel double- and triple-mutant backgrounds (**Figure 2.9A**). Akin to restored CglB in the single-mutant Δ*gltA* and Δ*gltB* strains (**Figure 2.10D**), restored CglB in Δ*gltABH* triple-mutant cells (grown in the presence of EDTA) was also rapidly degraded by treatment with Proteinase K (**Figure 2.11B**), indicating that localization of the gliding adhesin to the *M. xanthus* cell surface is independent of the Glt OM-platform.

Surface localization of CglB independent of the Glt OM platform was also probed via live-cell α-CglB immunolabelling in various strains with different combinations of OM Glt component deficiencies, grown in the absence/presence of EDTA. Most convincingly, even Δ*gltABH* triple-knockout cells (analogous to double-knockout combinations [**Figure 2.12**, *see purple lines*]) grown in the presence of EDTA displayed extensive surface decoration with the α-CglB antibody, which was lacking in non-EDTA-grown cells (**Figure 2.11C**, *see purple lines*). It is interesting that fluorescent clusters were detected even in $\Delta gltABH_{\mathrm{EDTA}}$ cells (albeit of a smaller size); this could be due to CglB–CglB interactions, or interaction with an as yet unidentified partner at the surface (**Figure 2.11C**).

Taken together, these Proteinase K-susceptibility and α-CglB immunolabelling data indicate that in the absence of all OM-platform β-barrel components, the lipoprotein CglB is still secreted to the cell surface. Therefore, CglB does not access the cell surface via a pore formed by GltABH; instead, the adhesin must become surface-localized via an as-yet-unknown mechanism after which it becomes shielded by members of the Glt OM platform.

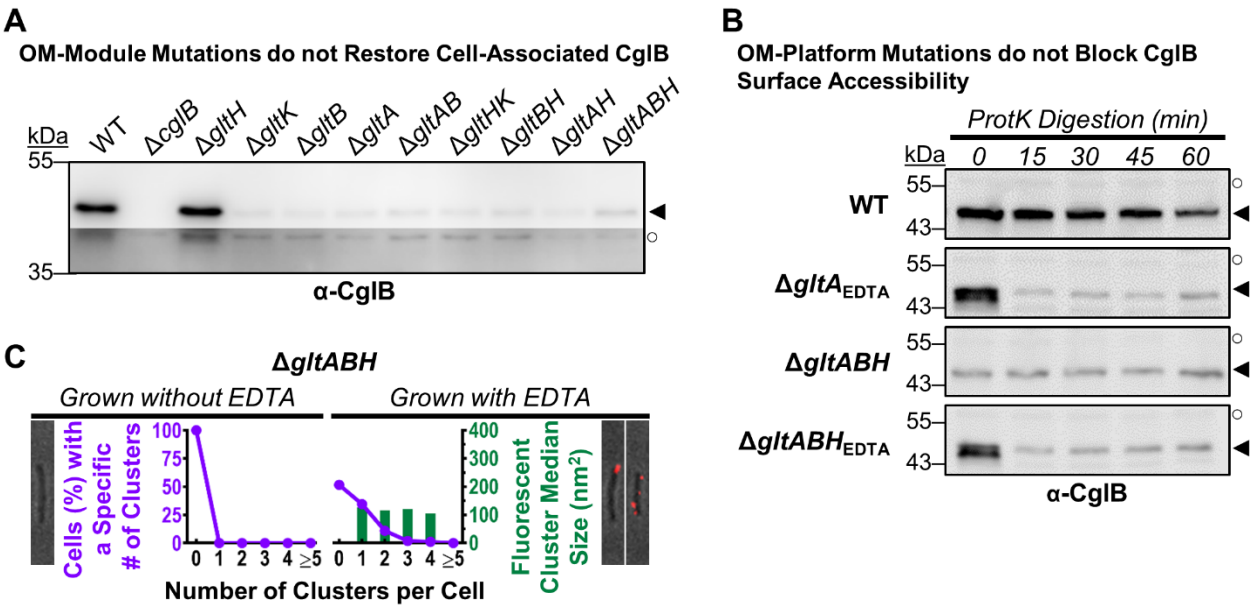

Figure 2.11. CglB secretion to the cell surface is not mediated by the Glt OM platform.

(A) α-CglB Western immunoblots for whole-cell extracts from different combinations of Δ*glt* OM-module mutations in the same strain. Legend: ◄, full-length CglB; ○, loading control (non-specific protein band labelled by α-CglB pAb).

(B) α-CglB Western immunoblots for protein samples from cells resuspended in TPM buffer and digested with exogenous Proteinase K. Aliquots of the digestion mixture were removed at 15-min intervals and TCA-precipitated to stop digestion. Legend: ◄, full-length CglB; ○, loading control (non-specific protein band labelled by α-CglB pAb).

(C) Fluorescence micrographs of live immunolabelled Δ*gltABH* cells grown with(out) EDTA (labelled with α-CglB 1º antibody, followed by goat α-rabbit 2º antibody conjugated to AlexaFluor647) on agar pads at 32 ºC. Representative images are provided for cluster labelling patterns observed on ~20% or more of analyzed cells for a given treatment. For cultures grown with(out) EDTA, the number of fluorescent clusters detected per cell was counted (*X-axis*) and compared against the proportion of cells with such a labelling phenotype (*purple left-side Y-axis*). The size of each cluster was also measured, with the median area (*dark green right-side Y-axis*) given for each labelling phenotype. The number of cells analyzed for each treatment is as follows (−/+ EDTA): Δ*gltABH* 370/344.

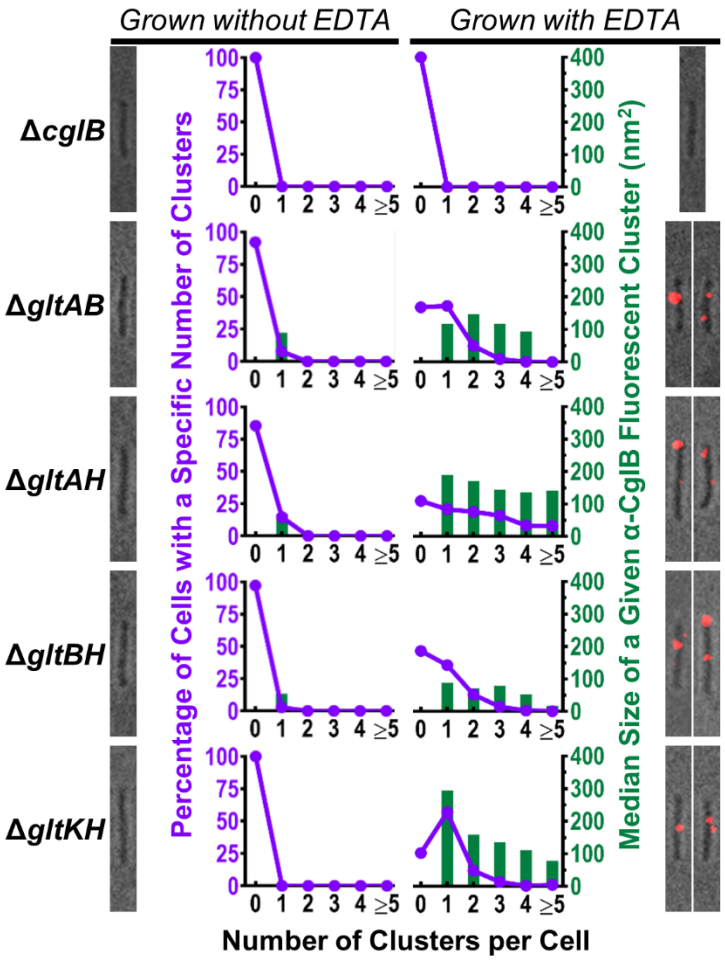

Figure 2.12. CglB localizes to the cell surface despite Glt OM-platform deficiencies.

Fluorescence micrographs of live immunolabelled Δ*cglB*, Δ*gltAB*, Δ*gltAH*, Δ*gltBH*, and Δ*gltHK* cells grown with(out) EDTA (labelled with α-CglB 1º antibody, followed by goat α-rabbit 2º antibody conjugated to AlexaFluor647) on agar pads at 32 ºC. Representative images are provided for cluster labelling patterns observed on ~20% or more of analyzed cells for a given strain and treatment. For each strain grown with(out) EDTA, the number of fluorescent clusters detected per cell was counted (X-axis) and compared against the proportion of cells with such a labelling phenotype (purple left-side Y-axis). The size of each cluster was also measured, with the median area (dark green right-side Y-axis) given for each labelling phenotype. The number of cells analyzed for each treatment is as follows (−/+ EDTA): Δ*cglB* 361/373, Δ*gltAB* 319/471, Δ*gltAH* 534/262, Δ*gltBH* 647/335, Δ*gltKH* 478/394.

2.3.6 CglB directly interacts with a GltABCHK heteroligomeric OM protein complex

Lastly, we set out to characterize the nature of the proposed Glt OM platform. We began by probing for any inter-dependencies within the OM-platform proteins given that GltA and GltB were already known to be reciprocally depleted in Δ*gltB* and Δ*gltA* single-mutant cells (respectively), and that insertion of GltA and GltB into the OM requires the function of GltK (Jakobczak *et al.*, 2015). The levels of GltA, GltB, GltH, and GltK in single-, double-, and triple-mutant backgrounds corresponding to various constituents of the OM module were thus tested. Consistent with previous data (Jakobczak *et al.*, 2015), both GltA and GltB were stably expressed at equivalent levels across all mutant combinations, except in instances where the *gltA* and/or *gltB* genes were deleted; neither GltH nor GltK had an impact on the levels of GltA or GltB. Conversely, GltH and GltK were stably expressed in all mutant backgrounds, except for strains carrying the respective deletion (**Figure 2.13A**). Therefore, while GltA affects the stability of GltB (and vice versa), neither GltH nor GltK affects the levels of any OM-module constituent.

To support the notion of a bonafide OM-platform protein complex, the Proteinase K susceptibility of a given constituent was also tested in the absence of a different OM-platform protein. The rationale was that cell-surface topology for various OM-platform proteins could be altered due to a disrupted interaction network resulting from the missing platform component. As previously detected (Jakobczak *et al.*, 2015), neither GltA nor GltB was stable in a mutant background lacking the other (**Figure 2.13A,B**). Absence of GltH rendered GltA and GltB more Proteinase K-sensitive (**Figure 2.13B**). Similarly, GltH was more sensitive to Proteinase K digestion in the absence of GltA or GltB (**Figure 2.13B**). The absence of GltK did not alter the Proteinase K susceptibility of any of the three integral OM β-barrels (**Figure 2.13B**).

Previously, the insertion of GltA and GltB into the OM was proposed to be compromised in the absence of GltK since GltA and GltB were not efficiently packaged into OMV samples from Δ*gltK* cells (Jakobczak *et al.*, 2015). Herein, GltA and GltB were not sensitive to Proteinase K digestion in the absence of GltK, but were indeed sensitive in the absence of GltH (**Figure 2.13B**), suggesting that the former two β-barrel proteins were accessible to the cell surface in the latter scenario. We thus tested the Proteinase K sensitivity of GltA and GltB in a Δ*gltHK* strain in which both of these β-barrel proteins are expressed at

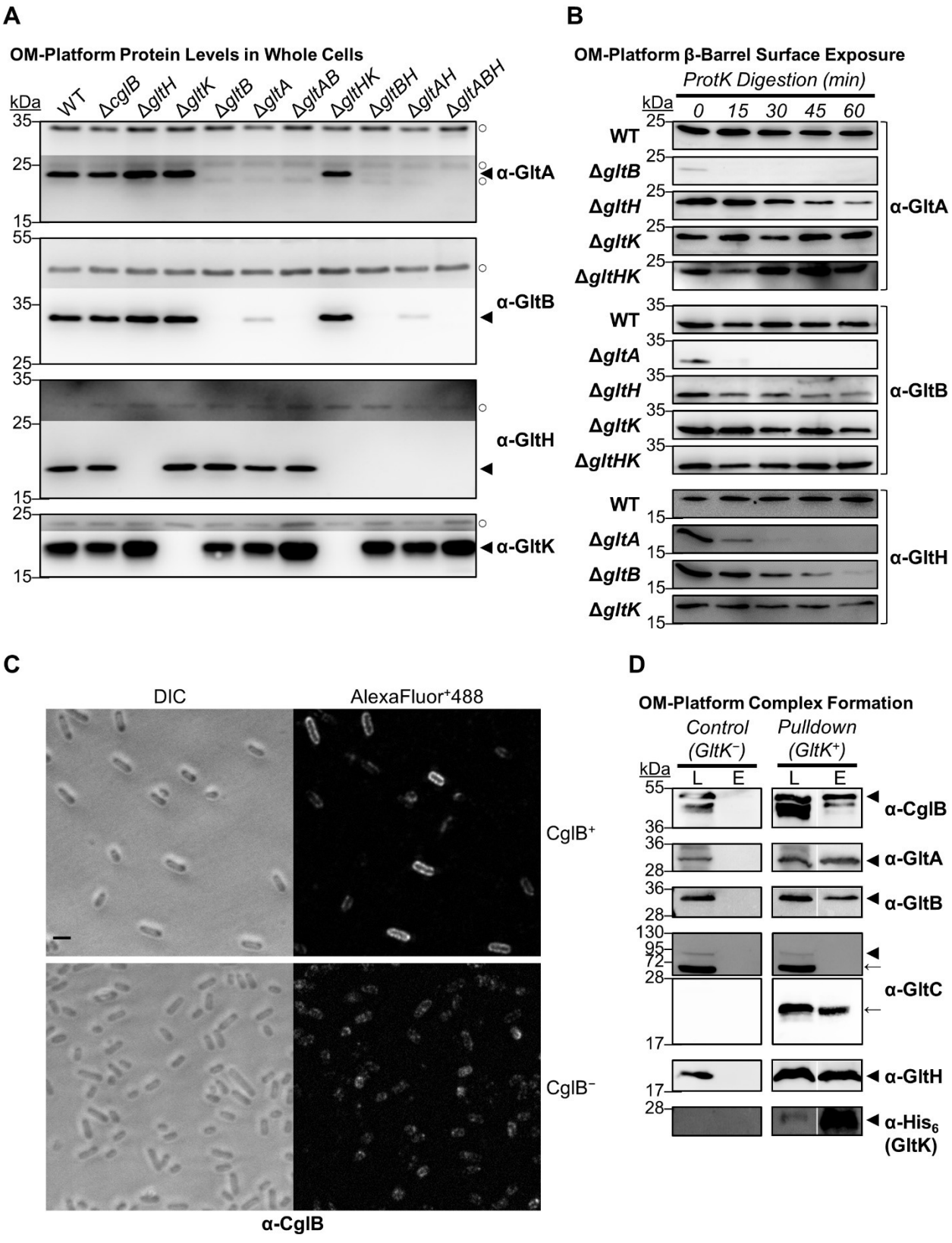
A
OM-Platform Protein Levels in Whole Cells
kDa
WT
ΔcglB
ΔgltH
ΔgltK
ΔgltB
ΔgltA
ΔgltAB
ΔgltHK
ΔgltBH
ΔgltAH
ΔgltABH
α-GltA
α-GltB
α-GltH
α-GltK
B
OM-Platform β-Barrel Surface Exposure
ProtK Digestion (min)
kDa
0
15
30
45
60
WT
ΔgltB
ΔgltH
ΔgltK
ΔgltHK
α-GltA
WT
ΔgltA
ΔgltH
ΔgltK
ΔgltHK
α-GltB
WT
ΔgltA
ΔgltB
ΔgltK
α-GltH
C
DIC
AlexaFluor+488
CglB+
CglB−
α-CglB
D
OM-Platform Complex Formation
Control (GltK−)
Pulldown (GltK+)
kDa
L
E
L
E
α-CglB
α-GltA
α-GltB
α-GltC
α-GltH
α-His6 (GltK)

Figure 2.13. CglB directly interacts with the Glt OM-platform heteroligomeric complex.
(A) Western immunoblots of GltA, GltB, GltH, and GltK in various single-, double-, and triple-mutant combinations of OM-platform constituents. Legend: ◄, full-length protein; ○, loading control (non-specific protein band labelled by the respective α-GltA/α-GltB/α-GltH/α-GltK pAb).
(B) Western immunoblots for Glt OM-platform β-barrel constituent susceptibility to digestion by Proteinase K in Glt OM-module mutant strains. Digestion aliquots were removed at 15-min intervals and TCA-precipitated to stop digestion.
(C) Fluorescence micrographs of *E. coli* BL21(DE3) cells immunolabelled with α-CglB 1º antibody, followed by goat α-rabbit 2º antibody conjugated to AlexaFluor Plus 488 ($AF^{+}488$). Cells had been transformed with the following plasmid combinations: "pCDF-Duet-$GltK^{6H}$+$GltBAC^{S}$ & pET-Duet-GltH-CglB" (for co-expression of GltA, GltB, GltC-StrepII, $GltK\text{-}His_6$, GltH, and CglB) or "pCDF-Duet and pET-Duet" (as empty-vector controls). Cells were induced overnight with 1.0 mM IPTG, then fixed with paraformaldehyde prior to immunolabelling. Scale bar: 2 μm.
(D) Western immunoblotting of purified OM-platform proteins from the pulldown assay (*right-side panels*) or negative control (*left-side panels*) using α-CglB, α-GltA, α-GltB, α-GltH, α-His (GltK), and α-GltC antibodies. Calculated molecular weights for monomeric forms of each protein construct (lacking signal peptide): CglB (42.3 kDa), GltA (25.4 kDa), GltB (27.5 kDa), GltC-StrepII (74.4 kDa), GltH (20.0 kDa), $GltK\text{-}His_6$ (17.5 kDa). Non-adjacent lanes from the same blot are separated by white spaces. Lane legend: L, column loading fraction; E, column elution fraction. Blot legend: ◄, full-length protein; ←, degradation product of the protein of interest.

WT levels (**Figure 2.13A**). In this double-mutant background, both GltA and GltB remained insensitive to digestion by Proteinase K located outside of the cell (**Figure 2.13B**), supporting the notion that GltA and GltB were not correctly inserted into the OM and were thus not surface-exposed in the absence of GltK and GltH. Therefore, GltK exerts its function on the OM module before that of GltH.

Finally, given the evidence for functional interplay between Glt OM-platform members, we directly tested complex formation between the Glt OM-platform proteins GltA, B, C, H, K and CglB using a biochemical pulldown approach. For this we constructed two plasmids allowing for expression of all six proteins in *E. coli* cells. The first plasmid contained *gltK* as a monocistronic sequence (encoded with a C-terminal hexa-histidine tag for pulldown experiments) as well as a synthetic operon of *gltB*, *gltA*, and *gltC-StrepII*, both downstream from T7-promoters (pCDF-Duet) (**Figure 2.14A**). This organisation was chosen to mimic the genetic organization of these genes on the *M. xanthus* chromosome (Jain *et al.*, 2021; Luciano *et al.*, 2011). (A control version of this plasmid, pACYC-Duet, was created lacking *gltK-His_6*). The second plasmid encoded *gltH* and *cglB* as a synthetic operon also downstream from a T7-promoter (pET-Duet) (**Figure 2.14A**). All genes were cloned in their entirety, including any signal sequences and lipoprotein processing motifs, an approach previously shown to maintain targeting of *M. xanthus* OM proteins to the OM of *E. coli* (Holkenbrink *et al.*, 2014). Following IPTG-induced expression in doubly-transformed cells, we first tested whether CglB

is also exposed at the cell surface in *E. coli* BL21(DE3) cells, probing intact cells by immunofluorescence with α-CglB primary antibodies followed by AlexaFluor^{+}488-labelled secondary antibodies. Interestingly, CglB was also detected at the *E. coli* BL21(DE3) surface in CglB^{+} cells as revealed by strong peripheral fluorescence around cells, which was not observed in CglB^{-} control cells (**Figure 2.13C**). This staining was not due to permeabilization during the labelling process because lysozyme treatment (which permeabilizes the cells) led to intense whole-cell fluorescence revealing the pool of CglB that had yet to be trafficked to the cell surface (**Figure 2.14B**).

We next performed pulldown assays on these induced cells using GltK-His$_6$ as bait. To preserve the integrity of any OM complexes, membrane fractions from lysed cells were gently solubilized using a combination of mild detergents (DDM and DM-NPG), followed by passage down a His-trap column, with retained proteins eluted with imidazole. As expected, GltK-His$_6$ was specifically retained on the column; remarkably, full-length GltA, GltB, GltH, and CglB were also retained on the column (**Figure 2.13D**, *triangle bands*).

These co-elution profiles reflect the formation of intact protein complexes, as when the experiment was repeated with plasmids encoding all proteins except GltK-His$_6$ (**Figure 2.14A**), these proteins were similarly expressed but not retained on the column (**Figure 2.13D**). Of note in our setup, a signal peptidase I-processed monomeric GltC (aa 25–673) with an 8-residue StrepII tag is predicted to have a molecular weight of ~74.4 kDa, similar to a previous construct cloned with a His$_6$ tag (Jakobczak *et al.*, 2015). In the latter, the monomeric form of this construct was found to migrate near 100 kDa (Jakobczak *et al.*, 2015). However, in our experiments, full-length monomeric GltC-StrepII could not be stably maintained, though specific smaller molecular-weight degradation bands were clearly enriched and consistently detected in control and pulldown membrane fractions, with these bands also co-eluting from the column in samples containing GltK-His$_6$ (**Figure 2.13D**, *arrow band*). Degradation bands were also detected for GltA, GltB, and CglB, but the relative signal intensity of these bands was minor in comparison (**Figure 2.14C**, *arrow bands*). In further support of complex formation, bands for GltA, GltB, and GltK-His$_6$ were also observed migrating higher in the gel, representing likely oligomeric assemblies incorporating each respective protein (**Figure 2.14C**, *asterisk bands*). Taken together, these data conclusively demonstrate that the OM proteins GltA, GltB, GltC, GltK, and GltH form a heteroligomeric complex together with the adhesin CglB. This complex is remarkably stable as it could be purified in a single-step pulldown assay without the addition of crosslinking agents.

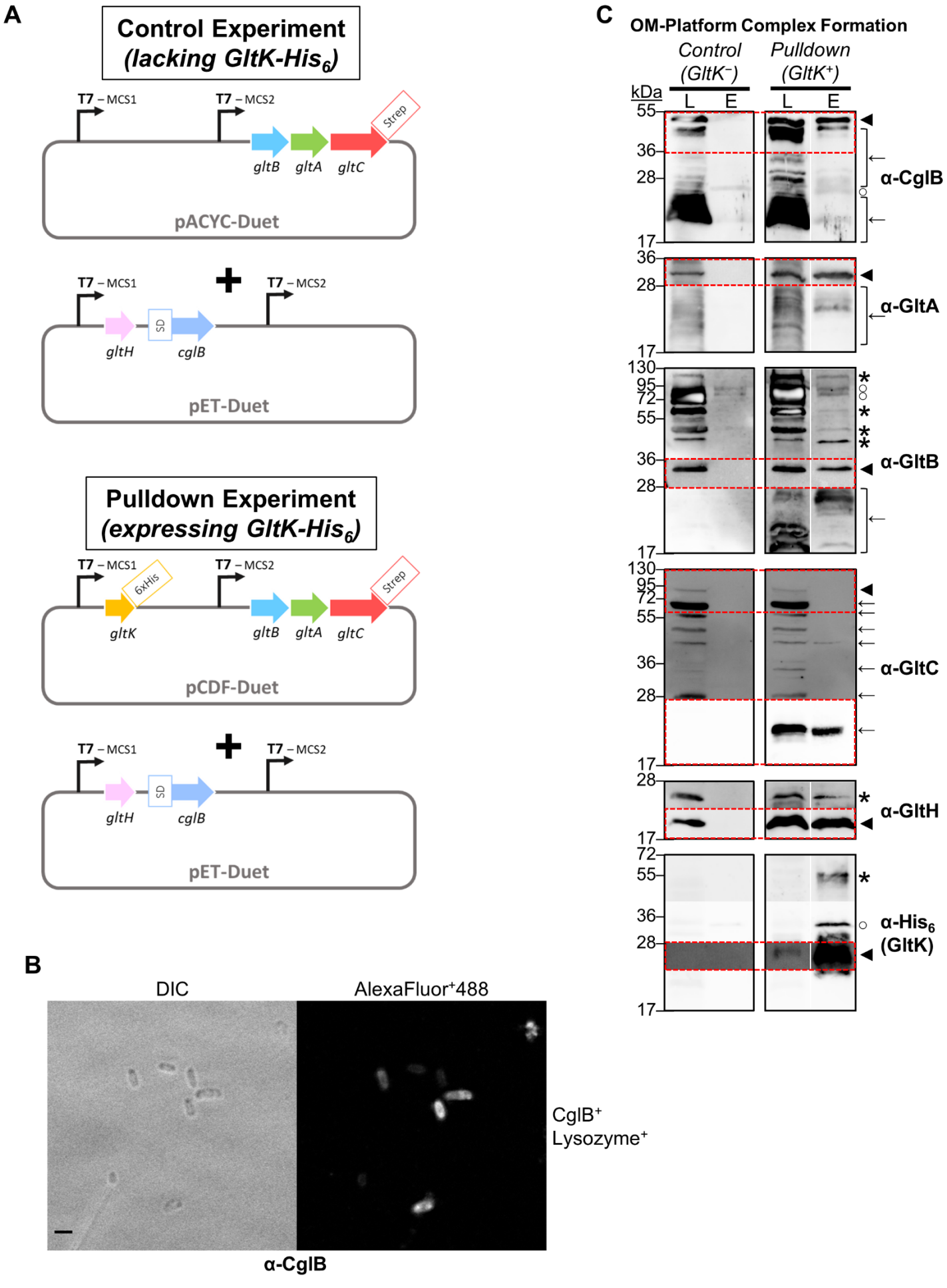
A
Control Experiment
(lacking GltK-His6)
T7 – MCS1
T7 – MCS2
gltB
gltA
gltC
Strep
pACYC-Duet
T7 – MCS1
T7 – MCS2
SD
gltH
cglB
pET-Duet
Pulldown Experiment
(expressing GltK-His6)
T7 – MCS1
6xHis
T7 – MCS2
gltK
gltB
gltA
gltC
Strep
pCDF-Duet
T7 – MCS1
T7 – MCS2
SD
gltH
cglB
pET-Duet
C
OM-Platform Complex Formation
Control
(GltK−)
Pulldown
(GltK+)
kDa
L
E
L
E
55
36
28
17
α-CglB
α-GltA
130
95
72
55
36
28
17
α-GltB
α-GltC
α-GltH
α-His6
(GltK)
B
DIC
AlexaFluor+488
CglB+
Lysozyme+
α-CglB

Figure 2.14. Heterologous expression and co-purification of the Glt OM complex with CglB.
(A) Plasmids for the expression of the OM-platform proteins and CglB in *E. coli* BL21(DE3). Different combinations of plasmids were designed for the pulldown assay (pCDF-Duet and pET-Duet) and the negative control (pACYC-Duet and pET-Duet). A C-terminally StrepII-tagged GltC, GltB and A were cloned into MSC2 of pCDF-Duet and pACYC-Duet vector whereas a C-terminally His_6-tagged GltK was cloned into the MSC1 of pCDF-Duet. The *cglB* and *gltH* sequences were cloned in tandem into pET-Duet MSC1 with an additional Shine Dalgarno (SD).
(B) Fluorescence micrographs of *E. coli* BL21(DE3) cells immunolabelled with α-CglB 1º antibody, followed by goat α-rabbit 2º antibody conjugated to AlexaFluor Plus 488 ($AF^{+}488$). Cells had been transformed with the following plasmids: "pCDF-Duet-$GltK^{6H}$+$GltBAC^{S}$ & pET-Duet-GltH-CglB" (for co-expression of GltA, GltB, GltC-StrepII, GltK-His_6, GltH, and CglB). Cells were induced overnight with 1.0 mM IPTG, fixed with paraformaldehyde, treated with lysozyme, then immunolabelled. Scale bar: 2 μm.
(C) Western immunoblotting of purified OM-platform proteins from the pulldown assay (*right-side panels*) or negative control (*left-side panels*) using α-CglB, α-GltA, α-GltB, α-GltH, α-His (GltK), and α-GltC antibodies. Calculated molecular weights for monomeric forms of each protein construct (lacking signal peptide): CglB (42.3 kDa), GltA (25.4 kDa), GltB (27.5 kDa), GltC-Strep (74.4 kDa), GltH (20.0 kDa), GltK-His_6 (17.5 kDa). Lane legend: L, column loading fraction; E, column elution fraction. Blot legend: ◄, full-length protein; *, oligomeric species of the protein of interest; ←, degradation products of the protein of interest; ○, non-specific protein band (detected in the elution fractions from both the control and pulldown samples) labelled by the respective α-CglB/α-GltB/α-His antibodies).

2.4 DISCUSSION

Previously, we demonstrated that on hard surfaces *Myxococcus* cells are propelled by directionally-transported Agl–Glt complexes that become tethered at bFAs where they exert traction forces against the underlying substratum (Faure *et al.*, 2016). However, the manner in which OM Glt proteins interact with the substratum and the possible implication of specific adhesins remained unclear. The characterization of CglB, a protein first studied >40 years ago (Hodgkin & Kaiser, 1977), and its functional interactions with the OM Glt proteins (**Figure 2.13B,D**) provides a potential solution to these questions.

Four main lines of evidence suggest that CglB is a cell-surface adhesin of the Agl-Glt complex:

(i) CglB contains a predicted VWA domain, which are typically found in proteins that interact with the extracellular matrix.

(ii) CglB becomes cell-surface exposed at bFA sites, where it forms fixed clusters that detach from the substratum (and remain cell-associated) when a bFA site reaches the lagging cell pole.

(iii) In the absence of CglB, trafficking motility complexes do not become immobilized, which would be expected if they fail to adhere to the surface. In addition, these trafficking complexes cannot transport surface-associated cargo in the absence of CglB.

(iv) CglB localizes to the cell surface where it is shielded by direct interaction with the Glt OM platform.

Below, we discuss possible adhesion mechanisms and outstanding questions for the future.

2.4.1 Mechanism of CglB secretion

While OM lipoproteins are generally thought to be exposed on the periplasmic leaflet of the OM, surface-exposed lipoproteins have recently come to the fore in bacterial cell biology, though the surface-exposure mechanisms for most have yet to be solved (Hooda & Moraes, 2018; Konovalova & Silhavy, 2015; Wilson & Bernstein, 2016). An open question thus remains as to how exactly CglB is able to access the cell surface and subsequently associate with the integral OM β-barrel platform. Interestingly, organizational parallels exist between CglB-containing Agl–Glt gliding machinery and bipartite iron-scavenging systems. In species of *Neisseria* and other bacterial pathogens, the cell-surface lipoproteins TbpB/LbpB (parallel: CglB) interact with the integral OM β-barrel TbpA/LbpA (parallel:

GltABH) to bind human transferrin/lactoferrin (respectively) and abstract iron. The TbpA/LbpA β-barrels contain a Ton box and are TonB-dependent transporters (parallel: GltA/B), which can then import the abstracted iron into the cell upon activation of the integral IM ExbBD-TonB (parallel: AglRQS) motor (Beddek & Schryvers, 2010; Pogoutse & Moraes, 2017). Recently, a new class of transporter (corresponding to DUF560) has been shown to mediate secretion of lipoproteins such as TbpB/LbpB (and soluble proteins) across the OM (Grossman *et al.*, 2021; Hooda *et al.*, 2016; Hooda *et al.*, 2017; Huynh *et al.*, 2022). However, such a proposed "Type 11 secretion system" is not encoded in the *M. xanthus* genome, suggesting that this is not the mechanism for CglB trans-OM export. Considering heterologously-expressed CglB can also be detected on the surface of *E. coli* BL21(DE3) cells (**Figure 2.13C**), the targeting mechanism for the adhesin may depend on a more general pathway rather than an organism-specific secretion system. For instance, one possibility would be for CglB to piggyback to the cell surface during Bam-mediated OM insertion of a "host" β-barrel (akin to surface lipoprotein stress sensor RcsF and OmpA (Tata *et al.*, 2021)). In *M. xanthus* however, none of the Glt OM-platform β-barrels are involved as CglB is still able to access the cell surface even in the absence of all three OM proteins.

2.4.2 Regulation of CglB exposure at the cell surface

CglB interacts with the OM platform and *in vivo* experiments suggest that surface exposure of CglB is regulated by this interaction. Unless CglB becomes associated with the OM platform, it is rapidly cleaved from the cell surface, presumably by the action of a metalloprotease (of which there are >150 encoded in the *M. xanthus* genome, as identified via the MEROPS database) (Rawlings *et al.*, 2018). With yet another parallel to iron-scavenging systems, the LbpB surface lipoprotein can be released into the extracellular milieu by a cell-surface serine protease (NalP, an autotransporter) (Roussel-Jazédé *et al.*, 2010). The functional significance of CglB cleavage is unclear as it is not detected in WT cells and is likely a by-product of the sensitized genetic backgrounds. One possibility could be that excessive cell-surface adhesin presence is detrimental to *M. xanthus* physiology by way of undesired cell–cell/substratum connections, and cells thus possess a cleanup mechanism with which to remove free adhesin from amongst the cell-surface lipopolysaccharide molecules (Saïdi *et al.*, 2022a) of the OM. Nevertheless, the data suggests that the OM platform selectively regulates the exposure of CglB since:

(i) Despite the abundance of CglB (as detected by western blot) (**Figure 2.10A**), only discrete foci are detected by immunofluorescence on gliding cells (mainly at the lagging cell pole) (**Figures 2.12, 2.10E**).

(ii) In addition, many more foci are detected in *gltA*, *B, K* (+EDTA) and *H* mutant cells, especially along the length of the cell body (**Figure 2.10E**), suggesting that many CglB–OM platform complexes are formed that are not detected by immunofluorescence.

(iii) CglB localizes all around the surface of *E. coli* BL21(DE3) cells when it is expressed together with GltABCHK (**Figure 2.13C**), suggesting that an additional clustering mechanism is present in *M. xanthus* cells.

In WT cells, CglB exposure may be coupled to adhesion via its recruitment by the Agl–Glt apparatus, which would lead to the major grouping of surface CglB clusters. Such coupling may be lost in the OM-platform mutants, leading to the formation of multiple (smaller) clusters. This hypothesis is consistent with the protection of CglB (from digestion by Proteinase K) afforded by its interaction(s) with the Glt OM-platform proteins. Structure determination will be needed to identify the precise interaction network of CglB with the OM-platform proteins and elucidate the manner in which interactions between three distinct β-barrel proteins (GltA,B,H) regulate CglB surface exposure.

2.4.3 Mechanism of adhesion

Interestingly, surface-exposed CglB clusters become inert when they reach the lagging cell pole, where bFAs are inactivated. We cannot currently infer the nature of any interactions CglB maintains at the lagging cell pole and it is possible that our immunolabelling procedure affects its dynamics at this location. Nevertheless, the CglB clusters can be recruited again to bFAs when cells reverse, which suggests that CglB may only be adhesive when coupled with active motor units; perhaps because it is selectively exposed, or because its adhesive properties become engaged through the mechanical action of the AglRQS motor, or both. In fact, interactions between the OM platform and the underlying Agl–Glt machinery could trigger CglB exposure at bFAs, thus ensuring just-in-time adhesion and force transduction. We propose that when the IM Agl motor recruits the OM platform at bFAs (Faure *et al.*, 2016), CglB becomes concentrated at Agl–Glt sites directly coupling adhesion to contractile forces exerted by the motor. This could occur following dynamic interactions between the IM motor and the OM platform in a manner similar to that proposed for the homologous Tol-Pal

complex in *E. coli*. The TolQR-TolA motor localizes at division septa where it is proposed to function as a conveyor belt to concentrate the OM lipoprotein Pal locally (Webby *et al.*, 2022).

In this process, the proton flow through the channel assembled by TolQR energizes conformational changes on the TolA protein, which can stretch through pores in the PG layer to interact with Pal at the inner face of the OM (Webby *et al.*, 2022). Although it remains to be shown, the predicted structures of the putative Agl motor-associated proteins suggest that they could operate like the TolA protein. Specifically, the IM proteins GltG and GltJ are both predicted to adopt TolA-like folds (Faure *et al.*, 2016; Islam & Mignot, 2015) and both OM β-barrel proteins GltA and GltB contain extended, unstructured N-terminal domains, with a potential TonB-box consensus sequence in the latter (Faure *et al.*, 2016). Conceptually, such a mechanism could be compared to the firing of a gunlock cannon: a projectile (CglB) is loaded into the front-most opening of a cannon barrel (GltABH), after which an arm (GltG/J) exerts mechanical force on a lanyard (TonB box on the Glt OM module), resulting in firing of the loaded projectile (CglB) through the barrel of the cannon (GltABH).

Finally, the extracellular CglB ligand remains to be discovered. Eukaryotic VWA domains, such as those found in integrins, are predominantly found in adhesins and ECM proteins (Whittaker & Hynes, 2002). Prokaryotic VWA domains have been less characterized but it was recently shown that bacterial pathogens use pilus adhesins, in type-I and type-IV pili, that adhere to host cell proteins via the VWA domains of tip proteins (Izoré *et al.*, 2010; Raynaud *et al.*, 2021; Treuner-Lange *et al.*, 2020). Since gliding motility implicates a complex ECM (Ducret *et al.*, 2013; Ducret *et al.*, 2012), the CglB VWA domain might bind to protein and/or polysaccharide components of the ECM. The recruitment of CglB at bFAs further highlights functional parallels between bFA and eFA mechanisms. In eukaryotic cells, the migration of surface-adhered cells via eFA-based locomotion involves the coordinated actions of a trans-envelope suite of proteins to transduce integrin-mediated cell–substratum adhesion to mechanical force and movement to propel the cell forward. In integrins, interaction with VWA ligands provoke large conformational changes that reinforce adhesion and trigger signal transduction (Shimaoka & Springer, 2003), thus probing the biophysical properties of the ECM. It would be interesting to test whether such properties are also present in CglB, perhaps to adjust bFA activity and composition in response to the extracellular environment. Such properties might be essential for multicellular behaviors (Islam *et al.*, 2020): similar to eukaryotic integrins, CglB could act as a sensor, regulating cell-cell interactions during development and predation.

2.5 MATERIALS AND METHODS

2.5.1 Bacterial cell culture and phenotypic analysis

M. xanthus strains were cultured in CYE (1% w/v Bacto Casitone peptone, 0.5% w/v yeast extract, 0.1% w/v $MgCl_2$, 10 mM MOPS [pH 7.4]) broth with shaking (220 rpm), or on CYE solidified with 1.5% agar, at 32 ºC. To examine the effects of protease inhibition on CglB liberation, cells were grown in the presence of individual protease inhibitor panel constituents (Sigma, Cat.# INHIB1) at the recommended concentration: 4-(2-Aminoethyl benzenesulfonyl fluoride HCl (AEBSF) (1 mM), ε-aminocaproic acid (EACA) (5 mg/mL), antipain HCl (100 μM), aprotinin (300 nM), benzamidine HCl hydrate (2 mM), bestatin HCl (40 μM), chymostatin (50 μg/mL), E-64 (10 μM), ethylenediaminetetraacetic acid disodium dihydrate (EDTA) (1 mM), N-ethylmaleimide (500 μM), leupeptin hemisulfate (75 μM), pepstatin A (1 μM), phosphoramidon disodium salt (10 μM), and soybean trypsin inhibitor (1 μM). Cell resuspensions were done in TPM buffer (10 mM Tris-HCl, pH 7.6, 8 mM $MgSO_4$, and 1 mM KH_2PO_4). All *M. xanthus* and *E. coli* strains used are listed in **Table 2.2** and **Table 2.3** (respectively). All plasmids used are listed in **Table 2.4**.

For vancomycin-susceptibility testing, 3 mL of CYE broth (in sterile 10 mL glass tubes) were inoculated to a starting OD_{600} of 0.05 in the absence/presence of EDTA (1 mM), with vancomycin added at increasing concentrations (0 to 100 μg/mL). Tubes were incubated with shaking (220 rpm) at 32 ºC for 26 h, followed by mixing via vortex and aspiration-and-ejection using a pipette to break up aggregates; 1 mL of culture was then used to read the OD_{600} via spectrophotometer in a disposable cuvette.

Table 2.2. *Myxococcus xanthus* strains used in this study.

Strain	Genotype/ Description	Construction	Source or Reference
DZ2	WT	Wild type	Laboratory collection
TM770	Ω*cglB*	DZ2 Ω*cglB*	This work
TM913	Δ*cglB*	DZ2 Δ*cglB*	This work
TM600	Δ*gltK*	DZ2 Δ*gltK* (pBJΔ*gltK*)	(Luciano *et al.*, 2011)
TM603	Δ*gltB*	DZ2 Δ*gltB* (pBJΔ*gltB*)	(Luciano *et al.*, 2011)
TM606	Δ*gltA*	DZ2 Δ*gltA* (pBJΔ*gltA*)	(Luciano *et al.*, 2011)
TM570	Δ*gltC*	DZ2 Δ*gltC* (pBJΔ*gltC*)	(Luciano *et al.*, 2011)
TM646	Δ*gltJ*	DZ2 Δ*gltJ*	This work
TM731	Δ*gltI*	DZ2 Δ*gltI*	This work
TM149	Δ*gltH*	DZ2 Δ*gltH* (pBJΔ*gltH*)	(Luciano *et al.*, 2011)
TM135	Δ*gltG*	DZ2 Δ*gltG* (pBJΔ*gltG*)	(Luciano *et al.*, 2011)
TM136	Δ*gltF*	DZ2 Δ*gltF* (pBJΔ*gltF*)	(Luciano *et al.*, 2011)
TM148	Δ*gltE*	DZ2 Δ*gltE* (pBJΔ*gltE*)	(Luciano *et al.*, 2011)
TM142	Δ*gltD*	DZ2 Δ*gltD* (pBJΔ*gltD*)	(Luciano *et al.*, 2011)
TM1157	Δ*gltK* Δ*gltH*	TM149 Δ*gltK* (pBJΔ*gltK*)	This work
TM1156	Δ*gltB* Δ*gltH*	TM149 Δ*gltB* (pBJΔ*gltB*)	This work
TM1158	Δ*gltA* Δ*gltH*	TM149 Δ*gltA* (pBJΔ*gltA*)	This work
TM1154	Δ*gltA* Δ*gltB*	DZ2 pBJΔ*gltBA*	This work
TM1397	Δ*gltA* Δ*gltB* Δ*gltH*	TM149 Δ*gltBA* (pBJΔ*gltBA*)	This work
TM829	WT + *aglZ-YFP*	DZ2 pBJ*AglZ-YFP*	(Mignot *et al.*, 2007)
TM1181	Δ*cglB* + *aglZ-YFP*	TM913 *aglZ-YFP* (pBJ*AglZ-YFP*)	This work
TM1159	Δ*cglB* + $cglB_{WT}$	TM913 $cglB_{WT}$ (pCglB$_{WT}$)	This work
TM1149	Δ*cglB* + $cglB_{D56A}$	TM913 $cglB_{D56A}$ (pCglB$_{D56A}$)	This work
TM1153	Δ*cglB* + $cglB_{S58A}$	TM913 $cglB_{S58A}$ (pCglB$_{S58A}$)	This work
TM1297	WT + *aglZ-mNeonGreen*	DZ2 pBJ*aglZ-mNeonGreen*	(Seef *et al.*, 2021)
SI96	WT + IMss-mCherry	WT DZ2 transformed with plasmid pSWU19-PpilA-IMss-mCherry	This work
SI97	Δ*gltK* + IMss-mCherry	Δ*gltK* transformed with plasmid pSWU19-PpilA-IMss-mCherry	This work
SI98	Δ*gltB* + IMss-mCherry	Δ*gltB* transformed with plasmid pSWU19-PpilA-IMss-mCherry	This work
SI99	Δ*gltA* + IMss-mCherry	Δ*gltA* transformed with plasmid pSWU19-PpilA-IMss-mCherry	This work
SI100	Δ*gltH* + IMss-mCherry	Δ*gltH* transformed with plasmid pSWU19-PpilA-IMss-mCherry	This work

Table 2.3. *Escherichia coli* strains used in this study.

Strain	Genotype/Description	Source or Reference
BL21(DE3)	*fhuA2* [lon] *ompT* gal *(λ DE3)* [dcm] Δ*hsdS* λ *DE3* = λ *sBamHIo* Δ*EcoRI-B* int::(*lacI*::P*lac*UV5::T7 gene1) i21 Δ*nin5*	Laboratory stock
DH5α	F-, Δ(argF-lac)U169, phoA, supE44, Δ(lacZ)M15, relA, endA, thi, hsdR	Laboratory stock

Table 2.4. Plasmids used in this study.

Plasmid	Genotype/Description	Construction	Source or Reference
pSWU30	Used for integration at phage Mx8 attB site (TetR)	/	Laboratory stock
$pCglB_{WT}$	pSWU30 with *cglB*	From pSWU30	This work
$pCglB_{D56A}$	pSWU30 with $cglB_{D56A}$	From $pCglB_{WT}$	This work
$pCglB_{S58A}$	pSWU30 with $cglB_{S58A}$	From $pCglB_{WT}$	This work
pSWU19-PpilA-IMss-mCherry	pSWU19 expressing IMss-mCherry under control of the *pilA* promotoer	From pSWU19	(Ducret *et al.*, 2013)
pBJ114	*galK*-containing vector for generation of in-frame deletions in *M. xanthus* (Kan^R)	/	Laboratory stock
pBJ*AglZ-YFP*	pBJ114 with a cassette allowing construction of the *aglZ-YFP* chimeric gene	From pBJ114	(Mignot *et al.*, 2007)
pBJΔ*gltK*	pBJ114 with a deletion cassette for *gltK*	From pBJ114	(Luciano *et al.*, 2011)
pBJΔ*gltB*	pBJ114 with a deletion cassette for *gltB*	From pBJ114	(Luciano *et al.*, 2011)
pBJΔ*gltA*	pBJ114 with a deletion cassette for *gltA*	From pBJ114	(Luciano *et al.*, 2011)
pBJΔ*gltBA*	pBJ114 with a deletion cassette for *gltBA*	From pBJ114	This work
pBJΔ*gltI*	pBJ114 with a deletion cassette for *gltI*	From pBJ114	(Luciano *et al.*, 2011)
pBJΔ*gltJ*	pBJ114 with a deletion cassette for *gltJ*	From pBJ114	(Faure *et al.*, 2016)
pCDF-duet1	Expression vector, *lacI*, P*T7*, Streptomycin Resistant (Sm^R).	/	Novagen
pCDF-$GltK^{6H}$-BAC^S	*gltK*-6xHis into MCS1 , *gltBA and gltC*-StrepII into MCS2 cloned into pCDF-duet 1 (Sm^R).	From pCDF-duet1	This work
pET-duet1	Expression vector, *lacI*, P*T7*, Ampicillin Resitant (Amp^R).	/	Novagen
pET-GltH-CglB	*gltH* and *cglB* (*cglB* is inserted with a shine dalgarno sequence) cloned into pET-duet 1 MCS1 (AmpR).	From pET-duet1	This work
pACYC-duet1	Expression vector, *lacI*,P*T7*, Chloramphenicol Resistant (ChloR).	/	Novagen
pACYC-$GltBAC^S$	gltBA and gltC-StrepII into MCS2 cloned into pACYC-duet 1, (ChloR).	From pACYC-duet1	This work

2.5.2 Mutagenesis of *cglB*

The upstream region of *cglB* (from -213 bp), including a promoter region (from -190 bp to -141 bp) predicted by BDGP (Reese, 2001), as well as *cglB* itself was amplified via PCR using Q5 high-fidelity DNA polymerase, followed by digestion of the product and plasmid pSWU30 with HindIII-HF (5') and SacI-HF (3'), then ligation via T4 DNA ligase (all enzymes from NEB) to yield $pCglB_{WT}$. Oligonucleotide primers for QuikChange site-directed mutagenesis were generated using PrimerX (http://bioinformatics.org/primerx/). Sequencing results were analyzed by Sequencher and/or ApE software.

2.5.3 Construction of CglB–OM-platform interaction constructs

Plasmids for expression of OM platform proteins and CglB in *E. coli*. PCRs were performed using the Q5 DNA polymerase and restriction enzymes were purchased from New England Biolabs and used according to the manufacturer's instructions. Custom oligonucleotides were synthesized by Eurogentec; sequences are available upon request.

The pCDF-$GltK^{6H}$ intermediate plasmid was constructed by restriction cloning (hot fusion technique). Briefly, the sequence encoding the full-length *gltK* gene (MXAN_2538, residues 1–555) was PCR-amplified using *M. xanthus* DZ2 chromosomal DNA as a template with forward and reverse primers (CDF-K^{6H}_Fw and CDF-K^{6H}_Rev) and Q5 DNA polymerase. The PCR product introduced a 5' NcoI truncated site and a 3' HindIII restriction site and a C-terminal His_6 extension. The *$gltK^{6H}$* PCR product was sub-cloned into the MCS1 pCDF-Duet1 (Novagen) corresponding restriction sites. To obtain the final construction pCDF-$GltK^{6H}$ – BAC^S, encoding for the operon structure *gltB, gltA* and *gltC*, a second step of restriction cloning was done by hot fusion technique. The full-length *gltB* (*MXAN_2539,* residues 1–828), *gltA* (*MXAN_2540,* residues 1–771) and *gltC* (*MXAN_2541,* residues 1–2022) genes were PCR-amplified using the primer pairs CDF-BAC^S_Fw (1)/CDF-BAC^S_Rev (1); CDF-BAC^S_Fw (2)/CDF-BAC^S_Rev (2) and CDF-BAC^S_Fw (3)/CDF-BAC^S_Rev (3). The PCR introduced a C-terminal streptavidin extension on *gltC*. The three PCR products were synthesized with 20-base-pair overhangs, from both 5' and 3'ends, corresponding to the designed overhangs genes regions and integration sites into the pCDF-$GltK^{6H}$ MCS2 plasmid.

The pACYC-BAC^S plasmid was constructed, as previously described, as pCDF-BAC^S but leaving the MCS1 polylinker site empty (the same primers were used). This plasmid was used as a negative control for the purification of the OM proteins.

The pET-GltH intermediate plasmid was also constructed by restriction cloning hot fusion technique. The full-length *gltH* was PCR amplified with the primers (pET-GltH_Fw and pET-GltH_Rev) and introduced a 5' NcoI truncated restriction site. The PCR product was then sub-cloned int the pET-Duet (Novagen) MCS1 at corresponding restriction sites. Finally, the *cglB* gene was amplified with the primers (pET-CglB_Fw and pET-CglB_Rev) by Q5 polymerase and so the PCR introduced a shine dalgarno (SD) sequence in 5' and overlaps regions from both 5' and 3' ends corresponding to the integration sites into pET-GltH plasmid.

All constructs were verified by DNA sequencing (Eurofins) and plasmids generated were saved into DH5α transformed cells.

2.5.4 Generation of α-CglB and α-GltC polyclonal antibodies

CglB (lacking signal peptide) elaborating a C-terminal hexa-histidine tag ($CglB_{21\text{-}416}$-His_6) was purified under denaturing conditions. Fractions were collected in 50 mM Tris pH 8.0, 300 mM NaCl, 250 mM imidazole, 6 M urea and used to immunize rabbits (Eurogentec). The α-CglB 1º pAb produced was then tested for specificity by using the wild-type and the Ω*cglB* strains. For GltC, a peptide corresponding to $GltC_{54\text{-}67}$ was synthesized then used to immunize rabbits to generate pAb (GenScript). The α-GltA, α-GltB, and α-GltH 1º pAb were raised previously (Jakobczak *et al.*, 2015; Luciano *et al.*, 2011). The α-His_6 antibody was commercially purchased (Sigma, #SAB4301134).

2.5.5 Immunofluorescence labelling of live *M. xanthus* cells

Specific volumes of overnight culture were sedimented via centrifugation (5000 × *g*, 5 min) such that pellet resuspension in 600 µL of TPM yielded an OD_{600} of 2.5. Following this wash, cell resuspensions were sedimented (5000 × *g*, 5 min). then resuspended in 600 µL of TPM+BSA (bovine serum albumin) (5% w/v), with α-CglB antiserum (1 µL for 3 mL of TPM+BSA). The solution was agitated for 1 h at 20 ºC on a Nutator platform, then sedimented (5000 × *g*, 5 min). The pellet was washed twice with TPM (600 µL), then resuspended in 600 µL of TPM+BSA with goat α-rabbit IgG Fab2 conjugated to AlexaFluor 647 (Cell Signaling Technologies) (1 µL mAb for 3 mL of TPM+BSA). The suspension was agitated for 1 h at 20 ºC on a Nutator platform (covered with aluminum foil), washed twice with TPM as described

above, then resuspended in 600 µL of TPM. Resuspensions of immunolabelled cells were spotted (2 µL) on glass-bottomed microscopy fluorodishes (World Precision Instruments) and overlaid with TPM 1.5% (w/v) agar pads. Cells were imaged using an Axio Observer 7 (Zeiss) inverted fluorescence microscope with heated chamber (32 ºC), with an alpha Plan-Apochromat 100× oil immersion objective, captured with 10% LED illumination intensity on an Axiocam 512 camera, at 15 s intervals (binning mode: 5×5). Phase contrast imaging was carried out without filters (100 ms acquisition time). AlexaFluor647 fluorescence was detected using the BP640/30 excitation filter and BP690/50 emission filter (200 ms acquisition time). AglZ-mNeonGreen fluorescence was detected using the BP470/40 excitation filter and BP525/50 emission filter (150 ms acquisition time).

2.5.6 Immunofluorescence labelling of fixed E. coli cells

Cells of *E. coli* BL21(DE3), cotransformed with either pCDF-Duet-GltK^{6H}+GltBAC^{S} and pET-Duet-GltH-CglB or pCDF-Duet and pET-Duet, were induced overnight in LB (1.0 mM IPTG, 16 ºC). The next day, cells (500 µL) from the induced cultures were fixed with 100 µL of 16 % paraformaldehyde, 0.2 µL of 25 % glutaraldehyde, and 20 µL of $NaPO_4$ (pH 7.4). Then, 10 µL of each mix was applied to wells of a commercial 2×9-well µ-Slide (Ibidi). Following incubation at RT (20 min), the wells were washed three times with 1× PBS. For the relevant samples, wells were then treated with GTE buffer containing lysozyme (1 µg/mL) at RT (4 min), followed by three washes with 1× PBS. Irrespective of treatment (or not) with lysozyme, wells were then left to air dry. For antibody labelling, all samples were incubated for 20 min at RT with 1× PBS containing 2% BSA. This buffer was then replaced by one of the same composition containing also α-CglB antibody (1:1000), and left to incubate overnight at 4 °C without agitation. After ten washes with 1× PBS, the samples were incubated with α-rabbit IgG AlexaFluor Plus 488 (Invitrogen, 1:200) for 4 h at 4 °C in the dark (without agitation) followed by ten washes with 1× PBS. Cells were imaged by epifluorescence with an inverted Eclipse TiE microscope with Perfect Focus (Nikon), using a 100× NA = 1.45 Phase Contrast objective and an ORCA-Flash4.0 digial CMOS camera (Hamamatsu) at RT. A mercury fluorescent lamp with green optical filter was used when necessary. Image stacks were prepared for publication using Fiji, with fluorescence micrographs subjected to background subtraction (rolling ball radius: 10 pixels).

2.5.7 Phylogeny and gene co-occurrence

This study explored 61 myxobacterial genomes, distributed within three suborders and nine families (Goldman *et al.*, 2006; Han *et al.*, 2013; Huntley *et al.*, 2011; Huntley *et al.*, 2013; Huntley *et al.*, 2012; Ivanova *et al.*, 2010; Li *et al.*, 2011; Müller *et al.*, 2013; Schneiker *et al.*, 2007; Sharma *et al.*, 2016a; Sharma *et al.*, 2018; Sharma *et al.*, 2016b; Sharma & Subramanian, 2017; Stevens *et al.*, 2014), in addition to 59 outgroup genomes (members from 32 non-Myxococcales Deltaproteobacteria, 4 α-, 6 β-, 9 γ-, 4 £-proteobacteria, 2 Firmicutes, 1 Actinobacteria, and 1 FCB group organism). Highly-conserved gapless concatenated alignment of 26 housekeeping protein sequences (Sharma *et al.*, 2016b; Wu & Eisen, 2008) was subjected to RAxML to build a maximum likelihood phylogenetic tree using JTT Substitution Matrix and 100 bootstrap values (Stamatakis, 2006). Sequential distribution of gliding motility genes, i.e. *agl*, *glt* (M1, G1 and G2 clusters) (Luciano *et al.*, 2011) and *cglB* (Nudleman *et al.*, 2005; Pathak & Wall, 2012; Rodriguez & Spormann, 1999) was identified within all 120 genomes under study using two iterations of homology searching via JackHMMER (HMMER 3.3.2 suite released in Nov. 2020) (Johnson *et al.*, 2010) with an E-value cut-off of $1e^{-5}$ and other default parameters. The relative distribution of gliding motility proteins was mapped to the multi-protein phylogeny using iTol v6.5.3 (Letunic & Bork, 2016). The strip to the right of the phylogeny depicts the taxonomic classes (from top to bottom: Myxococcales, non-Myxococcales δ-proteobacteria, α-, β-, γ-, £-proteobacteria, Actinobacteria, Firmicutes, and Fibrobacteres, respectively).

2.5.8 Tertiary structure homology detection & protein modelling

Identification of structural homologues to CglB was carried out using fold-recognition searches of the Protein Data Bank using HHpred (Söding *et al.*, 2005). Deep-learning-based relaxed tertiary structure modelling of CglB was carried out via AlphaFold using the ColabFold pipeline with default settings (https://colab.research.google.com/github/sokrypton/ColabFold/blob/main/AlphaFold2.ipynb) (Jumper *et al.*, 2021; Mirdita *et al.*, 2022). The highest-confidence CglB model was used to generate structural alignments and figures with PyMol (The PyMol Molecular Graphics System, Version 2.0, Schrödinger, LLC).

2.5.9 SDS-PAGE, in-gel fluorescence, and Western immunoblotting

For detection of proteins from whole cells via Western immunoblot, TPM-washed cells were sedimented and resuspended at OD_{600} 1.0 in 1× Laemmli sample buffer containing 5% β-mercaptoethanol for reducing SDS-PAGE (unless otherwise indicated). For analysis of CglB unfolding in the presence of reducing agent, TPM-washed cells were instead resuspended in 2× Laemmli (lacking reducing agent) and diluted to 1× with ddH_2O containing increasing concentrations of DTT (0 to 5 mM). Samples were boiled (10 min), loaded (20 µL) on 10-well 1 mm-thick gels, then resolved on 10% acrylamide gels (80 V for 45 min for stacking, 120 V for 75 min for resolving), then electroblotted (100 V for 60 min) to nitrocellulose membranes. Blots were rinsed with Tris-buffered saline (TBS) buffer, blocked for 30 min at room temperature with 5% (w/v) milk in TBS, then incubated rocking overnight in the 4 °C cold room in the presence of primary antibodies. Primary antisera were all used at a concentration of 1:10 000 in TBS with 0.05% Tween-20 (TBS-T). The next day, blots were rinsed twice (5 min) with TBS-T, incubated with goat α-rabbit 2° antibody conjugated to HRP (1:5000) (Bio-Rad) in TBS-T at room temperature (1 h), then rinsed twice (5 min) again with TBS-T. All immunoblots were developed using the SuperSignal West Pico (Thermo) chemiluminescence substrate, captured on either a GE Imager with ImageQuant software or an Amersham Imager 600 machine.

To monitor the resumption of CglB release from EDTA-grown cells, cells were sedimented via centrifuge (5000 × *g*, 5 min) and resuspended at an OD_{600} of 1.0 in 12.5 mL of fresh CYE or TPM and incubated at 20 °C at OD_{600} of 1. Each hour the OD_{600} was read to calculate the volume of culture to take out to get a final suspension of 100 µL at OD_{600} of 2. The volume was removed and sedimented (5000 × *g*, 5 min) and resuspended in 100 µL Laemmli buffer prior to use for Western immunoblotting.

For fractionated whole cell–supernatant–OMV samples in 1× Laemmli buffer, samples were boiled (10 min) and loaded (20 µL) on 15-well 4-20 % acrylamide precast gradient gels (Biorad). Supernatant-alone samples were similarly boiled and loaded on a cast 10% acrylamide gel. Gels were resolved at 120 V, followed by electroblotting to nitrocellulose membranes at 100 V. Immunodetection was performed with diluted polyclonal antisera as follows: α-CglB (1:10 000), α-MglA (1:5000), and α-GltK (1:5000). Detection via secondary antibody was done with goat α-rabbit mAb (1:5000) conjugated to HRP (Biorad).

Immunoblots were developed using the SuperSignal West Femto (Thermo) chemiluminescence substrate, captured on GE Imager with ImageQuant software.

For analysis of AglZ-YFP in-gel fluorescence, TPM-washed cells were resuspended in 1× non-reducing Laemmli sample buffer to an OD_{600} of 4.0. Cell resuspensions were heated for 30 min (65 °C), loaded (20 µL) on an 8% SDS-PAGE gel, and resolved for 45 min at 80 V, then 75 min at 120 V. Cultures, cell resuspensions, and SDS-PAGE gels (before, during, and after resolution) were all shielded from ambient light to reduce photobleaching of the YFP moiety. Resolved gels were scanned on a Typhoon FLA9500 flat-bed imager (GE Healthcare). AglZ-YFP was excited with a 473 nm laser, with fluorescence captured using the BPB1 filter (PMT 800). Pre-stained protein ladder bands were detected via excitation with a 635 nm laser and capture using the LPR filter (PMT 800). Quantification of band fluorescence intensity was performed using ImageJ via the "plot lanes" function, followed by determination of the area under the curve. AglZ-YFP signal for each lane was normalized to the faster-migrating auto-fluorescent band in the same lane; these values were then expressed as a percentage of the signal in WT cells for a given biological replicate.

For analysis of IMss-mCherry in-gel fluorescence (see below), SDS-PAGE-resolved (10% acrylamide; 80 V for 45 min, then 120V for 75 min) samples (20 µL) were shielded from light, then scanned on a Typhoon imager. The mCherry was excited with a 532 nm laser, with fluorescence capture using the LPR filter (PMT 800).

2.5.10 Sample fractionation

To separate supernatant and outer-membrane vesicle (OMV) fractions, WT, Δ*gltA*, Δ*gltB* and Δ*gltK* vegetative cells were grown in CYE medium to OD_{600} 0.7. Intact cells were first eliminated by sedimentation at 7830 rpm (10 min, RT). After addition of 1 mM PMSF, supernatants were sedimented at 125 000 × *g* (2 h, 4 °C). The resulting pellets (OMV fraction) and supernatants (soluble fractions) were then treated separately. The OMV pellets were washed with TPM, sedimented again at 125 000 × *g* (2 h, 4 °C), and then resuspended directly in 500 µL 1× Laemmli protein sample buffer. The soluble supernatant fractions were treated with TCA (10 % final concentration) for 30 min on ice and then sedimented at 11 000 rpm (1 h, 4 °C). The resulting pellets (precipitated proteins) were washed with 100% acetone, sedimented at 7830 rpm (10 min, 4 °C), and dried overnight at RT. Dried pellets were then resuspended in 1.5 mL TPM, sedimented at 15 000 rpm (30 min, 4 °C) and finally resuspended in 500 µL 1× Laemmli protein sample buffer.

For isolation of supernatant-alone samples, 10 mL CYE cultures (inoculated at OD_{600} 0.02) were grown overnight with shaking (220 rpm, 32 °C) to OD_{600} 0.6–1.0, sedimented (5000 × *g*, 10 min, 20 °C). Supernatants were then sedimented in an ultracentrifuge (Beckman, SW 41 Ti rotor, 120 000 × g, 75 min, 4 °C) to remove any remaining membrane material. Clarified 10 mL supernatant samples were treated with 1 mL 100% TCA to precipitate the proteins. Tubes were heated at 65 °C for 5 min, then spun (16 300 × *g*, 20 min, RT) to sediment precipitate in 2 mL microtubes. TCA-precipitated pellets were washed with 1 mL acetone, sedimented (16 300 × *g*, 20 min, RT), followed by supernatant aspiration. Protein pellets were left uncapped in the chemical hood overnight to ensure evaporation of acetone. Pellets were resuspended in 500 µL 2× Laemmli sample buffer lacking reducing agent, then diluted to 1× with ddH_2O.

2.5.11 Immunoprecipitation & mass spectrometry

For analysis of cleaved CglB in culture supernatants, cells of Δ*gltB* from 100 mL CYE cultures were first sedimented (4000 × *g*, 24 °C, 15 min), after which supernatants were decanted, pooled, and passed through a 0.2 µm syringe filter. Filtered supernatant was then concentrated using four Vivaspin20 columns (10 kDa cutoff) (Sartorius), spun at 8000 × *g* (20 °C) in a fixed-angle centrifuge, with the supernatant concentrated to the dead volume limit of each column. Concentrated supernatants (~ 80 µL each) were subsequently pooled, and diluted 1:2 with filter-sterilized 1× PBS (binding buffer) to equilibrate sample pH. Separately, a single 1 mL Pierce Protein A column (Thermo) per each pooled supernatant was equilibrated in filter-sterilized binding buffer at room temperature as per the manufacturer's instructions. Filtered α-CglB antiserum (1 mL) was sedimented in a microfuge to remove remnant cells and/or debris (4000 × *g*, 5 min), diluted 1:1 with binding buffer, then sedimented at 12 000 × *g* to clarify the sample as binding buffer addition may have resulted in lipoprotein precipitation. The Protein A column was primed by passage of 5 mL binding buffer. To bind antibody to the column, the 2 mL of diluted antiserum was added to the top of the column and allowed to drip through, followed by washing with 15 mL of binding buffer to remove unbound pAb. The ~ 960 µL of supernatant concentrate was added to the top of the column and allowed to distribute throughout the resin bed at room temperature (60 min). The column was then again washed with 15 mL binding buffer. To elute bound pAb (and any associated proteins) from the column, 5 mL of elution buffer (0.1 M glycine, pH to 2.5 with HCl) was added.

To analyze the protein content of the pull-down, 500 µL of column eluate was concentrated in a microfuge using a Vivaspin500 column (10 kDa cutoff) to a dead volume of ~20 µL, then diluted 1:1 with 2× reducing Laemmli sample buffer. Samples (20 µL) were run into the stacking gel via SDS-PAGE (80 V, 13 min). Gel bands stained with SimplyBlue Safestain were excised from the stacking portion of the gel and the proteins digested by trypsin or Endoproteinase Glu-C. Liquid chromatography coupled to tandem mass spectrometry (LC-MS/MS) analyses were performed on a Q-Exactive plus mass spectrometer (ThermoFisher Scientific) by staff at the Proteomics Platform of the Mediterranean Institute of Microbiology (Marseille). Processing of the spectra for protein identification was performed with Proteome Discoverer software (Thermo Scientific, versions 1.4.0.288 and 2.1.0.81).

2.5.12 Expression, purifications, and detection of the OM-platform proteins from *E. coli* cells

The pCDF-GltK^{6H}-GltBAC^{S} and pET-GltH-CglB plasmids were used to transform *E. coli* BL21(DE3) (Invitrogen). Cells were grown at 37 °C in lysogeny broth (LB) (BD, Difco), with 100 µg/mL streptomycin and ampicillin antibiotics (Sigma), to OD_{600} 0.8–0.9. Expression of the *gltKBACH* and *cglB* genes was induced with 1.0 mM IPTG overnight at 16 °C. The following day, cell pellets were resuspended in 50 mM Tris-HCl (pH 8.0), 50 mM NaCl, 1 mM EDTA, and 10 mM $MgCl_2$, supplemented with 10 µg/mL of DNase I and 10 µg/mL of lysozyme. The cell suspension was further broken using an Emulsiflex-C5 (Avestin). The broken cell suspension was clarified via centrifugation (26 000 × *g*, 15 min, 4 °C). The membrane fraction was then collected via high-speed centrifugation (195 000 × *g*, 45 min, 4 °C). Sedimented membranes were mechanically homogenized and solubilized in 50 mM Tris-HCl (pH 8.0), 50 mM NaCl, EDTA-free protease inhibitor (Roche), 0.5% (w/v) n-dodecyl-b-D-maltopyranoside (DDM, Anatrace), 0.75% (w/v) decylmaltose neopentyl glycol (DM-NPG, Anatrace) and 1 mM EDTA at 4 °C overnight. The suspension was then clarified by high-speed centrifugation (126 000 × *g*, 35 min, 4 °C). The clarified supernatant (supplemented with 20 mM imidazole) was loaded onto a 1-mL HisTrap HP (Cytivia) column and then washed with 50 mM Tris-HCl (pH 8.0), 50 mM NaCl, 0.05% (w/v) DM-NPG (Affinity buffer) with 50 mM imidazole at 4 °C. The OM-platform proteins were eluted in the same buffer supplemented instead with 250 mM imidazole. Peak fractions were pooled with 1× Laemmli buffer containing β-mercaptoethanol and 1 mM DTT to be used for WB.

For the negative control, we used the same protocols as previously described except that we transformed *E. coli* BL21(DE3) strain with the pACYC-BAC^S and pET-GltH-CglB plasmids. Cells were grown at 37 °C in LB with 100 μg/mL ampicillin and 30 μg/mL chloramphenicol antibiotics (Sigma).

For detection, SDS-PAGE was performed on Bio-rad Mini-PROTEAN systems using a standard protocol. For detection of proteins from pull down assay via Western immunoblot, the load and eluted fractions were resuspended in 1× Laemmli sample buffer containing β-mercaptoethanol and 1 mM DTT. Samples were boiled (10 min), loaded (10 μL for load and 20 μL for eluted fractions) on 10-well 1 mm-thick gels, resolved on 12% acrylamide gels (200 V during 45 min), then electroblotted (100 V for 60 min) to nitrocellulose membranes. Blots were blocked for 1 h at room temperature with 5% milk in PBS with 0.05% Tween-20 (PBS-T for α-GltC only) and TBS with 0.05% Tween-20 (TBS-T, for other antibodies), then incubated rocking overnight in the 4 °C cold room in 1:5000 α-CglB, 1:5000 α-GltB, 1:5000 α-GltA, 1:5000 α-His (i.e. GltK) and 1:5000 α-GltH mixture in milk 5% TBS-T, except for GltC-StrepII detection which was carried out with 1:500 α-GltC mixture in milk 5% PBS-T. The next day, blots were rinsed three times (10 min) with TBS-T or PBS-T, incubated with goat α-rabbit 2° antibody conjugated to HRP (1:5000) (Bio-Rad) in milk 5% TBS-T or PBS-T at room temperature (1 h), then rinsed three times (10 min) again with TBS-T or PBS-T. All immunoblots were developed using the SuperSignal West FEMTO (Thermo) chemiluminescence substrate, captured on an Image Quant LAS4000 Mini Imager with Image Quant software.

2.5.13 Proteinase K surface digestion

Cells were resuspended in TPM at OD_{600} 2.0, followed by addition of 200 μg/mL Proteinase K and a brief vortex pulse to mix. An aliquot (50 μL) was immediately removed at t = 0 and placed into a tube containing 5 μL of 100% trichloroacetic acid (TCA). Digestion mixtures were incubated at room temperature on a rocker platform, with aliquots removed every 15 min and placed into respective pre-aliquoted tubes of TCA. Upon removal of digestion reaction aliquots, TCA-containing sample tubes were heated at 65 °C for 5 min, chilled on ice, then sedimented at 14 000 × *g* (5 min). Following supernatant removal, precipitated protein pellets were washed via resuspension in 500 μL of 100% acetone. Samples were then sedimented as before (14 000 × *g*, 5 min), followed by careful aspiration of the supernatants. Tubes were left uncapped overnight in the fume hood to promote

evaporation of residual acetone, followed by storage at -80 ºC until needed. Precipitated protein pellets were resuspended in 50 µL 1× Laemmli sample buffer (with reducing agent as indicated) and analyzed via SDS-PAGE and Western immunoblot.

For EDTA-grown cells expressing the IMss-mCherry construct (Ducret *et al.*, 2013), the above protocol was modified so as to not denature the fluorophore. In brief, cells were similarly resuspended in TPM and digested with Proteinase K, with 50-µL aliquots removed at the same intervals. However, upon removal each aliquot was immediately transferred to a PCR tube, incubated at 95 ºC for 15 min in a thermocycler to inactivate the Proteinase K, then mixed with 50 µL of 2× Laemmli buffer lacking reducing agent. Samples were then resolved via SDS-PAGE and scanned for in-gel fluorescence (see below).

2.5.14 Motility and fluorescence analysis

For phase-contrast and fluorescence microscopy on agar pads, cells from exponentially-growing cultures were sedimented and resuspended in TPM buffer to OD_{600} 5.0, spotted (5 µL) on a glass coverslip, then overlaid with a pad of 1.5% agar prepared with TPM. For motility analysis, cells were left to adhere for 5 min prior to imaging at 32 ºC using a TE2000-E-PFS microscope (Nikon) with a 40× objective and a CoolSNAP HQ2 camera (Photometrics) with Metamorph software (Molecular Devices). AglZ-YFP fluorescence was imaged using a monolithic aluminum microscope (homemade) equipped with a 1.49 NA/100X objective (Nikon Instruments) and imaged on an iXon DU 897 EMCCD camera (Andor Technology). Illumination was provided by a 488 nm DPSS laser (Vortran Stradus), and sample positioning was performed using a P611 three-axis nanopositioner (Physik Instrument). Instrument control was programmed in LabView (National Instruments) providing integrated control of all components. Cell gliding speeds were calculated using the MicrobeJ module for FIJI (Ducret *et al.*, 2016) . Gliding cell montages were generated using FIJI. Kymograph panels were generated using the FIJI Kymograph Builder function. AglZ-YFP clusters were detected manually and tracked with the MTrackJ FIJI plugin. Using an R software script, the points of the AglZ-YFP cluster trajectories (x0, x1, … , xn; y0, y1, … , yn) were used to calculate the mean square displacement (MSD) at time

$$t = d2t = (xt - x0)2 + (yt - y0)2: \qquad MSD(t) = \frac{1}{t}\sum_0^t d_t^2$$

For total internal reflection fluorescence microscopy (TIRFM), imaging of real-time AglZ-YFP trafficking was performed as previously detailed in chitosan-coated polydimethylsiloxane (PDMS) microfluidic channels (Faure *et al.*, 2016). In brief, cells were injected into the chamber and left to adhere (30 min) without flow, with unadhered cells then removed via manual injection with TPM. TIRFM was performed on attached cells with active autofocus using an inverted microscope with 100× oil-immersion Plan-Achromat objective, atop a closed-loop piezoelectric stage. AglZ-YFP was excited with a 488-nm laser, with emission collected by the objective, through a dichroic mirror and bandpass filters, and captured by an emCCD camera. For imaging of the YFP channel in real time, 500 images were captured at 20 Hz (Faure *et al.*, 2016).

2.5.15 Flow chamber construction and bead assay

Prior to experiments, 1 mL of *M. xanthus* DZ2 WT+AglZ-YFP and mutant DZ2 Δ*cglB*+AglZ-YFP overnight culture was grown to OD_{600} ~0.6, sedimented (8000 rpm, 5 min), and resuspended in 400 mL TPM buffer. Flow chambers were made by combining two layers of double sided tape, a 1 mm-thick glass microscope slide, and a 100 μm-thick glass cover slip (#1.5) as previously described (Wang *et al.*, 2010). The tape was separated to allow a final volume of approximately 60 μL. Agarose (40 μL at 0.7%) dissolved in 6 M DMSO was injected into the chamber and allowed to sit at room temperature for 15 min. The chamber was washed with 400 μL TPM then injected with *M. xanthus* cells (60 μL) and left at room temperature to facilitate cell attachment to the agarose-coated surface for 30 min. Unattached cells were then thoroughly washed away with a total of 2 mL TPM media containing 10 mM glucose. The flow chamber was then mounted onto the microscope for imaging. For bead experiments, 1 μL of uncoated polystyrene beads (diameter 520 nm) (Bangs Laboratories) were washed and diluted in 1 mL TPM containing 10 mM glucose and injected into the flow chamber. Beads were optically trapped and placed about a third of the cell length away from the pole of the immobilized cell of interest.

2.5.16 Bead tracking and video analysis

For a chosen *M. xanthus* cell (WT or mutant), 3-min movies were recorded and analyzed using a custom MATLAB tracking code. The code uses filtering mechanisms to subtract the image background from that of the cell-attached bead. Firstly, an internal

MATLAB centroid function identified the *x,y* pixel values of the centre of the bead for each frame in the video, followed by pixel value conversion to microns. This was then used to compute motor-driven bead runs and velocities for each cell. The threshold value for a run was previously determined by disabling molecular motors and decreasing bead motion in WT cells by carefully injecting 20 μM of nigericin, a pH-gradient/proton motive force-inhibitory drug, into the mounted flow chamber. This drug concentration decreased bead velocity but not motor force production translated to the beads. In these previous experiments, 40 μM nigericin was used, leading to negligible bead motion (Balagam *et al.*, 2014).

2.5.17 Statistical analysis

For all comparisons of dataset distributions (**Figures. 2.2D, 2.4C-F, 2.4H, Figure 2.2A**) analyses of statistical significance were carried out via unpaired two-tailed Mann-Whitney test. Differences in mean values for AglZ-YFP fluorescence levels in WT vs. Δ*cglB* were evaluated for statistical significance using a Wilcoxon signed-rank test performed relative to the reference value of "100" for WT samples (**Figure 2.7Aii**). Differences in mean relative culture density values for vancomycin-sensitivity testing were compared for each mutant strain against WT for each antibiotic concentration tested; this analysis was carried out via 2-way ANOVA and Dunnett's multiple comparisons test with a single pooled variance (**Figure 2.9E,F**). All statistical analyses were carried out in GraphPad Prism (version 8) at a confidence interval of 95% ($p < 0.05$).

2.6 ACKNOWLEDGMENTS

The authors would like to thank (i) Joel Selkrig and Nicholas Nickerson for valuable suggestions and troubleshooting regarding protease accessibility, (ii) Anna Konovalova for constructive input on surface lipoproteins, (iii) Robert Fieldhouse for insightful discussions on protein modelling and evolutionary couplings, (iv) Sabrina Gauthier for cloning pSWU30-pCglB$_{WT}$, (v) Lotte Søgaard-Andersen for the kind gift of α-GltK, α-GltB, α-GltA, and α-GltC polyclonal antibodies, (vi) Alain Roussel and Renaud Vincentelli (CNRS – Aix-Marseille University, Architecture et function des macromolecules biologiques) for CglB protein used to generate pAb, and (vii) Régine Lebrun, Pascal Mansuelle, and Rémy Puppo of the Mediterranean Institute of Microbiology's Proteomics Platform for insightful discussions and sample processing for mass spectrometry.

2.7 FUNDING

Natural Sciences and Engineering Research Council of Canada, Discovery grant RGPIN-2016-06637 (STI, NYJ, FS)
Banting Research Foundation, Discovery Award 2018-1400 (STI)
Canadian Institutes of Health Research fellowship (STI)
Aix-Marseille University AMIDEX Excellence Program (STI)
PROTEO, The Quebec Network for Research on Protein Function, Engineering, and Applications studentship (NYJ, FS)
European Research Council, Advanced Grant JAWS (TM)
Bettencourt-Schueller Foundation, Coup d'élan pour la recherche française 2011 (TM)
National Science Foundation, grant CAREER PHY-0844466 (JWS)
Fondation ARC studentship (LMF)
Glenn Centers for Aging Research award (BPB)
National Institutes of Health award P50 GM071508 (BPS)

Chapitre 3 : Integrin-like adhesin CglD confers traction and stabilizes bacterial focal adhesions involved in myxobacterial gliding motility

Titre de l'article :

Integrin-like adhesin CglD confers traction and stabilizes bacterial focal adhesions involved in myxobacterial gliding motility

Auteurs :

Nicolas Y. Jolivet[1,2], Endao Han[3,4], Akeisha M. Belgrave[5,6], Fares Saïdi[1,2], Newsha Koushki[7], David J. Lemon[8], Laura M. Faure[9], Betty Fleuchot[9], Utkarsha Mahanta[10], Heng Jiang[11], Gaurav Sharma[10], Jean-Bernard Fiche[12], Benjamin P. Bratton[5,13,14], Mamoudou Diallo[15], Beiyan Nan[16,17], David R. Zusman[16], Guillaume Sudre[15], Anthony Garza[8], Marcelo Nollmann[12], Allen J. Ehrlicher[7], Olivier Théodoly[18], Joshua W. Shaevitz[4,5], Tâm Mignot[9], Salim T. Islam[1,2,9*]

1 Institut National de la Recherche Scientifique (INRS), Centre Armand-Frappier Santé Biotechnologie, Université du Québec, Institut Pasteur International Network, Laval, QC, Canada
2 PROTEO, the Quebec Network for Research on Protein Function, Engineering, and Applications, Université Laval, Quebec, QC, Canada.
3 Joseph Henry Laboratories of Physics, Princeton University, Princeton, NJ, USA
4 Division of Physics and Applied Physics, School of Physical and Mathematical Sciences, Nanyang Technological University, Singapore, Singapore
5 Lewis-Sigler Institute for Integrative Genomics, Princeton University, Princeton, NJ, USA
6 Integrative Sciences Program, Harrisburg University of Science & Technology, Harrisburg, PA, USA
7 Dept. of Bioengineering, McGill University, Montreal, QC, Canada
8 Dept. of Biology, Syracuse University, Syracuse, NY, USA
9 Laboratoire de Chimie Bactérienne, CNRS - Université Aix-Marseille UMR7283, Institut de Microbiologie de la Méditerranée, Marseille, France
10 Dept. of Biotechnology, Indian Institute of Technology Hyderabad, Sangareddy, Telangana, India
11 Centre for Biological Applications of Mass Spectrometry, Concordia University, Montreal, QC, Canada
12 Centre de Biochimie Structurale, CNRS UMR5048, INSERM U1054, Montpellier, France
13 Dept. of Pathology, Microbiology and Immunology, Vanderbilt University Medical Center, Nashville, TN, USA
14 Vanderbilt Institute for Infection, Immunology and Inflammation, Nashville, TN, USA
15 Ingénierie des Matériaux Polymères, Université Claude Bernard Lyon 1, Université de Lyon, CNRS UMR 5223, Villeurbanne, France
16 Dept. of Molecular and Cell Biology, University of California, Berkeley, CA, USA

[17] Dept. of Biology, Texas A&M University, College Station, TX, USA
[18] Laboratoire Adhésion et Inflammation, INSERM U1067, CNRS UMR 7333, Marseille, France

Soumission à *Science Advances*

Date de soumission : 29 juillet 2023

Contribution des auteurs :

Conceptualisation : **NYJ**, STI

Methodologie : **NYJ**, EH, AB, NK, DJL, HJ, GS, JBF, MD, STI

Développement de la technique de rhéométrie pour mesurer l'attachement des cellules

Informatique : EH, AB

Recherche : **NYJ**, EH, AB, NK, DJL, BF, LMF, FS, UM, JBF, BPB, MD, BN, STI

J'ai obtenu des données pour les figures 3.2 (Analyses HHpred, Modélisation Alphafold, Westernblot avec agent réducteur DTT, test de sensibilité à la protéinase K), 3.3 (modélisation Alphafold et alignement TMalign des domaines EGF-like), 3.4 (Westernblot pour le test de sensibilité au DTT de la protéine), 3.5ABC (Cultures et mesures des *swarm*s, observations des corps fructifères et l'analyse de rhéométrie), 3.7 (Observations des *flares* sur les différents milieux et analyses de microcopie des films sur ces milieux), 3.8 (test de l'impact du séchage sur la formation des *flares*), 3.9A (Mesure de la vitesse du gliding sur lame de verre avec gradient de calcium pour la souche Ω*pilA*), 3.12 (Westernblot ciblant CglD chez les mutants de la machinerie et test de sensibilité au DTT chez les mutants du module de la membrane externe de la machinerie), 3.13ABC (suivis et mesures des clusters d'adhésion focale (tailles et intensités), et 3.14A (Mesure de la fluorescence in-gel).

Visualisation : **NYJ**, EH, STI

Supervision : GS, DRZ, GS, AG, MN, AJE, OT, JWS, TM, STI

Ecriture—manuscrit initial : **NYJ**, STI

Ecriture—révision & édition : **NYJ**, EH, AB, GS, TM, STI

3.1 ABSTRACT

Integrins are crucial for eukaryotic cell attachment and motility within the extracellular matrix (ECM) via focal-adhesion formation, with their evolutionary emergence important for the development of multicellularity. Intriguingly, single gliding cells of the predatory deltaproteobacterium *Myxococcus xanthus* form bacterial focal-adhesion (bFA) sites; therein, helically-trafficked motors become immobilized at anchored locations through Glt apparatus association with cell-surface integrin αI-domain-like adhesin CglB. Using traction-force, bead-force, and total internal reflection-fluorescence microscopies combined with biochemical approaches, we herein identify the von Willebrand A domain-containing cell-surface lipoprotein CglD to be a β-integrin-like outer-membrane lipoprotein that functionally associates with and anchors the trans-envelope Glt–CglB gliding apparatus, stabilizing and efficiently anchoring this assembly at bFAs. Calcium dependence governs CglD importance, consistent with its integrated ECM eukaryotic cartilage oligomeric matrix protein domains. CglD thus confers mechanosensory and mechanotransductory capabilities to the gliding apparatus, helping explain bFA-mediated trans-envelope force transduction, from inner-membrane-embedded motors to the cell surface.

3.2 INTRODUCTION

Cellular motility on surfaces necessitates complex interactions between the cell and the underlying substratum across all biological kingdoms. In metazoans, translocating cells adhere to the extracellular matrix (ECM) via nucleation of integrin proteins linked to the internal actomyosin network (Kechagia *et al.*, 2019). Integrins are composed of an α and a β subunit, with half of all α variants, and all β variants, elaborating I-domains containing a von Willebrand A (VWA) module that binds specific ligands (Shimaoka & Springer, 2003); in turn, integrin adhesion to the ECM is mediated by their interaction with soluble ECM proteins such as cartilage oligomeric matrix protein (COMP) (**Figure 3.1**). Such adherence generates eukaryotic focal-adhesion (eFA) sites; these sites do not move (relative to the substratum) and transduce motor forces via induction of local traction, thus mediating cell motility relative to fixed points (Kanchanawong *et al.*, 2010). In bacteria such as Gram-negative *Myxococcus xanthus*, individual cells are able to glide on surfaces (without external appendages such as flagella or pili) using motorized (Agl) substratum-coupled gliding transducer (Glt) complexes that are transported towards the lagging cell pole (Faure *et al.*, 2016; Islam *et al.*, 2023);

similar to the abovementioned metazoan cells, these complexes in *M. xanthus* remain stationary relative to the substratum in a gliding cell and form bacterial focal adhesion (bFA) sites (Mignot *et al.*, 2007).

Myxococcus xanthus is a social predatory soil deltaproteobacterium with a complex developmental cycle (Muñoz-Dorado *et al.*, 2016). Under nutrient-limiting conditions, vegetative cells in a swarm biofilm aggregate, differentiate, and form multicellular spore-filled fruiting bodies. This complex life cycle is modulated by the interplay between several secreted polysaccharides and the motility of cells at the group and individual levels (Islam *et al.*, 2020; Saïdi *et al.*, 2021; Saïdi *et al.*, 2022b). Type IV pilus extension-and-retraction is responsible for the former, while as described, the latter is mediated by Agl–Glt-dependent gliding.

In gliding *M. xanthus* cells, the motorized trans-envelope Agl–Glt complex (Luciano *et al.*, 2011; Nan *et al.*, 2010) is assembled at the leading pole, and is transported towards the lagging pole along a trajectory matching a right-handed helix (Faure *et al.*, 2016). Upon reaching the ventral side of the cell in contact with the substratum, the motorized Agl–Glt apparatus becomes coupled to the substratum via unmasking of the αI VWA domain- containing adhesin CglB, which otherwise remains loaded in the outer-membrane (OM) module of the gliding complex until engaged (Islam *et al.*, 2023) (**Figure 3.1**). The OM module of the gliding apparatus is a hetero-oligomeric complex composed of the integral OM β-barrels GltA/B/H and periplasmically-oriented OM lipoprotein GltK, which along with OM-associated protein GltC (Islam *et al.*, 2023; Jakobczak *et al.*, 2015) form a complex that recruits and shields the surface-localized adhesin CglB (Islam *et al.*, 2023). Engagement of CglB results in Agl–Glt complex immobilization at bFA sites, allowing for force transduction across the cell envelope and gliding locomotion relative to the fixed bFA (Islam *et al.*, 2023).

Several factors were identified >45 years ago as important for gliding when random chemical mutagenesis screens revealed 5 classes of "conditional gliding" (*cgl*) mutations (*cglB/C/D/E/F*) that, in isolation, rendered cells gliding-null; however, mixing one class of these gliding-null mutant cells with another (e.g. *cglB* + *cglC*) resulted in a transient restoration ("stimulation") of gliding motility across the entire population (Hodgkin & Kaiser, 1977). These data suggested the missing factors between mutant classes could be physically transferred between cells and integrated into the defective gliding mechanism to transiently restore single-cell locomotion. The *cglB/C/E/F* factors were later identified as specific genes

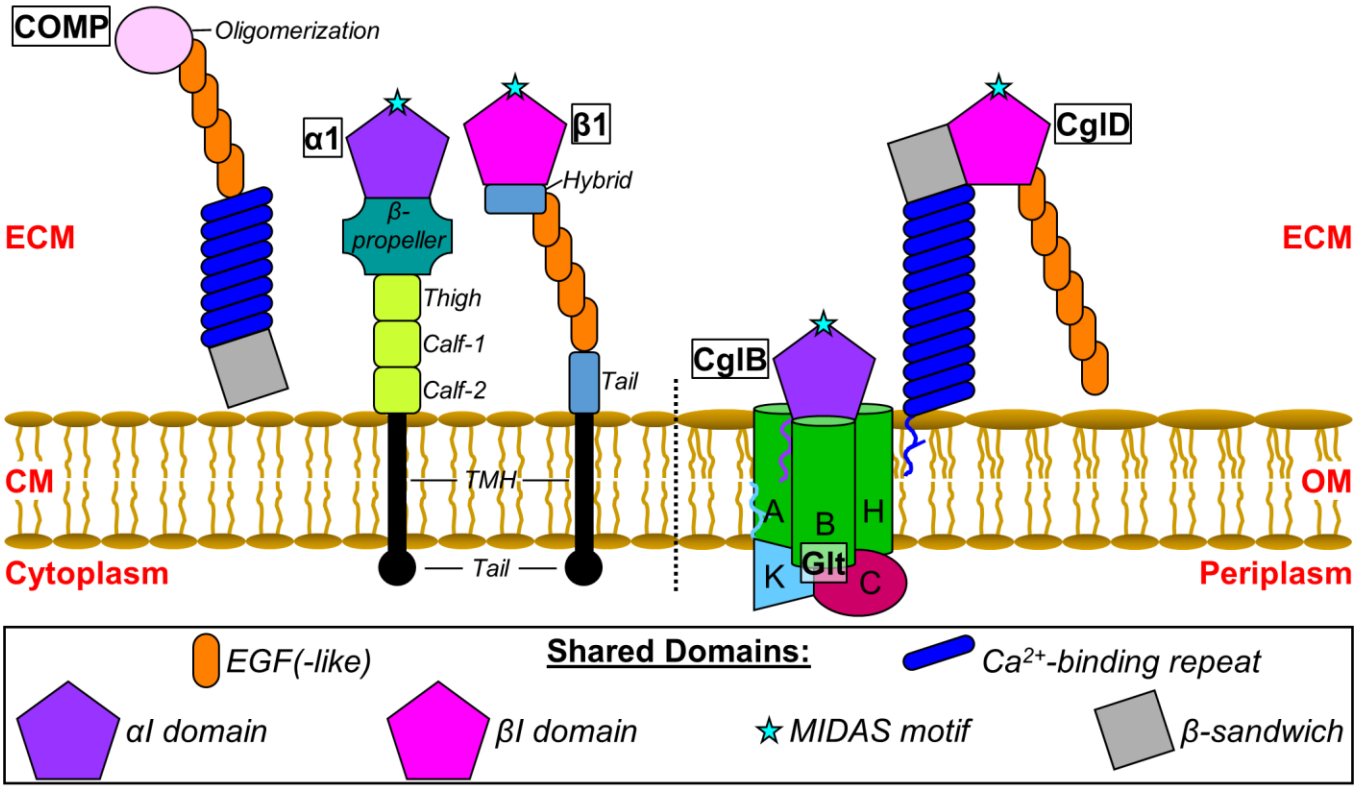

Figure 3.1: Domain schematic of eukaryotic integrin (-associated) proteins and proposed analogies with *M. xanthus* Cgl proteins.

Left: Domains of soluble COMP (cartilage oligomeric matrix protein) as well as cytoplasmic membrane (CM)-inserted α1 and β1 integrin subunits associated with the eukaryotic extracellular matrix (ECM). *Right:* Domains analogous to those found in integrins for *M. xanthus* outer-membrane (OM) lipoproteins CglB and CglD, associated with the OM module of the Glt trans-envelope complex. GltA/B/H are integral OM β-barrels. GltK is periplasmically-oriented OM lipoprotein. GltC is an OM-associated soluble periplasmic protein. Shared domains between the various eukaryotic and prokaryotic proteins have been indicated.

encoding OM(-associated) proteins of the gliding apparatus (CglB/GltK/GltH/GltF, respectively)(Luciano *et al.*, 2011; Pathak & Wall, 2012). However, the role of CglD in *M. xanthus* physiology has remained contentious, with conflicting reports as to its requirement and function; though the initial chemical mutant was reported to be gliding-null (Hodgkin & Kaiser, 1977), a subsequent clean gene-deletion mutant still resulted in gliding-capable cells, while a *cglD* missense mutation had a stronger gliding defect (Pathak & Wall, 2012). CglD has thus been proposed to have both an activation and an inhibition function in gliding motility (Pathak & Wall, 2012).

In this study, we reveal CglD to be a cell-surface β-integrin-like lipoprotein with COMP-like Ca^{2+}-binding capacity. This bacterial protein with structural homologies to eukaryotic ECM-binding components at eFAs is shown to analogously confer traction to the substratum in gliding bacterial cells, impacting bFA formation, stability, and positioning. In turn, this drastically influences both single-cell and community-level events that are essential to multicellular outcomes.

3.3 RESULTS

3.3.1 CglD is a β-integrin-like lipoprotein

To elucidate the contribution of CglD to the complex physiology of *M. xanthus*, we first set out identify structural motifs that could help explain its function. Fold-recognition analysis of CglD (1130 aa; predicted MW: 117 kDa) using HHpred revealed distinct high-confidence structural matches of the N- vs. C-terminal halves of the protein. CglD residues 40 – 430 were matched to the Ca^{2+}-binding domain of human cartilage oligomeric matrix protein (COMP, i.e. thrombospondin type-5; PDB 3FBY_B)(Tan *et al.*, 2009) (**Figure 3.2A**). COMP is a secreted glycoprotein that is engaged by integrins(Chen *et al.*, 2005) and impacts cellular attachment to, and structuration of, the extracellular matrix (ECM) in humans (Budde *et al.*, 2005; Chen *et al.*, 2007; Chen *et al.*, 2005; Di Cesare *et al.*, 2002; Halász *et al.*, 2007; Mann *et al.*, 2004; Thur *et al.*, 2001). The identified dodeca-repeating motif DxDxDG (Pathak & Wall, 2012) (**Figure 3.1**) would be consistent with a Ca^{2+}-dependence for the protein. Calculation of the 3D structure of CglD via AlphaFold2 (**Figure 3.3A-C**) revealed this putative Ca^{2+}-binding domain to form a predicted (largely unstructured) globular domain (**Figure 3.2B**), consistent with its COMP structural homologue (**Figure 3.2A**).

Conversely, CglD amino acids 644 – 1111 were identified as a match to the βI domain of human integrin β3 (i.e. CD61; PDB 3FCS_B) (**Figure 3.2A**); βI modules are ubiquitous in β integrins and include a VWA domain with a metal ion-dependent adhesion site (MIDAS) motif implicated in adhesion(Shimaoka & Springer, 2003). MIDAS motifs are a discontinuous structural element (Asp-x-Ser-x-Ser…Thr…Asp) that coordinate a divalent cation (e.g. Ca^{2+}/Mn^{2+}/Mg^{2+}), structurally modifying VWA domains upon binding of their ligand(s) to generate a high-affinity conformation toward the ligand(s). Based on the predicted structure for CglD, D656, S658, S660, T693/761, and D799 constitute the putative

MIDAS amino acids (**Figure 3.2B**); while the former three residues were previously predicted(Pathak & Wall, 2012), the remaining residues were identified based on their spatial proximity and orientation towards the canonical DxSxS tract. A mutant strain of *M. xanthus* encoding a chromosomal D656N variant of CglD was found to be compromised for gliding motility-dependent swarm-edge flare formation (Pathak & Wall, 2012), consistent with the MIDAS motif being functionally important for CglD.

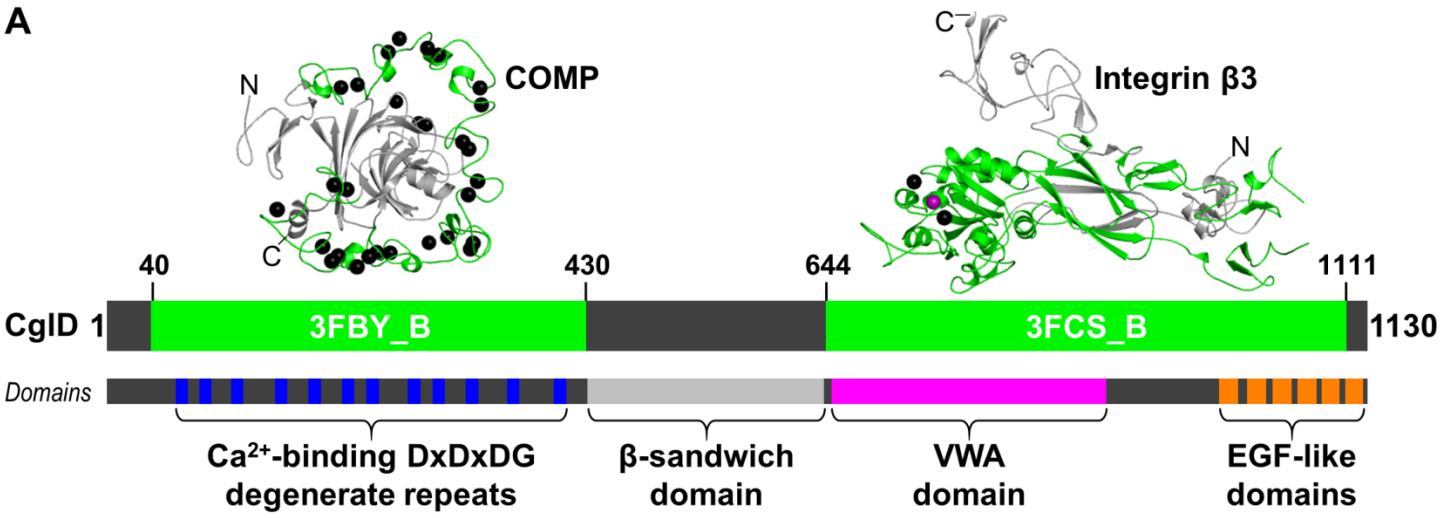
A
COMP
N
C
Integrin β3
C
N
40
430
644
1111
CgID 1
3FBY_B
3FCS_B
1130
Domains
Ca²⁺-binding DxDxDG degenerate repeats
β-sandwich domain
VWA domain
EGF-like domains

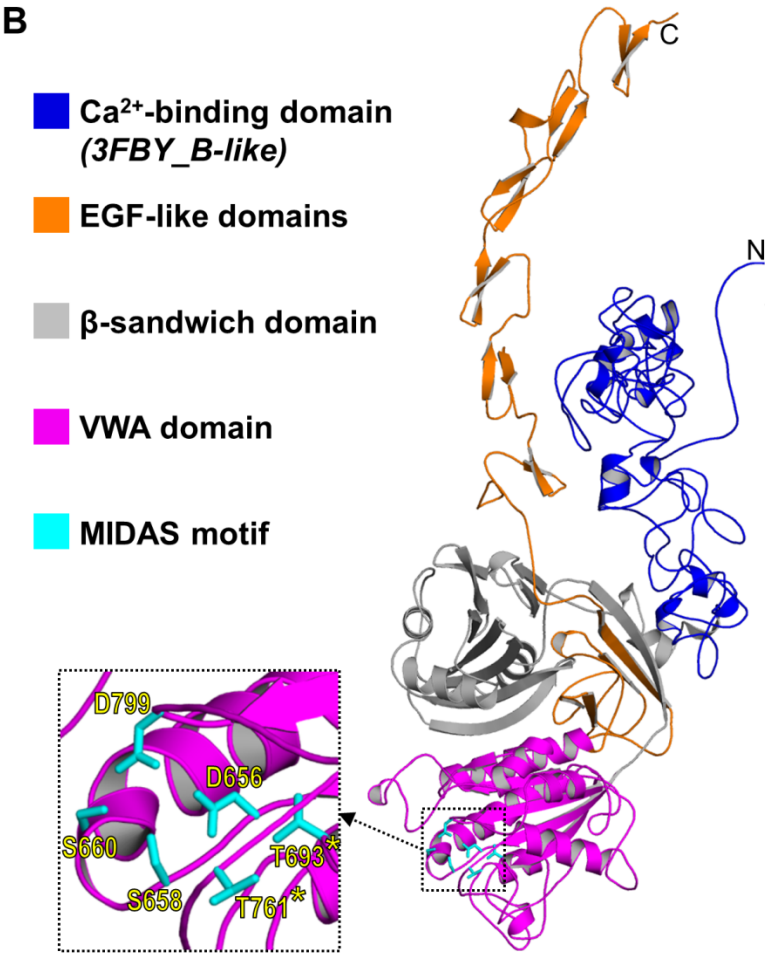
B
Ca²⁺-binding domain (3FBY_B-like)
EGF-like domains
β-sandwich domain
VWA domain
MIDAS motif
C
N
D799
D656
S660
T693*
S658
T761*

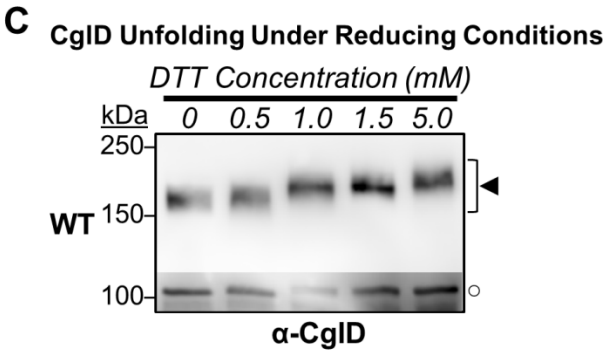
C
CgID Unfolding Under Reducing Conditions
DTT Concentration (mM)
kDa
0
0.5
1.0
1.5
5.0
250
150
100
WT
α-CgID

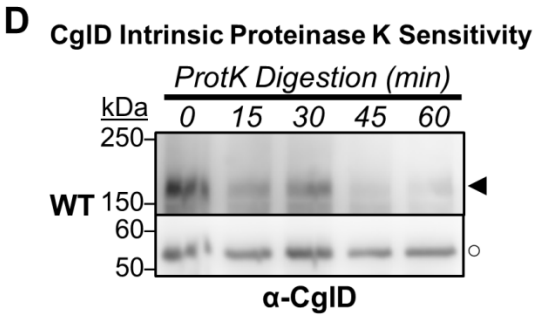
D
CgID Intrinsic Proteinase K Sensitivity
ProtK Digestion (min)
kDa
0
15
30
45
60
250
150
60
50
WT
α-CgID

Figure 3.2: CglD contains integrin-like VWA and Ca^{2+}-binding sites.

(A) Domain organization within *M. xanthus* CglD. Regions of CglD structural homology with X-ray crystal structures of COMP (PDB: 3FBY_B) and integrin β3 (PDB: 3FCS_B) are represented in *neon green* (as determined via HHpred fold recognition). *Black spheres* depicted in the template structures are co-crystalized Ca^{2+} ions. The various domains have been coloured as follows: Ca^{2+}-binding domains (*blue*); EGF-like domains (*orange*); β-sandwich (*grey*); VWA domain (*magenta*); MIDAS motif (*cyan*).
(B) Alphafold model of CglD protein, with domains coloured as in Panel A Inset: magnified view of the MIDAS motif, with putative amino acids indicated.
(C) α-CglD Western blot of WT whole-cell extracts treated with increasing concentrations of DTT to break disulphide bonds. The lower, darker zone on the blot corresponds to the section of the same blot image for which the contrast has been increased to highlight lower-intensity protein bands. Legend: ◄, full-length CglD; ○, loading control (labelled non-specifically by α-CglD pAb).
(D) Intact WT cells resuspended in TPM buffer and digested with exogenous Proteinase K. Aliquots of the digestion mixture were removed at 15-min intervals and TCA-precipitated to stop digestion. The lower zone on the blot corresponds to a lower section of the same blot image for which the contrast has been increased to highlight lower-intensity protein bands. Legend: ◄, full-length CglD; ○, non-specific loading control.

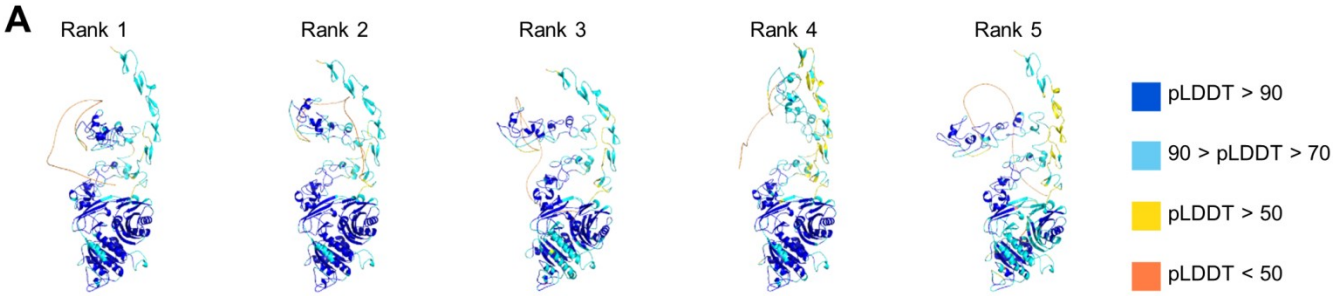
A
Rank 1
Rank 2
Rank 3
Rank 4
Rank 5
pLDDT > 90
90 > pLDDT > 70
pLDDT > 50
pLDDT < 50

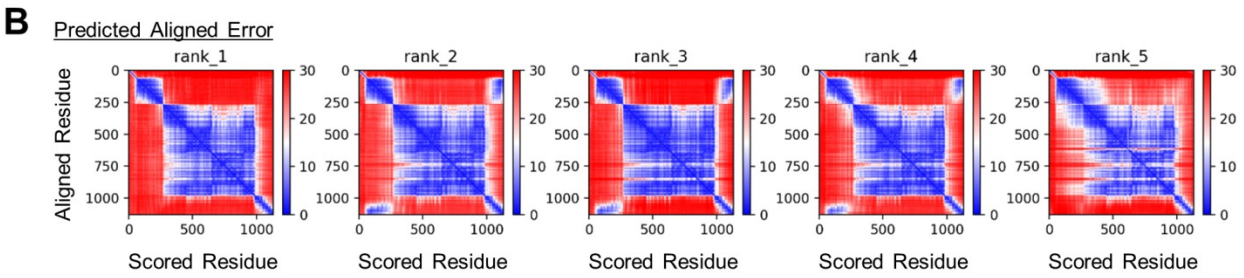
B
Predicted Aligned Error
rank_1
rank_2
rank_3
rank_4
rank_5
Aligned Residue
Scored Residue

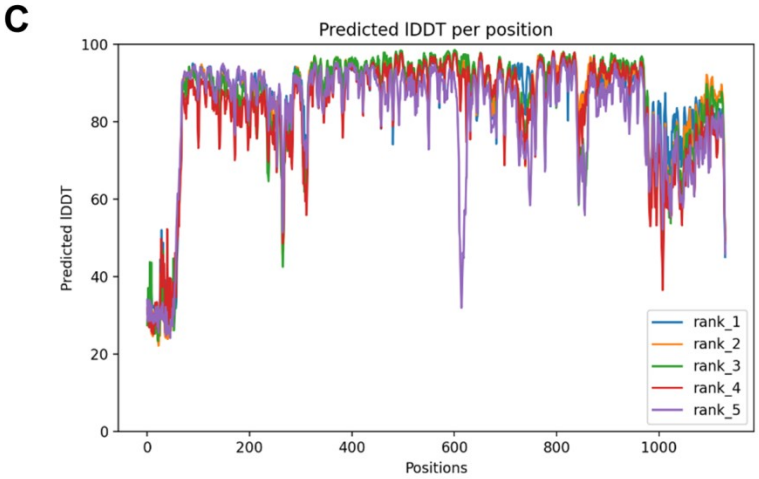
C
Predicted IDDT per position
Predicted IDDT
Positions
rank_1
rank_2
rank_3
rank_4
rank_5

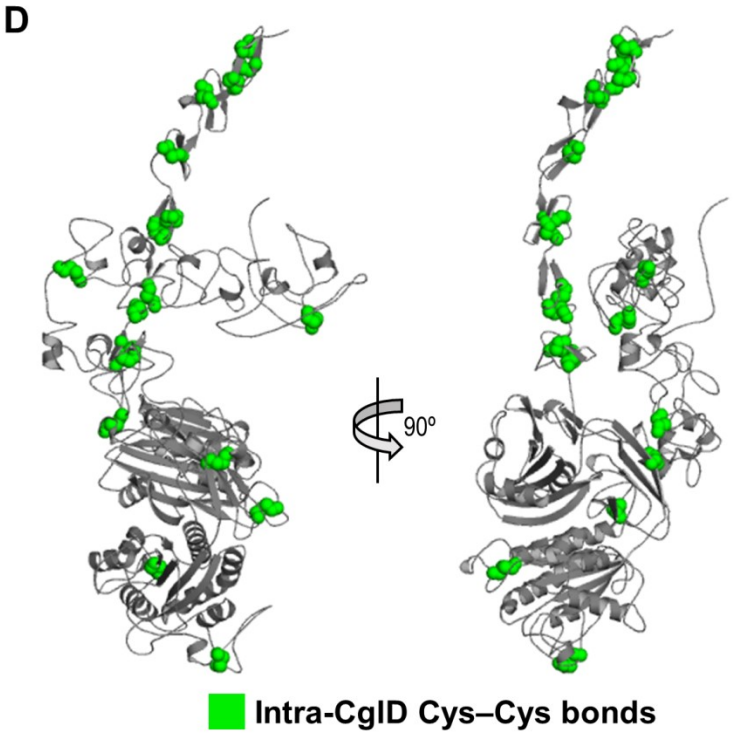
D
90°
Intra-CgID Cys–Cys bonds

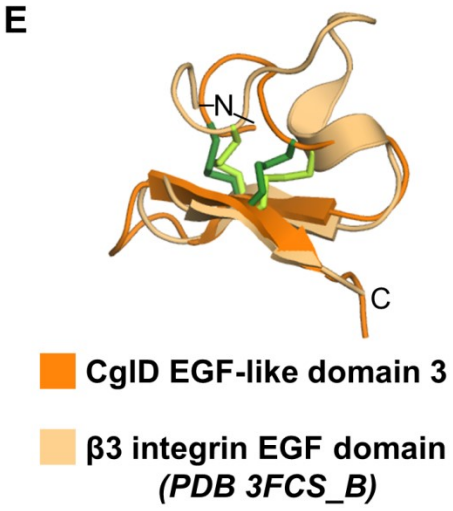
E
N
C
CgID EGF-like domain 3
β3 integrin EGF domain
(PDB 3FCS_B)

Figure 3.3. CglD AlphaFold prediction quality and structural homology.

(A) AlphaFold CglD models ranked from 1 to 5. Per-residue confidence scores (pLDDT: predicted local-distance difference test) are directly reported on the 3D structure of CglD (with the range of possible values from <50 [*orange*] to >90 [*blue*]).
(B) Corresponding predicted aligned error for each ranked model.
(C) Plot showing the corresponding pLDDT scores per residue for each ranked model.
(D) CglD model structure with highlighted (*green balls*) disulfide (Cys–Cys) bonds.
(E) Structural alignment of EGF-like Domain 3 of the CglD model structure (*dark orange*) with the EGF domain from β3-integrin (PDB: 3FCS_B) (*pale orange*). Disulfide bonds within each structure are indicated in *dark green* and *pale green*, respectively. Structures were aligned using TMalign.

Intriguingly, CglD was found to be a Cys-rich protein (46 of 1130 amino acids = 4.1%), with 18 predicted intra-protein disulphide bonds stabilizing various structural loops (**Figure 3.3D**). Titration of whole-cell lysates with reducing agent followed by α-CglD Western immunoblot analysis revealed CglD-specific bands shifting from faster to slower-migrating protein species, consistent with disulphide-dependent conformational stability of CglD (**Figure 3.2C**). Eleven of these disulphide bonds were located in repeating predicted anti-parallel domains resembling epidermal growth factor (EGF) in humans (**Figure 3.2B**, **3.3E**). Conversely, this unfolding of CglD was not impacted by the amount of Ca^{2+} to which the protein was exposed during cell growth (**Figure 3.4**), suggesting that any Ca^{2+}-binding capacity of the β-integrin-like protein may not serve to stabilize its own structure.

Given its' (i) overall domain arrangement, (ii) structural homologies to known human counterparts, and (iii) denaturation profiles, we conclude that CglD is a β-integrin-like protein with an integrated COMP module.

3.3.2 CglD is exposed at the cell surface

Lipoproteins in the OM were historically thought to localize to its periplasmic leaflet; however, cell-surface exposure of various lipoproteins is becoming more widely acknowledged(Cole *et al.*, 2021; Wilson & Bernstein, 2016), including with our recent determination of surface localization for the principal gliding adhesin lipoprotein CglB (Islam *et al.*, 2023). Given the calculated integrin-like structure of CglD (**Figure 3.2B**), we hypothesized that it too is exposed at the cell surface. We initially attempted immunolabelling of CglD (with α-CglD pAb) on live cells, but various fluorescent clusters were detected on both WT and Δ*cglD* cells. To overcome this ambiguity, we adopted an analogous approach to that used to test CglB surface exposure in the presence/absence of OM-module Glt proteins (Islam *et al.*, 2023). I.e. intact WT cells were digested with Proteinase K over the course of 60 min; aliquots removed at regular intervals revealed a steady decline in full-length CglD signal (with no visible accumulation of pAb-reactive degradation products) (**Figure 3.2D**). These data are consistent with β-integrin-like CglD being a surface-exposed lipoprotein

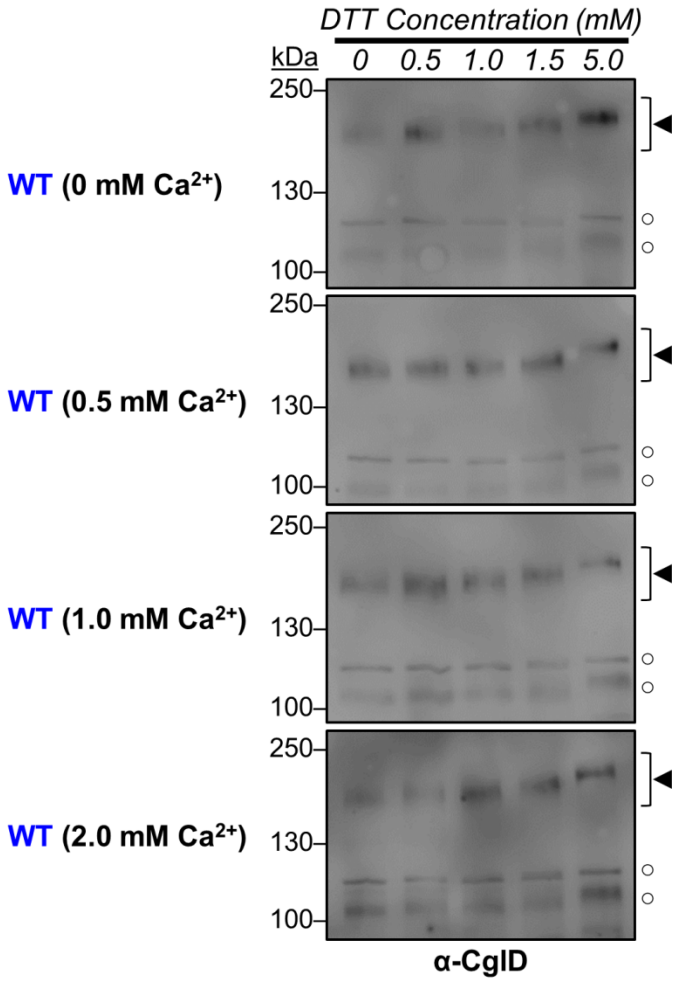

Figure 3.4. Ca^{2+} effect on CglD unfolding.

α-CglD Western blots of WT whole-cell extracts treated with increasing concentrations of DTT to break disulphide bonds. The four blots correspond to WT cultures grown in various concentrations of $CaCl_2$ (0 to 2 mM). Legend: ◄, full-length CglD; ○, loading controls (labelled non-specifically by α-CglD pAb).

.

3.3.3 CglD modulates *M. xanthus* community structuration/behaviour

As integrins in humans serve to interact with cells/substrata and structure the ECM, we set out to probe comparable community-level outputs in *M. xanthus*. Swarms of *M. xanthus* spreading on "soft" (0.5% w/v) agar plates form stratified biofilms of cells surrounded by ECM polysaccharides(Saïdi *et al.*, 2021). In the absence of β-integrin-like CglD, swarm expansion was consistently found to be negatively impacted; this community-level effect was not due to a potential defect in gliding motility at the single-cell level as swarm expansion in a gliding-deficient Δ*cglB* strain (compromised for surface-coupling of the gliding machinery) was instead found to be augmented relative to WT (**Figure 3.5A,B**), consistent with a previous report(Kaiser & Warrick, 2014). Similarly, developmental progression on minimal media requiring cell–cell aggregation was more drastically affected in the absence of CglD compared to the absence of CglB, further supporting a role for CglD in forming inter-cell connections in dense populations.

Swarm cohesiveness was also impacted by CglD, with larger clumps of fluorescent cells in WT swarms being sloughed off in response to increasing shear force applied by a rheometer (**Figure 3.5C**, **3.6**); however, as the same swarm cohesiveness phenotype was shown to depend on the principal gliding adhesin CglB (**Figure 3.5C**), this would suggest a role for CglD in gliding motility, consistent with previous reports(Hodgkin & Kaiser, 1977; Pathak & Wall, 2012), with gliding motility potentially rendering swarms more dynamic and hence less stable. Similarly, community-level responses to mechanical substratum changes were affected in the absence of CglD, as assayed via polymertropism response (i.e. changes in swarm aspect ratio) (**Figure 3.5D**). Polymertropism is a gliding- and glycocalyx-dependent phenomenon(Fontes & Kaiser, 1999; Saïdi *et al.*, 2021) in which swarms preferentially spread in an east–west direction, in response to aligned substratum polymers caused by north–south compression of the underlying agar matrix(Fontes & Kaiser, 1999; Lemon *et al.*, 2018; Lemon *et al.*, 2017). While the absence of CglB resulted in a severely-compromised polymertropism response, swarms lacking CglD displayed an intermediate polymertropism phenotype (**Figure 3.5D**), again implicating CglD in gliding motility (albeit in a non-essential capacity).

Taken together, the above-described data are consistent with β-integrin-like CglD playing roles in both community-level inter-cell interactions as well as gliding motility outcomes.

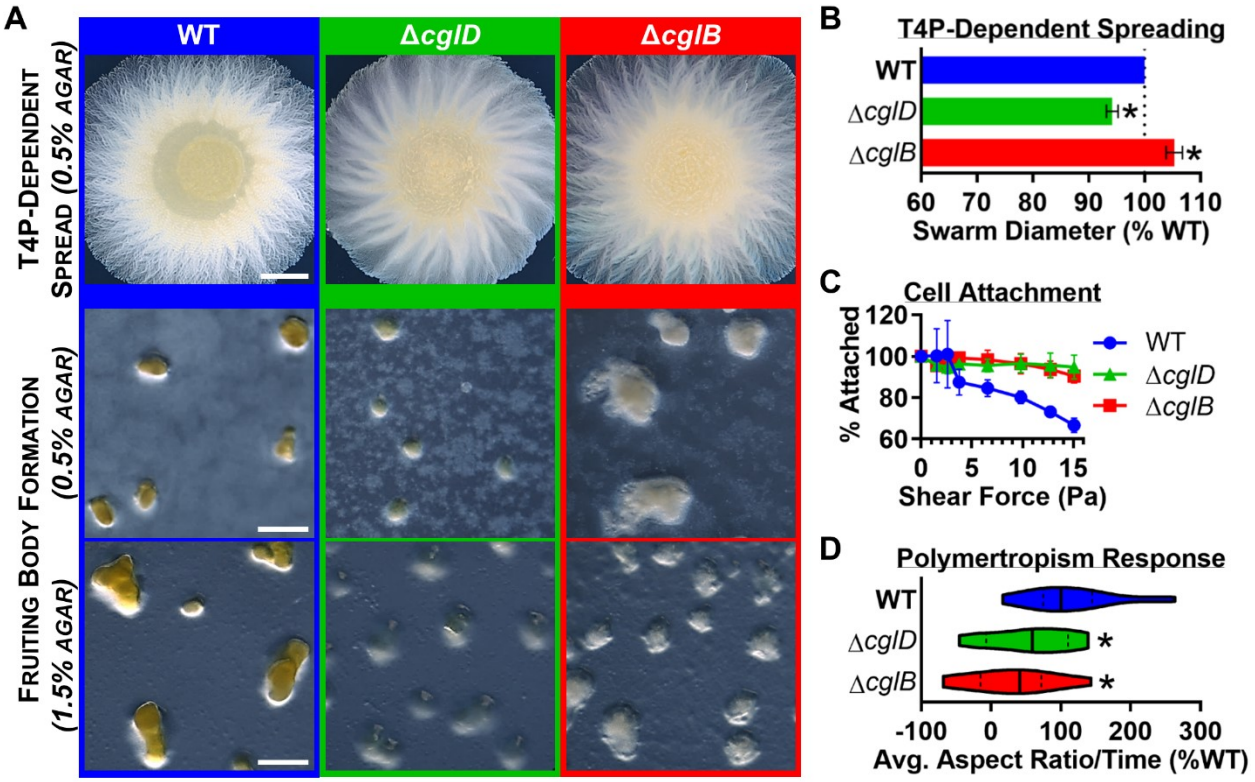

Figure 3.5: Impact of CglD deficiency on multicellular behaviours.

(A) Macroscopic phenotype comparison between WT, Δ*cglD* and Δ*cglB* strains. *Top row:* T4P-dependent swarm spreading on CYE 0.5% agar plates (scale bar: 4 mm). *Middle and bottom rows*: Fruiting body formation on CF 0.5% and 1.5% agar plates (respectively) after 72 h at 32 ºC (scale bar: 1 mm).

(B) Swarm diameter measurements for T4P-dependent spreading, normalized to WT (n = 5). Both Δ*cglD* and Δ*cglB* swarms displayed significantly different (*) swarm diameters compared to WT, as determined via Wilcoxon signed-rank test set relative to a reference value of 100 ($p < 0.05$).

(C) Swarm integrity analysis as determined via rheometric shearing of adhered fluorescent cell strains. Fluorescence values at all shear forces were normalized to the intensity from the initial image acquired prior to shear-force application. Each shear force point indicated is the mean of 3 biological replicates (± SEM). Increasing shear forces were applied for a duration of 1 min after which the force was increased to the next level via faster rotation of the rheometer arm.

(D) Polymertropism response determined by calculating the average aspect ratio of a swarm over time, normalized to the WT control strain run at the same time. Both Δ*cglD* and Δ*cglB* displayed significantly different dataset distributions (*) compared to the values for WT, as determined via Mann-Whitney test ($p < 0.05$).

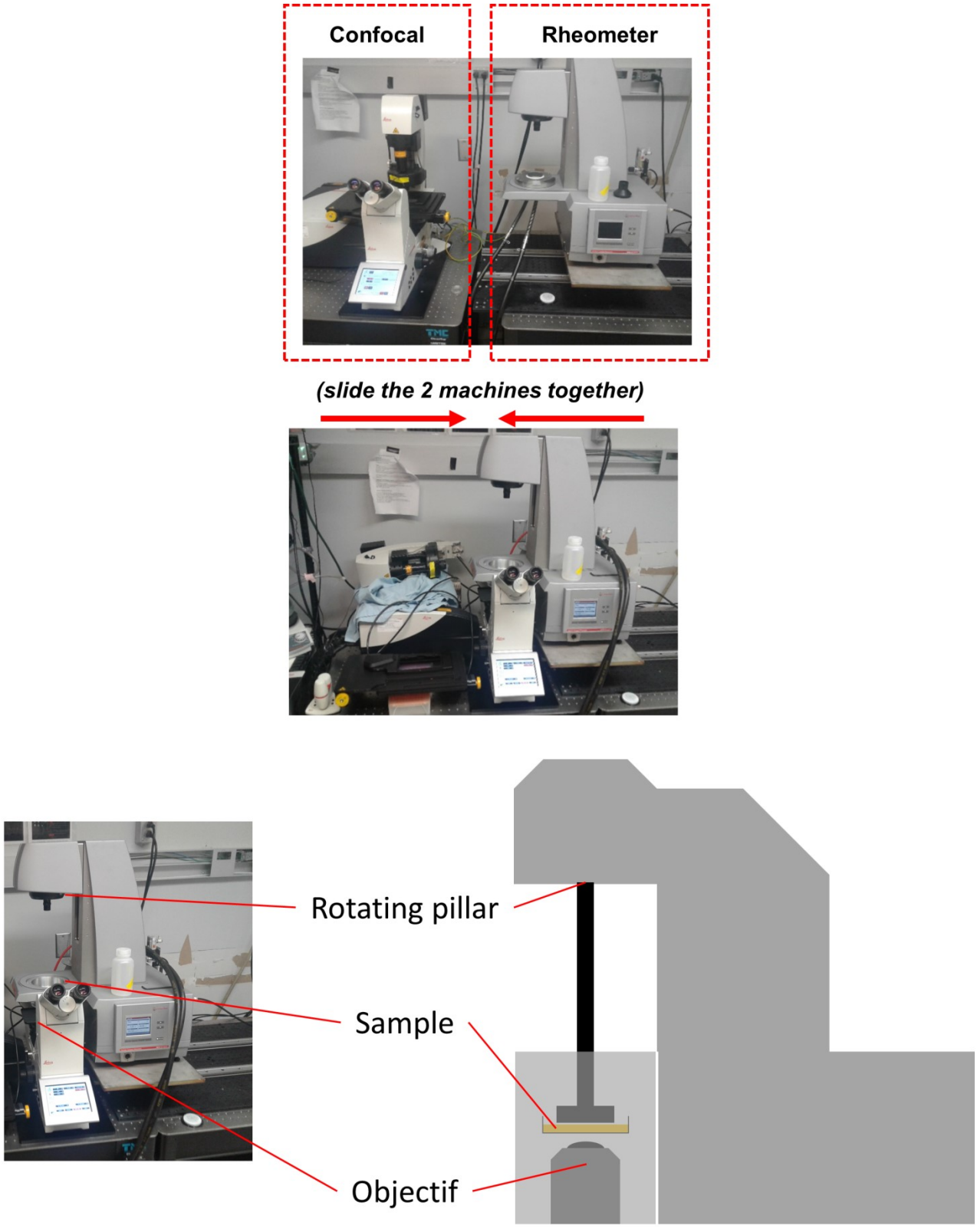

Figure 3.6. Depiction of the combined microscope and rheometer setup.

Top: Photographs of the separated microscope (*left*) and rheometer (*right*) (top pictures). Bottom: Photograph of the combined setup used for the rheometry imaging experiments. The diagram represents the combined device depicted with a sample on the glass-bottomed agar-coated fluorodishes used for imaging.

3.3.4 CglD promotes (but is not required for) gliding motility on deformable substrata

As the *cglD* locus was originally identified through its conditional importance for gliding motility, we next set out to reconcile the disparate datasets in which CglD has been postulated to either be required (Hodgkin & Kaiser, 1977) or not (Pathak & Wall, 2012) for gliding motility. We first compared gliding-dependent swarm-edge flare formation for WT and Δ*cglD* cells across diverse matrices, each characterized by a distinct elastic modulus (i.e. resistance to deformation). For agar (1.5% w/v), carrageenan (1.5% w/v), and gellan (0.6% w/v) matrices, gliding flares were clearly detected for both strains already after 7 h (**Figure 3.7A**). Incidentally, flares on gellan were considerably more prominent/noticeable compared to those on either carrageenan or (canonical) agar substrata (**Figure 3.7A**), suggesting that gellan-based matrices may be a superior alternative for the examination of myxobacterial gliding-flare formation. For both strains, individual and groups of cells were found to follow previously-carved troughs in the deformable matrices, further supporting the notion of sematectonic stigmergy (Gloag *et al.*, 2013; Saïdi *et al.*, 2021) — i.e. behavioural coordination within a population without direct interactions between individuals, accomplished via physical modifications of the local environment — being responsible for the eponymous "trail following" phenotype of myxobacteria atop agar matrices (Burchard, 1982; Islam & Mignot, 2015) (**Figure 3.7A**). At the level of individual cells, those lacking CglD were found to glide on the various substrata at slower speeds (**Figure 3.7B**) with less-frequent reversals of gliding direction (**Figure 3.7C**).

The only instance in which we found Δ*cglD* cells unable to manifest gliding-dependent flares compared to flare-forming WT cells was related to the drying conditions used for the agar matrix. Namely, freshly-poured "hard" (1.5% w/v) agar plates left to cool uncovered in the biohood for increasing 10-min intervals prior to covered drying on benchtop (2 h) and spotting of cells, sealing of the plate, and incubation for 24 h. These parameters were able to support gliding-flare formation in WT cells, but not in Δ*cglD* cells. Conversely, identical plates allowed to dry uncovered for longer in the biohood were indeed able to support gliding-flare formation in both strains (**Figure 3.8**). As such, the previously reported (Hodgkin & Kaiser, 1977) absolute requirement for CglD in agar-based gliding may have been (at least partially) due to the hydration state of the agar matrix being used.

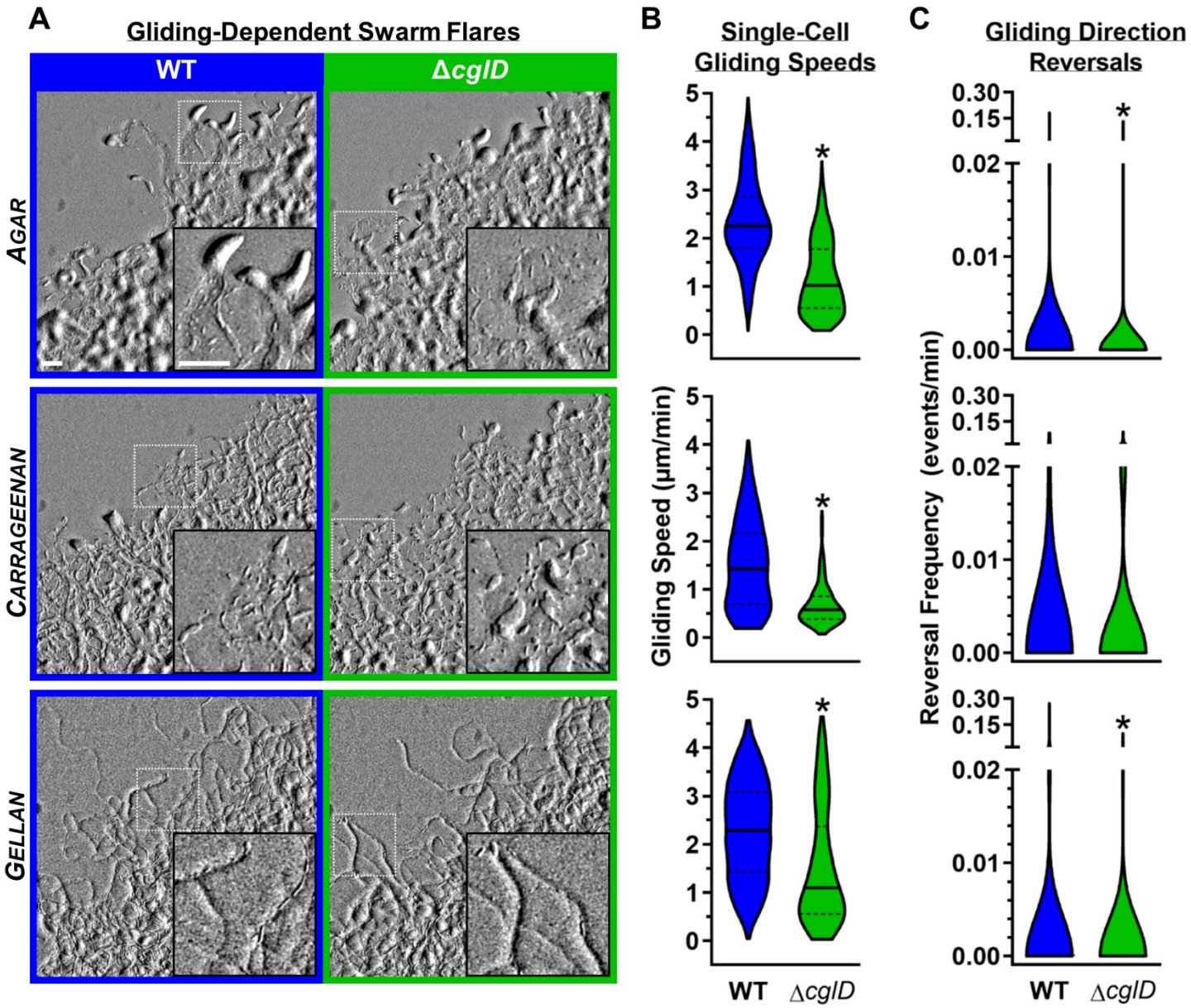

Figure 3.7: CglD deficiency impacts gliding motility across multiple substrata.

Each row referred to a specific gelling agents used: Agar 1.5 %, Carrageenan 1.5% and gellan 0.6% respectively from top to bottom.

(A) Gliding-dependent swarm-edge flares on CYE substrata solidified with 1.5% agar, 1.5% carrageenan, or 0.6% gellan. The insets represent magnified views of the indicated areas (*white dashed boxes*) showing deep furrows carved out by flare-leading cells, which can be followed by subsequent cells via sematectonic stigmergy. Scale bars at both magnifications: 50 μm.

(B) Violin plots of single-cell gliding-*event* speeds for WT and Δ*cglD* cells on pads solidified with different gelling agents across 3 biological replicates (agar: n_{WT} = 1534 events, $n_{\Delta cglD}$ = 1237 events; carrageenan: n_{WT} = 233 events, $n_{\Delta cglD}$ = 272 events; gellan: n_{WT} = 1826 events, $n_{\Delta cglD}$ = 627 events). The lower and upper boundaries of the plots correspond to the minimum and maximum values of the dataset, with the 25th and 75th percentiles displayed (*dashed black lines*). The median (*solid black line*) of each dataset is indicated. Asterisks denote datasets displaying

statistically significant (*) differences in distributions ($p < 0.0001$) between WT and Δ*cglD* cells, as determined via unpaired two-tailed Mann–Whitney tests.
(C) Violin plots of reversal events per minute for tracked WT and Δ*cglD* cells (see Panel B) on pads solidified with agar, carrageenan, or gellan across 3 biological replicates (agar: n_{WT} = 1534 events, $n_{\Delta cglD}$ = 1237 events; carrageenan: n_{WT} = 233 events, $n_{\Delta cglD}$ = 272 events; gellan: n_{WT} = 1826 events, $n_{\Delta cglD}$ = 627 events). The lower and upper boundaries of the plots correspond to the minimum and maximum values of the dataset, with the 25th and 75th percentiles as well as the median not distinguishable due to skewing of the data by non-reversing cells. Asterisks denote datasets displaying statistically significant (*) differences in distributions ($p < 0.0001$) between WT and Δ*cglD* cells, as determined via unpaired two-tailed Mann–Whitney tests.

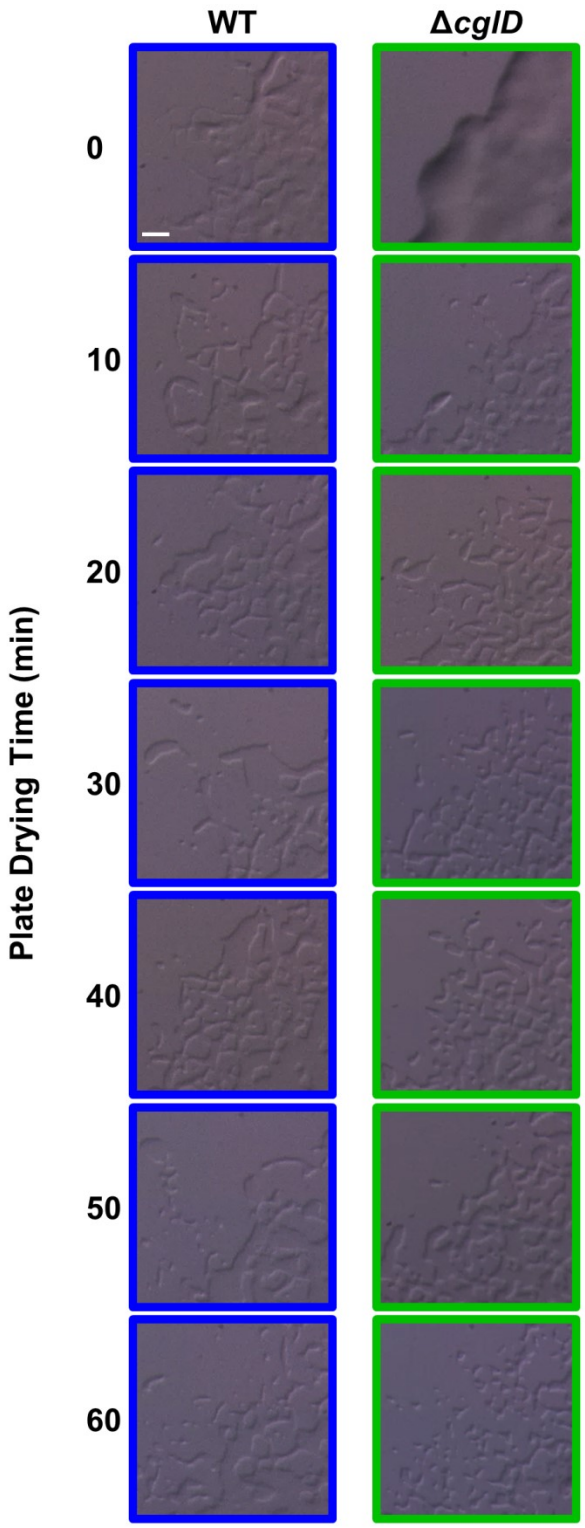

Figure 3.8. CglD sensivility to the dryness of the substrata.

Gliding motility flares on CYE hard substrata (scale bar: 50 μm) for WT (*blue*) and Δ*cglD* (*green*) cells. Each time point corresponds to the time that the CYE 1.5% agar plate was left to dry uncovered under the biohood prior to the spotting of cell suspension. Each image was captured after 24 h at 32 °C.

3.3.5 CglD is required for Ca^{2+}-dependent gliding motility on rigid substrata

With the high propensity of its β-integrin-like tertiary structure to bind calcium ions (**Figure 3.2A,B**), we next examined the contribution of Ca^{2+} to CglD-modulated gliding motility. To precisely control the amount of calcium present, Ca^{2+}-dependent single-cell motility was established in polydimethylsiloxane (PDMS) microfluidic chambers via use of non-deformable chitosan-functionalized glass substrata; as the concentration of Ca^{2+} in the chitosan preparation buffer increased, so too did the gliding speed of cells (**Figure 3.9A**). Cells lacking CglD were found to be severely compromised for Ca^{2+}-dependent gliding on chitosan-functionalized glass (**Figure 3.9B**), demonstrating the essentiality of the β-integrin-like surface protein in this context. Thus, while CglD is dispensable for single-cell gliding on deformable matrices, the β-integrin-like protein is necessary for single-cell locomotion on a rigid substratum in a calcium-dependent manner.

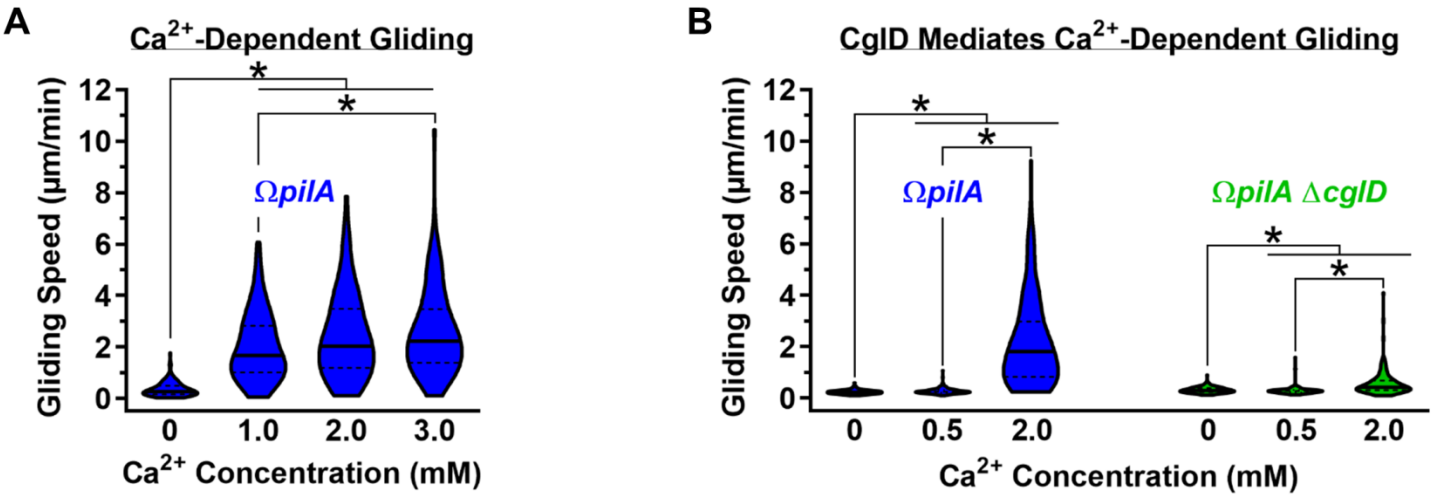

Figure 3.9: Single-cell gliding motility on non-deformable chitosan-functionalized glass is Ca^{2+}- and CglD-dependent.

(A) Violin plots of single-cell gliding event speeds for Ω*pilA* cells in PDMS microfluidic chambers atop chitosan-functionalized glass slides. $CaCl_2$ was present in increasing concentrations in separate microfluidic channels.

(B) Violin plots of single-cell gliding event speeds for Ω*pilA* and Ω*pilA* Δ*cglD* cells on glass coverslips coated with chitosan in the presence of increasing concentrations of $CaCl_2$ (n = 115 cells). For Panels A and B, the lower and upper boundaries of the plots correspond to the minimum and maximum values of the dataset, with the 25th and 75th percentiles displayed (*dashed lines*). The median (*solid black line*) of each dataset is indicated. Asterisks denote datasets displaying statistically significant differences in distributions ($p < .0001$) between various concentrations (*) as determined via unpaired two-tailed Mann–Whitney tests.

3.3.6 CglD confers traction to gliding cells

As eukaryotic integrins are widely known to exert traction forces on the substratum under a translocating cell (Brockman *et al.*, 2018), we postulated that β-integrin-like CglD may contribute to single-cell *M. xanthus* gliding in a comparable manner. To test this hypothesis, we undertook traction force microscopy (TFM) studies (Sabass *et al.*, 2017) optimized for single gliding cells of various strains. TFM depends on traction-induced displacement of fluorescent particles in a temporarily deformable matrix below a translocating cell; as such, an elastic substratum capable of "springing back" following cell passage and deformation (unlike agar, carrageenan, or gellan [**Figure 3.7A**]) is required. For this reason, we employed an elastic polyacrylamide (PAA) matrix coated in Ca^{2+}-infused chitosan. This substratum was indeed capable of supporting gliding motility in single cells encoding the full complement of gliding machinery genes, whereas cells lacking CglB (i.e. the principal adhesin of the gliding system) were expectedly gliding deficient. In contrast, cells lacking CglD were still able to glide on this substratum, albeit at a severely-reduced capacity (**Figure 3.10A**).

Analysis of the distribution of traction force under a gliding cell relative to its surroundings indicated that more traction was exerted at the leading pole than at the lagging pole in cells expressing CglD, consistent with the formation of bFA sites at the leading pole; in contrast, cells deficient for CglD were only able to exert minimal traction on the substratum above background levels (**Figure 3.10B,C**), providing a rationale for the considerably slower gliding speed in the latter cells (**Figure 3.10A**). As force is a (Islam *et al.*, 2023) vector quantity, in addition to its magnitude, we also examined the directionality of the applied traction force. Importantly, immediately under the leading halves of advancing cells, traction forces were exerted with a leftward orientation, while under the lagging halves of advancing cells, traction forces were applied with a rightward bias (**Figure 3.10B, *inset***).

Taken together, these data indicate that CglD contributes traction forces to the substratum under gliding cells. Moreover, the directionality of these forces provides independent corroboration that gliding *M. xanthus* cells undergo helical rotation of the cell along its long axis (Faure et al., 2016) while gliding.

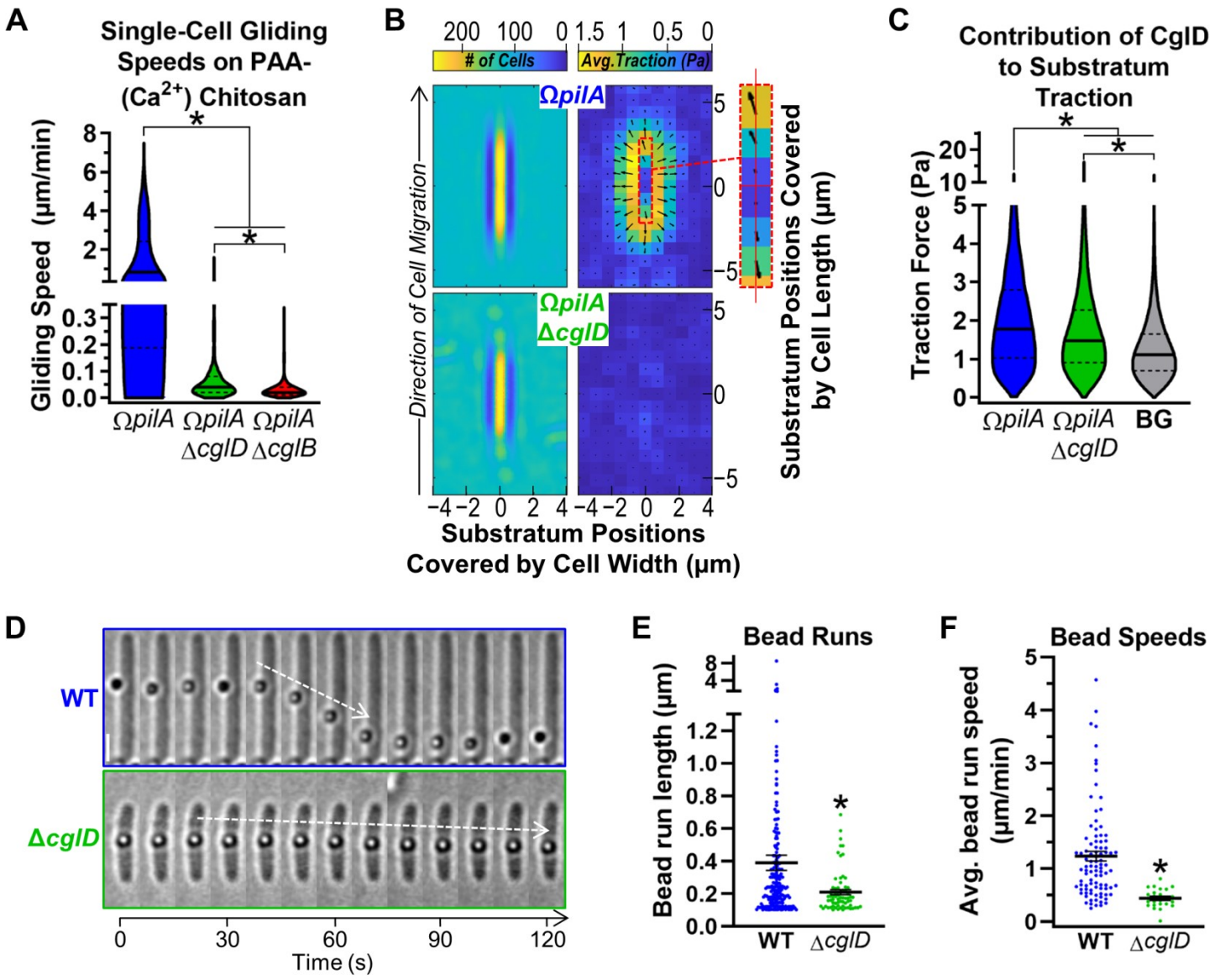

Figure 3.10: CglD engages the gliding substratum and transported cell-surface cargo.

(A) Violin plots of single-cell gliding event speeds for Ω*pilA*, Ω*pilA* Δ*cglD*, and Ω*pilA* Δ*cglB* cells on a polyacrylamide (PAA) substratum coated with chitosan in the presence of $CaCl_2$. The lower and upper boundaries of the plots correspond to the minimum and maximum values of the dataset, with the 25th and 75th percentiles displayed (*dashed black lines*). The median (*solid black line*) of each dataset is indicated. Asterisks denote datasets displaying statistically significant differences (*) in distributions ($p < 0.0001$) between each mutant strain and WT, as determined via unpaired two-tailed Mann–Whitney tests.

(B) Traction force applied on the substratum under a gliding *M. xanthus* cell as determined via traction force microscopy. *Left-side panel:* Heat map of average cell positioning during tracked motility run, displayed as average brightness for a particular position (measured in arbitrary units, A.U.). *Right-side panel:* Heat map of the average traction force magnitude applied under a gliding cell. Arrows originating from various squares indicate the average direction of the applied traction

force by the gliding cell. *Dashed red box:* Magnified view of the traction force readout immediately under CglD-containing gliding cells, indicating a horizontal skew to the direction of the applied forces.
(C) Violin-point representing the traction forces exerted on the substratum by gliding cells with(out) CglD. The background (BG) signal is displayed to denote the baseline threshold for the TFM readings. The lower and upper boundaries of the plots correspond to the minimum and maximum values of the dataset, with the 25th and 75th percentiles displayed (*dashed black lines*). The median (*solid black line*) of each dataset is indicated. Asterisks denote datasets displaying statistically significant differences (*) in distributions ($p < 0.0001$) between each strain as determined via unpaired two-tailed Mann–Whitney tests.
(D) Montage of the trafficking phenotypes of surface-deposited polystyrene beads on WT vs. Δ*cglD* cells.
(E) Lengths of trafficked polystyrene bead runs (> 0.1 μm) along immobilized live *M. xanthus* cells. Images from 10-s intervals were analyzed. The distributions of the two datasets are significantly different (*), as calculated via unpaired two-tailed Mann-Whitney U-test ($p = 0.0010$).
(F) Average speeds of trafficked polystyrene beads during bead runs. The distributions of the two datasets are significantly different (*), as calculated via unpaired two-tailed Mann-Whitney test ($p < 0.0001$).

3.3.7 CglD is directly involved in the gliding mechanism

The TFM data for strains with(out) CglD could be explained by one of two scenarios:

(i) CglD serves as a general cell-surface adhesin that non-specifically helps bring the cell into close contact with whatever is around it (e.g. the substratum or another cell), allowing CglB-mediated substratum-coupling of the Agl–Glt gliding apparatus to then take over and power cell locomotion.

(ii) CglD is a cell-surface adhesin that can specifically couple to the Agl–Glt machinery and assist with CglB-mediated substratum-coupling of the complex.

To examine the relationship between CglD and the known components of the gliding apparatus, we first probed the co-occurrence of *cglD* with *cglB* and *gltABCDEFGHIJK* across a range of representative complete bacterial genomes. As with *cglB* and the *glt* genes, *cglD* was highly conserved in members of the order Myxococcales, but was never found to be encoded in clusters for any of the known gliding-apparatus components. Sporadic instances of *cglD* in the absence of most of the gliding-machine genes were also detected, suggesting that *cglD* acquisition may have predated any co-option by the gliding apparatus in the Myxococcales (**Figure 3.11**).

To further distinguish between the two abovementioned possibilities for the TFM data, we employed bead-force microscopy; therein, using optical tweezers, a large (520 nm-diameter) polystyrene bead was deposited directly on the surface of *M. xanthus* cells, after which CglB-dependent Agl–Glt trafficking events (Islam *et al.*, 2023; Sun *et al.*, 2011) acting on the bead were quantified (**Figure 3.10D**). In this manner, a general requirement for CglD to help "recruit" the bead into close contact with the cell surface was negated. Compared to beads placed on WT cells, those deposited on Δ*cglD* cells were trafficked over shorter periods of time and at slower speeds (**Figure 3.10E,F**). If CglD did not specifically participate in surface-coupling of the bead to the Glt apparatus, the lengths and speeds of individual bead-run events should have been comparable between WT and Δ*cglD* cells; as this was not the case, the data support a direct involvement of CglD in coupling the internally-trafficked Agl–Glt apparatus to the cell-surface Glt OM platform containing CglB.


bootstrap
20
40
60
80
100
aglRQS (M1)
gltDEFGHIJ (G1)
gltKBAC (G2)
aglR
aglQ
aglS
gltD
gltE
gltF
gltG
gltH
gltI
gltJ
gltK
gltB
gltA
gltC
cglB
cglD
Myxococcus xanthus DK1622/DZ2
Myxococcus virescens DSM 2260
Myxococcus vastator AM301
Myxococcus macrosporus HW-1
Myxococcus macrosporus DSM 14697
Myxococcus hansupus
Pyxidicoccus fallax DSM 14698
Pyxidicoccus trucidator CA060A
Pyxidicoccus caerfyrddinensis CA032A
Myxococcus fulvus 124B02
Myxococcus stipitatus DSM 14675
Myxococcus eversor AB053B
Myxococcus llanfair...sis AM401
Corallococcus terminator CA054A
Corallococcus praedator CA031B
Corallococcus llansteffanensis CA051B
Corallococcus sicarius CA040B
Corallococcus carmarthensis CA043D
Corallococcus aberystwythensis AB050A
Corallococcus exercitus AB043B
Corallococcus interemptor AB047A
Corallococcus coralloides DSM 2259
Corallococcus exiguus DSM 14696
Corallococcus coralloides B035
Hyalangium minutum DSM 14724
Stigmatella aurantiaca DW4/3-1
Stigmatella erecta DSM 16858
Melittangium boletus DSM 14713
Archangium primigenium ATCC 29037
Cystobacter ferrugineus Cbfe23
Cystobacter fuscus DSM 52655
Archangium gephyra DSM 2261
Vitiosangium sp. GDMCC 1.1324
Archangium violaceum SDU34
Archangium violaceum SDU8
Simulacricoccus sp. 17bor-14
Aggregicoccus sp. 17bor-14
Vulgatibacter incomptus DSM 27710
Anaeromyxobacter sp. Fw109-5
Anaeromyxobacter dehalogenans 2CP-C
Anaeromyxobacter sp. K
Anaeromyxobacter dehalogenans 2CP-1
Kofleriaceae bacterium H4 MYX2
Haliangium ochraceum DSM 14365
Nannocystis exedens DSM 71
Enhygromyxa salina SWB007
Plesiocystis pacifica SIR-1
Pseudenhygromyxa sp. WMMC2535
Sandaracinus amylolyticus DSM 53668
Labilithrix luteola DSM 27648
Pajaroellobacter abortibovis
Polyangium spumosum DSM 14734
Polyangium fumosum DSM 14668
Minicystis rosea DSM 24000
Chondromyces apiculatus DSM 436
Chondromyces crocatus Cm c5
Sorangium cellulosum So ceGT47
Sorangium cellulosum So ce26
Sorangium cellulosum So ce56
Sorangium cellulosum So ce836
Sorangium cellulosum So0157-2
Bdellovibrio bacteriovorus HD100
Bacteriovorax marinus SJ
Pelobacter carbinolicus DSM 2380
Geobacter sulfurreducens KN400
Syntrophorhabdus aromaticivorans
Syntrophus aciditrophicus SB
Desulfomonile tiedjei DSM 6799
Desulfarculus baarsii DSM 2075
Desulfobacca acetoxidans DSM 11109
Syntrophobacter fumaroxidans MPOB
Desulfatibacillum alkenivorans AK 01
Desulfococcus oleovorans Hxd3
Desulfatirhabdium butyrativorans
Desulforegula conservatrix
Desulfobacterium autotrophicum HRM2
Desulfobacter curvatus
Desulfobacula toluolica Tol2
Desulfurivibrio alkaliphilus AHT2
Desulfobulbus propionicus DSM 2032
Desulfocapsa sulfexigens DSM 10523
Desulfobulbaceae bacterium BRH c16a
Desulfotalea psychrophila LSv54
Desulfonatronum thioautotrophicum
Desulfomicrobium baculatum DSM 4028
Desulfovermiculus halophilus
Desulfohalobium retbaense DSM 5692
Desulfocurvus vexinensis
Desulfovibrio hydrothermalis AM13
Lawsonia intracellularis N343
Deferrisoma camini
Magnetococcus marinus
Acetobacter cerevisiae
Erythrobacter litoralis
Sphingobium indicum
Nitrosomonas europaea
Sulfuricella denitrificans
Neisseria gonorrhoeae
Bordetella avium
Burkholderia cepacia
Methylibium petroleiphilum
Nitrosococcus halophilus
Cellvibrio japonicus
Pseudomonas aeruginosa
Marinobacter adhaerens
Hahella chejuensis
Aeromonas aquatica
Vibrio cholerae
Salmonella enterica
Escherichia coli
Hippea maritima DSM 10411
Desulfurella acetivorans
Helicobacter acinonychis
Campylobacter coli
Sulfurovum riftiae
Nitratifractor salsuginis
Mycobacterium bovis
Clostridium perfringens
Streptococcus sanguinis
Fibrobacter succinogenes
δ
α
β
γ
δ
ε
Actinobacteria
Firmicutes
FCB group
Myxococcales
Cystobacterineae
Nannocystineae
Sorangiineae

Figure 3.11. Co-occurrence and gene synteny of *cglD* in bacteria.
Taxonomic distribution and co-occurrence of *agl*, *glt*, *cglB*, and *cglD* genes in Proteobacteria. Bootstrap values at each node are indicated as shown in the left-side legend. Colour of gene hit indicates synteny with the G1 *gltDEFGHIJ* (*dark green*) or G2 *gltKBAC* (*green*) gene clusters or lack thereof (*light green*), respectively. Herein, synteny denotes a minimum of three genes in the vicinity of each other.

3.3.8 CglD presence is not affected by constituents of the Glt apparatus

As the bead-force microscopy results suggest that CglD functions in concert with the Glt apparatus, and given the previously-demonstrated cellular-retention dependence of CglB on certain constituents of the Glt OM module (Islam *et al.*, 2023), we probed for the presence of CglD in mutant strains of all known constituents of the gliding machinery. Unlike CglB (Islam *et al.*, 2023), CglD was found to be expressed and retained by the cell independently of any gliding-machinery defect (**Figure 3.12A**). Moreover, the folding state of CglD was not affected by the absence of any Glt OM-module protein (**Figure 3.12B**), reinforcing its lack of dependence on any Glt components for its retention by cells.

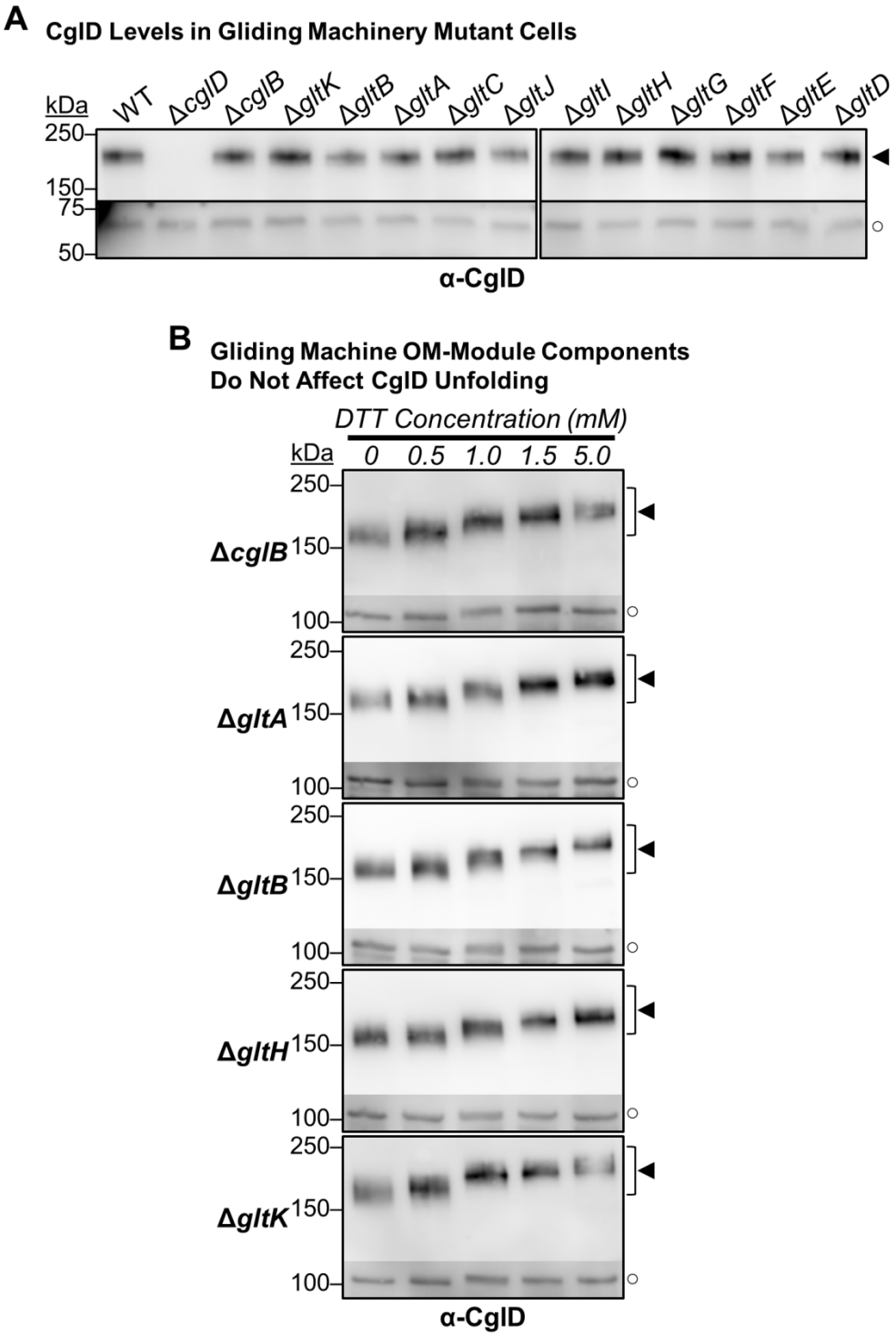

Figure 3.12: Glt components do not affect the cellular levels and unfolding of CglD.

(A) α-CglD Western blot of whole-cell extracts from *glt* and *cglB* mutants. The lower, darker zones on the blots corresponds to lower sections of the same blot images for which the contrast has been increased to highlight lower-intensity protein bands. **(B)** α-CglD Western blot of whole-cell extracts from Glt OM-module knockout strains, treated with increasing concentrations of DTT to break disulphide bonds. The lower, darker zones on the blots corresponds to the section of the same blot image for which the contrast has been increased to highlight lower-intensity protein bands. Legend for Panels A and B: ◄, full-length CglD. ○, loading control (non-specific protein band labelled by α-CglD antibody).

3.3.9 CglD stabilizes bFAs

With the results of bead-force microscopy implicating CglD function as being directly coupled to the gliding machinery, we examined possible structural and functional associations of CglD with the Glt machinery. Using sensitive analyses of raw mass spectra for prey proteins pulled down via purification of glutatathione S transferase (GST)-tagged bait proteins (Nan *et al.*, 2010), OM proteins CglD and GltA (as well as periplasmic GltE) were found to co-purify with the GST-tagged C-terminal domain of periplasmic GltD bait (**Table 3.1**), consistent with a functional linkage for these proteins with the gliding mechanism. Intriguingly, several putative metalloproteases were also pulled down with this bait construct, providing unexpected leads as to potential candidates that may be responsible for cleaving gliding motility adhesins (Islam *et al.*, 2023) from the surface of *M. xanthus* cells (**Table 3.1**).

We next probed the effect of CglD absence on the formation of bFAs in gliding cells (**Figure 3.13A**). To track the position of the AglRQS-energized Glt trans-envelope apparatus, fluorescently-tagged copies of the AglZ protein are followed in cells (Islam *et al.*, 2023; Jakobczak *et al.*, 2015; Luciano *et al.*, 2011; Mauriello *et al.*, 2009; Mignot *et al.*, 2007; Seef *et al.*, 2021; Sun *et al.*, 2011). AglZ is a cytoplasmic filament-forming coiled-coil protein that is required for gliding (Mauriello *et al.*, 2009; Yang *et al.*, 2004). We thus first compared bFA formation in gliding cells expressing AglZ-YFP with(out) CglD via fluorescence microscopy (**Figure 3.13A**). Contrary to the well-defined and compact bFA clusters formed by WT cells, CglD-deficient cells formed larger-yet-less-intense bFA clusters (**Figure 3.13B,C**), suggesting that bFAs in the absence of CglD are considerably more diffuse and misshapen. These bFA clusters in Δ*cglD* cells were also more prone to slippage, i.e. slight shifts in anchored position relative to the substratum, than WT cells (**Figure 3.13A**), suggesting an inefficient engagement of the bFA with the substratum in the absence of integrin-like CglD.

To achieve high temporal and spatial resolution, we further confined our AglZ-YFP-tracking analysis to clusters along the ventral plane of cells using total internal reflection fluorescence microscopy (TIRFM)(Faure *et al.*, 2016; Islam *et al.*, 2023) (**Figure 3.14**). While Glt complexes were found to traffic at equivalent speeds in both WT and Δ*cglD* cells (**Figure 3.13D**), complexes in the latter cells were trafficked at a higher frequency (**Figure 3.13E**) and were less stable (**Figure 3.13F**). Moreover, in the absence of CglD, fewer Glt complexes were found to traffic exclusively from the leading to the lagging cell poles, with more instead

demonstrating oscillatory behaviour with multiple changes in trafficking direction (**Figure 3.13G**).

Taken together, these data indicate that while CglD is not required for bFA formation, the β-integrin-like protein has a profound impact on the stability of bFA clusters needed for efficient gliding motility in *M. xanthus*.

Table 3.1 GltD (aa 800-1218)-GST pulldowns

Ensembl Gene ID	Gene Symbol	Accession	Description	Coverage [%]
MXAN_0962	*cglD*	Q1DDQ0	Putative **lipoprotein [OS=Myxococcus xanthus DK 1622]**	33
MXAN_1623	*MXAN_1623*	Q1DBU8	peptidase, M16 (pitrilysin) family [OS=Myxococcus xanthus DK 1622]	29
MXAN_1624	*MXAN_1624*	Q1DBU7	peptidase, M16 (pitrilysin) family [OS=Myxococcus xanthus DK 1622]	27
MXAN_1994	*rpsI*	Q1DAU4	30S ribosomal protein S9 [OS=Myxococcus xanthus DK 1622]	42
MXAN_2540	*gltA*	Q1D9B4	Uncharacterized **protein [OS=Myxococcus xanthus DK 1622]**	27
MXAN_2674	*MXAN_2674*	Q1D8Y2	Uncharacterized protein [OS=Myxococcus xanthus DK 1622]	51
MXAN_2703	*MXAN_2703*	Q1D8V3	putative cAMP phosphodiesterases class-II [OS=Myxococcus xanthus DK 1622]	31
MXAN_2728	*MXAN_2728*	Q1D8S8	putative NADH dehydrogenase I, G subunit [OS=Myxococcus xanthus DK 1622]	27
MXAN_2736	*MXAN_2736*	Q1D8S0	Uncharacterized protein [OS=Myxococcus xanthus DK 1622]	41
MXAN_3160	*MXAN_3160*	Q1D7L0	peptidase, M13 (neprilysin) family [OS=Myxococcus xanthus DK 1622]	32
MXAN_3581	*MXAN_3581*	Q1D6F2	Peptidyl-dipeptidase A [OS=Myxococcus xanthus DK 1622]	34
MXAN_3777	*guaB*	Q1D5W4	inosine-5'-monophosphate dehydrogenase [OS=Myxococcus xanthus DK 1622]	43

MXAN_3830	*MXAN_3830*	Q1D5R1	Uncharacterized protein [OS=Myxococcus xanthus DK 1622]	24
MXAN_4635	*MXAN_4635*	Q1D3H2	Uncharacterized protein [OS=Myxococcus xanthus DK 1622]	21
MXAN_4637	*MXAN_4637*	Q1D3H0	Uncharacterized protein [OS=Myxococcus xanthus DK 1622]	96
MXAN_4869	*gltE* ***(agIT)***	Q1D2U6	adventurous **gliding motility protein AglT [OS=Myxococcus xanthus DK 1622]**	24
MXAN_4894	*groES*	Q1D2S2	10 kDa chaperonin [OS=Myxococcus xanthus DK 1622]	41
MXAN_4895	*groEL*	Q1D2S1	60 kDa chaperonin 2 [OS=Myxococcus xanthus DK 1622]	70
MXAN_5040	*MXAN_5040*	Q1D2C8	Aldehyde dehydrogenase family protein [OS=Myxococcus xanthus DK 1622]	46
MXAN_5152	*crdB*	Q1D218	OmpA family protein [OS=Myxococcus xanthus DK 1622]	38
MXAN_5344	*rpsB*	Q1D1H9	30S ribosomal protein S2 [OS=Myxococcus xanthus DK 1622]	37
MXAN_5756	*tolB*	Q1D0D0	Protein TolB [OS=Myxococcus xanthus DK 1622]	23
MXAN_5933	*MXAN_5933*	Q1CZV3	peptidase, m48 (ste24 endopeptidase) family [OS=Myxococcus xanthus DK 1622]	36
MXAN_6106	*fibA*	Q1CZD2	matrix-associated zinc metalloprotease FibA [OS=Myxococcus xanthus DK 1622]	28
MXAN_6299	*pyk*	Q1CYU9	pyruvate kinase [OS=Myxococcus xanthus DK 1622]	35
MXAN_6337	*MXAN_6337*	Q1CYR1	putative isocitrate dehydrogenase, NAD-dependent [OS=Myxococcus xanthus DK 1622]	34
MXAN_6487	*MXAN_6487*	Q1CYB4	Outer membrane efflux protein domain protein	32

			[OS=Myxococcus xanthus DK 1622]	
MXAN_6516	*ahcY*	Q1CY84	Adenosylhomocysteinase [OS=Myxococcus xanthus DK 1622]	46
MXAN_6660	*MXAN_6660*	Q1CXU6	Uncharacterized protein [OS=Myxococcus xanthus DK 1622]	34
MXAN_6720	*MXAN_6720*	Q1CXN6	Putative lipoprotein [OS=Myxococcus xanthus DK 1622]	21

Full table in annex I.

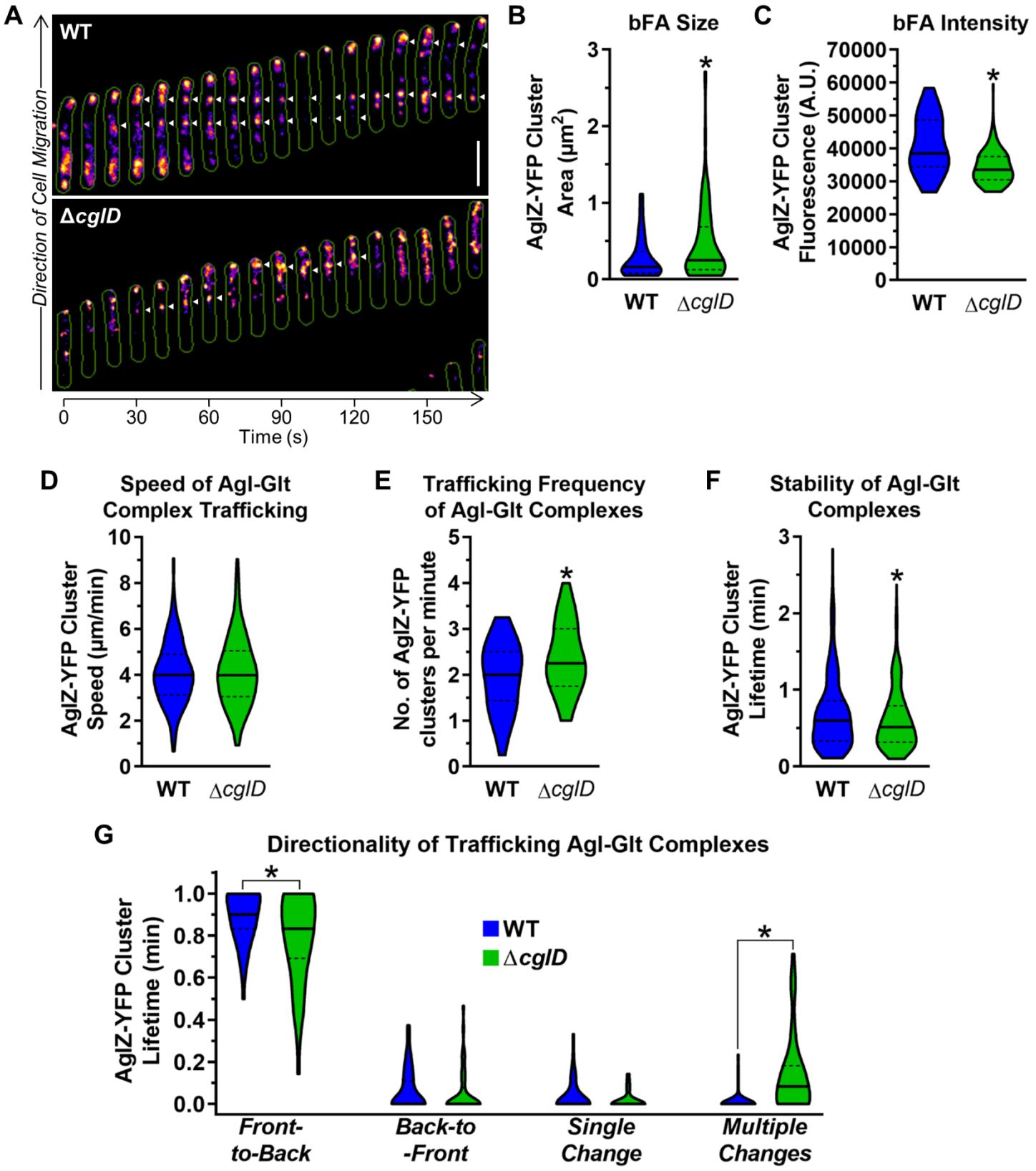
A
WT
ΔcglD
Direction of Cell Migration
0
30
60
90
120
150
Time (s)
B
bFA Size
AglZ-YFP Cluster Area (μm²)
WT
ΔcglD
C
bFA Intensity
AglZ-YFP Cluster Fluorescence (A.U.)
WT
ΔcglD
D
Speed of Agl-Glt Complex Trafficking
AglZ-YFP Cluster Speed (μm/min)
WT
ΔcglD
E
Trafficking Frequency of Agl-Glt Complexes
No. of AglZ-YFP clusters per minute
WT
ΔcglD
F
Stability of Agl-Glt Complexes
AglZ-YFP Cluster Lifetime (min)
WT
ΔcglD
G
Directionality of Trafficking Agl-Glt Complexes
AglZ-YFP Cluster Lifetime (min)
WT
ΔcglD
Front-to-Back
Back-to-Front
Single Change
Multiple Changes

Figure 3.13: CglD deficiency impacts numerous bFA properties.

(A) Fluorescence microscopy montage of gliding cells indicating bFA positions (*white arrowheads*) via AglZ-YFP fluorescence.
(B) Violin plot of bFA cluster size in WT and Δ*cglD* cells (n = 45 and 123, respectively).
(C) Violin plot of bFA cluster intensity in WT and Δ*cglD* cells (n = 45 and 123, respectively).
(D) Speed of Agl–Glt complex trafficking via TIRFM (of AglZ-YFP) on chitosan-coated glass surfaces in PDMS microfluidic chambers for WT and Δ*cglD* (n = 259 and 253 clusters, respectively) strains.
(E) Frequency of trafficking AglZ-YFP complexes via TIRFM (of AglZ-YFP) on chitosan-coated glass surfaces in PDMS microfluidic chambers for WT and Δ*cglD* (n =44 and 43 cells, respectively) strains.
(F) Stability of trafficking Agl–Glt complexes via TIRFM (of AglZ-YFP) on chitosan-coated glass surfaces in PDMS microfluidic chambers for WT and Δ*cglD* (n = 333 and 346 clusters, respectively) strains.
(G) Directionality of trafficked Agl–Glt complexes via TIRFM (of AglZ-YFP) on chitosan-coated glass surfaces for WT and Δ*cglD* (n = 44 and 43 cells, respectively) strains. “Front” and “back” are defined as cell poles with high and low AglZ-YFP fluorescence intensity, respectively. For Panels B–G, the lower and upper boundaries of the plots correspond to the minimum and maximum values of the dataset, with the 25th and 75th percentiles displayed (*dashed black lines*). The median (*solid black line*) of each dataset is indicated. Asterisks (*) denote datasets displaying statistically significant differences in distributions ($p < 0.05$) between various strains or conditions, as determined via unpaired two-tailed Mann–Whitney tests.

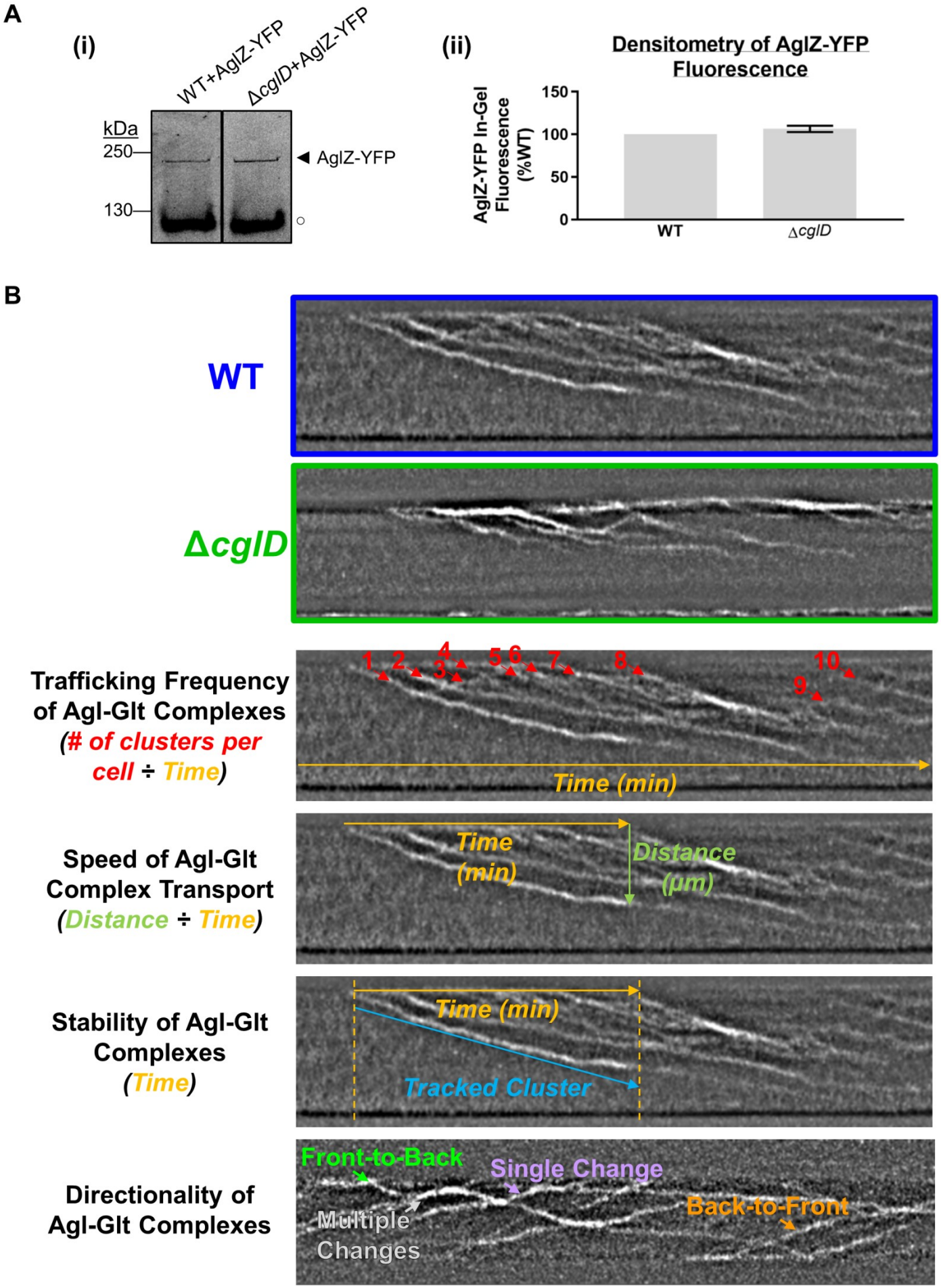
A
(i)
WT+AglZ-YFP
ΔcglD+AglZ-YFP
kDa
250
130
AglZ-YFP
(ii)
Densitometry of AglZ-YFP Fluorescence
AglZ-YFP In-Gel Fluorescence (%WT)
150
100
50
0
WT
ΔcglD
B
WT
ΔcglD
Trafficking Frequency of Agl-Glt Complexes
(# of clusters per cell ÷ Time)
1
2
3
4
5
6
7
8
9
10
Time (min)
Speed of Agl-Glt Complex Transport
(Distance ÷ Time)
Time (min)
Distance (μm)
Stability of Agl-Glt Complexes
(Time)
Time (min)
Tracked Cluster
Directionality of Agl-Glt Complexes
Front-to-Back
Single Change
Back-to-Front
Multiple Changes

Figure 3.14. State of AglZ-YFP in WT vs Δ*cglD* cells.
(A) In-gel fluorescence scan (*panel i*) and densitometry analysis (*panel ii*) of AglZ-YFP levels in WT vs. Δ*cglD* crude-cell lysates resolved via SDS-PAGE. Fluorescence levels were analyzed across five biological replicates and are displayed ± SEM. This difference was not statistically significant, as determined via Wilcoxon signed-rank test performed relative to a reference value of 100 (*p* value = 0.1875).
(B) Kymograph of AglZ-YFP localization in *M. xanthus* cells on chitosan-coated PDMS microfluidic chambers via TIRFM. Arrows in orange denote sequential kymograph slices over time. Arrows in cyan indicate positions of trafficked Agl–Glt clusters in the cell. The manners in which various fluorescent-cluster tracking data (see Figure 3.13D-G in the main text) were obtained have been indicated in the example images.

3.4 DISCUSSION

Based on the data presented in our investigation on *M. xanthus* CglD (from a unicellular bacterium that exhibits true multicellular physiology), this protein possesses the hallmarks of a cell-surface β-integrin-like lipoprotein that is directly involved in gliding motility via bFA stabilization. This finding is supported by multiple lines of evidence :

(i) CglD possesses β-integrin-like architecture, including a VWA domain (commonly found in ECM-interacting proteins), and also EGF-like repeats within a Cys-rich stalk
(ii) CglD is a surface-localized lipoprotein that co-elutes with members of the gliding motility apparatus
(iii) In the absence of CglD, trafficking motility complexes become poorly immobilized, consistent with non-optimal adherence of the complexes to the substratum. Furthermore, without CglD, these trafficking complexes are severely compromised for the transport of surface-associated cargo.
(iv) Cells lacking CglD display destabilized bFA clusters that oscillate more frequently, dissociate quicker, and display more diffuse signal patterns.

Below, we discuss potential CglD-modulated gliding complex adhesion as well as future avenues of investigation.

3.4.1 CglD-like β-integrin proteins

The presence of α/β-integrin-mediated adhesion machinery on the eukaryotic tree of life is an ancient occurrence, pre-dating the appearance of unikonts, i.e. eukaryotic cells with

a single flagellum, believed to be the ancestor of all metazoans (Sebé-Pedrós *et al.*, 2010). The long-standing evolutionary importance of these proteins is consistent with their capacity to bind not only ECM components in metazoans, but also numerous non-ECM ligands (LaFoya *et al.*, 2018).

Integrins were once thought to be exclusive to metazoans, but were later identified in so-called "lower" eukaryotes (Kang *et al.*, 2021; Sebé-Pedrós *et al.*, 2010). Exceptionally, the lone detection of a (β) integrin in a prokaryote (cyanobacterium *Trichodesmium erythraeum*) was attributed to a horizontal gene-transfer event (Sebé-Pedrós *et al.*, 2010). However, from our detection herein of β-integrin-like CglD homologues in a diverse selection of δ-proteobacteria, these data would support an ancestral function/role for β-integrin-like proteins in δ-proteobacterial physiology. It can be envisioned that such proteins could also be involved in adhesion to various substrata and/or other cells, but the link with gliding-motility machinery may only have developed past the divergence of the suborder Cystobacterineae, as the species therein encode CglD in addition to the full complement of known gliding machinery proteins (i.e. GltABCDEFGHIJK+CglB).

3.4.2 β-integrin-like CglD as a mechanosensor and mechanotransducer for bFA initiation & stabilization

Integrins in eukaryotic cells have long been known to serve as biomechanical sensors of the local environment, being able to distinguish between different substratum rigidities, and in turn transmitting this information via an outside–in mechanism to effect internal cellular changes that regulate adhesion and eukaryotic cell motility (Kechagia *et al.*, 2019). This process is very quick, with integrins being able to detect force and transmit a signal to augment adhesion in under a second (Strohmeyer *et al.*, 2017). Herein, we have shown that substratum polymer alignment and rigidity is a mitigating factor for CglD-deficient cells, whereas WT cells are more adaptable and highly motile. This would be consistent with β-integrin-like CglD having a role in distinguishing between soft/hard matrices, akin to the scenario with eukaryotic integrins.

As traction forces are applied on nascent eukaryotic integrin adhesions, this leads to integrin clustering and the maturation of eFAs (Kechagia *et al.*, 2019). In the absence of CglD, we observed gliding *M. xanthus* cells to be defective for bFA clustering and stability, with the bFA signal in Δ*cglD* cells being less intense, more diffuse, shorter lived, and highly oscillatory.

Thus, in addition to its mechanosensory capacity, our data support a mechanotransductory role for CglD in initiating and maintaining AglRQS directed motorized transport at bFA sites.

3.4.3 Potential CglD interactions with the gliding apparatus

Mechanosensory and mechanotransductory functions for CglD would heavily implicate interactions of this β-integrin-like protein with the OM module of the trans-envelope gliding apparatus, considering CglD is an OM lipoprotein with no discernible OM-spanning domains. This contention is supported by the analysis of mass spectrometry data from GST-tagged pulldowns in broth-grown cells; through use of a GST-tagged C-terminal domain of periplasmic GltD as bait, periplasmic GltE, but more importantly OM CglD and GltA were reproducibly pulled down. These data could indicate that in a non-surface-engaged state, CglD may already associate with members of the Glt OM module. Functional analogies exist for eukaryotic integrin proteins: when not engaged/activated, integrins are believed to adopt a "resting state" conformation that does not fully associate with their ligands. However, upon binding of the target ligand, integrins undergo a conformational change to an "activated state" in which the VWA domain interacts with the ligand, changing the conformation of the ectodomains into an unbent form. In turn, this transmits a signal across the cytoplasmic membrane to the tail domain of each integrin subunit, leading to activation of multiple cytoplasmic proteins and eFA formation. Interestingly, integrins are receptors involved in cellular adhesion and COMP in humans has been found to affect cellular attachment. Moreover, COMP-based mediation of cell attachment is carried out through interaction with α5β1 integrin in the presence of Ca^{2+} ions (Chen *et al.*, 2005). Such COMP–integrin interactions have been proposed to be mediated via COMP binding of the MIDAS motif of β-integrin subunits (Arnaout *et al.*, 2007; Xiong *et al.*, 2002).

As such, the integrated Ca^{2+}-binding COMP domain of CglD may promote interaction with an integrin-like protein. As the presence/absence of Ca^{2+} or Glt OM-module proteins did not alter its own conformational stability in broth-grown cells, this may indicate that the CglD COMP domain may be responsible for interactions with the portions of the Glt OM-module, most likely CglB (as the latter is structurally homologous with an integrin αI-domain VWA module)(Islam *et al.*, 2023); however, such an interaction would be favoured in a gliding cell in which the substratum has been actively engaged by CglD in concert with CglB-GltABHK. This in turn would result in stabilization of the bFA, allowing the anchored gliding motility complexes accumulated at this site to promote efficient single-cell gliding motility.

3.4.4 Potential role for the glycocalyx in bFA activity

The glycocalyx of eukaryotic cells has been shown to greatly impact integrin-mediated cell adhesion and force transduction. The mechanical resistance of this (protein-impregnated) cell-surface polysaccharide layer can regulate the clustering of integrins(Paszek *et al.*, 2009; Paszek *et al.*, 2014). Intriguingly, for almost a century myxobacterial single-cell gliding motility has been associated with a so-called "slime" polysaccharide (Jahn, 1924). Though the phase-bright nature of trails commonly found behind gliding myxobacteria on agar pads was discovered to simply be due to physical depressions left behind in the agar matrix (Gloag *et al.*, 2016), a polymeric substance left behind gliding cells was still detected on rigid substrata (Ducret *et al.*, 2012). This deposited polymer is distinct from the known secreted exopolysaccharide (EPS), biosurfactant polysaccharide (BPS), and major spore coat (MASC) polysaccharide, as well as the LPS-capping O-antigen polysaccharide (Ducret *et al.*, 2012; Islam *et al.*, 2020; Saïdi *et al.*, 2021) of *M. xanthus*. Moreover, gliding *M. xanthus* cells detected over slime trails were suggested to be more strongly adhered to the substratum (Ducret *et al.*, 2012). In line with known eukaryotic integrin function and the data presented herein, an important role of slime with respect to *M. xanthus* gliding may thus be to facilitate CglD-mediated bFA clustering to support efficient single-cell gliding motility. A role for the *M. xanthus* glycocalyx in regulating CglD-dependent gliding promotion would also be consistent with our previous data showing that BPS$^-$ cells, which have a more compact cell-surface glycocalyx, are hyper-polymertropic (Saïdi *et al.*, 2021); they are exceptionally responsive (in a gliding-dependent manner (Fontes & Kaiser, 1999)) to mechanical alignment of polymers in compressed substrata, exhibiting preferential swarm expansion along the aligned polymers.

3.5 CONCLUSION

Ultimately, the findings in this investigation reinforce and highlight the exciting parallels between bFA-mediated prokaryotic gliding and eFA-mediated eukaryotic motility. In turn, this opens possibilities for understanding the evolution of complexity in integrin-mediated cell translocation and its contribution to the development of true multicellular physiology across biological kingdoms.

3.6 MATERIALS AND METHODS

3.6.1 Bacterial cell culture

Strains of *M. xanthus* (Table 3.2) were grown at 32 °C in CYE liquid medium (1% Bacto Casitone Peptone, 0.5% Yeast Extract, 0.1% $MgCl_2$, 10mM MOPS [pH 7.4]) with shaking (220 rpm) or on CYE medium solidified with 1.5% (w/v) agar. Cell resuspensions were carried out in TPM buffer (10 mM Tris-HCl [pH 7.6], 8 mM $MgSO_4$, 1 mM KH_2PO_4).

3.6.2 Phenotypic Analyses

For all phenotypic analyses, 5 µL of cells resuspended in TPM (at an optical density at 600 nm [OD_{600}] of 5.0) were spotted on various substrata. Gliding-flare observations were acquired with an Olympus SZX16 stereoscope equipped with an ILLT base and UC90 4K camera, using CellSens software (Olympus). For gliding-flare analysis, cells in TPM were spotted on CYE 1.5% (w/v) agar, 1.5% (w/v) carrageenan, or 0.6% (w/v) gellan plates and incubated at 32 °C for 7 h. Flares were imaged using the SDF PLAPO 2×PFC objective, with 6.3× zoom, and a fully-open aperture. The illumination wheel was set halfway between the brightfield and empty slots for optimal cross-illumination of the sample. Image acquisition was carried out using linear colour, 50 ms acquisition time, 16.6 dB gain, and a white balance calibrated against an empty zone of the plate.

For T4P-dependent swarm-spreading and fruiting body analysis, images were acquired with an Olympus SZ61 stereoscope with an ILLT base. Swarm spreading was captured at 0.67× zoom, using dark-field illumination, while fruiting bodies were captured at 32× zoom, using full oblique illumination. For swarm-spreading, cells were spotted on CYE 0.5% (w/v) agar plates, while for fruiting body formation, cells were spotted on CF (0.15% casitone [w/v], 10 mM MOPS, 1 mM KH_2PO_4, 8 mM $MgSO_4$, complemented with 0.02% $(NH_4)_2SO_4$ and 2% $Na_3C_6H_5O_8$), with 1.5% or 0.5% (w/v) agar for phenotype plates. Swarm-spreading and fruiting-body plates were imaged after incubation for 72 h at 32 °C. Swarm diameters were measured using CellSens software.

Table 3.2. Bacterial strains used in this study.

Strain	Genotype/ Description	Construction	Source or Reference
DZ2	WT	Wild type	(Campos & Zusman, 1975; Islam *et al.*, 2023)
TM913	Δ*cglB*	DZ2 Δ*cglB*	(Islam *et al.*, 2023)
TM490.1	Δ*cglD*	DZ2 Δ*cglD*	This work
TM600	Δ*gltK*	DZ2 Δ*gltK* (pBJΔ*gltK*)	(Luciano *et al.*, 2011)
TM603	Δ*gltB*	DZ2 Δ*gltB* (pBJΔ*gltB*)	(Luciano *et al.*, 2011)
TM606	Δ*gltA*	DZ2 Δ*gltA* (pBJΔ*gltA*)	(Luciano *et al.*, 2011)
TM570	Δ*gltC*	DZ2 Δ*gltC* (pBJΔ*gltC*)	(Luciano *et al.*, 2011)
TM646	Δ*gltJ*	DZ2 Δ*gltJ*	(Islam *et al.*, 2023)
TM731	Δ*gltI*	DZ2 Δ*gltI*	(Islam *et al.*, 2023)
TM149	Δ*gltH*	DZ2 Δ*gltH* (pBJΔ*gltH*)	(Luciano *et al.*, 2011)
TM135	Δ*gltG*	DZ2 Δ*gltG* (pBJΔ*gltG*)	(Luciano *et al.*, 2011)
TM136	Δ*gltF*	DZ2 Δ*gltF* (pBJΔ*gltF*)	(Luciano *et al.*, 2011)
TM148	Δ*gltE*	DZ2 Δ*gltE* (pBJΔ*gltE*)	(Luciano *et al.*, 2011)
TM142	Δ*gltD*	DZ2 Δ*gltD* (pBJΔ*gltD*)	(Luciano *et al.*, 2011)
TM293	Ω*pilA*	DZ2 Ω*mxan_5783* (Tet^R cassette insertion)	(Saïdi *et al.*, 2021)
SI7	Ω*pilA* + Δ*cglB*	DZ2 Δ*cglB* Ω*mxan_5783* (Tet^R cassette insertion)	(Islam *et al.*, 2023)
TM492	Ω*pilA* + Δ*cglD*	DZ2 Δ*cglD* Ω*mxan_5783* (Tet^R cassette insertion)	This work
TM829	WT + *aglZ-YFP*	DZ2 pBJ*AglZ-YFP*	(Mignot *et al.*, 2007)
TM1181	Δ*cglB* + *aglZ-YFP*	TM913 *aglZ-YFP* (pBJ*AglZ-YFP*)	(Islam *et al.*, 2023)
TM1219	Δ*cglD* + *aglZ-YFP*	TM490 *aglZ-YFP* (pBJ*AglZ-YFP*)	This work
SI101	WT + *OMss-mCherry*	DZ2 OMss-mCherry (pSWU19-OMss-mCherry)	This work
SI102	Δ*cglB* + *OMss-mCherry*	TM913 OMss-mCherry (pSWU19-OMss-mCherry)	This work
SI103	Δ*cglD* + *OMss-mCherry*	TM490 OMss-mCherry (pSWU19-OMss-mCherry)	This work

3.6.3 Rheometry and cell detachment

A volume (1 mL) of molten CYE 1.5% (w/v) agar was deposited in 35 mm-diameter FluoroDish (World Precision Intruments) as a substratum for *M. xanthus* cells. After

solidification of the medium, cells from overnight cultures of WT/Δ*cglD*/Δ*cglB* expressing OMss-mCherry were resuspended in TPM (OD_{600} 5.0), with 5 µL deposited on the agar matrix followed by incubation at 32 °C for 4 h. The inoculated FluoroDishes were then loaded in the rheometer (Anton Paar MCR302), with this setup combined with a confocal microscope (Leica SP8). Glycerol (60%, 1.5 mL) was added to the FluoroDish between the rotating foot of the rheometer and the swarm. Fluorescence images are captured by the confocal microscope (mCherry detection, laser: 552 nm, 10× magnification, HCX PL APO CS 10×/0.40 dry objective) prior to rotation of the rheometer (i.e. Shear Force: 0), and after each rotation speed increase to follow swarm disintegration. Images at different shear forces were then analysed with Fiji to measure the fluorescent signal, with readings normalized to that detected at "0" shear force for each strain.

3.6.4 Polymertropism response

Aspect ratio (AR) analyses were performed using previously-described methods(Fontes & Kaiser, 1999; Lemon *et al.*, 2018; Lemon *et al.*, 2017; Saïdi *et al.*, 2021). In brief, *M. xanthus* cells were grown overnight in CYE medium at 28 °C to a density of approximately 5×10^8 cells/mL. Subsequently, the cells were sedimented, (4 000 × *g*, 10 min), resuspended in CYE broth to a density of 5×10^9 cells/mL, and used to inoculate (4 µL) compressed and uncompressed round 85-mm CTTYE (1% casitone [w/v], 2% yeast extract [w/v], 10 mM Tris-HCl [pH 8.0], 1 mM KH_2PO_4, 8 mM $MgSO_4$) agar plates. To compress the agar, a section of Tygon tubing (outer diameter: 5.56 mm, length: 1 cm) was inserted against the plate wall. The cells on these plates were inoculated at a distance of 43 mm from the inserted tubing. Following incubation at 30 °C for 24, 52, 90, 120, and 144 hours, the perimeters of the colonies were marked at each time interval. The aspect ratio (AR) of each swarm was calculated for each time point by dividing the colony width by the colony height. A round swarm would yield an AR ≈ 1, while a flattened swarm would have an AR > 1. Linear best-fit lines were determined for each replicate dataset, and the AR/time ratio was calculated. Average slope values were calculated for each strain and normalized to the WT strain.

3.6.5 SDS-PAGE, in-gel fluorescence, and Western immunoblotting

To probe for AglZ-YFP in-gel fluorescence, 10 mL cultures of WT and Δ*cglD* cells expressing AglZ-YFP were grown overnight in CYE broth with shaking (220 rpm) at 32 ºC. Cells from these cultures were then sedimented via centrifuge (5000 × *g*, 5 min, room temperature), followed by decanting of the supernatant and resuspension of the cells in 10 mL of TPM via vortex. The OD_{600} of each TPM resuspension was determined, followed by sufficient removal of volume so that resuspension of the removed cells in 500 µL would yield a final OD_{600} of 2.0; these removed cell volumes were thus sedimented as above, resuspended in 500 µL of 1× Laemmli SDS-PAGE sample buffer lacking reducing agent, then heated at 65 ºC (30 min). From these samples, 20 µL of equilibrated cell resuspensions (along with 10 µL of pre-stained protein ladder) were loaded on a 10-well 8% polyacrylamide gel, and resolved via SDS-PAGE at 80 V (45 min) then 120 V (75 min). These gels were then scanned with a Typhoon FLA9500 fluorescence scanner (GE Healthcare), using the 473-nm laser to excite AglZ-YFP, and the BPB1 filter (PMT 800) to capture in-gel fluorescence. Bands corresponding to the pre-stained ladder were excited with the 635-nm laser and detected using the LPR filter (PMT 800). Fluorescence intensity of the detected AglZ-YFP bands was obtained using the "plot lanes" function of ImageJ, after which the area under the curve was determined. This signal was normalized to the faster-migrating autofluorescent band in the same lane. These values were subsequently expressed as a percentage of the WT signal for each biological replicate.

To detect CglD from whole-cell lysates, cells were harvested after overnight growth, washed in TPM buffer, and resuspended at an OD_{600}) of 1.0 in 1× Laemmli SDS-PAGE sample buffer containing 5% β-mercaptoethanol. Samples were then boiled for 10 min, and 20 µL of each sample were loaded onto 10-well 1-mm 10% acrylamide gels. Sample resolution through gels was conducted in two stages: 45 min at 80 V through the stacking gel, followed by 105 minutes at 120 V through the resolving gel. Resolved samples were subsequently transferred to nitrocellulose membranes via electroblotting at 100 V for 60 min. Membranes were rinsed in Tris-buffered saline (TBS), blocked with TBS containing 5% milk powder (w/v) at 4 °C for 30 min, then incubated overnight with gentle rocking at 4 °C in TBS containing 0.05% Tween 20 (v/v), 5% milk powder (w/v), and a 1:10 000 dilution of the primary pAb α-CglD anti-serum. The next day, blots were washed twice in TBS with 0.05% Tween 20 and then incubated with a goat α-rabbit secondary antibody conjugated to horseradish peroxidase

(Biorad) at a 1:5 000 dilution in TBS with 0.05% Tween 20 and 5% milk for 60 min. After two additional washes in TBS with 0.05% Tween 20, the blots were developed using the SuperSignal West Pico chemiluminescence substrate (Thermo) and captured using an Amersham Imager 600 machine.

3.6.6 Single-cell microscopy analysis

For phase-contrast microscopy on pads, cells were cultured overnight at 32 °C, washed, and resuspended in TPM buffer to an OD_{600} of 2.0. Resuspended cells were then spotted (3 μL) onto a glass coverslip, atop which a pad made of 1.5% agarose (w/v) in TPM buffer was overlaid. Cells were left to associate with the pad for 5 min before imaging at 32 °C using a Zeiss Axio Observer 7 microscope with a 40× objective and an Axiocam 512 camera.

For phase-contrast microscopy on chitosan devices, cells were grown under the same conditions but resuspended in TPM buffer containing $CaCl_2$ (2 mM). Subsequently, 1 mL of the cell suspension was loaded into the device. After a brief incubation period, the cells were washed with TPM buffer containing $CaCl_2$ before imaging. Similar to the previous setup, the cells were allowed to settle for 15 min before imaging at 32 °C as above. Calculation of cell gliding speeds was performed using the MicrobeJ plugin for FIJI (Ducret *et al.*, 2016), while reversal events (switching of cell gliding direction) were manually counted.

To probe for AglZ-YFP cluster fluorescence on agarose pads, imaging was conducted using an in-house-made aluminum monolithic microscope equipped with a 1.49 NA/100× objective (Nikon). Imaging was performed with an iXon DU 897 electron-multiplying charge-coupled device (EMCCD) camera (Andor Technology), with illumination achieved using a 488-nm diode-pumped solid-state (DPSS) laser (Vortran Stradus). Sample positioning was carried out using a P611 three-axis nanopositioner (Physik Instrument). LabView (National Instruments) was used to program instrument control and integrate control of all components. From these datasets, kymographs were generated using the “Kymograph Builder" function in FIJI. Manual selection of AglZ-YFP clusters was performed, followed by tracking using the MTrackJ FIJI plugin.

To achieve high temporal resolution for real-time AglZ-YFP trafficking, TIRFM was carried out as previously described (Faure *et al.*, 2016; Islam *et al.*, 2023) using chitosan-coated PDMS microfluidic channels. In summary, cells were injected into the chamber and allowed to adhere for 30 min without flow. Any unadhered cells were subsequently removed

by manually injecting TPM. TIRFM was performed on the attached cells using an inverted microscope equipped with a 100× oil-immersion Plan-Achromat objective and a closed-loop piezoelectric stage for active autofocus. AglZ-YFP was excited using a 488-nm laser, and the emission was collected by the objective, passed through a dichroic mirror and band-pass filters, and captured by an EMCCD camera. To capture real-time images of the YFP channel, a total of 500 images were taken at a rate of 20 Hz (Faure *et al.*, 2016; Islam *et al.*, 2023).

3.6.7 Chitosan coating for single-cell analyses

PDMS microfluidic devices were fabricated using a mold. A PDMS mixture was prepared by combining the polymer and crosslinker (in a ratio of 10:1) using the Sylgard 184 Microchem kit. The mixture was thoroughly mixed and then centrifuged for 5 min (500 × *g*) to remove any trapped air bubbles. The prepared PDMS mixture was then poured onto the mold. The mold was placed under vacuum for 20 min to remove any remaining micro air bubbles from the mixture. Afterward, the mold with the PDMS was incubated in an oven at 65 °C for 2 h. Once the PDMS device was cured, it was carefully separated from the mold, and small holes with a diameter of 1.2 mm were created as entry and exit points. The PDMS devices were then cleaned using ethanol and water. Glass coverslips (for mounting the PDMS devices) were cleaned using the same method and were plasma-activated for 30 min using the Basic Plasma Cleaner (Harrick Plasma) on the "HI" setting. The PDMS devices were also plasma-activated for 2 min on the "LOW" setting. Following activation, the coverslips and PDMS devices were carefully aligned and pressed together. The assembled device was then incubated overnight at 65 °C, then stored at room temperature until needed. Prior to seeding the device with cells, chitosan solution (100 mg chitosan powder [shrimp, <75% deacetylated, Sigma], dissolved in 10 mL dilute acetic acid, pH 4.0) containing increasing concentrations of $CaCl_2$ was injected into the channel(s) to be used, allowed to adsorb for 30 min, then washed with TPM (1 mL).

To compare the effect of Ca^{2+} on gliding in the presence/absence of CglD, borosilicate glass microscope cover slips (75 × 25 × 0.17 mm) were first rinsed with 95% EtOH and ddH_2O, dried under a stream of N_2 gas, then treated in a plasma cleaner for 10 min to generate silanol groups on the glass surface to improve chitosan adsorption. Each coverslip was then fixed atop a spin-coating pedestal with double-sided tape, after which chitosan solutions (100 mg chitosan dissolved in 10 mL dilute acetic acid, pH 4.0) supplemented with 0, 0.5, or 2.0 mM

$CaCl_2$ were spotted atop the pedestal-mounted coverslip, followed by spinning at 2000 rpm for 5 min. Coverslips were then carefully removed from the pedestal and dipped into dilute acetic acid solution (pH 4.0) using tweezers to remove all excess deposited chitosan, leaving behind only chitosan chains directly adsorbed to the glass surface, then stored at room temperature. Prior to inoculation with cells, 1 mL of ddH_2O was added to each coverslip to rehydrate the chitosan. After 30 min, excess water was removed via decanting, then 5 µL of cells resuspended in TPM (OD_{600} 0.5) were added to the centre of each rehydrated coverslip, then covered with a square coverslip and left to adhere for a minimum of 2 h at room temperature. Cells were then imaged on a Nikon Eclipse TE2000 microscope (40× magnification, DIA illumination) at 32 °C for 5 min, with images acquired at 30-s intervals.

3.6.8 Testing of CglD susceptibility to Proteinase K and DTT

Susceptibility to Proteinase K was assayed as previously described(Islam *et al.*, 2023). In brief, cells from overnight cultures were resuspended to an OD_{600} of 2.0 in 600 µL of TPM buffer. Afterwards, 6 µL of Proteinase K (New England Biolabs) was added to the cell resuspension. At each designated time point, 100 µL of digestion reaction volume were removed, mixed with trichloroacetic acid (10% final concentration) to halt digestion, and kept on ice. Digestion aliquots were then twice resuspended in 1 mL acetone and sedimented at 16 000 × *g* (5 min), then left uncapped overnight in a fumehood to allow for residuel acetone to evaporate. Precipitated protein pellets were then resuspended in 100 µL of 1× Laemmli buffer with β-mercaptoethanol. Samples were subsequently boiled and processed for Western blot analysis as outlined above.

To probe for disulfide-based denaturation differences dependent on Glt OM-complex mutant background, Samples were prepared by growing overnight cultures and resuspending cells in TPM buffer at an OD_{600} of 4.0 with various concentrations of DTT, ranging from 0 to 5 mM. The samples were then mixed with 2× Laemmli buffer lacking reducing agent to reach a final OD_{600} of 2.0, followed by boiling and processing for Western blot analysis as outlined above.

3.6.9 Phylogeny and gene co-occurrence

Sixty-one-order Myxococcales genomes, belonging to three suborders and nine families(Goldman *et al.*, 2006; Han *et al.*, 2013; Huntley *et al.*, 2011; Huntley *et al.*, 2013; Huntley *et al.*, 2012; Ivanova *et al.*, 2010; Li *et al.*, 2011; Müller *et al.*, 2013; Schneiker *et al.*, 2007; Sharma *et al.*, 2016a; Sharma *et al.*, 2018; Sharma *et al.*, 2016b; Sharma & Subramanian, 2017; Stevens *et al.*, 2014), in addition to 59 outgroup genomes (members from 32 non-Myxococcales Deltaproteobacteria, 4 α-, 6 β-, 9 γ-, 4 ε-proteobacteria, 2 Firmicutes, 1 Actinobacteria, and 1 FCB group organism) were selected for this study. To build a maximum-likelihood phylogenetic tree, gapless concatenated alignment of 26 housekeeping protein sequences (Sharma *et al.*, 2016b; Wu & Eisen, 2008) was subjected to RAxML with JTT Substitution Model and 100 bootstrap values (Stamatakis, 2006). Sequential distribution of gliding motility genes, i.e. *agl*, *glt* (M1, G1 and G2 clusters) (Luciano *et al.*, 2011) along with *cglB* (Nudleman *et al.*, 2005; Pathak & Wall, 2012; Rodriguez & Spormann, 1999) and *cglD* was identified within all 120 genomes under study using homology searching via tBLASTn and JackHMMER (HMMER 3.3.2 suite released in Nov. 2020)(Johnson *et al.*, 2010) with two iterative search rounds and an E-value cut-off of $1e^{-5}$. Visualization of the relative distribution of gliding motility proteins in the multi-protein phylogeny was done using iTol v6.5.3 (Letunic & Bork, 2016). The strip to the right of the phylogeny depicts the taxonomic classes (from top to bottom: Myxococcales, non-Myxococcales δ-proteobacteria, α-, β-, γ-, ε-proteobacteria, Actinobacteria, Firmicutes, and Fibrobacteres, respectively).

3.6.10 Tertiary structure homology detection and protein modeling

Structural homologues to CglD (MXAN_0962) were identified via fold-recognition analysis by HHpred (Zimmermann *et al.*, 2018) against protein structures in the PDB_mmCIF70 and PDB_mmCIF30 databases of structures deposited in the Protein Data Bank. Top hits were based on the highest probability scores. Tertiary structure modelling of CglD was carried out using the ColabFold pipeline to run AlphaFold with default settings (Jumper *et al.*, 2021; Mirdita *et al.*, 2022). The highest-confidence CglD model structure was used to generate structural alignments with known proteins using TM-align (Zhang & Skolnick, 2005). All structure figures were created with PyMol.

3.6.11 Traction force microscopy

To grow the various strains tested, cells were first recovered from a frozen stock via streaking on a CTTYE (1% peptone, 0.2% yeast extract, 10 mM Tris, 1 mM KH_2PO_4, and 8 mM $MgSO_4$, pH 7.6) 1.5% agar plate, incubated at 32 ºC. Vegetative cells were then used to inoculate a 10 mL CTTYE liquid culture in a flask, with shaking incubation overnight at 32 ºC.

For TFM imaging, the samples were prepared using 35 mm diameter Petri dishes with a glass bottom (Thermo Fisher, prod. #150682). The inner surface of the glass was plasma cleaned, treated with 2 vol.% 3-(Trimethoxysilyl)propyl methacrylate (TMSPMA) for 2 min, washed three times with pure ethanol, and dried(Herrick *et al.*, 2013). To generate the polyacrylamide (PAA) hydrogel substrate, a 0.25 mL PAA solution (18.8 µL 40% acrylamide, 7.5 µL 2% Bis, 0.222 mL DI water, 1.25 µL 10% ammonium persulfate solution, and 0.375 µL TEMED) was prepared. Suspended fluorescent particles (5 µL, FluoSpheres Carboxylate-Modified Microspheres, 0.04 µm, red-orange fluorescent (565/580), 5% solids) were also added to the mixture. For each substratum, 15 µL of the PAA solution was dispensed on the glass bottom of the petri dish, overlaid with a 12 mm diameter glass coverslip (Thermo Fisher 12CIR-1), and allowed to gelate for 30 min. Following gelation, the coverslip was gently removed and the substratum was soaked in chitosan solution (10 mg chitosan, dissolved in 3 mL 0.2 M acetic acid, and then diluted 1:50) for at least 45 min. The substratum was then washed three times by adding CTTYE and soaking it for ~10 min. Finally, all liquid was aspirated from the Petri dish, with excess residue carefully wicked away with a kimwipe.

Upon preparation of the substratum, 2 µL of *M. xanthus* cell suspension (OD_{550} 0.7) was added to the top of the gel matrix, with cells left to adhere for 10 min, followed by removal of excess liquid on top of the gel via wicking with a Kimwipe. Petri dishes were then covered again and incubated at 32 ºC for 1 h. Following incubation, a 12 mm diameter coverslip was added on top of the gel and gently compressed so that it was uniformly attached to the gel surface. A chamber was then created around the PAA gel in each Petri dish using a 2 mm-thick laser-cut acrylic spacer and a 22 mm × 22 mm glass coverslip. Lastly, the edges of this chamber were sealed with Valap (1/3 vaseline, 1/3 lanolin, and 1/3 paraffin by weight).

Images for TFM were captured with a commercial Nikon Ti-E microscope with Perfect Focus System (PFS) and Yokogawa CSU-21 spinning disk confocal. We used a Nikon 60× Apo Water Immersion objective with long working distance and an Andor Zyla 4.2 sCMOS camera. There was an extra 1.5× magnification through the base of the microscope, so the

total magnification of our images was 90×. In each acquisition, one brightfield image was recorded to observe the cells, followed immediately by a fluorescence acquisition using one laser (561 nm light) for the fluorescent particles. To prevent damage to the bacterial cells from the laser, laser power was kept low (10%). The time between sequential acquisitions was 15 s. Throughout the imaging process, the samples were kept at 25 ºC through use of a temperature-controlled cabinet.

Brightfield and laser images were analyzed separately. For the laser images, the slow drift was first removed via tracking the motion of the fluorescent particles in the substratum and measuring the mean velocity of the substratum as an intact solid body. This was followed by use of a band-pass filter to highlight the fluorescent particles. A custom PIV algorithm was then used to measure the displacement of the particles. Lastly, following established methods(Plotnikov *et al.*, 2014; Sabass *et al.*, 2008), traction was reconstructed from the displacement field of the gel. The same analysis method was used for analyzing both the dilute-cell and cell-layer samples.

The brightfield images were used to track the motion of individual cells in the dilute regime. The original images were processed, binarized, and segregated, so that the center of mass for each cell could be located. Cell motion was then tracked using the Matlab version of the Particle Tracking Velocimetry (PTV) code developed by Blair and Dufresne(Blair & Dufresne, 2023). Using the positions of the cells in every frame, we calculated their speeds. Through analysis of the defined rectangular area (14.7 μm wide and 22 μm long, with the long axis parallel to the cell body) centered around individual cells, the distribution of traction generated by single cells was measured. For cell layers, the motion of individual cells was no longer tracked. Regions for analyses were selected in which the cells were concentrated and formed a monolayer, with traction measurements recorded across the entire field of view.

3.6.12 Flow chamber construction and bead-force microscopy

For bead-force microscopy assays, AglZ-YFP-expressing WT and Δ*cglB* strains of *M. xanthus* were grown shaking in CYE broth overnight at 32 ºC to OD_{600} ~0.6., after which 1 mL of culture was sedimented (8000 rpm, 5 min). The pellet was resuspended in 400 μL TPM buffer. Flow chambers were constructed using two layers of double-sided tape, a 1 mm-thick microscope slide, and a 100 μm-thick glass cover slip (#1.5) to allow a final volume of approximately 60 μL as previously described(Islam *et al.*, 2023; Sun *et al.*, 2011). To facilitate cell attachment, agarose

(40 μL at 0.7% w/v) dissolved in 6 M DMSO was injected into the chamber and allowed to sit at room temperature for 15 min. The chamber was then washed with 400 μL TPM, followed by injection of *M. xanthus* cells (60 μL) into the chamber and left to sit at room temperature onto the agarose-coated surface for 30 min. Unattached cells were then thoroughly washed away with a total of 2 mL TPM media containing 10 mM glucose. The flow chamber was then mounted onto the microscope for imaging.

Uncoated polystyrene beads (diameter 520 nm; Bangs Laboratories) were washed and diluted in 1 mL TPM containing 10 mM glucose and injected into the chamber (1 μL). Single beads were optically trapped and placed near the midpoint of the cell length for each immobilized cell of interest.

3.6.13 Bead tracking and video analysis

Cells of *M. xanthus* with surface-deposited beads were imaged for 3 min, with images captured every 10 s. Movies were analyzed using a custom MATLAB tracking code. Prior to tracking beads, the code filtered and subtracted the background of the image from the cell-attached bead. An internal MATLAB centroid function was then used to identify the center of the bead and converted the *x*,*y* pixel values of the center of the bead in each frame to microns. The *x*,*y* position values of the bead center were then used to compute bead displacements to identify and extract individual motor-driven bead runs. Injection of nigericin (20 μM), a pH gradient/proton-motive force inhibitory drug, into the flow chamber with WT cells was also carried out; this drug was used to disable the molecular motors and reduce bead motion without impacting motor force production allowing us to determine a threshold for a bead run. Similar previous experiments led to negligible bead motion(Sun *et al.*, 2011). Bead runs were characterized as how far the bead displaced above the determined threshold in a single given direction without halting. The displacement for each individual motor-driven bead run was used to compute the average bead speed (μm/min) per run for WT and Δ*cglD* cells.

3.6.14 Analysis of GST affinity chromatography data via mass spectrometry

In duplicate, C-terminal amino acids 800–1218 of *M. xanthus* GltD (formerly AgmU), fused to glutathione-S-transferase (GST), were previously heterologously expressed in *E. coli*,

purified, and used as bait to pull down potential interactors from *M. xanthus* whole-cell lysate (with GST by itself used as a control to identify non-specific binders). Pulldown samples were then digested with trypsin, with raw tandem mass spectra acquired at the UC Berkeley Proteomics/Mass Spectrometry Laboratory using a Thermo LTQ XL mass spectrometer(Nan *et al.*, 2010). Herein, the raw MudPIT mass spectra from these GST-affinity pulldowns were processed using Thermo Proteome Discoverer software (v2.4.1.15) with the SEQUEST search engine at the Concordia University Centre for Biological Applications of Mass Spectrometry. Database searches were carried out against the UniProt *Myxococcus xanthus* DK 1622 proteome database (UP000002402, v2017-10-25). The enzyme for the database search was chosen as trypsin (full), with maximum missed cleavage sites set to 3. Mass tolerances of the precursor and fragment ions were set at 1.0 Da. Dynamic modifications on Methionine (oxidation, +15.995 Da), protein N-terminus (Acetyl, +42.011; Met-loss, -131.040; Met-loss-Acetyl, -89.030) and static modifications on Cysteine (carbamidomethyl, +57.021 Da) were allowed. Only peptides with high confidence were reported. The XCorr confidence thresholds were applied with the factory default values, as 1.5 for z = 1, 2.0 for z = 2, 2.5 for z = 3 and 3.0 for z >=4 ions. To stringently identify "MXAN_" proteins pulled down via the GltD bait, non-specific hits pulled down with the GST-alone controls were first subtracted from GltD-GST hit lists, followed by removal of hits not meeting the quality threshold (2.5 minimum peptides, 26 average score, 16% average coverage) and not detected across both replicates.

3.7 ACKNOWLEDGMENTS

We would like to thank A. Roussel and R. Vincentelli (CNRS–Aix-Marseille University, Architecture et fonction des macromolécules biologiques) for CglD protein used to generate pAb; the Confocal Imaging Facility, a Nikon Center of Excellence, in the Department of Molecular Biology at Princeton University for instrument use and technical advice; G. Laevsky in particular for his support and suggestions.

3.8 FUNDING

This work was funded by Natural Sciences and Engineering Research Council of Canada (NSERC) grants RGPIN-2016-06637 and RGPIN-2023-05576 (to S.T.I.) as well as EQPEQ/472339-2015 and RGPIN-2020-07169 (to A.J.E.); the Banting Research Foundation Discovery Award 2018-1400 (to S.T.I.); the Canadian Institutes of Health Research postdoctoral fellowship (to S.T.I.); the Aix-Marseille University AMIDEX Excellence Program (to S.T.I.); PROTEO, The Quebec Network for Research on Protein Function, Engineering, and Applications studentships (to N.Y.J. and F.S.); the European Research Council, advanced grant JAWS (to T.M.); the Bettencourt-Schueller Foundation, Coup d'élan pour la recherche française 2011 (to T.M.); the National Science Foundation (NSF) grants CAREER PHY-0844466 (to J.W.S.) and PHY-1734030 through the Centre for the Physics of Biological Function (to E.H.); the Fondation ARC studentship (to L.M.F.); the Glenn Centers for Aging Research award (to B.P.B.); National Institutes of Health award P50 GM071508 (to B.P.B.) as well as grants GM20509 (to D.R.Z.) and GM129000 (to B.N.); seed grant from the Indian Institute of Technology Hyderabad (to G.S.); and an INSPIRE grant from the Department of Science and Technology, India (to G.S.).

Chapitre 4 : DISCUSSION GÉNÉRALE

Avant mes travaux de thèse, le mécanisme de *gliding* chez les myxobactéries faisait encore l'objet de vifs débats, et de discussions entre les modèles de propulsion via le *slime*, de pincement du peptidoglycane et des bFAs. C'est dans ce contexte que j'ai entamé mes travaux de doctorat.

À l'époque, on savait que les protéines Agl–Glt était nécessaire à la formation des bFAs et *gliding* des cellules individuelles (Faure *et al.*, 2016); mais le mécanisme par lequel les complexes transmembranaires Agl–Glt se couplaient au substrat et transmettaient les forces à travers l'enveloppe cellulaire était inconnu. En parallèle, les fonctions des protéines CglB et CglD, connues depuis plus de 45 ans comme étant importantes pour la motilité de type *gliding*, restaient méconnues (Hodgkin & Kaiser, 1977; Pathak & Wall, 2012; Spormann, 1999).

Au cours de mes travaux, j'ai réussi à démontrer avec succès que CglB et CglD étaient tous deux des membres essentiels de l'appareil de motilité de *gliding*. La première protéine étant nécessaire pour ancrer les complexes Agl–Glt aux sites des bFAs (Islam *et al.*, 2023), tandis que la seconde est essentielle pour stabiliser ces complexes aux bFAs et conférer la traction au substrat. **CGLB, PROTÉINE IMPLIQUÉE DANS LE *GLIDING***

4.1.1 CglB, l'adhésine essentielle à la fixation

Les travaux sur la protéine CglB ont permis de mettre en avant des fonctions potentielles de la protéine. En premiers lieux, l'étude bio-informatique de la séquence protéique et de la structure a mis en évidence un domaine VWA et un motif MIDAS. Ce genre de domaine est retrouvé dans le vivant chez les protéines qui interagissent avec la matrice extracellulaire, notamment chez les eucaryotes (Whittaker & Hynes, 2002). Par ailleurs, les études biochimiques et d'immunofluorescence ont montré que la protéine CglB est exposée à la surface externe des cellules et se colocalise avec les adhésions focales. De plus, en l'absence de la protéine CglB, le suivi des bFAs a montré que ces derniers n'étaient pas immobiles confirmant que l'hypothèse que CglB intervenait dans la fixation du complexe à la surface, et non au transport du complexe lui-même. Enfin, les travaux de biochimie et de microscopie chez *M. xanthus* — combinés à l'expression hétérologue des protéines connues du complexe de la membrane externe de la machinerie de *gliding* dans une souche d'*E. coli* — ont pu

confirmer l'interaction directe de la protéine CglB avec le complexe Glt de la membrane externe, indiquant que CglB fait partie de la machinerie Agl–Glt.

4.1.2 Comment CglB est sécrétée ?

Ces premiers travaux ouvrent la voie à de nouvelles thématiques de recherche pour approfondir la compréhension de la machinerie de *gliding*. La première portant sur les mécanismes intervenant dans l'exposition de la protéine CglB à la membrane externe. En effet, de plus en plus de lipoprotéines sont identifiées et/ou proposées d'être exposées à la surface, mais les mécanismes restent incertains (Hooda & Moraes, 2018; Konovalova & Silhavy, 2015; Wilson & Bernstein, 2016). La sécrétion de CglB à travers le périplasme et la membrane externe ne semble pas faire intervenir les protéines Glt du complexe de la membrane externe (Islam *et al.*, 2023). Comme mentionné dans la discussion du chapitre 2, une hypothèse possible pour la sécrétion de CglB à la membrane externe est qu'un système commun à *M. xanthus* et *E. coli* BL21 (DE3) permet l'export de la protéine dans la membrane externe. Des travaux récents ont montré que le système de sécrétion de type II (T2SS) est essentiel à l'observation de *gliding* chez *M. xanthus* (Zuckerman *et al.*, 2022). Les conclusions de ces travaux sont que la protéine du T2SS, GspD, est essentielle à la survie de la bactérie (les travaux ont donc été réalisés avec un mutant Δ*gspD* complémenté avec un gène *gspD* inductible). En plus, les auteurs ont montré que les structures observées sur le substrat (via microscopie électronique à transmission) autour d'un pôle des cellules — qu'ils ont postulé être du *slime* — requière la fonction du T2SS. Néanmoins, il n'est pas possible de savoir si l'absence de *slime* entraine l'absence de *gliding*, ou l'inverse. J'émets donc l'hypothèse que le T2SS permettrait la sécrétion de CglB à la membrane externe et donc que son absence dans les travaux mentionnés plus haut entraine l'absence de CglB à la membrane externe et donc l'absence de *gliding*, entrainant l'absence de trainées observables déposées sur les substrats par les cellules motiles. Afin de vérifier cette hypothèse, il pourrait être intéressant de tester de l'immunofluorescence pour marquer CglB dans les souches Δ*gspD*. Il peut être aussi intéressant de tester, par la même méthode des souches d'*E. coli* (exprimant la protéine CglB de façon hétérologue) ne présentant pas le T2SS (Dunstan *et al.*, 2015). L'ensemble de ces deux résultats, associé à des Western-Blots pour s'assurer de la production de la protéine CglB permettrait de confirmer que le T2SS est bien responsable de la sécrétion de CglB à la membrane externe.

4.1.3 Quel est le mécanisme de clivage de CglB ?

Le second axe de recherche ouvert par les travaux sur la protéine CglB est le mécanisme et rôle de clivage de la protéine mis en évidence par les travaux de biochimie avec l'EDTA. L'hypothèse mise en avant serait que l'exposition de la protéine CglB doit être régulée par la protection mise en place par le complexe Glt de la membrane externe. De ce fait, une meilleure compréhension des interactions entre CglB et ce complexe pourrait mettre à jour les mécanismes de régulation. Par ailleurs, le clivage de CglB a été montré comme étant dépendant de la présence d'ion divalent, ce qui pourrait indiquer que la présence de calcium, ion divalent, est nécessaire à la régulation de l'exposition de CglB. L'utilisation de chélateur plus spécifique (EGTA) pourrait confirmer l'ion divalent régulant l'exposition de CglB.

4.1.4 Quel est le lien entre les protéines du périplasme et le module à la membrane externe ?

Le troisième axe de discussion porte sur le mécanisme général de la mise en place de l'adhésion et de la mise en action de CglB comme adhésine fixant la surface à la membrane externe. Ce point de recherche vise à proposer une description plus complète et détaillée de chaque étape, de la mise en place de CglB au module de la membrane externe, à la fixation de la surface, et au détachement de CglB de la surface. Dans le modèle que nous proposons, certaines interactions protéiques notamment entre les protéines GltG/J avec le module de la membrane externe n'ont pas été confirmées. De plus, les mécanismes permettant le transfert d'énergie du moteur AglRQS à travers le périplasme vers le complexe de membrane externe restent incertains.

4.1.5 Quels sont les ligands de l'homologue de l'intégrine-αI, CglB ?

Le quatrième axe de recherche ouvert par l'étude de CglB est celui du ligand et de la possibilité que CglB ait d'autres fonctions que la fixation, mais aussi un rôle de senseur intervenant dans la mise en place de comportement multicellulaire. En effet, l'homologie de structure de CglB avec un domaine αI d'une intégrine et les nombreuses fonctions qu'ont ces dernières chez les eucaryotes suggèrent que CglB pourrait également avoir des fonctions de transduction de signal en plus de la fonction d'adhésion mise en avant dans l'étude.

Les travaux sur CglB ont donc mis en avant une protéine impliquée dans la fixation des surfaces lors du *gliding* au site de bFAe, et ont montré le lien entre cette protéine d'adhésion avec la machinerie connue de *gliding*. D'autre part, les travaux sur la seconde protéine de fonction inconnue (CglD) ont permis de mettre en avant des éléments complémentaires aux travaux réalisés jusqu'ici (Hodgkin & Kaiser, 1977; Pathak & Wall, 2012).

4.2 CGLD, UNE ADHÉSINE PARTENAIRE

4.2.1 CglD, une seconde protéine homologue aux intégrines

L'ensemble des résultats de recherche portant sur CglD (la seconde protéine de fonction inconnue) ont mis en avant certains éléments permettant de renforcer les hypothèses présentées lors de l'étude de la protéine CglB. Tout d'abord, l'étude d'homologie de structure a montré que CglD comportait un domaine homologue au COMP (*cartilage oligomeric matrix protein*), un domaine VWA, et un domaine EGF-*like* typique des intégrines eucaryotes. De plus, la protéine CglD est localisée à la surface de la membrane externe tout comme la protéine CglB et les intégrines.

Par ailleurs, la protéine CglD est co-éluée avec les protéines de la machinerie Agl–Glt, supportant un lien entre la protéine et le complexe de *gliding* de la membrane externe.

En l'absence de la protéine CglD, le *gliding* est moins efficace et le trafic de charge associée à la membrane externe est également compromis, ce qui renforce le lien entre CglD et le *gliding*.

Enfin, les résultats de suivi de cluster d'adhésion focale via AglZ ont montré que ces derniers étaient moins stables et moins regroupés. Le constat que CglD possède un domaine « intégrine-*like* » et que son absence perturbe la mise en place de l'adhésion focale m'a permis d'avancés que CglD pourrait jouer un rôle déterminant dans la perception de la surface et dans la mise en place du complexe de bFA, permettant la fixation efficace de la surface et du *gliding* sur la surface.

4.2.2 CglD, une protéine mécanosenseur ?

Il est connu que les intégrines eucaryotes peuvent jouer un rôle de senseur pour reconnaitre les surfaces et entrainer la formation d'eFA (Kechagia *et al.*, 2019). L'efficacité de *gliding* étant compromise sur certaines surfaces en l'absence de CglD tend à montrer que CglD a un rôle de reconnaissance de surfaces, comparable à celui observé chez les intégrines eucaryotes.

Néanmoins, des questions restent sans réponse à ce jour, notamment la question du mécanisme de communication de CglD avec le reste de la machinerie Agl–Glt. En effet, mon étude n'a pas mis en évidence d'élément indiquant comment le signal serait transmis de CglD vers le reste de la machinerie. Les travaux portant sur les intégrines eucaryotes montrent que les domaines transmembranaires ont la fonction de porter le signal vers une voie de signalisation intracellulaire, mais à ce jour aucun élément n'a indiqué quel domaine de CglD serait transmembranaire ou interagirait directement avec des protéines de la membrane externe. La présence d'un domaine intégré de fixation de calcium (COMP) à la protéine pourrait jouer un rôle dans l'interaction avec les protéines de la membrane externe de la machinerie Agl–Glt et, en général, à la stabilisation des bFAs.

Par ailleurs nombre des interrogations concernant la protéine CglB peuvent être appliquées à la protéine CglD : quel est le mécanisme de sécrétion ? Quels sont les ligands de CglD ? Quels sont les domaines d'interaction entre CglD et les protéines Agl–Glt ?

Néanmoins, ces travaux de recherches nous permettent de mieux comprendre les mécanismes de *gliding* par adhésion focale chez *M. xanthus*. Et ensemble, ces deux articles permettent de mettre en avant plusieurs modèles de fonctionnement de mise en place du *gliding* et de l'adhésion focale chez *M. xanthus*, en se basant sur des modèles eucaryotes et les travaux précédents.

4.3 PERSPECTIVES GÉNÉRALES DE RECHERCHE

En perspective de recherches, et pour compléter les ouvertures présentées dans les articles associés à cette thèse, je propose la mise en place de 3 axes de recherches.

4.3.1 Interaction de la machinerie et ligands

Premièrement, la mise en évidence des interactions protéiques entre les protéines GltK/C/B/A et du module de la membrane externe et les protéines du périplasme GltG et GltJ. L'observation de domaine TonB-*box-like* et en N terminal des protéines GltB et GltA et la confirmation d'une interaction de ces domaines avec des protéines de la membrane externe tendraient à valider une partie du modèle présenté jusqu'alors. De plus une caractérisation de la structure de la machinerie Agl–Glt dans son ensemble par cristallographie ou par microscopie électronique permettrait de confirmer ou d'infirmer plusieurs points du modèle, notamment concernant les interactions protéines-protéines entre les différents modules (Faure *et al.*, 2016).

Deuxièmement, l'identification du (ou des) ligand(s) des protéines intégrines-homologues identifiées permettrait de mieux caractériser leurs fonctions proposées et mettre en évidences les changements de conformations ces dernières, ainsi que les potentielles transductions de signal. De plus, les forces mécaniques requises pour activer la formation des bFAs et d'adhésion sur la surface, ainsi que les forces d'adhésion une fois l'adhésion formée restent à être déterminées.

Ces deux premières perspectives de développement permettraient de mieux comprendre la machinerie de *gliding* chez *M. xanthus*, mais pourront également apporter de nouvelles perspectives de recherches à l'étude des adhésion focales chez d'autres modèles qui présentent des homologies de fonctionnement comme c'est le cas chez la bactérie *F. johnsoniae* qui présente un modèle de *gliding* avec bFA (Nelson *et al.*, 2008) ; ou encore comme chez les eucaryotes dont le parallèle avec notre modèle d'étude a été mis en avant au cours de mes recherches.

4.3.2 Régulation et stabilisation des bFAs

Une seconde perspective de recherches que je propose est d'étudier le lien entre les intégrines et la polarisation des cellules. En effet, la polarisation des cellules est contrôlée par l'accumulation des protéines MglA et MglB (respectivement au pôle avant et arrière des

cellules) (Zhang *et al.*, 2010) en collaboration avec les protéines MglC, RomR et le système Frz (Carreira *et al.*, 2023). La présence de MglB au pôle de la cellule permet le désassemblage de la machinerie via son interaction avec le domaine ZnR de la protéine GltJ (Mignot *et al.*, 2023; Treuner-Lange *et al.*, 2015). Ce contrôle du désassemblage du complexe de *gliding* par MglB, associé à la perturbation de l'assemblage observée chez le mutant Δ*cglD* met en avant un lien potentiel entre la régulation, la formation de la machinerie de gliding par le système MglA/MglB/GltJ/AglZ et la stabilisation de celle-ci par les intégrines CglB et CglD. Sachant que les intégrines sont connues chez les Eucaryotes pour permettre le transfert du signal de la surface des cellules vers le cytoplasme (Kechagia *et al.*, 2019), on peut emmètre l'hypothèse que les « intégrines » CglB/CglD transmettent un signal de désassemblage la protéine GltJ qui permettrait un renforcerait le mécanisme d'hydrolyse de MglA-GTP par MglB.

4.3.3 Stigmergie et coordination des cellules

Une dernière perspective de recherches que je propose porte également sur le ligand, mais sous le point de vue de sa provenance et de sa fonction pour la mise en place des comportements multicellulaires. Une hypothèse présentée depuis plusieurs années est que le *slime*, composé de polysaccarides et de vésicules de la membrane externe, jouerait un rôle dans la régulation du *gliding* et dans la coordination des cellules. Une hypothèse que nous pouvons ajouter est que le ligand de ces intégrines serait sécrété dans le *slime*. La présence d'un ligand des intégrines-like dans ce *slime* confirmerait cette hypothèse et poserait la base d'une potentielle coordination des cellules par stigmergie chez *M. xanthus* via la production de polysaccarides et la reconnaissance de ces derniers par des intégrines lors du *gliding*, permettant de confirmer l'importance du *gliding* des cellules individuelles pour les comportements multicellulaires. Ce quatrième axe de recherche est ciblé autour de la compréhension des mécanismes de coordinations cellulaires. En effet, l'absence de système conventionnel de *quorum sensing* (qui est le système de référence pour la coordination d'action complexe chez les procaryotes,) et les nombreux comportements témoignant d'action coordonnée chez *M. xanthus*, n'est compatible qu'en présence d'un système non caractérisé de coordinations des cellules.

La proposition d'une stigmergie faisant intervenir le *slime*, en opposition à la stigmergie sematectonique identifiée jusqu'alors pour expliquer les *flares* (Gloag *et al.*, 2016; Gloag *et al.*, 2015), expliquerait la fonction du *slime* et répondrait à la problématique d'absence de système de *quorum sensing*. L'utilisation d'un dépôt de polysaccarides comme

moyens de coordinations a été déjà mise en évidence chez d'autres espèces bactériennes (Stahl *et al.*, 1983; Zhao *et al.*, 2013). Par ailleurs, une stigmergie par reconnaissance du *slime* déposée lors du *gliding* expliquerait également l'importance pour les *Myxococcales* d'avoir conservé la machinerie de *gliding* au cours de l'évolution : ces protéines intégrines-homologue seraient l'outil protéique pour reconnaitre les signaux des autres cellules, permettant la coordination des cellules lors des comportements complexes, tels que la prédation ou la formation de corps fructifères. L'exploration de ces hypothèses de recherches permettrait de faire le lien entre le *gliding* des cellules individuelles, la production des polysaccarides et la coordination des comportements multicellulaires observés chez *M. xanthus*.

Le développement de ces 3 propositions de recherche permettra de mieux comprendre le *gliding* chez *M. xanthus,* mais aussi de mieux appréhender les mécanismes d'adhésion focale chez les eucaryotes. Par ailleurs l'étude de la fonction des protéines intégrines-homologues chez notre modèle d'études pourrait également donner une nouvelle compréhension des mécanismes de coordinations des cellules.

BIBLIOGRAPHIE GÉNERALE

Adan-Kubo J, Uenoyama A, Arata T & Miyata M (2006) Morphology of isolated Gli349, a leg protein responsible for Mycoplasma mobile gliding via glass binding, revealed by rotary shadowing electron microscopy. *J. Bacteriol.* 188(8):2821-2828.

Allen RD (1981) Motility. *J. Cell Biol.* 91(3):148.

Anderson AR & Vasiev BN (2005) An individual based model of rippling movement in a myxobacteria population. *J. Theor. Biol.* 234(3):341-349.

Arnaout MA, Goodman SL & Xiong J-P (2007) Structure and mechanics of integrin-based cell adhesion. *Curr. Opin. Cell Biol.* 19(5):495-507.

Arora S, Bhat V & Mittal A (2007) Correlating single cell motility with population growth dynamics for flagellated bacteria. *Biotechnol. Bioeng.* 97(6):1644-1649.

Babalola OO (2010) Beneficial bacteria of agricultural importance. *Biotechnol. Lett.* 32(11):1559-1570.

Balagam R, Litwin DB, Czerwinski F, Sun M, Kaplan HB, Shaevitz JW & Igoshin OA (2014) Myxococcus xanthus gliding motors are elastically coupled to the substrate as predicted by the focal adhesion model of gliding motility. *PLoS Comput. Biol.* 10(5):e1003619.

Barczyk M, Carracedo S & Gullberg D (2010) Integrins. *Cell Tissue Res.* 339(1):269-280.

Beddek AJ & Schryvers AB (2010) The lactoferrin receptor complex in gram negative bacteria. *BioMetals* 23(3):377-386.

Beebe JM (1941) The morphology and cytology of *Myxococcus xanthus*, N. Sp. *J. Bacteriol.* 42(2):193-223.

Belas R (2014) Biofilms, flagella, and mechanosensing of surfaces by bacteria. *Trends Microbiol.* 22(9):517-527.

Berg HC (1976) How spirochetes may swim. *J. Theor. Biol.* 56(2):269-273.

Berg HC (2003) The rotary motor of bacterial flagella. *Annu. Rev. Biochem.* 72(1):19-54.

Berg HC (2004) *E. coli in Motion.* Springer,

Berg HC & Turner L (1979) Movement of microorganisms in viscous environments. *Nature* 278(5702):349-351.

Berleman JE, Chumley T, Cheung P & Kirby JR (2006) Rippling is a predatory behavior in Myxococcus xanthus. *J. Bacteriol.* 188(16):5888-5895.

Berry J-L & Pelicic V (2015) Exceptionally widespread nanomachines composed of type IV pilins: the prokaryotic Swiss Army knives. *FEMS Microbiol. Rev.* 39(1):134-154.

Bhat S, Zhu X, Patel RP, Orlando R & Shimkets LJ (2011) Identification and localization of *Myxococcus xanthus* porins and lipoproteins. *PLoS One* 6(11):e27475.

Blair D & Dufresne E (2023) *The Matlab particle tracking code repository.* https://site.physics.georgetown.edu/matlab/index.html

Braun TF, Khubbar MK, Saffarini DA & McBride MJ (2005) Flavobacterium johnsoniae gliding motility genes identified by mariner mutagenesis. *J. Bacteriol.* 187(20):6943-6952.

Braun TF & McBride MJ (2005) Flavobacterium johnsoniae GldJ is a lipoprotein that is required for gliding motility. *J. Bacteriol.* 187(8):2628-2637.

Bretl DJ & Kirby JR (2016) Molecular mechanisms of signaling in Myxococcus xanthus development. *J. Mol. Biol.* 428(19):3805-3830.

Brockman JM, Blanchard AT, Pui-Yan V, Derricotte WD, Zhang Y, Fay ME, Lam WA, Evangelista FA, Mattheyses AL & Salaita K (2018) Mapping the 3D orientation of piconewton integrin traction forces. *Nat. Meth.* 15(2):115-118.

Budde B, Blumbach K, Ylöstalo J, Zaucke F, Ehlen HWA, Wagener R, Ala-Kokko L, Paulsson M, Bruckner P & Grässel S (2005) Altered integration of matrilin-3 into cartilage extracellular matrix in the absence of collagen IX. *Mol. Cell. Biol.* 25(23):10465-10478.

Burchard RP (1982) Trail following by gliding bacteria. *J. Bacteriol.* 152(1):495-501.

Burrows LL (2012) Pseudomonas aeruginosa twitching motility: type IV pili in action. *Annu. Rev. Microbiol.* 66(1):493-520.

Campbell ID & Humphries MJ (2011) Integrin structure, activation, and interactions. *Cold Spring Harb. perspect. biol.* 3(3):a004994.

Campos JM & Zusman DR (1975) Regulation of development in *Myxococcus xanthus*: effect of 3':5'-cyclic AMP, ADP, and nutrition. *Proc. Natl. Acad. Sci. USA* 72(2):518-522.

Carreira LAM, Szadkowski D, Lometto S, Hochberg GK & Søgaard-Andersen L (2023) Molecular basis and design principles of switchable front-rear polarity and directional migration in Myxococcus xanthus. *Nat. Commun.* 14(1):4056.

Chang Y-W, Rettberg LA, Treuner-Lange A, Iwasa J, Søgaard-Andersen L & Jensen GJ (2016) Architecture of the type IVa pilus machine. *Science* 351(6278):aad2001.

Chao KL, Shang X, Greenfield J, Linden SB, Alreja AB, Nelson DC & Herzberg O (2022) Structure of *Escherichia coli* O157:H7 bacteriophage CBA120 tailspike protein 4 baseplate anchor and tailspike assembly domains (TSP4-N). *Sci. Rep.* 12(1):2061.

Chen FH, Herndon ME, Patel N, Hecht JT, Tuan RS & Lawler J (2007) Interaction of cartilage oligomeric matrix protein/thrombospondin 5 with aggrecan. *J. Biol. Chem.* 282(34):24591-24598.

Chen FH, Thomas AO, Hecht JT, Goldring MB & Lawler J (2005) Cartilage oligomeric matrix protein/thrombospondin 5 supports chondrocyte attachment through interaction with integrins. *J. Biol. Chem.* 280(38):32655-32661.

Cheng C, Wang H, Ma T, Han X, Yang Y, Sun J, Chen Z, Yu H, Hang Y & Liu F (2018) Flagellar basal body structural proteins FlhB, FliM, and FliY are required for flagellar-associated protein expression in Listeria monocytogenes. *Front. Microbiol.* 9:208.

Cheng S & Brooks III CL (2013) Viral capsid proteins are segregated in structural fold space. *PLOS Comput. Biol.* 9(2):e1002905.

Claessen D, Rozen DE, Kuipers OP, Sogaard-Andersen L & van Wezel GP (2014) Bacterial solutions to multicellularity: a tale of biofilms, filaments and fruiting bodies. *Nat. Rev. Microbiol.* 12(2):115-124.

Cohen EJ, Nakane D, Kabata Y, Hendrixson DR, Nishizaka T & Beeby M (2020) Campylobacter jejuni motility integrates specialized cell shape, flagellar filament, and motor, to coordinate action of its opposed flagella. *PLoS Pathog.* 16(7):e1008620.

Cole GB, Bateman TJ & Moraes TF (2021) The surface lipoproteins of gram-negative bacteria: protectors and foragers in harsh environments. *J. Biol. Chem.* 296:100147.

Daniels R, Vanderleyden J & Michiels J (2004) Quorum sensing and swarming migration in bacteria. *FEMS Microbiol. Rev.* 28(3):261-289.

Darnton NC, Turner L, Rojevsky S & Berg HC (2010) Dynamics of bacterial swarming. *Biophys. J.* 98(10):2082-2090.

Di Cesare PE, Chen FS, Moergelin M, Carlson CS, Leslie MP, Perris R & Fang C (2002) Matrix–matrix interaction of cartilage oligomeric matrix protein and fibronectin. *Matrix Biol.* 21(5):461-470.

Dong X, Zhao B, Lin F-Y, Lu C, Rogers BN & Springer TA (2018) High integrin αVβ6 affinity reached by hybrid domain deletion slows ligand-binding on-rate. *Proc. Natl. Acad. Sci. USA* 115(7):E1429-E1436.

Ducret A, Fleuchot B, Bergam P & Mignot T (2013) Direct live imaging of cell–cell protein transfer by transient outer membrane fusion in *Myxococcus xanthus*. *eLife* 2:e00868.

Ducret A, Quardokus EM & Brun YV (2016) MicrobeJ, a tool for high throughput bacterial cell detection and quantitative analysis. *Nat. Microbiol.* 1(7):16077.

Ducret A, Valignat M-P, Mouhamar F, Mignot T & Theodoly O (2012) Wet-surface-enhanced ellipsometric contrast microscopy identifies slime as a major adhesion factor during bacterial surface motility. *Proc. Natl. Acad. Sci. USA* 109(25):10036-10041.

Dunstan RA, Hay ID, Wilksch JJ, Schittenhelm RB, Purcell AW, Clark J, Costin A, Ramm G, Strugnell RA & Lithgow T (2015) Assembly of the secretion pores GspD, Wza and CsgG into bacterial outer membranes does not require the Omp85 proteins BamA or TamA. *Mol. Microbiol.* 97(4):616-629.

Dworkin M (1963) Nutritional regulation of morphogenesis in Myxococcus xanthus. *J. Bacteriol.* 86(1):67-72.

Dworkin M & Voelz H (1962) The formation and germination of microcysts in Myxococcus xanthus. *Microbiology* 28(1):81-85.

Ellison CK, Dalia TN, Vidal Ceballos A, Wang JC-Y, Biais N, Brun YV & Dalia AB (2018) Retraction of DNA-bound type IV competence pili initiates DNA uptake during natural transformation in Vibrio cholerae. *Nat. Microbiol.* 3(7):773-780.

Ellison CK, Kan J, Dillard RS, Kysela DT, Ducret A, Berne C, Hampton CM, Ke Z, Wright ER & Biais N (2017) Obstruction of pilus retraction stimulates bacterial surface sensing. *Science* 358(6362):535-538.

Evans KJ, Lambert C & Sockett RE (2007) Predation by Bdellovibrio bacteriovorus HD100 requires type IV pili. *J. Bacteriol.* 189(13):4850-4859.

Faure LM, Fiche J-B, Espinosa L, Ducret A, Anantharaman V, Luciano J, Lhospice S, Islam ST, Tréguier J, Sotes M, Kuru E, Van Nieuwenhze MS, Brun Y, Théodoly O, L A, Nollmann M & Mignot T (2016) The mechanism of force transmission at bacterial focal adhesion complexes. *Nature* 539(7630):530-535.

Fontes M & Kaiser D (1999) *Myxococcus* cells respond to elastic forces in their substrate. *Proc. Natl. Acad. Sci. USA* 96(14):8052-8057.

Fu G, Bandaria JN, Le Gall AV, Fan X, Yildiz A, Mignot T, Zusman DR & Nan B (2018) MotAB-like machinery drives the movement of MreB filaments during bacterial gliding motility. *Proc. Natl. Acad. Sci. USA* 115(10):2484-2489.

Geiger B, Bershadsky A, Pankov R & Yamada KM (2001) Transmembrane crosstalk between the extracellular matrix and the cytoskeleton. *Nat. Rev. Mol. Cell Biol.* 2(11):793-805.

Gloag ES, Javed MA, Wang H, Gee ML, Wade SA, Turnbull L & Whitchurch CB (2013) Stigmergy: A key driver of self-organization in bacterial biofilms. *Communicative & integrative biology* 6(6):e27331.

Gloag ES, Turnbull L, Javed MA, Wang H, Gee ML, Wade SA & Whitchurch CB (2016) Stigmergy co-ordinates multicellular collective behaviours during *Myxococcus xanthus* surface migration. *Sci. Rep.* 6:26005.

Gloag ES, Turnbull L & Whitchurch CB (2015) Bacterial stigmergy: an organising principle of multicellular collective behaviours of bacteria. *Scientifica (Cairo)* 2015:387342.

Goldman BS, Nierman WC, Kaiser D, Slater SC, Durkin AS, Eisen JA, Ronning CM, Barbazuk WB, Blanchard M, Field C, Halling C, Hinkle G, Iartchuk O, Kim HS, Mackenzie C, Madupu R, Miller N, Shvartsbeyn A, Sullivan SA, Vaudin M, Wiegand R & Kaplan HB (2006) Evolution of sensory complexity recorded in a myxobacterial genome. *Proc. Natl. Acad. Sci. USA* 103(41):15200-15205.

Gram C (1884) Ueber die isolirte Farbung der Schizomyceten in Schnitt-und Trockenpraparaten. *Fortschritte der Medicin* 2:185-189.

Grosberg RK & Strathmann RR (2007) The evolution of multicellularity: a minor major transition? *Annu. Rev. Ecol. Evol. Syst.* 38(1):621-654.

Grossart H-P, Riemann L & Azam F (2001) Bacterial motility in the sea and its ecological implications. *Aquat. Microb. Ecol.* 25(3):247-258.

Grossman AS, Mauer TJ, Forest KT, Goodrich-Blair H & Comstock LE (2021) A widespread bacterial secretion system with diverse substrates. *mBio* 12(4):e01956-01921.

Guttenplan SB, Shaw S & Kearns DB (2013) The cell biology of peritrichous flagella in B acillus subtilis. *Mol. Microbiol.* 87(1):211-229.
Halász K, Kassner A, Mörgelin M & Heinegård D (2007) COMP acts as a catalyst in collagen fibrillogenesis. *J. Biol. Chem.* 282(43):31166-31173.
Han K, Li ZF, Peng R, Zhu LP, Zhou T, Wang LG, Li SG, Zhang XB, Hu W, Wu ZH, Qin N & Li YZ (2013) Extraordinary expansion of a *Sorangium cellulosum* genome from an alkaline milieu. *Sci. Rep.* 3:2101.
Harris BZ, Kaiser D & Singer M (1998) The guanosine nucleotide (p) ppGpp initiates development and A-factor production inMyxococcus xanthus. *Genes Dev.* 12(7):1022-1035.
Harshey RM & Matsuyama T (1994) Dimorphic transition in Escherichia coli and Salmonella typhimurium: surface-induced differentiation into hyperflagellate swarmer cells. *Proc. Natl. Acad. Sci. USA* 91(18):8631-8635.
Hart BA & Zahler SA (1966) Lytic enzyme produced by Myxococcus xanthus. *J. Bacteriol.* 92(6):1632-1637.
Herrick WG, Nguyen TV, Sleiman M, McRae S, Emrick TS & Peyton SR (2013) PEG-phosphorylcholine hydrogels as tunable and versatile platforms for mechanobiology. *Biomacromolecules* 14(7):2294-2304.
Hodgkin J & Kaiser D (1977) Cell-to-cell stimulation of movement in nonmotile mutants of *Myxococcus*. *Proc. Natl. Acad. Sci. USA* 74(7):2938-2942.
Hodgkin J & Kaiser D (1979) Genetics of gliding motility in *Myxococcus xanthus* (myxobacterales): two gene systems control movement. *Mol. Gen. Genet.* 171(2):177-191.
Holkenbrink C, Hoiczyk E, Kahnt J & Higgs PI (2014) Synthesis and assembly of a novel glycan layer in *Myxococcus xanthus* spores. *J. Biol. Chem.* 289(46):32364-32378.
Hooda Y, Lai CC-L, Judd A, Buckwalter CM, Shin HE, Gray-Owen SD & Moraes TF (2016) Slam is an outer membrane protein that is required for the surface display of lipidated virulence factors in *Neisseria*. *Nat. Microbiol.* 1(4):16009.
Hooda Y, Lai CCL & Moraes TF (2017) Identification of a large family of Slam-dependent surface lipoproteins in Gram-negative bacteria. *Front. Cell. Infect. Microbiol.* 7(207):207.
Hooda Y & Moraes TF (2018) Translocation of lipoproteins to the surface of gram negative bacteria. *Curr. Opin. Struct. Biol.* 51:73-79.
Humphries MJ, Symonds EJ & Mould AP (2003) Mapping functional residues onto integrin crystal structures. *Curr. Opin. Struct. Biol.* 13(2):236-243.
Huntley S, Hamann N, Wegener-Feldbrugge S, Treuner-Lange A, Kube M, Reinhardt R, Klages S, Muller R, Ronning CM, Nierman WC & Sogaard-Andersen L (2011) Comparative genomic analysis of fruiting body formation in Myxococcales. *Molecular biology and evolution* 28(2):1083-1097.
Huntley S, Kneip S, Treuner-Lange A & Søgaard-Andersen L (2013) Complete genome sequence of *Myxococcus stipitatus* strain DSM 14675, a fruiting myxobacterium. *Genome Announc.* 1(2):e00100-00113.
Huntley S, Zhang Y, Treuner-Lange A, Kneip S, Sensen CW & Sogaard-Andersen L (2012) Complete genome sequence of the fruiting myxobacterium *Corallococcus coralloides* DSM 2259. *J. Bacteriol.* 194(11):3012-3013.
Huynh MS, Hooda Y, Li YR, Jagielnicki M, Lai CC-L & Moraes TF (2022) Reconstitution of surface lipoprotein translocation through the Slam translocon. *eLife* 11:e72822.
Hynes RO (2002) Integrins: bidirectional, allosteric signaling machines. *Cell* 110(6):673-687.
Imhaus AF & Duménil G (2014) The number of Neisseria meningitidis type IV pili determines host cell interaction. *EMBO J.* 33(16):1767-1783.
Islam ST, Jolivet NY, Cuzin C, Belgrave AM, My L, Fleuchot B, Faure LM, Mahanta U, Kezzo AA, Saïdi F, Sharma G, Fiche J-B, Bratton BP, Herrou J, Nollmann M, Shaevitz JW, Durand E & Mignot T (2023) Unmasking of the von Willebrand A-domain surface adhesin CglB at

bacterial focal adhesions mediates myxobacterial gliding motility. *Sci. Adv.* 9(8):eabq0619.
Islam ST & Lam JS (2013) Topological mapping methods for α-helical bacterial membrane proteins – an update and a guide. *MicrobiologyOpen* 2(2):350-364.
Islam ST & Mignot T (2015) The mysterious nature of bacterial surface (gliding) motility: a focal adhesion-based mechanism in *Myxococcus xanthus*. *Semin. Cell Dev. Biol.* 46:143-154.
Islam ST, Vergara Alvarez I, Saïdi F, Guiseppi A, Vinogradov E, Sharma G, Espinosa L, Morrone C, Brasseur G, Guillemot J-F, Benarouche A, Bridot J-L, Ravicoularamin G, Cagna A, Gauthier C, Singer M, Fierobe H-P, Mignot T & Mauriello EMF (2020) Modulation of bacterial multicellularity via spatio-specific polysaccharide secretion. *PLoS Biol.* 18(6):e3000728.
Ivanova N, Daum C, Lang E, Abt B, Kopitz M, Saunders E, Lapidus A, Lucas S, Glavina Del Rio T, Nolan M, Tice H, Copeland A, Cheng J-F, Chen F, Bruce D, Goodwin L, Pitluck S, Mavromatis K, Pati A, Mikhailova N, Chen A, Palaniappan K, Land M, Hauser L, Chang Y-J, Jeffries CD, Detter JC, Brettin T, Rohde M, Göker M, Bristow J, Markowitz V, Eisen JA, Hugenholtz P, Kyrpides NC & Klenk H-P (2010) Complete genome sequence of Haliangium ochraceum type strain (SMP-2T). *Stand. Genomic Sci.* 2(1):96-106.
Izoré T, Contreras-Martel C, El Mortaji L, Manzano C, Terrasse R, Vernet T, Di Guilmi AM & Dessen A (2010) Structural basis of host cell recognition by the pilus adhesin from *Streptococcus pneumoniae*. *Structure* 18(1):106-115.
Izzard C & Lochner LR (1976) Cell-to-substrate contacts in living fibroblasts: an interference reflexion study with an evaluation of the technique. *J. Cell Sci.* 21(1):129-159.
Jahn E (1924) I. Fam. Archangiaceae. *Beiträge zur botanischen Protistologie. I. Die Polyangiden*, Jahn E (Édit.) Gebruder Borntraeger, Leipzig. p 66-72.
Jain R, Habermann BH & Mignot T (2021) Complete genome assembly of *Myxococcus xanthus* strain DZ2 using long high-fidelity (hifi) reads generated with PacBio technology. *Microbiol. Resour. Announc.* 10(28):e00530-00521.
Jakobczak B, Keilberg D, Wuichet K & Søgaard-Andersen L (2015) Contact- and protein transfer-dependent stimulation of assembly of the gliding motility machinery in *Myxococcus xanthus*. *PLOS Genet.* 11(7):e1005341.
Jakovljevic V, Leonardy S, Hoppert M & Søgaard-Andersen L (2008) PilB and PilT are ATPases acting antagonistically in type IV pilus function in Myxococcus xanthus. *J. Bacteriol.* 190(7):2411-2421.
Jarrell KF & Albers S-V (2012) The archaellum: an old motility structure with a new name. *Trends Microbiol.* 20(7):307-312.
Johnson LS, Eddy SR & Portugaly E (2010) Hidden Markov model speed heuristic and iterative HMM search procedure. *BMC Bioinformatics* 11(1):431.
Josenhans C & Suerbaum S (2002) The role of motility as a virulence factor in bacteria. *Int. J. Med. Microbiol.* 291(8):605-614.
Jumper J, Evans R, Pritzel A, Green T, Figurnov M, Ronneberger O, Tunyasuvunakool K, Bates R, Žídek A, Potapenko A, Bridgland A, Meyer C, Kohl SAA, Ballard AJ, Cowie A, Romera-Paredes B, Nikolov S, Jain R, Adler J, Back T, Petersen S, Reiman D, Clancy E, Zielinski M, Steinegger M, Pacholska M, Berghammer T, Bodenstein S, Silver D, Vinyals O, Senior AW, Kavukcuoglu K, Kohli P & Hassabis D (2021) Highly accurate protein structure prediction with AlphaFold. *Nature* 596(7873):583-589.
Kahnt Jr, Aguiluz K, Koch Jr, Treuner-Lange A, Konovalova A, Huntley S, Hoppert M, Søgaard-Andersen L & Hedderich R (2010) Profiling the outer membrane proteome during growth and development of the social bacterium *Myxococcus xanthus* by selective biotinylation and analyses of outer membrane vesicles. *J. Proteome Res.* 9(10):5197-5208.
Kaiser D (1979) Social gliding is correlated with the presence of pili in Myxococcus xanthus. *Proc. Natl. Acad. Sci. USA* 76(11):5952-5956.

Kaiser D (2004) Signaling in myxobacteria. *Annu. Rev. Microbiol.* 58:75-98.
Kaiser D & Warrick H (2014) Transmission of a signal that synchronizes cell movements in swarms of *Myxococcus xanthus*. *Proc. Natl. Acad. Sci. USA* 111(36):13105-13110.
Kanchanawong P, Shtengel G, Pasapera AM, Ramko EB, Davidson MW, Hess HF & Waterman CM (2010) Nanoscale architecture of integrin-based cell adhesions. *Nature* 468(7323):580-584.
Kang S, Tice AK, Stairs CW, Jones RE, Lahr DJG & Brown MW (2021) The integrin-mediated adhesive complex in the ancestor of animals, fungi, and amoebae. *Curr. Biol.* 31(14):3073-3085.e3073.
Kearns DB (2010) A field guide to bacterial swarming motility. *Nat. Rev. Microbiol.* 8(9):634-644.
Kechagia JZ, Ivaska J & Roca-Cusachs P (2019) Integrins as biomechanical sensors of the microenvironment. *Nat. Rev. Mol. Cell Biol.* 20(8):457-473.
Konovalova A, Petters T & Søgaard-Andersen L (2010) Extracellular biology of *Myxococcus xanthus*. *FEMS Microbiol. Rev.* 34(2):89-106.
Konovalova A & Silhavy TJ (2015) Outer membrane lipoprotein biogenesis: Lol is not the end. *Philos. Trans. R. Soc. Lond. B Biol. Sci.* 370(1679).
Korotkov KV, Sandkvist M & Hol WG (2012) The type II secretion system: biogenesis, molecular architecture and mechanism. *Nat. Rev. Microbiol.* 10(5):336-351.
Krieg NR (1976) Biology of the chemoheterotrophic spirilla. *Bacteriol. Rev.* 40(1):55-115.
Krieg NR, Tomelty JP & Wells Jr JS (1967) Inhibitio of Flagellar Coordination in Spirillum volutans. *J. Bacteriol.* 94(5):1431-1436.
Krishnan V, Dwivedi P, Kim BJ, Samal A, Macon K, Ma X, Mishra A, Doran KS, Ton-That H & Narayana SVL (2013) Structure of *Streptococcus agalactiae* tip pilin GBS104: a model for GBS pili assembly and host interactions. *Acta Crystallogr. D Biol. Crystallogr.* 69(6):1073-1089.
LaFoya B, Munroe JA, Miyamoto A, Detweiler MA, Crow JJ, Gazdik T & Albig AR (2018) Beyond the matrix: the many non-ECM ligands for integrins. *Int. J. Mol. Sci.* 19(2):449.
Lauber F, Deme JC, Lea SM & Berks BC (2018) Type 9 secretion system structures reveal a new protein transport mechanism. *Nature* 564(7734):77-82.
Lee J-O, Bankston LA, Arnaout MA & Liddington RC (1995a) Two conformations of the integrin A-domain (I-domain): a pathway for activation? *Structure* 3(12):1333-1340.
Lee J-O, Rieu P, Arnaout MA & Liddington R (1995b) Crystal structure of the A domain from the a subunit of integrin CR3 (CD11 b/CD18). *Cell* 80(4):631-638.
Leeuwenhoek AV (1677) Observations, communicated to the publisher by Mr. Antony van Leewenhoeck, in a dutch letter of the 9th Octob. 1676. here English'd: concerning little animals by him observed in rain-well-sea- and snow water; as also in water wherein pepper had lain infused. *Philos. Trans. R. Soc. Lond. B Biol. Sci.* 12(133):821-831.
Lemon DJ, Schutzman DA & Garza AG (2018) Bacterial surface spreading is more efficient on nematically aligned polysaccharide substrates. *J. Bacteriol.* 200(7):e00610-00617.
Lemon DJ, Yang X, Srivastava P, Luk Y-Y & Garza AG (2017) Polymertropism of rod-shaped bacteria: movement along aligned polysaccharide fibers. *Sci. Rep.* 7(1):7643.
Letunic I & Bork P (2016) Interactive tree of life (iTOL) v3: an online tool for the display and annotation of phylogenetic and other trees. *Nucleic Acids Res.* 44(W1):W242-W245.
Li Y, Sun H, Ma X, Lu A, Lux R, Zusman D & Shi W (2003) Extracellular polysaccharides mediate pilus retraction during social motility of Myxococcus xanthus. *Proc. Natl. Acad. Sci. USA* 100(9):5443-5448.
Li Z-F, Li X, Liu H, Liu X, Han K, Wu Z-H, Hu W, Li F-f & Li Y-Z (2011) Genome sequence of the halotolerant marine bacterium *Myxococcus fulvus* HW-1. *J. Bacteriol.* 193(18):5015-5016.
Liu S, Calderwood DA & Ginsberg MH (2000) Integrin cytoplasmic domain-binding proteins. *J. Cell Sci.* 113(20):3563-3571.

Luciano J, Agrebi R, Le Gall AV, Wartel M, Fiegna F, Ducret A, Brochier-Armanet C & Mignot T (2011) Emergence and modular evolution of a novel motility machinery in bacteria. *PLOS Genet.* 7(9):e1002268.

Maier B & Wong GC (2015) How bacteria use type IV pili machinery on surfaces. *Trends Microbiol.* 23(12):775-788.

Mann HH, Özbek S, Engel J, Paulsson M & Wagener R (2004) Interactions between the cartilage oligomeric matrix protein and matrilins: implications for matrix assembly and the pathogenesis of chondrodysplasias. *J. Biol. Chem.* 279(24):25294-25298.

Mauriello EMF, Mouhamar F, Nan B, Ducret A, Dai D, Zusman DR & Mignot T (2010) Bacterial motility complexes require the actin-like protein, MreB and the Ras homologue, MglA. *EMBO J.* 29(2):315-326.

Mauriello EMF, Nan B & Zusman DR (2009) AglZ regulates adventurous (A-) motility in *Myxococcus xanthus* through its interaction with the cytoplasmic receptor, FrzCD. *Mol. Microbiol.* 72(4):964-977.

Mignot T (2007) The elusive engine in *Myxococcus xanthus* gliding motility. *Cell. Mol. Life Sci.* 64(21):2733-2745.

Mignot T, Attia B, My L, Castaing JP, Dinet C, Le Guenno H, Schmidt V, Espinosa L, Anantharaman V & Aravind L (2023) A novel molecular switch controls assembly of bacterial focal adhesions.

Mignot T, Shaevitz JW, Hartzell PL & Zusman DR (2007) Evidence that focal adhesion complexes power bacterial gliding motility. *Science* 315(5813):853-856.

Minamino T, Imada K & Namba K (2008) Molecular motors of the bacterial flagella. *Curr. Opin. Struct. Biol.* 18(6):693-701.

Mirdita M, Schütze K, Moriwaki Y, Heo L, Ovchinnikov S & Steinegger M (2022) ColabFold: making protein folding accessible to all. *Nat. Methods* 19(6):679-682.

Miyata M (2008) Centipede and inchworm models to explain Mycoplasma gliding. *Trends Microbiol.* 16(1):6-12.

Miyata M (2010) Unique centipede mechanism of Mycoplasma gliding. *Annu. Rev. Microbiol.* 64:519-537.

Miyata M, Robinson RC, Uyeda TQP, Fukumori Y, Fukushima S, Haruta S, Homma M, Inaba K, Ito M, Kaito C, Kato K, Kenri T, Kinosita Y, Kojima S, Minamino T, Mori H, Nakamura S, Nakane D, Nakayama K, Nishiyama M, Shibata S, Shimabukuro K, Tamakoshi M, Taoka A, Tashiro Y, Tulum I, Wada H & Wakabayashi K (2020) Tree of motility - A proposed history of motility systems in the tree of life. *Genes Cells* 25(1):6-21.

Miyata M & Uenoyama A (2002) Movement on the cell surface of the gliding bacterium, Mycoplasma mobile, is limited to its head-like structure. *FEMS Microbiol. Lett.* 215(2):285-289.

Mizutani M, Sasajima Y & Miyata M (2021) Force and stepwise movements of gliding motility in human pathogenic bacterium Mycoplasma pneumoniae. *Front. Microbiol.* 12:2691.

Müller S, Willett JW, Bahr SM, Darnell CL, Hummels KR, Dong CK, Vlamakis HC & Kirby JR (2013) Draft genome sequence of *Myxococcus xanthus* wild-type strain DZ2, a model organism for predation and development. *Genome Announc.* 1(3):e00217-00213.

Muñoz-Dorado J, Marcos-Torres FJ, García-Bravo E, Moraleda-Muñoz A & Pérez J (2016) Myxobacteria: moving, killing, feeding, and surviving together. *Front. Microbiol.* 7:781.

Nakamura S & Minamino T (2019) Flagella-driven motility of bacteria. *Biomolecules* 9(7):279.

Nakane D & Miyata M (2007) Cytoskeletal “jellyfish” structure of Mycoplasma mobile. *Proc. Natl. Acad. Sci. USA* 104(49):19518-19523.

Nakane D, Sato K, Wada H, McBride MJ & Nakayama K (2013) Helical flow of surface protein required for bacterial gliding motility. *Proc. Natl. Acad. Sci. USA* 110(27):11145-11150.

Nan B, Bandaria JN, Moghtaderi A, Sun I-H, Yildiz A & Zusman DR (2013) Flagella stator homologs function as motors for myxobacterial gliding motility by moving in helical trajectories. *Proc. Natl. Acad. Sci. USA* 110(16):E1508-E1513.
Nan B, Chen J, Neu JC, Berry RM, Oster G & Zusman DR (2011) Myxobacteria gliding motility requires cytoskeleton rotation powered by proton motive force. *Proc. Natl. Acad. Sci. USA* 108(6):2498-2503.
Nan B, Mauriello EMF, Sun I-H, Wong A & Zusman DR (2010) A multi-protein complex from *Myxococcus xanthus* required for bacterial gliding motility. *Mol. Microbiol.* 76(6):1539-1554.
Nan B, McBride Mark J, Chen J, Zusman David R & Oster G (2014) Bacteria that glide with helical tracks. *Curr. Biol.* 24(4):R169-R173.
Nan B & Zusman DR (2016) Novel mechanisms power bacterial gliding motility. *Mol. Microbiol.* 101(2):186-193.
Nelson SS, Bollampalli S & McBride MJ (2008) SprB is a cell surface component of the *Flavobacterium johnsoniae* gliding motility machinery. *J. Bacteriol.* 190(8):2851-2857.
Noinaj N, Guillier M, Barnard TJ & Buchanan SK (2010) TonB-dependent transporters: regulation, structure, and function. *Annu. Rev. Microbiol.* 64:43-60.
Nonaka T, Adan-Kubo J & Miyata M (2010) Triskelion structure of the Gli521 protein, involved in the gliding mechanism of Mycoplasma mobile. *J. Bacteriol.* 192(3):636-642.
Nudleman E, Wall D & Kaiser D (2005) Cell-to-cell transfer of bacterial outer membrane lipoproteins. *Science* 309(125):125-127.
O'Connor KA & Zusman DR (1991) Development in Myxococcus xanthus involves differentiation into two cell types, peripheral rods and spores. *J. Bacteriol.* 173(11):3318-3333.
Ohtani N & Miyata M (2007) Identification of a novel nucleoside triphosphatase from Mycoplasma mobile: a prime candidate motor for gliding motility. *Biochem. J.* 403(1):71-77.
Oliveira NM, Foster KR & Durham WM (2016) Single-cell twitching chemotaxis in developing biofilms. *Proc. Natl. Acad. Sci. USA* 113(23):6532-6537.
Partridge JD & Harshey RM (2013) Swarming: flexible roaming plans. *J. Bacteriol.* 195(5):909-918.
Paszek MJ, Boettiger D, Weaver VM & Hammer DA (2009) Integrin clustering is driven by mechanical resistance from the glycocalyx and the substrate. *PLOS Comput. Biol.* 5(12):e1000604.
Paszek MJ, DuFort CC, Rossier O, Bainer R, Mouw JK, Godula K, Hudak JE, Lakins JN, Wijekoon AC, Cassereau L, Rubashkin MG, Magbanua MJ, Thorn KS, Davidson MW, Rugo HS, Park JW, Hammer DA, Giannone G, Bertozzi CR & Weaver VM (2014) The cancer glycocalyx mechanically primes integrin-mediated growth and survival. *Nature* 511(7509):319-325.
Pathak DT & Wall D (2012) Identification of the *cglC*, *cglD*, *cglE*, and *cglF* genes and their role in cell contact-dependent gliding motility in *Myxococcus xanthus*. *J. Bacteriol.* 194(8):1940-1949.
Pathak DT, Wei X, Bucuvalas A, Haft DH, Gerloff DL & Wall D (2012) Cell contact–dependent outer membrane exchange in Myxobacteria: genetic determinants and mechanism. *PLoS Genet.* 8(4):e1002626.
Pérez-Burgos M & Søgaard-Andersen L (2020) Biosynthesis and function of cell-surface polysaccharides in the social bacterium Myxococcus xanthus. *Biol. Chem.* 401(12):1375-1387.
Persat A, Inclan YF, Engel JN, Stone HA & Gitai Z (2015) Type IV pili mechanochemically regulate virulence factors in Pseudomonas aeruginosa. *Proc. Natl. Acad. Sci. USA* 112(24):7563-7568.
Piepenbrink KH (2019) DNA uptake by type IV filaments. *Front. Mol. Biosci.* 6:1.

Plotnikov SV, Sabass B, Schwarz US & Waterman CM (2014) Chapter 20 - High-resolution traction force microscopy. *Methods Cell Biol.*, Waters JC & Wittman T (Édit.) Academic Press, Vol 123. p 367-394.

Pogoutse AK & Moraes TF (2017) Iron acquisition through the bacterial transferrin receptor. *Crit. Rev. Biochem. Mol. Biol.* 52(3):314-326.

Qian J & Gao H (2010) Soft matrices suppress cooperative behaviors among receptor-ligand bonds in cell adhesion. *PLoS One* 5(8):e12342.

Rawlings ND, Barrett AJ, Thomas PD, Huang X, Bateman A & Finn RD (2018) The MEROPS database of proteolytic enzymes, their substrates and inhibitors in 2017 and a comparison with peptidases in the PANTHER database. *Nucl. Acids Res.* 46(D1):D624-D632.

Raynaud C, Sheppard D, Berry J-L, Gurung I & Pelicic V (2021) PilB from *Streptococcus sanguinis* is a bimodular type IV pilin with a direct role in adhesion. *Proc. Natl. Acad. Sci. USA* 118(22):e2102092118.

Reese MG (2001) Application of a time-delay neural network to promoter annotation in the *Drosophila melanogaster* genome. *Comput. Chem.* 26(1):51-56.

Reichenbach H (1966) Myxococcus spp.(Myxobacteriales) Schwarmentwickling und Bildung von Protocysten. *Encyclopaedia Cinematographica*.

Rodriguez AM & Spormann AM (1999) Genetic and molecular analysis of *cglB*, a gene essential for single-cell gliding in *Myxococcus xanthus*. *J. Bacteriol.* 181(14):4381-4390.

Roussel-Jazédé V, Jongerius I, Bos MP, Tommassen J & van Ulsen P (2010) NalP-mediated proteolytic release of lactoferrin-binding protein B from the meningococcal cell surface. *Infect. Immun.* 78(7):3083-3089.

Ruiz N, Falcone B, Kahne D & Silhavy TJ (2005) Chemical conditionality: a genetic strategy to probe organelle assembly. *Cell* 121(2):307-317.

Sabass B, Gardel ML, Waterman CM & Schwarz US (2008) High resolution traction force microscopy based on experimental and computational advances. *Biophys. J.* 94(1):207-220.

Sabass B, Koch MD, Liu G, Stone HA & Shaevitz JW (2017) Force generation by groups of migrating bacteria. *Proc. Natl. Acad. Sci. USA* 114(28):7266-7271.

Saïdi F, Gamboa Marin OJ, Veytia-Bucheli JI, Vinogradov E, Ravicoularamin G, Jolivet NY, Kezzo AA, Ramirez Esquivel E, Panda A, Sharma G, Vincent SP, Gauthier C & Islam ST (2022a) Evaluation of azido 3-deoxy-D-*manno*-oct-2-ulosonic acid (Kdo) analogues for click chemistry-mediated metabolic labeling of *Myxococcus xanthus* DZ2 lipopolysaccharide. *ACS Omega* 7(39):34997-35013.

Saïdi F, Jolivet NY, Lemon DJ, Nakamura A, Belgrave AM, Garza AG, Veyrier FJ & Islam ST (2021) Bacterial glycocalyx integrity drives multicellular swarm biofilm dynamism. *Mol. Microbiol.* 116(4):1151-1172.

Saïdi F, Mahanta U, Panda A, Kezzo AA, Jolivet NY, Bitazar R, John G, Martinez M, Mellouk A, Calmettes C, Chang Y-W, Sharma G & Islam ST (2022b) Bacterial outer membrane polysaccharide export (OPX) proteins occupy three structural classes with selective β-barrel porin requirements for polymer secretion. *Microbiol. Spectr.* 10(5):e01290-01222.

Schneiker S, Perlova O, Kaiser O, Gerth K, Alici A, Altmeyer MO, Bartels D, Bekel T, Beyer S, Bode E, Bode HB, Bolten CJ, Choudhuri JV, Doss S, Elnakady YA, Frank B, Gaigalat L, Goesmann A, Groeger C, Gross F, Jelsbak L, Jelsbak L, Kalinowski J, Kegler C, Knauber T, Konietzny S, Kopp M, Krause L, Krug D, Linke B, Mahmud T, Martinez-Arias R, McHardy AC, Merai M, Meyer F, Mormann S, Munoz-Dorado J, Perez J, Pradella S, Rachid S, Raddatz G, Rosenau F, Ruckert C, Sasse F, Scharfe M, Schuster SC, Suen G, Treuner-Lange A, Velicer GJ, Vorholter F-J, Weissman KJ, Welch RD, Wenzel SC, Whitworth DE, Wilhelm S, Wittmann C, Blocker H, Puhler A & Muller R (2007) Complete genome sequence of the myxobacterium *Sorangium cellulosum*. *Nat. Biotech.* 25(11):1281-1289.

Schuhmacher JS, Thormann KM & Bange G (2015) How bacteria maintain location and number of flagella? *FEMS Microbiol. Rev.* 39(6):812-822.
Sebé-Pedrós A, Roger AJ, Lang FB, King N & Ruiz-Trillo I (2010) Ancient origin of the integrin-mediated adhesion and signaling machinery. *Proc. Natl. Acad. Sci. USA* 107(22):10142-10147.
Seef S, Herrou J, de Boissier P, My L, Brasseur G, Robert D, Jain R, Mercier R, Cascales E, Habermann BH & Mignot T (2021) A Tad-like apparatus is required for contact-dependent prey killing in predatory social bacteria. *eLife* 10:e72409.
Sharma G, Khatri I & Subramanian S (2016a) Complete genome of the starch-degrading myxobacteria *Sandaracinus amylolyticus* DSM 53668T. *Genome Biol. Evol.* 8(8):2520-2529.
Sharma G, Khatri I & Subramanian S (2018) Comparative genomics of myxobacterial chemosensory systems. *J. Bacteriol.* 200(3):e00620-00617.
Sharma G, Narwani T & Subramanian S (2016b) Complete genome sequence and comparative genomics of a novel myxobacterium *Myxococcus hansupus*. *PLoS One* 11(2):e0148593.
Sharma G & Subramanian S (2017) Unravelling the complete genome of *Archangium gephyra* DSM 2261T and evolutionary insights into myxobacterial chitinases. *Genome Biol. Evol.* 9(5):1304-1311.
Shattil SJ, Kim C & Ginsberg MH (2010) The final steps of integrin activation: the end game. *Nat. Rev. Mol. Cell Biol.* 11(4):288-300.
Shimaoka M & Springer TA (2003) Therapeutic antagonists and conformational regulation of integrin function. *Nat. Rev. Drug Discov.* 2(9):703-716.
Shimaoka M, Takagi J & Springer TA (2002) Conformational regulation of integrin structure and function. *Annu. Rev. Biophys. Biomol. Struct.* 31(1):485-516.
Shimkets L & Seale T (1975) Fruiting-body formation and myxospore differentiation and germination in Mxyococcus xanthus viewed by scanning electron microscopy. *J. Bacteriol.* 121(2):711-720.
Shrivastava A, Johnston JJ, Van Baaren JM & McBride MJ (2013) Flavobacterium johnsoniae GldK, GldL, GldM, and SprA are required for secretion of the cell surface gliding motility adhesins SprB and RemA. *J. Bacteriol.* 195(14):3201-3212.
Shrivastava A, Rhodes RG, Pochiraju S, Nakane D & McBride MJ (2012) Flavobacterium johnsoniae RemA is a mobile cell surface lectin involved in gliding. *J. Bacteriol.* 194(14):3678-3688.
Shultis DD, Purdy MD, Banchs CN & Wiener MC (2006) Outer membrane active transport: structure of the BtuB:TonB complex. *Science* 312(5778):1396-1399.
Silverman M & Simon M (1974) Flagellar rotation and the mechanism of bacterial motility. *Nature* 249(5452):73-74.
Skerker JM & Berg HC (2001) Direct observation of extension and retraction of type IV pili. *Proc. Natl. Acad. Sci. USA* 98(12):6901-6904.
Sliusarenko O, Zusman DR & Oster G (2007) The motors powering A-motility in Myxococcus xanthus are distributed along the cell body. *J. Bacteriol.* 189(21):7920-7921.
Söding J, Biegert A & Lupas AN (2005) The HHpred interactive server for protein homology detection and structure prediction. *Nucl. Acids Res.* 33(suppl 2):W244-W248.
Song G, Koksal AC, Lu C & Springer TA (2012) Shape change in the receptor for gliding motility in *Plasmodium* sporozoites. *Proc. Natl. Acad. Sci. USA* 109(52):21420-21425.
Song G & Springer TA (2014) Structures of the *Toxoplasma* gliding motility adhesin. *Proc. Natl. Acad. Sci. USA* 111(13):4862-4867.
Spormann AM (1999) Gliding motility in bacteria: insights from studies of Myxococcus xanthus. *Microbiol. Mol. Biol. Rev.* 63(3):621-641.
Stahl SJ, Stewart KR & Williams FD (1983) Extracellular slime associated with Proteus mirabilis during swarming. *J. Bacteriol.* 154(2):930-937.

Stamatakis A (2006) RAxML-VI-HPC: maximum likelihood-based phylogenetic analyses with thousands of taxa and mixed models. *Bioinform.* 22(21):2688-2690.
Stanier RY & Van Niel C (1962) The concept of a bacterium. *Archiv für Mikrobiologie* 42:17-35.
Stevens DC, Young J, Carmichael R, Tan J & Taylor RE (2014) Draft genome sequence of gephyronic acid producer *Cystobacter violaceus* strain Cb vi76. *Genome Announc.* 2(6):e01299-01214.
Strohmeyer N, Bharadwaj M, Costell M, Fässler R & Müller DJ (2017) Fibronectin-bound α5β1 integrins sense load and signal to reinforce adhesion in less than a second. *Nat. Mat.* 16(12):1262-1270.
Sun M, Wartel M, Cascales E, Shaevitz JW & Mignot T (2011) Motor-driven intracellular transport powers bacterial gliding motility. *Proc. Natl. Acad. Sci. USA* 108(18):7559-7564.
Sun Z, Guo SS & Fässler R (2016) Integrin-mediated mechanotransduction. *J. Cell Biol.* 215(4):445-456.
Talà L, Fineberg A, Kukura P & Persat A (2019) Pseudomonas aeruginosa orchestrates twitching motility by sequential control of type IV pili movements. *Nat. Microbiol.* 4(5):774-780.
Tamkun JW, DeSimone DW, Fonda D, Patel RS, Buck C, Horwitz AF & Hynes RO (1986) Structure of integrin, a glycoprotein involved in the transmembrane linkage between fibronectin and actin. *Cell* 46(2):271-282.
Tan K, Duquette M, Joachimiak A & Lawler J (2009) The crystal structure of the signature domain of cartilage oligomeric matrix protein: implications for collagen, glycosaminoglycan and integrin binding. *FASEB J.* 23(8):2490-2501.
Tata M, Kumar S, Lach SR, Saha S, Hart EM & Konovalova A (2021) High-throughput suppressor screen demonstrates that RcsF monitors outer membrane integrity and not Bam complex function. *Proc. Natl. Acad. Sci. USA* 118(32):e2100369118.
Thur J, Rosenberg K, Nitsche DP, Pihlajamaa T, Ala-Kokko L, Heinegård D, Paulsson M & Maurer P (2001) Mutations in cartilage oligomeric matrix protein causing pseudoachondroplasia and multiple epiphyseal dysplasia affect binding of calcium and collagen I, II, and IX. *J. Biol. Chem.* 276(9):6083-6092.
Tréguier J, Bugnicourt L, Gay G, Diallo M, Islam ST, Toro A, David L, Théodoly O, Sudre G & Mignot T (2019) Chitosan films for microfluidic studies of single bacteria and perspectives for antibiotic susceptibility testing. *mBio* 10(4):e01375-01319.
Treuner-Lange A, Chang Y-W, Glatter T, Herfurth M, Lindow S, Chreifi G, Jensen GJ & Søgaard-Andersen L (2020) PilY1 and minor pilins form a complex priming the type IVa pilus in *Myxococcus xanthus*. *Nat. Commun.* 11(1):5054.
Treuner-Lange A, Macia E, Guzzo M, Hot E, Faure L, Jakobczak B, Espinosa L, Alcor D, Ducret A, Keilberg D, Castaing JP, Gervais SL, Franco M, Søgaard-Andersen L & Mignot T (2015) The small G-protein MglA connects to the MreB actin cytoskeleton at bacterial focal adhesions. *J. Cell Biol.* 210(2):243-256.
Uenoyama A, Kusumoto A & Miyata M (2004) Identification of a 349-kilodalton protein (Gli349) responsible for cytadherence and glass binding during gliding of Mycoplasma mobile. *J. Bacteriol.* 186(5):1537-1545.
Uenoyama A & Miyata M (2005) Identification of a 123-kilodalton protein (Gli123) involved in machinery for gliding motility of Mycoplasma mobile. *J. Bacteriol.* 187(16):5578-5584.
Uenoyama A, Seto S, Nakane D & Miyata M (2009) Regions on Gli349 and Gli521 protein molecules directly involved in movements of Mycoplasma mobile gliding machinery, suggested by use of inhibitory antibodies and mutants. *J. Bacteriol.* 191(6):1982-1985.
van Leeuwenhoek A (1677) Observations, communicated to the publisher by Mr. Antony van Leewenhoeck, in a dutch letter of the 9th Octob. 1676. here English'd: concerning little animals by him observed in rain-well-sea- and snow water; as also in water wherein pepper had lain infused. *Phil. Trans.* 12(133):821-831.

Vincent MS, Comas Hervada C, Sebban-Kreuzer C, Le Guenno H, Chabalier M, Kosta A, Guerlesquin F, Mignot T, McBride MJ & Cascales E (2022) Dynamic proton-dependent motors power type IX secretion and gliding motility in Flavobacterium. *PLos Biol.* 20(3):e3001443.
Wadhwa N & Berg HC (2022) Bacterial motility: machinery and mechanisms. *Nat. Rev. Microbiol.* 20(3):161-173.
Wall D & Kaiser D (1999) Type IV pili and cell motility. *Mol. Microbiol.* 32(1):01-10.
Wang S, Arellano-Santoyo H, Combs PA & Shaevitz JW (2010) Measuring the bending stiffness of bacterial cells using an optical trap. *J. Vis. Exp.* doi:10.3791/2012(38):e2012.
Webby MN, Williams-Jones DP, Press C & Kleanthous C (2022) Force-generation by the trans-envelope Tol-Pal system. *Front. Microbiol.* 13:852176.
Whittaker CA & Hynes RO (2002) Distribution and evolution of von Willebrand/integrin A domains: widely dispersed domains with roles in cell adhesion and elsewhere. *Mol. Biol. Cell* 13(10):3369-3387.
Wilson MM & Bernstein HD (2016) Surface-exposed lipoproteins: an emerging secretion phenomenon in Gram-negative bacteria. *Trends Microbiol.* 24(3):198-208.
Wolgemuth C, Hoiczyk E, Kaiser D & Oster G (2002) How myxobacteria glide. *Curr. Biol.* 12(5):369-377.
Wolgemuth CW (2005) Force and flexibility of flailing myxobacteria. *Biophys. J.* 89(2):945-950.
Wolgemuth CW, Charon NW, Goldstein SF & Goldstein RE (2006) The flagellar cytoskeleton of the spirochetes. *Microb. Physiol.* 11(3-5):221-227.
Wu M & Eisen JA (2008) A simple, fast, and accurate method of phylogenomic inference. *Genome Biol.* 9(10):R151.
Wu SS & Kaiser D (1995) Genetic and functional evidence that type IV pili are required for social gliding motility in Myxococcus xanthus. *Mol. Microbiol.* 18(3):547-558.
Xie C, Zhu J, Chen X, Mi L, Nishida N & Springer TA (2010) Structure of an integrin with an αI domain, complement receptor type 4. *EMBO J.* 29(3):666-679.
Xiong J-P, Stehle T, Diefenbach B, Zhang R, Dunker R, Scott DL, Joachimiak A, Goodman SL & Arnaout MA (2001) Crystal structure of the extracellular segment of integrin αVβ3. *Science* 294(5541):339-345.
Xiong J-P, Stehle T, Zhang R, Joachimiak A, Frech M, Goodman SL & Arnaout MA (2002) Crystal structure of the extracellular segment of integrin αVβ3 in complex with an Arg-Gly-Asp ligand. *Science* 296(5565):151-155.
Xue S, Mercier R, Guiseppi A, Kosta A, De Cegli R, Gagnot S, Mignot T & Mauriello EM (2022) The differential expression of PilY1 proteins by the HsfBA phosphorelay allows twitching motility in the absence of exopolysaccharides. *PLoS Genet.* 18(4):e1010188.
Yang R, Bartle S, Otto R, Stassinopoulos A, Rogers M, Plamann L & Hartzell P (2004) AglZ is a filament-forming coiled-coil protein required for adventurous gliding motility of *Myxococcus xanthus*. *J. Bacteriol.* 186(18):6168-6178.
Youderian P, Burke N, White DJ & Hartzell PL (2003) Identification of genes required for adventurous gliding motility in *Myxococcus xanthus* with the transposable element *mariner*. *Mol. Microbiol.* 49(2):555-570.
Yu R & Kaiser D (2007) Gliding motility and polarized slime secretion. *Mol. Microbiol.* 63(2):454-467.
Zamir E & Geiger B (2001) Molecular complexity and dynamics of cell-matrix adhesions. *J. Cell Sci.* 114(20):3583-3590.
Zhang Y, Ducret A, Shaevitz J & Mignot T (2012) From individual cell motility to collective behaviors: insights from a prokaryote, *Myxococcus xanthus*. *FEMS Microbiol. Rev.* 36(1):149-164.

Zhang Y, Franco M, Ducret A & Mignot T (2010) A bacterial Ras-like small GTP-binding protein and its cognate GAP establish a dynamic spatial polarity axis to control directed motility. *PLoS Biol.* 8(7):e1000430.

Zhang Y & Skolnick J (2005) TM-align: a protein structure alignment algorithm based on the TM-score. *Nucl. Acids Res.* 33(7):2302-2309.

Zhao K, Tseng BS, Beckerman B, Jin F, Gibiansky ML, Harrison JJ, Luijten E, Parsek MR & Wong GCL (2013) Psl trails guide exploration and microcolony formation in *Pseudomonas aeruginosa* biofilms. *Nature* 497(7449):388-391.

Zhu J, Luo B-H, Xiao T, Zhang C, Nishida N & Springer TA (2008) Structure of a complete integrin ectodomain in a physiologic resting state and activation and deactivation by applied forces. *Mol. Cell* 32(6):849-861.

Zimmermann L, Stephens A, Nam S-Z, Rau D, Kübler J, Lozajic M, Gabler F, Söding J, Lupas AN & Alva V (2018) A completely reimplemented MPI Bioinformatics Toolkit with a new HHpred server at its core. *J. Mol. Biol.* 430(15):2237-2243.

Zuckerman DM, So JMT & Hoiczyk E (2022) Type two secretion systems secretins are necessary for exopolymeric slime secretion in cyanobacteria and myxobacteria. *BioRxiv* 10.1101/2022.03.08.483542:2022.2003.2008.483542.

Zusman DR, Scott AE, Yang Z & Kirby JR (2007) Chemosensory pathways, motility and development in Myxococcus xanthus. *Nat. Rev. Microbiol.* 5(11):862-872.

ANNEXE I : TABLE 3.1 GLTD (AA 800-1218)-GST PULLDOWNS

Ensembl Gene ID	Gene Symbol	Accession	Description
MXAN_0962	**cglD**	**Q1DDQ0**	**Putative lipoprotein [OS=Myxococcus xanthus DK 1622]**
MXAN_1623	MXAN_1623	Q1DBU8	peptidase, M16 (pitrilysin) family [OS=Myxococcus xanthus DK 1622]
MXAN_1624	MXAN_1624	Q1DBU7	peptidase, M16 (pitrilysin) family [OS=Myxococcus xanthus DK 1622]
MXAN_1994	rpsI	Q1DAU4	30S ribosomal protein S9 [OS=Myxococcus xanthus DK 1622]
MXAN_2540	**gltA**	**Q1D9B4**	**Uncharacterized protein [OS=Myxococcus xanthus DK 1622]**
MXAN_2674	MXAN_2674	Q1D8Y2	Uncharacterized protein [OS=Myxococcus xanthus DK 1622]
MXAN_2703	MXAN_2703	Q1D8V3	putative cAMP phosphodiesterases class-II [OS=Myxococcus xanthus DK 1622]
MXAN_2728	MXAN_2728	Q1D8S8	putative NADH dehydrogenase I, G subunit [OS=Myxococcus xanthus DK 1622]
MXAN_2736	MXAN_2736	Q1D8S0	Uncharacterized protein [OS=Myxococcus xanthus DK 1622]
MXAN_3160	MXAN_3160	Q1D7L0	peptidase, M13 (neprilysin) family [OS=Myxococcus xanthus DK 1622]
MXAN_3581	MXAN_3581	Q1D6F2	Peptidyl-dipeptidase A [OS=Myxococcus xanthus DK 1622]
MXAN_3777	guaB	Q1D5W4	inosine-5'-monophosphate dehydrogenase [OS=Myxococcus xanthus DK 1622]
MXAN_3830	MXAN_3830	Q1D5R1	Uncharacterized protein [OS=Myxococcus xanthus DK 1622]
MXAN_4635	MXAN_4635	Q1D3H2	Uncharacterized protein [OS=Myxococcus xanthus DK 1622]
MXAN_4637	MXAN_4637	Q1D3H0	Uncharacterized protein [OS=Myxococcus xanthus DK 1622]

Coverage [%]	AvgCoverage	# Peptides	# PSMs	# Unique Peptides	AvgUniPeps	# AAs	MW [kDa]	calc. pI	Score Sequest HT: Sequest HT
33	**18,5**	**24**	**78**	**24**	**13,5**	**1130**	**117**	**4,37**	**285,55**
29	16,5	14	105	14	8	478	53,2	5,81	327,63
27	17	13	194	13	8	473	51,1	8,5	562,25
42	31	5	36	5	3,5	133	14,9	10,95	123,42
27	**16**	**4**	**12**	**4**	**2,5**	**256**	**27,8**	**6,35**	**40,8**
51	35	6	16	6	4	135	14,9	10,13	48,13
31	20	5	64	5	3	251	27,6	7,5	214,45
27	22,5	10	48	10	8,5	541	59,3	8,68	144,93
41	25	5	262	5	3	78	9,1	9,17	734,79
32	17	18	141	18	9,5	703	78,4	7,05	400,15
34	18	20	80	20	10,5	624	70	6,8	199,2
43	23,5	17	70	17	9,5	485	52	7,11	190,36
24	16	5	23	5	3	325	35,9	6,23	69,78
21	25	5	393	5	5,5	240	24,7	11,12	1103,85
96	66	10	154	10	6,5	113	11,6	4,79	385,58

AvgScore	# Peptides (by Search Engine): Sequest HT	Biological Process	Cellular Component	Molecular Function	Pfam IDs
151,835	**24**				
173,67	14			catalytic activity;metal ion binding	Pf00675, Pf05193
284,22	13			catalytic activity;metal ion binding	Pf00675, Pf05193
69,81	5	metabolic process	ribosome	structural molecule activity	Pf00380, Pf02120
26,975	**4**				
30,055	6				
108,775	5	metabolic process		catalytic activity	Pf00753, Pf02112, Pf12706
86,73	10	metabolic process	membrane	catalytic activity;metal ion binding	Pf00384, Pf10588, Pf13510
368,16	5				
202,485	18	metabolic process		catalytic activity	Pf01431, Pf05649
101,725	20	metabolic process	membrane	catalytic activity	Pf01401, Pf10303
103,12	17	metabolic process		catalytic activity;metal ion binding;nucleotide binding	Pf00478, Pf00571, Pf01070, Pf03060
36,2	5				
582,46	5				Pf04519
206,365	10				Pf04519, Pf10988

KEGG Pathways	# Protein Pathway Groups
	0
	0
	0
Ribosome	1
	0
	0
	0
Oxidative phosphorylation; Metabolic pathways	2
	0
	0
	0
Metabolic pathways; Purine metabolism; Biosynthesis of secondary metabolites	3
	0
	0
	0

Ensembl Gene ID	Gene Symbol	Accession	Description
MXAN_4869	**gltE (agIT)**	**Q1D2U6**	**adventurous gliding motility protein AgIT [OS=Myxococcus xanthus DK 1622]**
MXAN_4894	groES	Q1D2S2	10 kDa chaperonin [OS=Myxococcus xanthus DK 1622]
MXAN_4895	groEL	Q1D2S1	60 kDa chaperonin 2 [OS=Myxococcus xanthus DK 1622]
MXAN_5040	MXAN_5040	Q1D2C8	Aldehyde dehydrogenase family protein [OS=Myxococcus xanthus DK 1622]
MXAN_5152	crdB	Q1D218	OmpA family protein [OS=Myxococcus xanthus DK 1622]
MXAN_5344	rpsB	Q1D1H9	30S ribosomal protein S2 [OS=Myxococcus xanthus DK 1622]
MXAN_5756	tolB	Q1D0D0	Protein TolB [OS=Myxococcus xanthus DK 1622]
MXAN_5933	MXAN_5933	Q1CZV3	peptidase, m48 (ste24 endopeptidase) family [OS=Myxococcus xanthus DK 1622]
MXAN_6106	fibA	Q1CZD2	matrix-associated zinc metalloprotease FibA [OS=Myxococcus xanthus DK 1622]
MXAN_6299	pyk	Q1CYU9	pyruvate kinase [OS=Myxococcus xanthus DK 1622]
MXAN_6337	MXAN_6337	Q1CYR1	putative isocitrate dehydrogenase, NAD-dependent [OS=Myxococcus xanthus DK 1622]
MXAN_6487	MXAN_6487	Q1CYB4	Outer membrane efflux protein domain protein [OS=Myxococcus xanthus DK 1622]
MXAN_6516	ahcY	Q1CY84	Adenosylhomocysteinase [OS=Myxococcus xanthus DK 1622]
MXAN_6660	MXAN_6660	Q1CXU6	Uncharacterized protein [OS=Myxococcus xanthus DK 1622]

Coverage [%]	AvgCoverage	# Peptides	# PSMs	# Unique Peptides	AvgUniPeps	# AAs	MW [kDa]	calc. pI	Score Sequest HT: Sequest HT
24	**16,5**	**9**	**41**	**9**	**6**	**478**	**51,5**	**6,4**	**130,87**
41	25	5	20	5	3	96	10,6	7,25	54,09
70	49	36	404	27	17,5	549	57,9	5,3	1280,21
46	24,5	20	151	20	11	506	55,8	6,55	403,36
38	22	6	78	6	4	249	26,3	4,83	216,11
37	20	12	43	12	6,5	312	34,4	9,11	114,04
23	18	6	14	6	5	431	46	8,21	36,85
36	19	10	53	10	5,5	274	29,2	9,16	140,69
28	17	15	131	15	9,5	744	79,8	5,43	424,72
35	18,5	13	70	13	7	477	51,5	8	180,74
34	42,5	8	183	8	10,5	334	35,8	6,81	579,87
32	19,5	13	65	13	8	467	50,2	5,47	161,18
46	33	29	693	29	18,5	476	52,3	6,54	2043,52
34	26,5	8	36	8	5,5	250	25,3	4,6	93,9

AvgScore	# Peptides (by Search Engine): Sequest HT	Biological Process	Cellular Component	Molecular Function	Pfam IDs
74,265	**9**			**protein binding**	**Pf00515, Pf13414, Pf13424, Pf13429, Pf13432, Pf14559**
27,8	5	metabolic process	cytoplasm	nucleotide binding	Pf00166
689,33	36	metabolic process	cytoplasm	nucleotide binding	Pf00118
209,175	20	metabolic process		catalytic activity	Pf00171
112,15	6		membrane		Pf00691
62,94	12	metabolic process	ribosome	structural molecule activity	Pf00318
26,3	6	metabolic process;transport		catalytic activity;protein binding	Pf00930, Pf04052, Pf07676, Pf10647, Pf14583
71,205	10	metabolic process		catalytic activity	Pf01435
226,825	15	metabolic process		catalytic activity	Pf01447, Pf02868, Pf04151, Pf07504
95,01	13	metabolic process		catalytic activity;metal ion binding	Pf00224, Pf02887
523,92	8	metabolic process		catalytic activity;nucleotide binding	Pf00180, Pf04166
83,955	13	transport		transporter activity	Pf02321
1093,34	29	metabolic process;transport	cytoplasm	catalytic activity;nucleotide binding	Pf00670, Pf01262, Pf02254, Pf02826, Pf05221
57,14	8				

KEGG Pathways	# Protein Pathway Groups
	0
	0
RNA degradation	1
Biosynthesis of secondary metabolites; Glycolysis / Gluconeogenesis; Pyruvate metabolism; Microbial metabolism in diverse environments; Metabolic pathways	5
	0
Ribosome	1
	0
	0
	0
Glycolysis / Gluconeogenesis; Biosynthesis of secondary metabolites; Microbial metabolism in diverse environments; Metabolic pathways; Carbon metabolism; Biosynthesis of amino acids; Pyruvate metabolism; Purine metabolism; Biosynthesis of antibiotics	9
Biosynthesis of antibiotics; Biosynthesis of secondary metabolites; Citrate cycle (TCA cycle); Biosynthesis of amino acids; Microbial metabolism in diverse environments; Carbon metabolism; Metabolic pathways; 2-Oxocarboxylic acid metabolism	8
	0
Metabolic pathways; Cysteine and methionine metabolism	2
	0

Ensembl Gene ID	Gene Symbol	Accession	Description
MXAN_6720	MXAN_6720	Q1CXN6	Putative lipoprotein [OS=Myxococcus xanthus DK 1622]
MXAN_6829	MXAN_6829	Q1CXC7	putative late embryogenesis abundant-like protein [OS=Myxococcus xanthus DK 1622]
MXAN_7212	MXAN_7212	Q1CW98	Uncharacterized protein [OS=Myxococcus xanthus DK 1622]

Coverage [%]	AvgCoverage	# Peptides	# PSMs	# Unique Peptides	AvgUniPeps	# AAs	MW [kDa]	calc. pI	Score Sequest HT: Sequest HT
21	18	3	693	3	2,5	115	11,4	6,52	2437,07
29	16,5	5	28	5	3	256	26,9	9,85	79,21
56	42,5	7	30	7	5	148	14,8	6,54	93,35

xx

AvgScore	# Peptides (by Search Engine): Sequest HT	Biological Process	Cellular Component	Molecular Function	Pfam IDs
1294,49	3				
41,98	5	response to stimulus			Pf03168
58,945	7				

KEGG Pathways	# Protein Pathway Groups
	0
	0
	0

ANNEXE II : PUBLICATIONS EN CO-AUTEUR

1) Evaluation of Azido 3-Deoxy-d-manno-oct-2-ulosonic Acid (Kdo) Analogues for Click Chemistry-Mediated Metabolic Labeling of *Myxococcus xanthus* DZ2 Lipopolysaccharide

Fares Saïdi, Oscar Javier Gamboa Marin, José Ignacio Veytia-Bucheli, Evgeny Vinogradov, Gokulakrishnan Ravicoularamin, **Nicolas Y. Jolivet**, Ahmad A. Kezzo, Eric Ramirez Esquivel, Adyasha Panda, Gaurav Sharma, Stéphane P. Vincent, Charles Gauthier, Salim T. Islam

ACS Omega, 2022, volume 7, issue 39, p.34997–35013

September 23, 2022

https://doi.org/10.1021/acsomega.2c03711

2) Bacterial outer-membrane polysaccharide export (OPX) proteins occupy three structural classes with selective β-barrel porin requirements for polymer secretion

Fares Saïdi†, Utkarsha Mahanta†, Adyasha Panda, **Nicolas Y. Jolivet**, Razieh Bitazar, Gavin John, Matthew Martinez, Abdelkader Mellouk, Charles Calmettes, Yi-Wei Chang, Gaurav Sharma, Salim T. Islam

†contribution égale

Microbiology Spectrum, 2022, volume 10, issue 5, p.01290–01222

October 6, 2022

https://doi.org/10.1128/spectrum.01290-22

3) Bacterial glycocalyx integrity drives multicellular swarm biofilm dynamism

Fares Saïdi, **Nicolas Y. Jolivet**, David J. Lemon, Arnaldo Nakamura, Anthony G. Garza, Frédéric J. Veyrier, Salim T. Islam

Molecular Microbiology, 2021, volume 166, issue 4, p.1151–1172

August 29, 2021

https://doi.org/10.1111/mmi.14803